PALACKÝ UNIVERSITY OLOMOUC

Faculty of Science

Department of Biochemistry

Developmental expression and localization of END-BINDING 1 c and PHOSPHOLIPASE D ALPHA 1 proteins

Ph.D. Thesis

Author:	**Mgr. Dominik Novák**
Study program:	P1406 Biochemistry
Supervisor:	Prof. RNDr. Jozef Šamaj, DrSc.
Form of study:	Full-time study
Submitted:	June 2018

Dedicated to Anička, Magdalenka and Inuška

I hereby declare that this Ph.D. thesis has been written solely by me. All the sources cited in this thesis are listed in the reference list. All published results included in this work are approved by co-authors.

In Olomouc,

Dominik Novák

Poděkování

Chtěl bych poděkovat mému školiteli, profesoru Jozefu Šamajovi za jeho vedení, pondělní porady s cennými radami, za možnost strávit stáž s rodinou, za trpělivost a pomoc během sepisování disertační práce. Kromě toho bych rád poděkoval skoro profesorovi Miroslavu Ovečkovi a všem ostatním kolegům z Oddělení Buněčné Biologie.

Taktéž mnohé díky profesoru Teunovi Munnikovi za možnost být na tři měsíce členem jeho týmu.

Zvlášť vřele bych chtěl poděkovat mojí milované ženě Aničce a skvělým dceruškám Magdalence a Inušce a take celé rodině!

V neposlední řadě patří mé díky všem blízkým.

Tato práce byla financována z grantu č. LO1204 (Udržitelný rozvoj výzkumu v Centru Regionu Haná) z národního programu udržitelnosti I, MŠMT ČR.

Tato práce byla podpořena Grantovou agenturou České Republiky (GAČR), 16-22044S, Funkční regulace fosfolipasy D alfa 1 prostřednictvím MPK3 závislé fosforylace.

Acknowledgements

I wish to express my thanks to my supervisor Prof. Jozef Šamaj for his leadership, Monday meetings with valuable suggestions, opportunity to take the internship with my family, patience and help during the assembly of the present thesis. Furthermore, I would like to thank nerly Prof. Miroslav Ovečka and all members of Deparment of Cell Biology.

My thanks belong also to Prof. Teun Munnik for the opportunity to be a member of his team for three months.

Especially, I would like to thank my lovely wife Anička and awesome daughters Magdalenka and Inuška and to whole family!

Last, but not least I would like to thank all close people around me.

This work was funded by grant No. LO1204 (Sustainable development of research in the Centre of the Region Haná) from the National Program of Sustainability I, MEYS, Czech Republic.

This work was supported by Czech Science Foundation (GAČR), 16-22044S, Regulation of phospholipase D alpha 1 function by MPK3-dependent phosphorylation.

Bibliografická identifikace

Jméno a příjmení autora:	Mgr. Dominik Novák
Název práce:	Vývojová exprese a lokalizace proteinů END-BINDING 1 c a FOSFOLIPASA D ALFA 1
Typ práce:	Disertační
Pracoviště:	Centrum regionu Haná pro biotechnologický a zemědělský výzkum, Oddělení buněčné biologie, Přírodovědecká fakulta, Univerzita Palackého v Olomouci
Vedoucí práce:	Prof. RNDr. Jozef Šamaj, DrSc.
Rok obhajoby práce:	2018
Klíčová slova:	END-BINDING 1 c (EB1c), AT5G67270, jádro, kořenová špička, vývoj, přechodná zóna kořene, light-sheet mikroskopie, *Arabidopsis thaliana*, lokalizace, mikrotubuly, FOSFOLIPASA D ALFA 1 (PLDα1), AT3G15730
Počet stran:	179
Počet příloh:	4
Jazyk:	Anglický

Abstrakt

Tato disertační práce je zaměřena na END-BINDING protein 1c (EB1c) a protein FOSFOLIPASA D ALFA 1 (PLDα1) a zahrnuje jejich vývojovou expresi a lokalizaci v semenáčcích *Arabidopsis thaliana* za použití pokročilých mikroskopických technik.

Hlavní kořen vyšších rostlin je anatomicky definován v bočním směru existencí zástupů buněk v konkrétních pletivech, podélně pak přítomností odlišných vývojových zón. Pro rostliny specifický EB1c, který je u *Arabidopsis thaliana* jedním ze tří členů EB1 proteinové rodiny, vykazuje v nedělících se buňkách kořenové špičky výraznou jadernou lokalizaci. Za použití moderního „light-sheet“ fluorescenčního mikroskopu

(LSFM) jsme kvantifikovali vývojově regulovanou expresi GFP-značeného proteinu EB1c, která byla kontrolována nativním *EB1c* promotorem. Kvantifikace byla provedena ve vztahu k velikosti buněčných jader v různých kořenových pletivech (epidermis, primární kůra, endodermis) a v jednotlivých kořenových vývojových zónách (meristém, přechodná a prodlužovací zóna). Naše výsledky podpořily teorii, že v kořenové špičce hraje přechodná zóna jedinečnou úlohu v programování buněk během jejich vývoje při přechodu z rychlého dělení k diferenciaci. Kromě toho byl klonován fúzní konstrukt *DRONPA* s *EB1c* pod kontrolou vlastního *EB1c* promotoru, který byl přechodně transformován do listů *Nicotiana benthamiana* a stabilně do rostlin *Arabidopsis thaliana*. Fotoaktivační lokalizační mikroskopie (PALM) ukázala bodovou akumulaci EB1c-DRONPA proteinu v buněčných jádrech.

PLDα1 protein a jeho produkt kyselina fosfatidová, hrají důležitou roli v mnoha fyziologických a buněčných procesech. Zaměřili jsme se na studium vývojového expresního vzoru a subcelulární lokalizaci tohoto proteinu za použití kombinace LSFM, mikroskopie se strukturovaným osvětlením (SIM), mikroskopie s rotujícím diskem a konfokální mikroskopie. Knock-out *pldα1* mutanti, komplementovaní fúzním proteinem PLDα1-YFP pod kontrolou vlastního *PLDα1* promotoru, vykazovali vyšší akumulaci PLDα1-YFP v kořenové čepičce a ve špičkách rostoucích kořenových vlásků. V epidermálních buňkách listů, řapíků a hypokotylů byl PLDα1-YFP lokalizován v cytoplazmě, a vykazoval zvýšenou akumulaci v oblasti kortikální cytoplazmatické vrstvy. Nicméně v dělících se kořenových a řapíkových buňkách byl PLDα1-YFP obohacený v dělícím vřeténku a fragmoplastu, což naznačila jeho kolokalizace s mikrotubuly. Tato studie ukázala vývojově kontrolovanou expresi a subcelulární lokalizaci PLDα1 proteinu jak v dělících se, tak nedělících se buňkách.

Bibliographical identification

Author´s first name and surname:	Mgr. Dominik Novák
Title:	Developmental expression and localization of END-BINDING 1 c and PHOSPHOLIPASE D ALPHA 1 proteins
Type of thesis:	Ph.D.
Department:	Centre of the Region Haná for Biotechnological and Agricultural Research, Department of Cell Biology, Faculty of Science, Palacký University Olomouc
Supervisor:	Prof. RNDr. Jozef Šamaj, DrSc.
The year of presentation:	2018
Key words:	END-BINDING 1 c (EB1c), AT5G67270, nucleus, root apex, development, root transition zone, light-sheet microscopy, *Arabidopsis thaliana*, localization, microtubules, PHOSPHOLIPASE D ALPHA 1 (PLDα1), AT3G15730
Number of pages:	179
Number of appendixes:	4
Language:	English

Abstract

This Ph.D. thesis is focused mainly on END-BINDING protein 1c (EB1c) and PHOSPHOLIPASE D ALPHA 1 (PLDα1) protein including their developmental expression and localization in *Arabidopsis thaliana* seedlings using advanced microscopy techniques.

Primary root of higher plants is anatomically defined laterally by the existence of cell files in particular tissues and longitudinally by the presence of distinct developmental zones. Plant specific EB1c, one of the three members of EB1 protein family of

Arabidopsis thaliana, shows prominent nuclear localization in non-dividing cells in the root apex. Using advanced light-sheet fluorescence microscopy (LSFM), we quantified developmentally regulated expression levels of GFP-tagged EB1c protein under the control of native *EB1c* promoter. This was done in relation to the nuclear sizes in diverse root tissues (epidermis, cortex and endodermis) and root developmental zones (meristematic, transition and elongation zone). Our results supported the unique role of the transition root zone in the developmental cell reprogramming during the transition of cells from cell proliferation to cell differentiation in the developing root apex. Moreover, *DRONPA*-tagged *EB1c* construct under the control of *EB1c* native promoter was cloned, transiently transformed to *Nicotiana benthamiana* leaves and stably transformed to *Arabidopsis thaliana* plants. Photoactivation localization microscopy showed spot-like accumulation of EB1c-DRONPA in the nucleus.

PLDα1 and its product phosphatidic acid play important roles in many cellular and physiological processes. Here we aimed to study developmental expression pattern and subcellular localization of PLDα1 using combination of LSFM, structured illumination microscopy, spinning disk and confocal microscopy. Complemented knock-out *pldα1* mutants with YFP-tagged PLDα1 under control of *PLDα1* native promoter showed higher accumulation of PLDα1-YFP in the root cap and in tips of growing root hairs. In aerial parts PLDα1-YFP was localized in the cytoplasm with enhanced accumulation in the cortical cytoplasmic layer of epidermal non-dividing cells of leaves, petioles and hypocotyls. However, in dividing root and petiole cells PLDα1-YFP was enriched in mitotic spindles and phragmoplasts, as suggested by co-visualization with microtubules. This study revealed developmentally-controlled expression and subcellular localization of PLDα1 in dividing and non-dividing cells.

Content

Aim of work

- Summary of the recent knowledge on cytoskeleton, mitogen activated protein kinases, end-binding 1 focused on EB1c protein, phospholipases focused on PLDα1 and microscopy.
- Developmental localization and quantification of EB1c protein in Arabidopsis root using light-sheet fluorescence microscopy.
- Preparation of *proEB1c::EB1c:DRONPA* and its transient transformation in *Nicotiana benthamiana* leaves and stable transformation in *Arabidopsis thaliana* plants.
- Identification and transformation of *pldα1* mutant with *proPLDα1::PLDα1:YFP* construct.
- Investigation of developmental expression pattern and subcellular localization of PLDα1-YFP in Arabidopsis seedlings.

Introduction

Novák D.

Introduction to the cytoskeleton

Cells of higher plants are immobile and tightly enclosed in cell walls. On the other hand, vigorous movements can be observed inside plant cells. The plant cytoskeleton is essential for these intracellular movements. In general, cytoskeleton determines shape and growth orientation of cells, contributes to organelle and macromolecule movements, and plays a crucial role in the cell division and in the programmed cell death (Smertenko and Franklin-Tong, 2011; Zhang and Dawe, 2011). The plant cytoskeleton is composed of microtubules (MTs) and actin filaments (AFs) (Wasteneys, 2002). Both components of cytoskeleton are evolutionarily highly conserved and highly dynamic in living cells.

Microtubules

MTs in plant cells were first investigated by transmission electron microscope (TEM) during the 1960s (Ledbetter and Porter, 1963). They form tubular polymers of 13 protofilaments, which are composed from two globular proteins, α- and β-tubulin making heterodimers. Inner diameter of MT cylinder in TEM is 14 nm while outer diameter is 25 nm (Tilney et al., 1973). In Arabidopsis, 6 isoforms of α- and 9 isoforms of β-tubulin were discovered (Kopczak et al., 1992). MT structure is polarized with a dynamic plus-end which ends up with β-tubulin and is responsible for most of the end-wise growth/shrinkage of the MT, while minus-end is ending with α-tubulin.

Plant MT systems include cortical MT arrays (**Fig. 1A**), the preprophase band (PPB), the mitotic spindle and the phragmoplast. Precise coordination of MT reorganization is necessary for proper cell expansion and division. Cortical MTs are located beneath the plasma membrane (PM) and close to the cell wall and usually form parallel arrays coordinated with the axis of expansion. In the G2 phase of the cell cycle, MTs create a cortical ring surrounding the nucleus at the equatorial plane which is called the PPB (**Fig. 1B**). PPB is the determinant of cell division plane orientation. Decomposition of nuclear envelope and PPB disassembly coincide with the formation of the MT-based mitotic spindle. The function of the mitotic spindle (**Fig. 1C**) is the faithful separation of chromosomes. In plant cells, spindle poles are not tightly focused in the polar regions and this relates to the absence of defined microtubule organizing centers such as the centrosomes of animal cells (Baskin and Cande, 1990). At the end of anaphase, the mitotic spindle gives its place to the phragmoplast. The phragmoplast is bipolar and

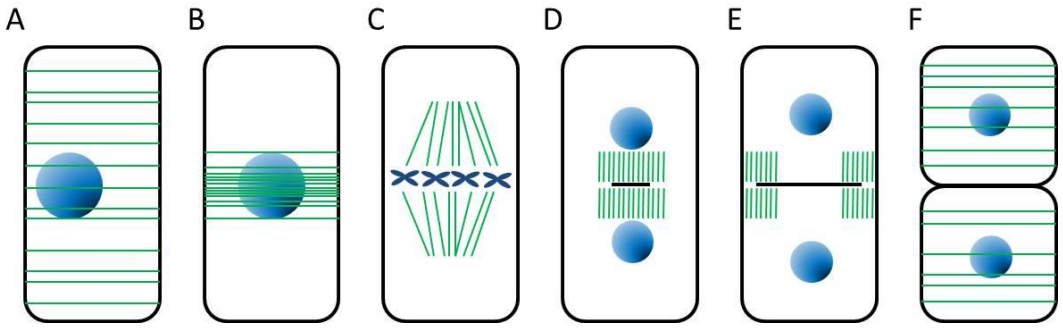

Fig. 1 The schematic illustration of microtubule arrays (green) through plant cell cycle showing position of nuclei and chromosomes (blue). (**A**) Interphase cell with cortical microtubules, (**B**) cell in G2 phase with preprophase band, (**C**) metaphase spindle, (**D**) early phragmoplast, (**E**) late phragmoplast, (**F**) interphase G1 cells. Adapted from Wasteneys, (2002).

built by antiparallel MT systems, in a way that plus ends are orientated towards the cell midplane (**Fig. 1D**). Phragmoplast is expanding centrifugally from the middle of the dividing cell to the parental cell wall and follows the plane predefined by the PPB (**Fig. 1E**). After cell division, MTs are abundant at the periphery of nucleus and radiate toward the cell cortex. This perinuclear MT array is transient (Hasezawa et al., 2000). After this stage, MTs accumulate at the cell periphery in the close association with the PM (**Fig. 1F**).

Plant MTs have been successfully visualized using both green fluorescent protein (GFP)-tubulin fusions (Nakamura et al., 2004) and GFP-tagged microtubule-associated proteins (MAPs) such as mammalian MICROTUBULE-ASSOCIATED PROTEIN 4 (MAP4) (Marc et al., 1998), several isoforms of Arabidopsis microtubule-associated proteins 65 (MAP65) or members of the End-Binding 1 protein family (Van Damme et al., 2004).

Actin cytoskeleton

The actin cytoskeleton plays important roles in plant cell morphogenesis, division, expansion and organelle positioning. Actin cytoskeleton is a continuously re-arranging intracellular scaffold. Filamentous actin (F-actin) together with myosins coordinates cytoplasmic streaming in plant cells. Formation of F-actin network depends on the biochemical interactions of actin monomers and actin-binding proteins (ABPs). Actin filament cables and networks participate on organelle motility, vesicle trafficking, vacuolar morphogenesis, and regulate exocytotic vesicle delivery and fusion (Hussey at al., 2006). Properties of actin cytoskeleton depend also on F-actin depolymerization into

monomeric globular actin (G-actin). Actin filaments having diameter of 7 nm are more flexible than MTs and they are composed of two helical intertwined fibers with a "barbed" and "pointed" end. Actin filaments exhibit different dynamic properties on individual fiber ends (Li and Gundersen, 2008).

Actin depolymerization can be induced several drugs from which latrunculins and cytochalasins are the most frequently used. Latrunculins are capable of reversible and rapid disruption of the actin cytoskeleton. Latrunculin B binds to the ATP-binding (adenosine triphosphate) pocket of G-actin and changes its structure, therefore prevents incorporation of such G-actin to the F-actin. The lack of free G-actin for actin polymerization changes ratio between G-actin and F-actin and results in actin depolymerization (Morton et al., 2000). Cytochalasins are capping free ends of F-actin which prevents the addition of G-actin, and such inhibition of polymerization causes actin depolymerization (Brown and Spudich, 1979). Disrupted actin cytoskeleton affects developmental processes like root elongation (Baluska et al., 2001), root hair formation (Baluska at al., 2000), trichome elongation (Mathur et al., 1999) and vesicular transport (Voigt at al., 2005a).

ABPs control nucleation, polymerization, capping, severing and crosslinking of actin filaments (dos Remedios et al., 2003; Thomas et al., 2009; Winder and Ayscough, 2005). G-actin can spontaneously form new actin filaments under its high concentration. In living cells, G-actin is prevented from spontaneous nucleation by actin-sequestering proteins. Constructs based on the carboxy-terminal (C-terminal) actin-binding domain 2 of Arabidopsis fimbrin fABD2 (Sheahan et al., 2004; Voigt et al., 2005b), C-terminus of mouse talin which is unable to nucleate actin polymerization (Kost et al., 1998) and fluorescently tagged 17 amino acid actin-binding peptide known as LifeAct (Riedl et al., 2008; Era et al., 2009) were developed to visualize F-actin in plant cells. Crosslinking of actin filaments into bundles is essential for the assembly and stabilization of specific cytoskeletal structures. Evolutionary conserved family of actin bundling proteins contains two LIM domains. Actin bundles are formed by WLIM1 proteins binding to single actin filaments and promoting their interaction and zippering (Hoffmann et al., 2014).

Introduction to mitogen activated protein kinases

Because all plants are sessile organisms, they developed strategies to survive and adapt to the environment. These adaptations include dynamic changes in enzymatic activities and gene expression profiles. Phosphorylation of proteins is the most frequent post-translational modification and it is performed by protein kinases. Mitogen-activated protein kinases (MAPKs) are organized in conserved signalling cascades which play important roles in signal transduction of diverse environmental conditions and hormonal changes across all eukaryotes (Colcombet and Hirt, 2008). Arabidopsis MAPK cascades are involved in signalling pathways activated by abiotic stresses such as heat, cold, wounding, salt, ultra violet (UV) or osmotic shock. The main activated MAPKs in Arabidopsis are MITOGEN-ACTIVATED PROTEIN KINASE 3 (MPK3), MITOGEN-ACTIVATED PROTEIN KINASE 4 (MPK4) and MITOGEN-ACTIVATED PROTEIN KINASE 6 (MPK6) (Colcombet and Hirt, 2008) and these three kinases are also most studied. MAPK cascade typically consists of three kinases: mitogen-activated protein kinase kinase kinase (MAPKKK or MAP3K), which reversibly phosphorylates mitogen-activated protein kinase kinase (MAPKK or MAP2K), finally phosphorylating downstream MAPK (**Fig. 2**). MAPKKKs are serine/threonine kinases which phosphorylate conserved S/T-X3-5-S/T motif in the activation loop of MAPKK (Tanoue and Nishida, 2003). Subsequently, dual-specific MAPKKs phosphorylate both threonine and tyrosine residues of conserved T-X-Y motifs of MAPKs (Keshet and Seger, 2010). Phosphorylated MAPKs regulate activities of different targets (substrates) including cytoskeletal proteins (Šamajová et al., 2013), other protein kinases or transcription factors (Ishihama and Yoshioka, 2012). In some cases, one additional tier of phosphorylation includes upstream MAPKKK activators that are known as MAPKKK kinases (MAPKKKKs or MAP4Ks) (Keshet and Seger, 2010). Sequencing of Arabidopsis genome revealed over 60 putative genes for MAPKKKs, 10 for MAPKKs and 20 for MAPKs (Colcombet and Hirt, 2008). Since number of MAPKKKs is higher in comparison to MAPKKs and MAPKs there is extensive cross talk and redundancy in MAPK signalling (Jonak et al., 2002). Moreover, individual MAPKs can be activated by diverse stimuli (Lee et al., 2008) and multiple MAPKs can be activated by single stimulus (Andreasson and Ellis, 2010). One substrate can be also activated by multiple MAPKs. For example, MICROTUBULE ASSOCIATED PROTEIN 65-1 (MAP65-1) can be phosphorylated *in vitro* by diverse MAPKs, mainly by MPK4 and MPK6 (Smertenko et al., 2006). A phosphoproteomic study identified 39 potential

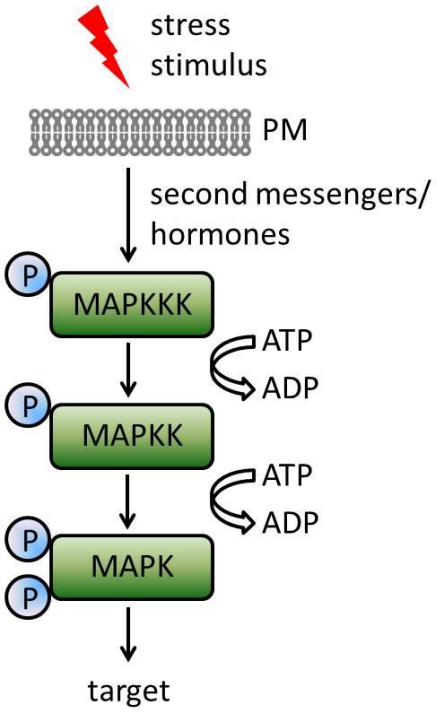

Fig. 2 The schematic illustration of MAPK signalling cascade. PM – plasma membrane. Adapted from Smékalová et al., (2014).

substrates of MPK6 and 48 substrates of MPK3 while 26 of them were common for both kinases (Feilner et al., 2005).

MAPKs play important role as key regulators of plant cytokinesis by regulation of phragmoplast MTs. The MAP65-1 protein, which bundles antiparallel MTs by forming 25 nm dimeric cross-bridges, is active in all cell division stages excluding prometaphase and metaphase. Activity of MAP65-1 is strictly controlled and this control is provided by phosphorylation which lowers its affinity for the microtubule surface (Smertenko et al., 2006). MAP65-1 binds to the PPB, however, as the PPB disassembles, protein becomes mainly cytoplasmic (Smertenko et al., 2004). During prometaphase and metaphase, MAP65-1 is hyperphosphorylated by cyclin-dependent kinase (CDK), MPK4 and MPK6 (Smertenko et al., 2006; Sasabe et al., 2011). This phosphorylation inhibits MAP65-1 activity and prevents its binding to the mitotic spindle. As the chromosomes are separated, MAP65-1 associates with MTs again in anaphase and it is strictly localized in the midzone of spindle and in the midzone of phragmoplast during telophase (Smertenko et al., 2004). Furthermore, interactions between MPK6, MAP65-1 and MTs were confirmed by co-immunoprecipitation assays and quantitative co-localization studies (Smékalová et al., 2014). Moreover, expression of non

phosphorylatable MAP65-1 caused accumulation of MTs in metaphase spindle midzone and delay from metaphase to anaphase transition (Smertenko et al., 2006). These results confirm that MAP65-1 dynamically interacts with MTs, its activity is regulated in a cell cycle-dependent manner and is inhibited by phosphorylation provided by MAPKs. Next, MAP65-1 dependent modulation of MTs organization is controlled and affected by binding of MAP65-1 to phosphatidic acid (PA). Thus PA, as a product of PHOSPHOLIPASE D ALPHA 1 (PLDα1), regulates MAP65-1 during plant response to the salt stress (Zhang et al., 2012). In this case, PLDα1 seems to be related to the both MAPKs and cytoskeleton. However, direct functional regulation of PLDα1 by reversible MAPK-dependent phosphorylation was not reported so far. Using *in silico* prediction approach with Group-based Prediction System ver. 2.1 (Xue et al., 2011), PLDα1 was significantly deemed to contain Pro directed Ser/Thr motif (SP-motif) with serine at the position 481 which can serve as a potential MAPK phosphorylation site.

Assistance *in silico* predictions identified other potential cytoskeletal proteins, which are activated by MAPK phosphorylation. Among others, END-BINDING 1 c (EB1c) protein was identified as a potential target of MAPKs (Šamajová et al., 2013). Substrates of MAPKs require two sequential motives (Bardwell et al., 2009). The first one is docking motif (D-domain), which is responsible for interaction with MAPKs, and the second one is SP-motif. EB1c contains five SP-motifs and one D-domain with KRKLIVNLDV sequence (Šamajová et al., 2013). In 2015, interaction and phosphorylation of EB1c by MPK6 was confirmed by immunopurification of EB1c-GFP and *in vitro* kinase assay (Kohoutová et al., 2015).

General introduction to Arabidopsis root

Primary root (**Fig. 3**) of higher plants is anatomically defined in lateral direction by the existence of distinct cell files forming individual tissues such as epidermis (also called rhizodermis), representing the outer root layer, cortex, endodermis, pericycle and stele containing phloem, procambium, metaxylem and protoxylem. All these tissues originate from stem cells surrounding the root quiescent center (Weigel and Jurgens, 2002). In addition, root tip is protected by root cap consisting of columella and lateral root cap cells. Longitudinally, root is defined by occurrence of distinct developmental zones such as meristematic region which is followed by post-mitotic transition, elongation and differentiation zones (Verbelen et al., 2006; Baluška and Mancuso, 2013).

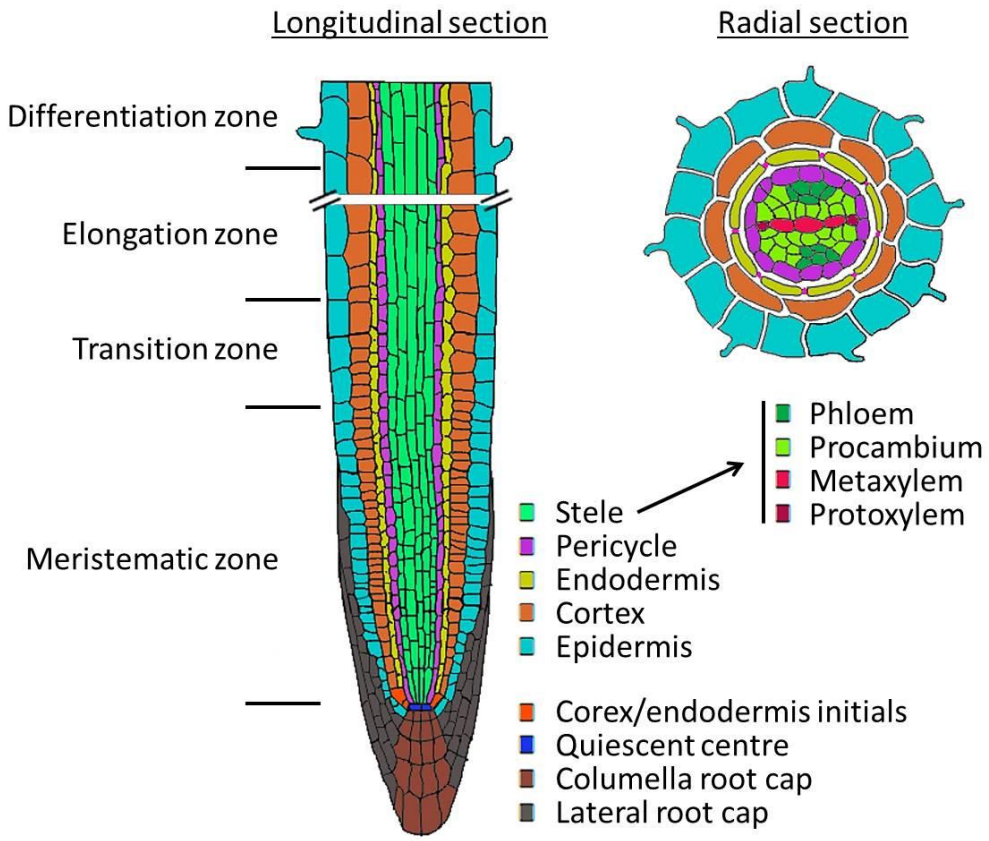

Fig. 3 Longitudinal and radial organization of Arabidopsis root. Root zonation into individual developmental zones consisting of meristematic, transition, elongation and differentiation zones. Radial section of root in the differentiation zone. Adapted from De Smet et al., (2015).

The meristematic zone is defined by successive cell divisions of actively dividing cells (van der Weele et al., 2003). The transition zone is interpolated between the meristematic and the elongation zone (Baluška et al., 1990). Cells of this zone exhibit unique physiological behaviors including hormone fluxes, oscillations of ions and specific patterns of gene expression (Benková and Hejatko, 2009; McLamore et al., 2010; Baluška and Mancuso, 2013). In the elongation zone, cells are switching from mitotic to endoreduplication cycles and increase deoxyribonucleic acid (DNA) amount in their nuclei (Hayashi et al., 2013). This switch from mitosis to endoreduplication causes inactivation of mitotic CDKs (Adachi et al., 2011).

Introduction to EB1c

Microtubule plus-end tracking proteins

MT plus-end tracking proteins (+TIPs) are conserved proteins in eukaryotes and regulate MTs plus-end dynamics (Jiang and Akhmanova, 2011). First identified +TIPs were plant proteins from End-Binding 1 (EB1) family (Chan et al., 2003).

EB1

The EB1 protein family represents a typical example of +TIPs. EB1 proteins regulate spindle MT dynamics (Draviam et al., 2006), serve for recruitment of other +TIPs (Akhmanova and Steinmetz, 2008) and might be targeted to kinetochores (Tirnauer et al., 2002). They are composed of C-terminal EB1 unique homology domain (EBH) responsible for EB1 dimerization and interaction with other proteins. Moreover, C-terminal part contains autoinhibitory domain interacting with amino-terminal (N-terminal) calponin-homology (CH) domain (Hayashi et al., 2005) which is also responsible for the interaction with MTs (Komarova et al., 2009).

Arabidopsis genome encodes three EB1 proteins, namely END-BINDING 1 a (EB1a) (At3g47690), END-BINDING 1 b (EB1b) (At5g62500) and EB1c (At5g67270) (Bisgrove et al., 2008). EB1a and EB1b are typical members of MTs +TIPs. When fused with GFP under the control of native promotor, all EB1 members localize to mitotic spindle and phragmoplast, however, only EB1a and EB1b decorate the plus ends of cortical MTs during the interphase (Chan et al., 2003; Mathur et al., 2003; Komaki et al., 2010). In contrast, EB1c shows nuclear localization during the interphase and seems to have some different functions (Bisgrove et al., 2008; Komaki et al., 2010). EB1a and EB1b share 78% identity at amino acid (AA) level. EB1c shares only 49% homology with EB1a and EB1b (Bisgrove et al., 2008). EB1a and EB1b, but not EB1c, possess acidic AA residues on C-terminal tail showing autoinhibitory function. EB1a and EB1b can form both homodimers and heterodimers.

EB1c

Plant specific EB1c of *Arabidopsis thaliana* (**Fig. 4**) shows prominent nuclear localization in non-dividing interphase and post-cytokinetic cells of root apex (Komaki et al., 2010, Novák et al., 2016). In comparison to EB1a and EB1b, C-terminal part of EB1c contains nuclear localization sequence (NLS) including basic residues and protein

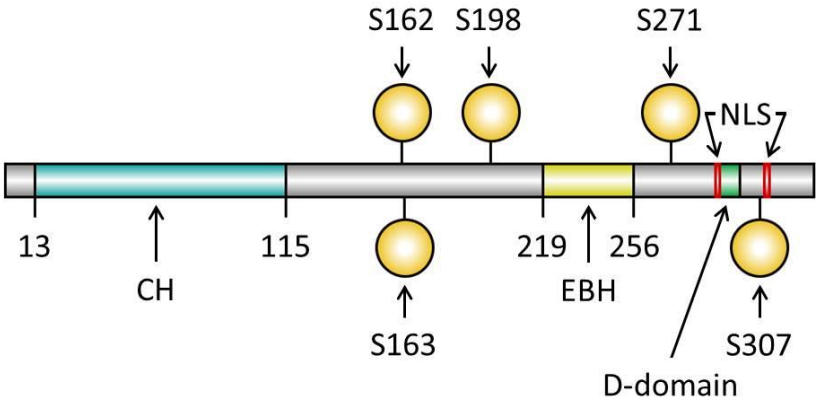

Fig. 4 Graphical depiction of EB1c protein with its domains. CH – calponin homology domain responsible for the interaction with MTs, EBH – EB1 unique homology domain responsible for dimerization and interaction with other proteins, S162/163/198/271/307 – SP motifs with serine which can serve as potential mitogen-activated protein kinase (MAPK) phosphorylation site, D-domain in position 289-299 is responsible for interaction with MAPKs, NLS – nuclear localization sequences with basic residues in positions 289-291 and 309-311. Created with IBS software (http://ibs.biocuckoo.org/).

becomes actively transported to the nucleus at the end of cytokinesis (Bisgrove et al., 2008). EB1c forms only homodimers. In addition, EB1c contains five SP-motives at positions 162, 163, 198, 271 and 307 and one D-domain motif KRKLIVNLDV at positions 289-298 which is targeted by protein kinases implicated in the cell cycle including MAPK and CDK (Šamajová et al., 2013). It is known that proteins from animal EB1 family are regulated by phosphorylation (Tamura and Draviam, 2012). Recently, interaction between EB1c and MAPK called MPK6 was shown in plants (Kohoutová et al., 2015). Knock-out (KO) *eb1c* (mutant of END-BINDING 1 c) mutants are hypersensitive to MT disrupting drugs (Bisgrove et al., 2008) and show fragmented phragmoplasts and collapsed spindles more frequently than double *eb1a eb1b* (mutant of END-BINDING 1 a and END-BINDING 1 b) mutants (Komaki et al., 2010). This effect is more pronounced after treatment with oryzalin, a MT depolymerizing drug. Altogether, these data indicate that EB1c plays important role in chromosome segregation in plants.

Introduction to phospholipases

Lipases are serine hydrolases defined as triacylglycerol acyl hydrolases (E.C. 3.1.1.3.) widespread in nature (Casas-Godoy et al., 2012). Lipases catalyze hydrolysis of the ester bond of mono-, di- and tri-glycerides into glycerol and fatty acid.

Phospholipases

Phospholipids are major components of all biological membranes in all living organisms. Phospholipases (PLs) can cleave various bonds in phospholipids, and they are widespread in nature. PLs are divided to four major classes: A (subdivided in A1 and A2), B, C and D. These classes are distinguished by the type of catalytic reaction (**Fig. 5**). The phospholipases A (PLA1 and PLA2) produce free fatty acid and 1-acyl lysophospholipid or 2-acyl lysophospolipid, respectively. Phospholipase B (PLB) cleaves fatty acid linked to the lysophospholipid (it is also named lysophospholipase). Phospholipase C (PLC) cleaves glycerophosphate bond like phosphodiesterase while phospholipase D (PLD) cleaves phosphodieteric bond (phosphorus-oxygen) after the phosphate. PLs A1, A2, C and D have been partially characterized in plants (Wang, 2001). They play important roles in cellular regulations, lipid degradation and membrane lipid remodeling (Wang, 2004). These cellular regulations include signalling, responses to drought (Sang et al., 2001), salt (Hong et al., 2008) and other abiotic and biotic stresses, vesicular trafficking, secretion, stomatal opening and closure (Jiang et al., 2014), cytoskeletal remodeling (Zhang et al., 2012) and promoting pollen tube growth. Furthermore, some phospholipases are involved in biosynthesis of storage lipids like triacylglycerol.

PLA

PLA hydrolyzes phospholipids to produce free fatty acids and lysophospholipids. PLA generated free fatty acid such as linolenic acid can be converted into oxylipin compounds such as jasmonic acid (JA) and its derivatives. Generally, PLA products play important roles in several biological processes including cell elongation, biosynthesis of JA and gravitropism. PLA superfamily has two subtypes, namely PLA1 and PLA2. Twelve isoforms of PLA1 and four of PLA2 have been identified in Arabidopsis genome (Ryu, 2004).

PLC

PLC hydrolyzes phospholipids to produce phosphorylated head group and diacylglycerol (DAG). Plants have three different groups of PLCs. In Arabidopsis, the first one is nonspecific PLC (NPC with 6 members), the second one is phosphoinositide-specific PLC (PI-PLC with 9 members) and the third one is glycosylphosphatidylinositol PLC (GPI-PLC, GPI-PLD activity has not been characterized in plants) (Nakamura et al., 2005; Peters et al., 2010). NPC hydrolyzes

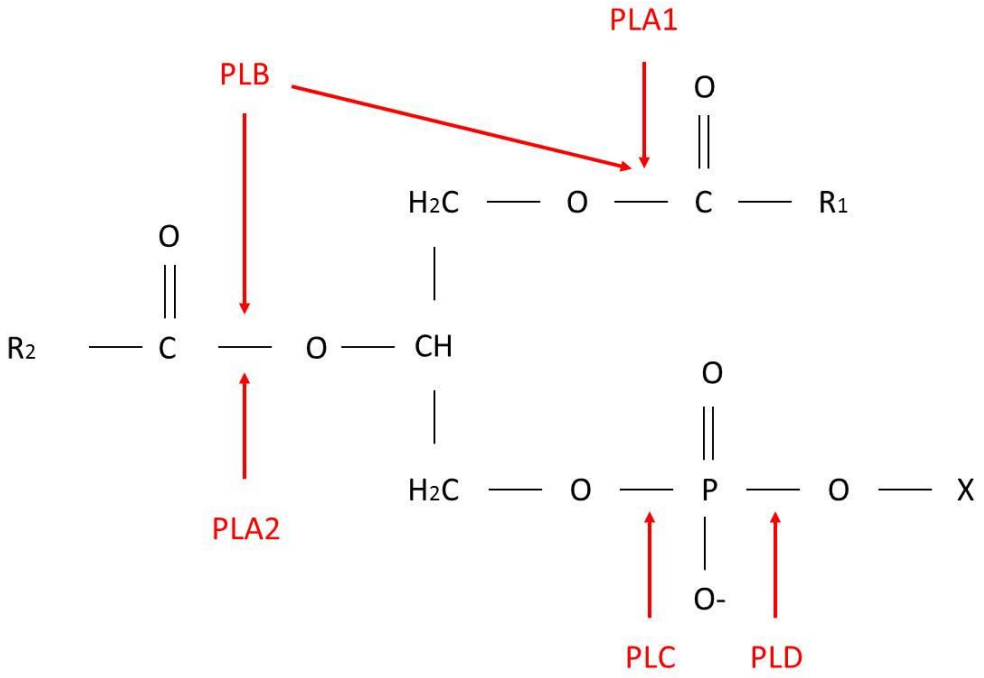

Fig. 5 Hydrolysis of phospholipids by phospholipases PLA1, PLA2, PLB, PLC and PLD. Arrows shows sites of cleavage. R1 and R2 represent hydrophobic fatty acid tail, X represent hydrophilic head group of phospholipids. Adapted from Aloulou et al., (2012).

ordinary membrane phospholipids like phophatidylcholine (PC) and phosphatidylethanolamine (PE), PI-PLC hydrolyzes phosphoinositides and GPI-PLC hydrolyzes GPI-anchored proteins (Wang, 2001). PA can be formed by combination of PLC and diacylglycerolkinase (DGK with 7 members in Arabidopsis). DAG can be produced by PI-PLC and NPC. Further, DGK phosphorylates DAG to the PA (Arisz et al., 2009).

PLD

Family of PLD enzymes (E.C. 3.1.4.4.) represents the main group of membrane phospholipid enzymes in plants. PLDs catalyze the hydrolysis of structural glycerophospholipids, e.g. PC, PE and phosphatidylglycerol (PG) as substrates (Pappan et al., 1998) to produce membrane-derived secondary messenger PA. This process of transphosphatidylation of water producing PA, also produces free soluble head group e.g. choline or ethanolamine, respectively (Munnik and Musgrave, 2001). Genome of the *Arabidopsis thaliana* contains twelve *PLD* genes in comparison to only two genes in animals and one in yeast (Eliáš et al., 2002; Wang et al., 2012). Plant PLDs can be subdivided to six classes: α (α1, α2, α3), β (β1, β2), γ (γ1, γ2, γ3), δ, ε and ζ (ζ1, ζ2)

based on their gene architecture, domain structures, sequence similarities, protein sequence homology and biochemical properties (Qin and Wang, 2002).

PA

PA is minor phospholipid in Arabidopsis membranes, constituting approximately 1% of total phospholipids. Nevertheless, PA level can change dramatically in response to stimuli, such as wounding or pathogen attack. PA is present in all membranes of living cells. The largest PA pool in the plant cells is located in endoplasmic reticulum (ER), followed by chloroplast and mitochondria (Testerink and Munnik, 2011). PA is composed from various species with different length of carbon chain and number of double bonds. The major PA carbon chains in Arabidopsis are 16:0-18:2; 16:0-18:3; 18:2-18:2; 18:2-18:3 and 18:3-18:3 (Hong et al., 2010). These differences in acyl species affect properties of PA interactions with different proteins. PA has been reported to bind to protein phosphatases, protein kinases, lipid kinases, transcription factors, and proteins involved in cytoskeletal remodeling and vesicular trafficking. The formation of PA and other signalling lipids in response to stress is transient. The enzymes, that break PA down are equally important for its signalling function as those which are involved in PA synthesis (Testerink and Munnik, 2011). Enzymes, dephosphorylating PA include lipid phosphate phosphatases and PA hydrolases acting on phosphoric monoester bonds. On the other hand, PA can be phosphorylated by PA kinase (van Schooten et al., 2006). It is also important to mention that PA is not only signalling molecule, but it is an important intermediate of lipid biosynthesis. Data indicate that the PA signal transduction is mediated by PA binding to specific protein targets (Testerink and Munnik, 2005). This PA binding regulates protein activity and conformational changes (Testerink and Munnik, 2005). In addition, local accumulation of PA has strong effect on membrane curvature and surface charge (Kooijman et al., 2003).

Reaction catalyzed by PLD

The transphosphatidylation reaction is catalyzed in two steps. In the first step, the head group is removed, and in the second one, covalent phosphatidyl-PLD product is formed between histidine nucleophile residue (in one HKD motif) and phosphorus. Histidine residue from second HKD motif acts as general acid in the cleavage of phosphodiester bond (Stuckey and Dixon, 1999). PLD catalyzes transphosphatidylation reaction in the presence of primary alcohol. This reaction is unique to PLD and can be used for

identification of enzyme activity *in vivo*. Phosphatidyl moiety is transferred to a primary alcohol (R-OH), such as 1-buthanol to produce phosphatidylbuthanol (Heller, 1978; Quarles and Dawson, 1969). Formation of the phosphatidylalcohol can be used like an indicator for PLD activity while alcohol treatments have been used to investigate PLD function. Production of PA is activated in stress responses by both PLDs and PLC while DGK also contributes to PA production (Meijer and Munnik, 2003).

The presence of high concentration of Ca^{2+} (millimolar concentration) and acidic pH are essential for *in vitro* activation of PLDα class but it does not require inclusion of phosphatidylinositolbisphosphate (PIP_2) in the lipid substrate. Ca^{2+} requirement by PLDα1 is similar to physiological conditions. PHOSPHOLIPASE D BETA (PLDβ) and PHOSPHOLIPASE D GAMMA (PLDγ) classes require PIP_2, neutral pH and micromolar concentration of Ca^{2+} *in vitro*. PHOSPHOLIPASE D DELTA (PLDδ) is PIP_2 independent, active at micromolar to millimolar concentrations of Ca^{2+} at neutral pH, and it is stimulated by free monounsaturated fatty acid oleate (Qin et al., 2002). PHOSPHOLIPASE D EPSILON (PLDε) is active at similar conditions to PLDα1 and PLDδ, and it requires oleic acid for activity with micromolar concentration of Ca^{2+} (Hong et al., 2009). In contrast, two members of PHOSPHOLIPASE D ZETA (PLDζ) class do not require Ca^{2+} but they require neutral pH and PIP_2 (Qin and Wang, 2002). In plants, PLD activity is also regulated by α-subunits of heterotrimeric G-proteins (Lein and Saalbach, 2001) and by actin cytoskeleton (Kusner et al., 2003). Requirements of PLDs and their distinct biochemical properties are summarized in **Tab. 1**.

PLD subclasses

PLDα

PHOSPHOLIPASE D ALPHA 2 (PLDα2) is much more similar to PLDα1 than PHOSPHOLIPASE D ALPHA 3 (PLDα3) in terms of sequence and expression pattern while expression level of PLDα1 is much higher than PLDα3. PLDα3 enhances root growth under hyperosmotic stress and plays a positive role during salt and drought stress (Hong et al., 2008). KO mutant of PHOSPHOLIPASE D ALPHA 3 (*pldα3*) plants are more sensitive to hyperosmotic stress caused by salinity in comparison to *PLDα1* overexpressing (OE) plants. Under water deficiency and salt stress *pldα3* mutants show reduced root growth. Moreover, these mutants exhibit delayed flowering. Opposite situation is in OE *PLDα3* plants showing early flowering enabling to complete life cycle earlier (Hong et al., 2008).

Tab. 1 Requirements of Arabidopsis PLDs and their substrate preferences.

Type	Group	Ca^{2+}	pH	PIP2	Substrate preference
		Requirement			
C2 PLDs	PLDα1	mM	acidic	no	PC>PE
	PLDα2	mM	acidic	no	PC=PE
	PLDα3	mM	acidic	no	PC<PE
	PLDβ1	μM	neutral	yes	PC=PE
	PLDβ2	μM	neutral	yes	PC=PE
	PLDγ1	μM	neutral	yes	PC<PE
	PLDγ2	μM	neutral	yes	PC<PE
	PLDγ3	μM	neutral	yes	PC<PE
	PLDδ	μM<mM	neutral	no	PE>PC
	PLDε	mM	acidic/neutral	no	PC>PE>PG
PX PH PLDs	PLDζ1	no	neutral	yes	PC
	PLDζ2	no	neutral	yes	PC

PLDδ

It has been shown that membrane-bound PLDδ is activated in response to H_2O_2 produced after salt and dehydration stress. This suggests that PLDδ plays an important role in the protection of cells against damage by reactive oxygen species (ROS) (Zhang et al., 2003).

PLDε

PLDε is mainly associated with PM and is active under similar conditions to PLDα1, PLDβ and PLDδ (Hong et al., 2009). The expression level of *PLDε* is much lower than for *PLDα1*. KO *pldε* (mutant of PHOSPHOLIPASE D EPSILON) mutants exhibit 50% of PA level in comparison to the wild type. They show shorter lateral roots. In contrast, OE *PLDε* plants display better root growth as wild type, and they have higher biomass production (Hong et al., 2009).

PLD protein domains

Most PLD enzymes in eukaryotes possess at N-terminus calcium-dependent phospholipid-binding domain (C2), whereas mammalian and plant members of PLDζ contain Phox Homology (PX) and Pleckstrin Homology (PH) domains responsible for lipid binding. Characteristic active site at C-terminus consists of two duplicated and conserved HxKxxxxD domains (HKD) essential for lipase activity (Bargmann and Munnik, 2006). Both HKD motifs interact with each other to form the reactive center and they are separated by more than 300 AA in Arabidopsis (Qin and Wang, 2002). Point mutations of conserved histidines to asparagines in the HKD motifs uncovered

that these residues are critical for enzyme reactivity (Gottlin et al., 1998). PLDs in Arabidopsis can be subdivided into two groups. Ten PLDs (from subfamilies α, β, γ, δ and ε) contain C2 domain while two (from subfamily ζ) share more homology with mammalian and yeast PLDs and contain PX and PH lipid-binding domains. PX and PH domains mediate binding of PLDs to the membrane where they are linked to polyphosphoinositide signalling (van Leeuwen et al., 2004). Moreover, C2 PH and PX domains are implicated in protein-protein interactions while C2 domain binds Ca^{2+} and phospholipids. This C2 domain consists of about 130 AA. Studies on mammalian PLDs proved that the PX domain is more critical for PLD activity in comparison to the PH domain. These results were obtained by deletion studies (Sung et al., 1999a; Sung et al., 1999b).

According to their functional domains PLDs can be subdivided into two groups (**Fig. 6**): the Pleckstrin homology and Phox homology domain-containing PLDs (PX/PH-PLDs) and the calcium-dependent phospholipid binding domain-containing PLDs (C2-PLDs) (Hong et al., 2016). Interestingly, PLDβ1 contains actin binding site which is located after second HKD motif (Kusner et al., 2002). PLDα1 protein contains DRY homologue motif (between AA residues 562 and 586) interacting with small G alpha protein and stimulating its GTPase activity (Zhao and Wang, 2004). Finally, PLDδ contains oleate-binding domain which is located after the first HKD motif (Wang and Wang, 2001).

PLD substrates

PLDs with C2 domains mainly utilize these substrates: PC, PE and PG (Qin and Wang, 2002). PLDα1, α3 and ε prefer PC and PE. PLDδ and γ1 prefer PE before PC. PLDα3 and PLDε can hydrolyze phosphatidylserine (PS) with low activity (Hong et al., 2008; Hong et al., 2009). Phosphatidylinositol activity has not been detected in the case of Arabidopsis PLDs tested *in vitro* (Li et al., 2009). PLDs with PX and PH domains mainly utilize PC as substrate (Qin and Wang, 2002).

PLD localization

PLDα1 is the most abundant PLD and its expression and subcellular localization is developmentally controlled (Fan et al., 1999). PLDα1 fluorescently tagged with YELLOW FLUORESCENT PROTEIN (YFP) and expressed under native promoter showed accumulation in the root cap and epidermis with considerably higher expression in thichoblasts before and during root hair formation and growth. PLDα1-YFP

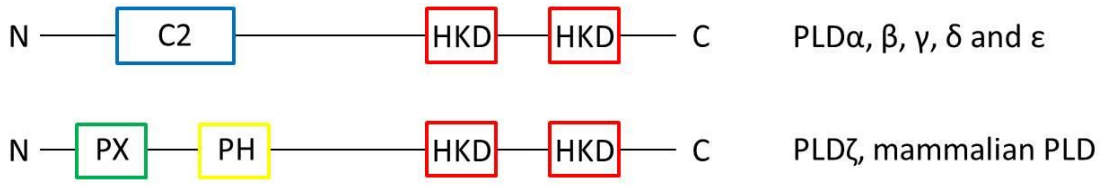

Fig. 6 Functional domains of PLDs. Each PLD contains two HKD catalytic domains in C-terminus. PLDα, -β, -γ, -δ and -ε possess C2 domain, whereas PLDζ and mammalian PLDs contain PX and PH domains. Adapted from Bargmann and Munnik (2006).

accumulated mainly in tips of growing root hairs. In root cap cells and in cells of root transition zone PLDα1-YFP showed cytoplasmic subcellular localization. In aerial parts of plants it was also localized in the cytoplasm showing enhanced accumulation in the cortical cytoplasmic layer of epidermal non-dividing cells of hypocotyls, leaves and leaf petioles (Novák et al., 2018). PLDγ was detected in the PM, intracellular membrane, nuclear and mitochondrial subcellular fractions of Arabidopsis leaves (Fan et al., 1999). PLDζ2 is localized to the tonoplast (Yamaryo et al., 2008) while PLDα3, PLDδ and PLDε are associated with the PM (Hong et al., 2009; Hong et al., 2008).

PLD interactions

PLDs interact with different proteins. These proteins regulate PLD activity, localization and function. Arabidopsis PLDα1 interacts with heterotrimeric Gα protein to mediate abscisic acid (ABA) signalling (Zhao and Wang, 2004; Mishra et al., 2006). Oxidative stress promotes PLDδ and glyceraldehyde-3-phosphate dehydrogenase interaction. This interaction can increase activity of PLDδ and promotes ABA induced stomatal closure (Kim et al., 2013). PLDs also interact with cytoskeleton. PLDδ has been identified as protein binding cortical microtubules and actin 7 in pull-down assay (Ho et al., 2009; Andreeva et al., 2009).

PLDs and plant hormones

ABA

ABA as an important phytohormone plays roles in responses to various stresses including drought, cold and salinity. ABA promotes stomatal closure during water deficiency, and it is involved in seed dormancy and plant senescence. PLDs are also involved in all these processes (Fan et al., 1997; Sang et al., 2001; Zhang et al., 2004). In this respect, ABA induced stomatal closure in *Arabidopsis thaliana* ecotype Columbia-0 (Col-0) plants was impaired in *pldα1* (knock-out mutant of

PHOSPHOLIPASE D ALPHA 1) mutants (Jiang et al., 2014, Novák et al., 2018). Zhang et al. (2009) created model in which ABA induced PLDα1 activity and its product PA stimulate NADPH oxidase activity. Subsequently, NADPH oxidase produces H_2O_2 which regulates stomata activity trough NO, finally leading to the stomatal closure. *pldα1* mutants failed in stomatal H_2O_2 production in response to ABA.

SA

Salicylic acid (SA) plays important roles in plant senescence, flowering, germination, pathogen attack and thermotolerance. SA induces PLD activation in Arabidopsis cell suspensions after 45 min and causes PA accumulation. Incubation of these cells with primary alcohols abolished this PLD activation and PA accumulation, and inhibited SA-responsive genes such as *PATHOGENESIS-RELATED1* and *WRKY38* (Krinke et al., 2009). According to these results, PLD activity is upstream of the SA responsive genes. SA also induced PLD-dependent production of PA, resulting in activation of NADPH-oxidase and H_2O_2 production which caused stomatal closure. Again this can be inhibited by treatment with 1-buthanol (Kalachova et al., 2013).

PLDs and wounding

Plant wounding can be induced by many factors. It can be triggered by herbivores, freezing, pathogen attack or by strong wind. All these factors cause loss of cell membrane integrity and increase level of PA. Such wounding-induced high PA levels are significantly reduced in *PLDα1* silenced or *pldα1* KO plants, which also leads to diminished JA production (Wang et al., 2000). PA produced in response to wounding serves as a precursor for JA synthesis.

PLDs and phosphate starvation

The phosphorus in phospholipids can serve as phosphate reserve in plant cells. During phosphate starvation membrane phospholipids are replaced by glycolipids (Andersson et al., 2005). The main involvement in phosphate starvation displays PLDζ subclass (Li et al., 2006). PA produced by PLDζ2 is dephosphorylated by PA-phosphatase, P_i is released and DAG is produced as a precursor for galactolipid synthesis (Cruz-Ramírez et al., 2006).

PLDs, pathogens and symbionts

PLDs and PA are involved in plant immunity and resistance against pathogens. Rice PLDα1 is recruited to the plasma membrane during pathogen *Xanthomonas oryzae*

attack (Young et al., 1996). *pldα1* mutants display enhanced resistance to pathogenic fungi powdery mildew in comparison to *pldδ* (knock-out mutant of PHOSPHOLIPASE D DELTA) showing enhanced susceptibility. *pldα1/δ* (double knock-out mutant of PHOSPHOLIPASE D ALPHA 1 and PHOSPHOLIPASE D DELTA) shows similar fungal resistance as *pldα1* mutant, while GFP-tagged PLDδ accumulated at the PM around fungal penetration site (Zhang et al., 2018).

In Arabidopsis, fungus *Piriformospora indica* colonizes roots and promotes roots growth. This process requires PA, which activates 3-PHOSPHOINOSITIDE-DEPENDENT PROTEIN KINASE1 activating Oxidative Signal inducible 1 signalling pathway. This signalling cascade is completely impaired in *pldα1/δ* double mutant where PA is not produced (Camehl et al., 2011).

PLDα1

Arabidopsis PLDα1 protein (AT3G15730) contain C2 lipid binding domain on N-terminus (position 1-110 in AA sequence) and two HKD domains responsible for lipase activity (position 327-366 and 656-683 in AA sequence). According to PhosPhAt 4.0 database (Durek et al., 2010) SP-motif at position 481 can serve as potential MAPK phosphorylation site (**Fig 7**). PLDα1 is active in the presence of 20-100 mM Ca^{2+}, by adding detergents it can be lowered to 5mM Ca^{2+}. N-acylethanolamines (NAEs) are endogenous inhibitors of PLDα1 (Motes et al., 2005). These NAEs can by potentially produced by PLDγ and PLDβ (Austin-Brown and Chapman, 2002).

In response to plant wounding, e.g. after herbivore attack, PLDα1 is activated in cells and its product PA plays very important role (Wang, 2000). KO *pldα1* mutant exhibits reduced production of PA while PA production is completely eliminated in double *pldα1/δ* mutant. Surprisingly, JA biosynthesis was not affected in this double *pldα1/δ* mutant (Bargmann et al., 2009a). Abundance of PLDα1 was decreased after wortmannin treatment in Arabidopsis roots (Takáč et al., 2012). Wortmannin inhibits phosphatidyl inositol kinases and causes clustering and fusion of multivesicular bodies and trans-Golgi network which results in the inhibition of vacuolar trafficking.

PA, as product of PLD, regulates MAP65-1 in response to the salt stress (Zhang et al., 2012). MAP65-1 protein forms 25 nm cross-bridges between MTs during their bundling (Smertenko et al., 2004). This protein binds to PA localized at the plasma membrane, and enhances MTs polymerization and bundling. Under normal conditions, wild type

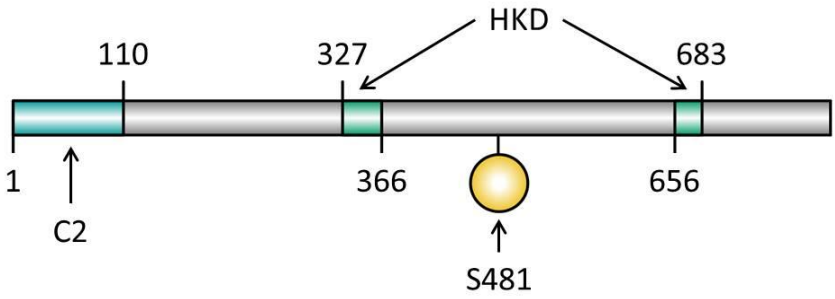

Fig. 7 Graphical depiction of PLDα1 protein with its domains. C2 – calcium-dependent lipid-binding domain, HKD – HxKxxxxD domains essential for lipase activity, S481 – SP motif with serine at the position 481 which can serve as potential MAPK phosphorylation site. Created with IBS software (http://ibs.biocuckoo.org/).

and *pldα1* showed no obvious differences in MT organization and density. Salt stress affects association of MTs and MAP65-1 leading to MTs disorganization in the *pldα1* mutant. This process can be alleviated by adding PA (16:0-18:2). Treatment with 1-butanol (0.4%) or co-treatment with 1-butanol (0.1%) and NaCl led to MTs depolymerization in wild type and *pldα1* mutant. This process can be also alleviated by adding PA. By contrast, 2-butanol, which is not PLDα1 substrate, has no effect on MTs (Zhang et al., 2012). MAP65-1 binds to PA with fatty acid chains 16:0-18:1; 16:0-18:2; 18:0-18:1 and 18:0-18:2. Thus, PA produced by PLDα1 binds to MAP65-1 which leads to MTs polymerization and stabilization and increase salt tolerance, but PLDα1 itself does not bind to MTs or MAP65-1 (Zhang et al., 2012). Mutation of the PA-binding domain of MAP65-1 resulted in destabilization of cortical MTs and enhanced cell death under salt stress (Zhang et al., 2012). Moreover, overexpression of MAP65-1 improves

NaCl tolerance of Arabidopsis cells, which is more obvious in the wild type than in the *pldα1* mutant. On the other hand, double *pldα1 x map65-1* mutant (double knock-out mutant of PHOSPHOLIPASE D ALPHA 1 and MICROTUBULE ASSOCIATED PROTEIN 65-1) showed greater sensitivity to NaCl in comparison to single mutants (Zhang et al., 2012).

During NaCl exposure, Na^+ ions enter root, which leads to signalling response. MAPK called MPK6 has been identified as target of PA in response to salinity while *pldα1* mutant showed lower level of MPK6 activity. PA binds and stimulates MPK6 which inhibits MAP65-1 activity through phosphorylation (Yu et al., 2010). MAP65-1 inhibition results in less prominent MT bundling, (Smertenko et al., 2006; Beck et al.,

2010) which might cause MT disorganization after stress exposure. On the other hand, PA also binds to MAP65-1 and increases MT polymerization activity (Zhang et al., 2012). In Arabidopsis, MAP65-1 contains two microtubule binding domains, MTB1 and MTB2 (Smertenko et al., 2008). MTB2 harbors the phosphorylation sites (from 495 to 587 residues) which controls MAP65-1 activity (Smertenko et al., 2006; Smertenko et al., 2008). The PA binding domains in MAP65-1 (from 1 to 150 and from 340 to 494 residues) are different from microtubule binding domains (Zhang et al., 2012), which suggest that MAP65-1 regulations by MAPKs and PA are different.

Introduction to microscopy

Widefield epifluorescence microscopy

The simplest method for imaging fluorescently labeled samples is widefield epifluorescence microscopy. This method is cost-effective and can be easily adapted for *in vitro* and *in vivo* analysis. Speed of imaging depends on numerical aperture (NA) of objective, properties of camera and fluorophore spectral properties. Resolution of widefield microscopy is limited by the Abbe diffraction limit: $d = \lambda / 2n \sin\theta$ (λ = wavelength, $n \sin\theta$ = NA). For example, for green light fluorophore with wavelength about 500 nm and objective with NA=1, the Abbe limit is roughly 250 nm. Another limitation for microscopy is signal-to-noise ratio (SNR) during sample imaging. Widefield microscopy is characteristic by relatively low SNR.

Confocal laser scanning microscopy

Fluorescent objects outside the focal plane produce high levels of background signal. Therefore, optical sectioning techniques have been developed to reduce this out-of-focus signal and confocal laser scanning microscopy (CLSM) significantly reduces the unspecific background caused by out-of-focus light (**Fig. 8**). This method has high SNR and improves resolution as compared to widefield fluorescence microscopy. Another advantage of CLSM is depth of imaging. CLSM platforms use point illumination with focused laser beam scanning across the sample in order to construct an image. Pinhole in front of detector is used to eliminate out-of-focus illumination. Optimal aperture of pinhole depends on NA of objective and spectral characteristics of the fluorophore. An increased resolution is at the cost of decreased signal intensity because much of fluorescence signal from sample is blocked at the pinhole. Considering the speed of CLSM, it is the best technique for non-dynamic processes or fixed samples.

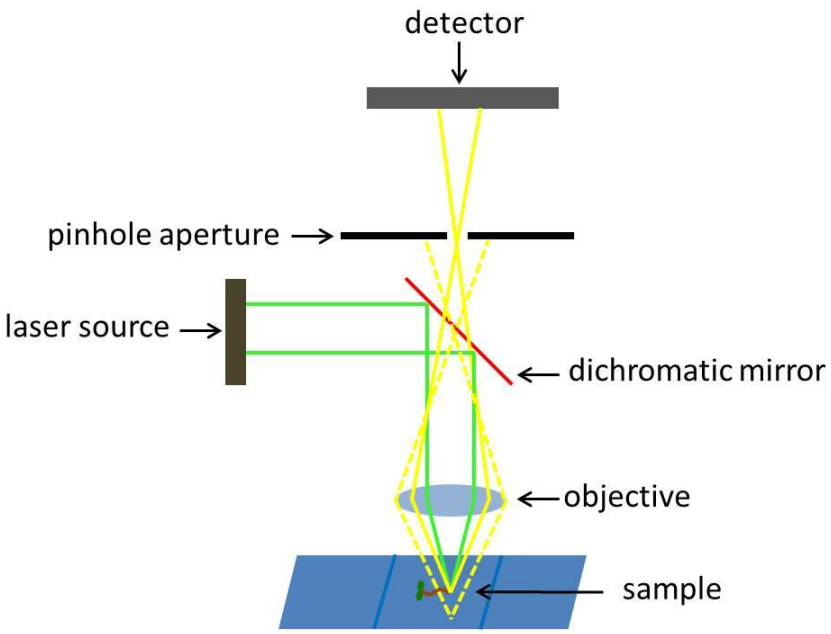

Fig. 8 Diagram of confocal microscope principle. Full yellow lines show focused light pathway passing through pinhole aperture, while discontinuous lines show out-of-focus light pathway blocked at pinhole. Adapted from Cox, (2002).

In comparison to CLSM, image acquisition speeds can be increased using spinning disk microscopy.

Spinning disk microscopy

Nipkow disk developed by Paul Nipkow in 1884 is central part of all modern spinning disk confocal microscopes. The disk design was significantly improved by Yokogawa Corp. This disk rotates and contains multiple pinholes which are designed to cover every location of an image. While most light does not pass the disk, the light going through the pinholes forms an array of minibeams corresponding to the pinhole pattern. In the Yokogawa design, the module includes a disk with 20 000 pinholes, which are helically arranged to cover entire field of view during rotation. In the microscope is also second disk with microlenses which directs light to pinholes. If disk rotates with 1800 rpm, 360 full frames are acquired per second (Gräf et al., 2005). If coupled with charge-coupled device (CCD) or complementary metal–oxide–semiconductor (sCMOS) cameras it is an optimal microscopy system for near widefield sample exposure, and it is speeding up the acquisition times to the limits which are set bycamera exposure times. Therefore spinning disk microscope can document very fast processes while parallel dual channel acquisition is also possible.

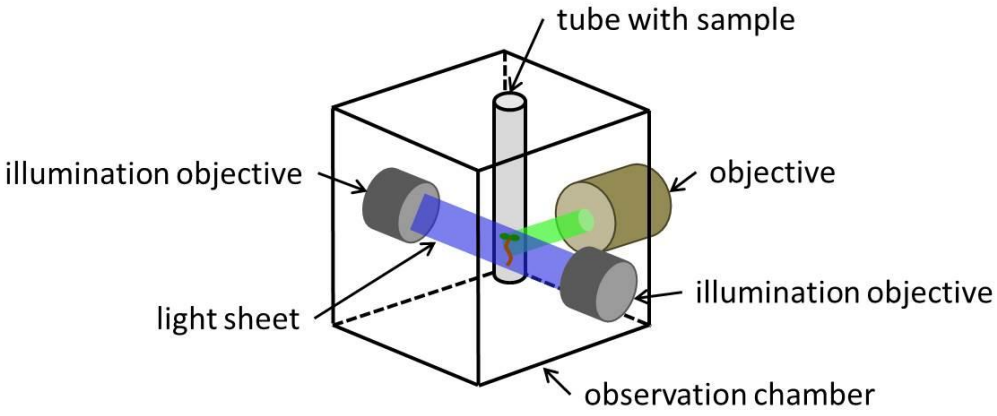

Fig. 9 Schematic organization of light-sheet fluorescence microscope. It describes the arrangement of sample the in tube, illumination objectives for generation of light-sheet and the acquisition of the image by detection objective, all arranged in the observation chamber. Adapted from Ovečka et al., (2015).

Light-sheet fluorescence microscopy

Light-sheet fluorescence microscopy (LSFM) combines advantages of fast widefield microscopes with 4D imaging. The primary goal of LSFM is to work under conditions that are close to the conditions in nature (Maizel et al., 2011). Seeds or seedlings are placed on solid medium in the glass capillary, plastic tube or directly on its surface. Sample capillary is oriented vertically in a specially designed chamber filled with liquid medium. LSFM uses a low NA objective lens to focus a sheet of light on the sample. Illumination of the specimen is from one side while emitted light is collected at a perpendicular axis (Maizel et al., 2011). Fluorophore illumination is achieved by thin sheet of light oriented orthogonally to the detection path. Only fluorophores which are localized close to the focal plane of the detection system are excited. These fluorophores contribute to the image and out-of-focus excitation is eliminated. Sample in the capillary is mounted on rotor and can be rotated at 360° (Weber and Huisken, 2011). Energy used in LSFM for excitation is much lower in comparison to widefield microscopes or CLSM. This provides possibility to perform long-term imaging experiments, prevents fluorophore bleaching and reduces phototoxicity. Preparation of the sample includes immobilization of seeds or seedlings in agarose or Phytagel medium in glass capillaries, fluorinated ethylene propylene (FEP) tubes or syringes. These are loaded into observation chamber (**Fig. 9**) which is filled with liquid culture medium for live-cell imaging of growing seedlings or germinating seeds (Ovečka et al.,

2015). LSFM is low-invasive method enabling long term imaging of plant growth and development.

Developmental Nuclear Localization and Quantification of GFP-Tagged EB1c in *Arabidopsis* Root Using Light-Sheet Microscopy

Novák D, Kuchařová A, Ovečka M, Komis G, Šamaj J.

Material and Methods

Molecular methods

Genomic DNA isolated from fresh leaves of 7 d old *Arabidopsis thaliana* (L.) Heynh. (ecotype Columbia) seedlings was used for amplification of the complete coding region of *EB1c* gene together with its upstream promoter region. *EB1c* promoter region was identified according to previously published data (Komaki et al., 2010) and designed using Arabidopsis Sequence Viewer (http://arabidopsis.org). The promoter sequence *pEB1c* was suggested to comprise of 663 base pairs upstream of the start codon of the *EB1c* gene. For the cloning, we used Gateway® technology. Primers were designed according to manufacturer's instructions. Whole genomic fragment was recombined into pDONR207 Gateway® vector and subsequently transferred by LR recombination reaction into the Gateway® destination vector pGWB450 (Nakagawa et al., 2007) designed for C-terminal GFP fusion with kanamycin resistance for plant selection. All recombinations were confirmed by sequencing. Expression vector pGWB450::*pEB1c::EB1c:GFP* was transformed into *Agrobacterium tumefaciens*, strain GV3101. Transformed Agrobacteria were used for several independent transformations of Arabidopsis plants (Clough and Bent, 1998; Davis et al., 2009). Seedlings were selected on kanamycin (50 mg/ml) selection medium to identify T1 transgenic plants. T1 transformants carrying *pEB1c::EB1c:GFP* constructs were checked for phenotype in comparison to control plants. No phenotypes were discerned and thus the T2 generation of Arabidopsis plants expressing pGWB450::*pEB1c::EB1c:GFP* was harvested and used for further experiments.

Protein extraction, SDS-PAGE and immunoblotting

12 d old Arabidopsis plants expressing EB1c-GFP were analysed on fluorescent stereomicroscope Leica MZ FLIII (Leica Microsystems, Germany) for EB1c-GFP signal. Protein extraction was carried out from roots of plants expressing EB1c-GFP and from wild type *Arabidopsis thaliana* (L.) Heynh. (ecotype Columbia). Roots were harvested, weighted, flesh frozen and immediately ground in the liquid nitrogen. Powder was extracted in extraction buffer (1:1, w/v) (50 mM Na-HEPES pH 7.5, 150 mM NaCl, 1 mM $MgCl_2.6H_2O$, 1 mM EGTA, 1 mM DTT, 1 mM NaF) supplemented with protease inhibitors Complete (Roche, Germany) and phosphatase inhibitors PhosStop (Roche, Germany). Crude extract was centrifuged 10 min, 8000 *g* at 4°C.

Resulting supernatant was used for SDS-PAGE and subsequent western blot analysis. 15 µg of total protein was loaded on 8% sodium dodecyl sulphate-polyacrylamide gel electrophoresis (SDS-PAGE) gels followed by immunoblotting with polyvinylidene difluoride (PVDF) membrane and Western blotted with antibody against GFP (anti GFP rabbit ABCAM AB290) in dilution of 1:2000. Secondary antibody (goat anti-rabbit, Santa Cruz Biotechnology) was used in dilution of 1:5000. After incubation in enhanced chemiluminescence (ECL) reagents (according to manufacturer instructions), immunoreactive bands were documented using the BioRad ChemiDoc™ MP System.

Plant material and sample preparation for light-sheet microscopy imaging

Seeds of *Arabidopsis thaliana* (L.) Heynh. (ecotype Columbia) transgenic line expressing *pEB1::cEB1c:GFP* were surface sterilized, plated onto solidified ½ Murashige & Skoog (MS) medium and kept in 4°C for 4 days. After this period seeds were transferred to round 90 × 25 mm Petri dishes filled with 80 ml of ½ MS medium solidified with 0.6% w/v Phytagel (Sigma-Aldrich, USA), and placed into small depressions facilitating gravitropic root growth inside solidified culture medium. Plates were cultivated in culture chamber horizontally for 2 d at 22°C, 50% humidity, 16/8-h light/dark cycle. After germination of seedlings when they were 1 d old, they were enclosed by FEP tube with an inner diameter of 1.1 mm and wall thickness of 0.2 mm (Wolf-Technik, Germany). FEP tubes were carefully inserted into culture medium to enclose individual seedling inside (Ovečka et al., 2015). After 24 h seedlings in FEP tubes were removed from the plate, transferred to the microscope and prepared for imaging. All experiments and measurements were done on 2 d old seedlings.

Light-sheet microscopy

Developmental live cell imaging was done with the Lightsheet Z.1 fluorescence microscope (Carl Zeiss, Germany), equipped with W Plan-Apochromat 20×/1.0 NA water immersion detection objective (Carl Zeiss, Germany) and LSFM 10x/0.2 NA illumination objective (Carl Zeiss, Germany). Seedlings were imaged using dual-side illumination by a light-sheet modulated into a pivot scan mode, with excitation laser line 488 nm and with emission filter BP505-545. Image acquisition was done every two minutes in Z-stack mode for a time period of 2-5 h. Scaling of images in x, y and z dimensions was 0.228 x 0.228 x 0.477 µm. To prevent the movement of the growing root apex out of the field of view, images were acquired in two subsequent views

coordinated to each other in y coordinate. Images were recorded with the PCO.Edge sCMOS camera (PCO AG, Germany) with the exposure time 25 ms.

Measurements, statistical analyses and in silico predictions

From images of the whole root acquired using Zen 2014 software (Carl Zeiss, Germany) subsets of data were created, with defined x-, y- and z- dimensions comprising whole volume of several nuclei from one particular cell file. Several subsets were created in order to segment nuclei of all cells of particular cell file in ordered positions from the stem cells surrounding quiescence center of the root up to visible cell differentiation at the end of elongation zone. All subsets were transformed to 2D images using Maximum intensity projection function of the Zen 2014 software. In all images uniform correction of brightness and contrast was done before they were exported for image analysis. All quantitative data were produced with publicly available software CellProfiler 2.1.1 (http://www.cellprofiler.org, Carpenter at al., 2006, Lamprecht et al., 2007). Nuclear area from 2D images that represent surface projection of the nuclear volume (referred herein as nuclear surface area) was measured as the actual number of pixels in the manually defined region multiplied by the pixel area. Mean intensity values were calculated as the average pixel intensity in the defined region, integrated intensity values were calculated as the total pixel intensity in the defined region. Values were subsequently normalized to a 0-1 range using the following formula: $x_N=(x_i-x_{min})/x_{max}-x_{min}$ (where x_N= normalized intensity, x_i=absolute intensity, x_{min}= minimum absolute intensity and x_{max}= maximum absolute intensity). Thus, all biological variables within measured root tips were brought into the comparable proportions and plant – to – plant differences in the expression of EB1c-GFP were compensated. Data from 4 individual cell files were collected and evaluated separately for epidermis, cortex and endodermis from two independent experiments (two independent roots). Final statistical data evaluation and plot production was done with Microsoft Excel software.

Prediction of putative nuclear export sequences was performed using the NetNES 1.1 server with the accession numbers of the three *Arabidopsis thaliana* EB1 isoforms (EB1a, AT3G47690; EB1b, AT5G62500; and EB1c, AT5G67270) (la Cour et al., 2004). For protein domain structure illustration, DOG 1.0 illustrator was used (Ren et al., 2009).

Results

We studied the *in vivo* subcellular nuclear localization of the EB1c protein during root development in stably transformed *Arabidopsis thaliana* plants. Beside the already published presence of NLS in EB1c protein sequence (Komaki et al., 2010), our *in silico* search using NetNES 1.1 prediction server (la Cour et al., 2004) revealed the occurrence of putative nuclear export signals at positions 213L, 215I, 217S and 218L for EB1c. At the same respect, we compared the other EB1 family members in Arabidopsis, EB1a and EB1b. NES was not predicted for EB1b, while for EB1a, there is one prediction at position 193I albeit with a low score over the threshold. We prepared *EB1c:GFP* construct driven by its own promoter. The 663 bp long promoter sequence and the complete coding region of *EB1c* gene were cloned using Gateway® technology into the binary vector and subsequently transformed into *A. thaliana* plants (ecotype Col-0) while T2 generation of plants was used for experiments. To prove the expression of EB1c-GFP fusion protein in the plants, we performed SDS-PAGE with subsequent Western-blot analysis using seedlings expressing EB1c-GFP and Col-0 as a negative control (**Fig. 10A**). EB1c-GFP protein signal was clearly detected using anti-GFP antibody at the molecular mass corresponding to 64 kDa which is the predicted size of the fusion protein. As negative controls, we used extracts from untransformed wild type plants as well as extracts from plants expressing EB1c-GFP treated only with secondary antibody (**Fig. 10A**).

Root growth and development require passage of root cells through successive developmental zones. Large extend of this process from spatial and temporal point of view requires special microscopic applications for effective live cell imaging. Developmental light-sheet microscopy overcomes these limitations and allows real-time or time-lapse imaging of whole developing seedlings (Ovečka et al., 2015). We performed live cell imaging with seedlings growing over a period between 2-5 h inside the light-sheet microscope. EB1c-GFP was localized in nuclei of all non-dividing root cells within the root apex, with particularly strong expression level in cells of the root meristematic zone (**Fig. 10B**). General overview of EB1c-GFP expressing roots revealed zonation of the root apex into different cell developmental zones, namely into meristematic, transition, elongation and differentiation zones (**Fig. 10B**). Seedlings were prepared and cultivated in cylinders of Phytagel-solidified culture medium. During

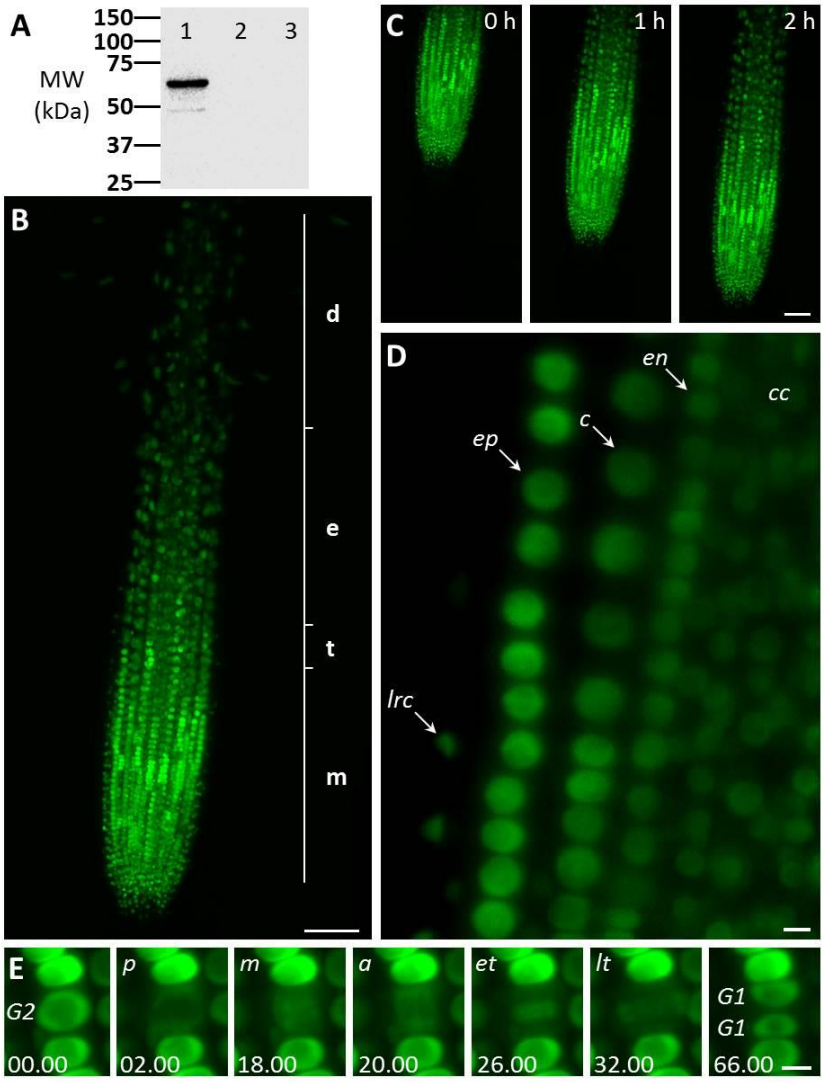

Fig. 10 Characterization of transgenic *Arabidopsis thaliana* plants expressing EB1c-GFP driven by EB1c own promoter and localization of EB1c-GFP. (**A**) SDS-PAGE followed by western blot analysis using anti-GFP antibody from protein extract of *A. thaliana* T2 plants expressing EB1c-GFP (lane 1), protein extract from untransformed Col plants (lane 2) and protein extract from Arabidopsis plants expressing EB1c-GFP immunoblotted only with secondary antibody (lane 3). MW – Molecular weight. (**B**) General overview of the root tip of 2 d old *A. thaliana* seedling expressing EB1c-GFP. Average root zonation into individual cell developmental zones consisting meristematic zone (m), transition zone (t), elongation zone (e) and differentiation zone (d) is depicted. EB1c-GFP was localized in nuclei of root cells, with particularly strong expression level in cells of the root meristematic zone. (**C**) Live cell imaging of seedling growing inside of the light-sheet microscope over the period of 2 h. (**D**) Localization of EB1c-GFP by light-sheet microscopy in cells of individual root tissue layers, in epidermis (ep), cortex (c), endodermis (en), central cylinder (cc) and lateral root cap cells (lrc). In all imaged tissues, light-sheet microscopy revealed clearly nuclear localization of EB1c-GFP in root cells. (**E**) Localization of EB1c-GFP by light-sheet microscopy during mitotic cell division of root cells in the meristematic zone. EB1c-GFP relocated from G2 stage nuclei to spindle in prophase (p), metaphase (m) and anaphase (a), to phragmoplast at early and late telophase (et, lt), and redistributed back to reconstructed G1 stage nuclei after cell division. Time progression of the cell division is indicated in min. Pictures (B-E) were performed in collaboration with Dr. Miroslav Ovečka. Scale bar = 50 μm in (B, C) and 5 μm in (D, E).

imaging over a range of several hours, seedlings exhibited undisturbed continuous root growth inside of the microscope (**Fig. 10C,** Supporting Information Movie S1).

Average root growth rate of 2 d old seedlings expressing EB1c-GFP in the light-sheet microscope was 1.686 (± 0.721) $\mu m.min^{-1}$ (±SD, n=6).

Light-sheet microscopy, in addition to time-lapse imaging of the entire root development, allowed localization of EB1c-GFP at the cellular and subcellular levels. At the level of cellular resolution, this method was suitable for visualization not only surface cells and tissues of the root, like lateral root cap cells and epidermis, but further allowed visualization of individual cells from inner tissues of the Arabidopsis root including the cortex, the endodermis and the central cylinder. In all imaged tissues, light-sheet microscopy revealed clearly nuclear localization of EB1c-GFP in root cells (**Fig. 10D**). Subcellular resolution of the light-sheet microscopy was documented during mitotic cell division of root cells in the meristematic zone, where EB1c-GFP relocated from G2 stage nuclei to mitotic spindles and cytokinetic phragmoplasts during the respective cell division stages and finally was redistributed back to reconstituted G1 stage nuclei after completing cell division (**Fig. 10E**).

The longitudinal developmental zonation of the root apex of plants expressing EB1c-GFP fusion protein into different developmental zones was determined in individual cell files of epidermis (**Fig. 11A-D**, arrows in B and C denote the first cell of each consecutive zone), cortex (**Fig. 11E-H**, arrows in F and G denote the first cell of each consecutive zone) and endodermis (**Fig. 11I-L**, arrows in J and K denote the first cell of each consecutive zone). The cell arrangement in the meristematic zone of the epidermis was influenced by frequent cell divisions rather than by cell elongation (along longitudinal root axis). This leads to generation of tightly-packed wide but very short cells, with compressed nuclei (**Fig. 11A**). Very similar cell and nuclear shapes were observed within the meristematic zone in the cortex layer (**Fig. 11E**). In the endodermis nuclei of cells in the meristematic zone appeared smaller and due to different ratio between cell width and cell height their shape was not deformed to the same extent as in the epidermis and the cortex (c.f. **Fig. 11A, E** and **11I**). With termination of the mitotic activity in the meristematic zone, cell sizes and shapes were changing. At the end of the meristematic zone, nuclei became round and larger in all three layers (**Fig. 11B, F, J**). Before starting rapid cell elongation, however, there was a population of cells with short length, as indicated by short and similar distance between nuclei of individual cells

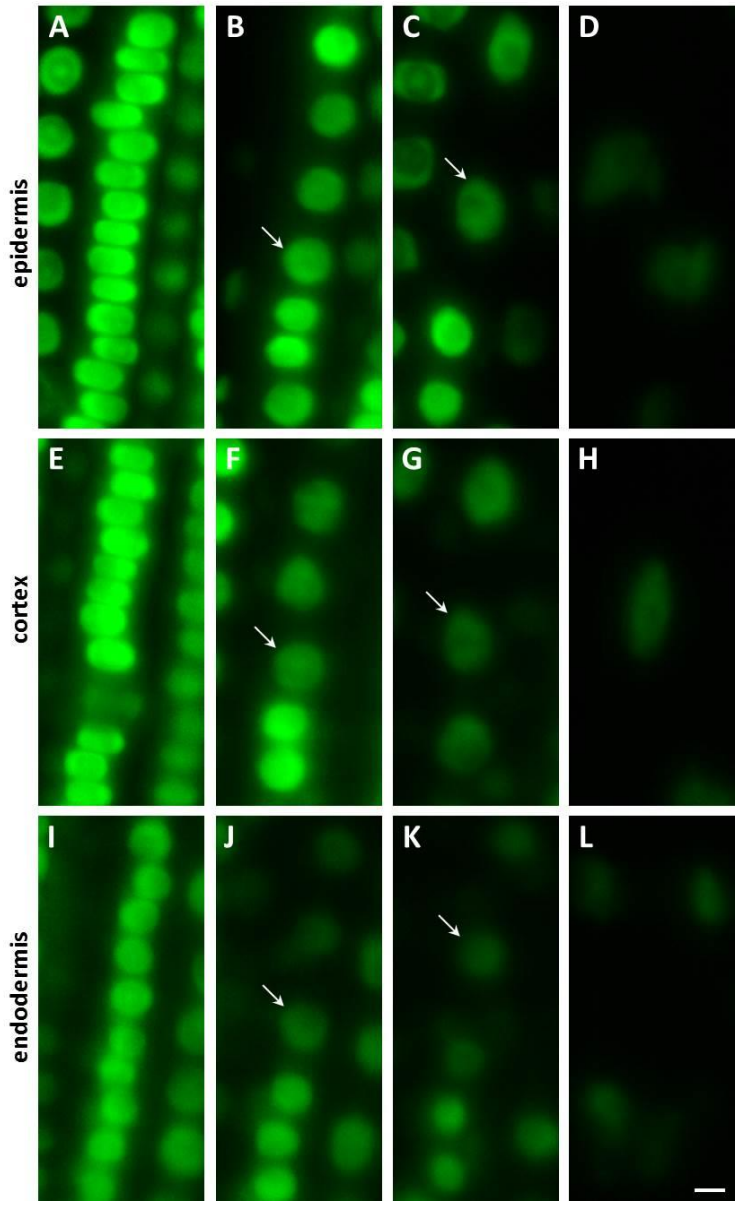

Fig. 11 Shoot-ward developmental zonation in the root apex of transgenic *Arabidopsis thaliana* plants expressing EB1c-GFP protein. Cell arrangement and position were assessed in individual cell files of epidermis (**A**-**D**), cortex (**E**-**H**) and endodermis (**I**-**L**). Typical appearance of cells in each tissue layer with nuclear localization of EB1c-GFP is shown for meristematic zone (**A**, **E**, **I**), at the meristem-transition zone border (**B**, **F**, **J**), at the transition zone-elongation zone border (**C**, **G**, **K**) and within the elongation zone (**D**, **H**, **L**). Arrows define nuclei of first cell within the transition zone (**B**, **F**, **J**) and first cell within the elongation zone (**C**, **G**, **K**). Fluorescence intensity of images is presented to the scale recorded during the acquisition of each individual cell type. Picture was prepared in collaboration with Dr. Miroslav Ovečka. Scale bar = 5 μm.

(**Fig. 11B, F, J**). In addition, they showed reduction in the EB1c-GFP fluorescence intensity. Based on these characteristics, an onset of the transition zone placed before rapid cell elongation could be identified in each cell file of epidermis (**Fig. 11B**), cortex (**Fig. 11F**) and endodermis (**Fig. 11J**). Cells from the transition zone of each tissue layer

entered subsequently cell elongation zone, which was indicated by further changes in the nucleus size, EB1c-GFP fluorescence intensity and apparent dilatation of distances between neighbour nuclei within the cell files (**Fig. 11C, G, K**). Rapid cell elongation was connected with apparent enlargement of nuclei in epidermis (**Fig. 11D**) and cortex (**Fig. 11H**), changes in nuclear shape in all three tissue layers (**Fig. 11D, H, L**) and further reduction in EB1c-GFP fluorescence intensity.

To characterize the distribution of EB1c-GFP in the apex of Arabidopsis root in detail, we quantified the intensity of EB1c-GFP nuclear fluorescence in the previously defined root cell developmental zones (meristem, transition zone, elongation zone and differentiation zone). The quantitative evaluation of the EB1c-GFP protein content in interphase nuclei of root cells was performed in light-sheet images acquired in 4D modes (encompassing x, y, z and t dimensions). In individual cell files of the epidermis, the cortex and the endodermis all interphase nuclei in order were taken into account, starting from the stem cell niche region and progressing up to cell elongation before cells reached the zone of cell differentiation (i.e. as evidenced by root hair emergence in the root epidermis). In each cell file, the meristem – to – transition zone border (**Fig. 11B, F, J**) and the transition zone – to – elongation zone border (**Fig. 11C, G, K**) were identified. Parameters for identification of particular borders and range of individual cell developmental zones included the spatial extent of the cell division, size and fluorescence intensity reference values from nuclei of cells in G1 and G2 stages, increase in the nuclear size after termination of the cell division, and increase in the distance between nuclei of individual cells in the elongation zone. Thus, all cells in each cell file were topologically divided into meristematic zone, transition zone and elongation zone (**Fig. 10B)**.

Values of nuclear surface area and EB1c-GFP mean signal intensity for quantitative evaluation were plotted against cell position counted from the stem cells surrounding quiescence center. Both parameters were measured and evaluated separately for the epidermis, the cortex and the endodermis. We found that in all tissues, as cells proceeded from proliferation to the differentiation, the nuclear surface area increased while fluorescence intensity of EB1c-GFP signal decreased. This trend was apparent from quantification of individual cell files of the epidermis (**Fig. 12A**), the cortex (**Fig. 12B**) and the endodermis (**Fig. 12C**). The meristematic zone, actively dividing cells contained the smallest nuclei exhibiting the highest EB1c-GFP content. In the transition

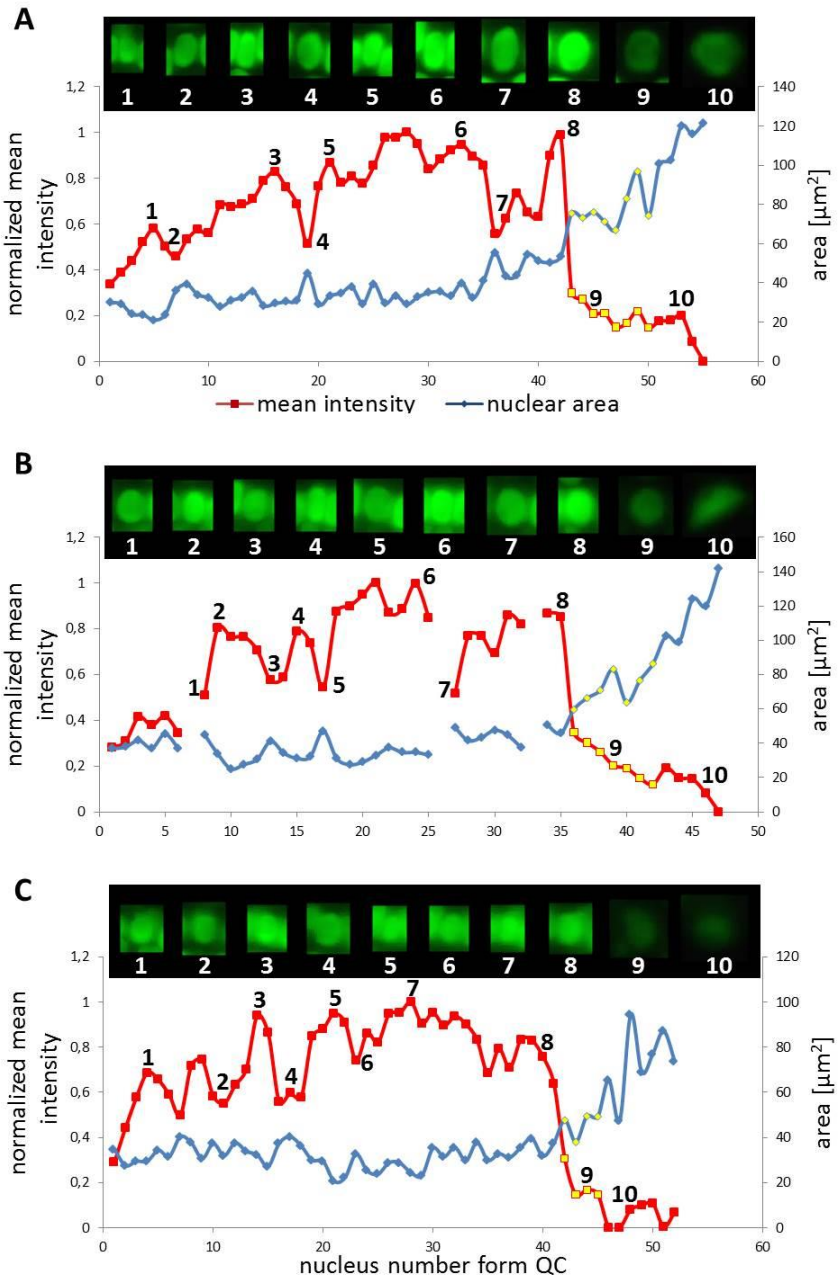

Fig. 12 Nuclear surface area and nuclear EB1c-GFP mean signal intensity distribution in root developmental zones of the root apex in individual cell files. Relationship between nuclear area (blue line) and nuclear EB1c-GFP mean signal intensity (red line) in respect to cell position counted from the stem cells surrounding quiescent center in individual cell file of epidermis (**A**), cortex (**B**) and endodermis (**C**). Values for nuclei in the transition zone are highlighted by yellow points, which allow distinguishing also meristematic zone (appearing before the transition zone) and elongation zone (appearing after the transition zone). Inset images over the lines show individual nuclei of cells at the actual position, documenting changes in nuclear shape, size and mean EB1c-GFP fluorescence intensity. Major vertical axis (on the left) represents the values for the normalized mean intensity and minor vertical axis (on the right) represents values for area measurements. Horizontal axis represents the actual cell position counted from the stem cells surrounding quiescent center (QC). Data are shown for one representative cell file from each tissue layer. Interruptions of the curve in the cortex (**B**) are caused by presence of dividing cells within the file. Graphs were prepared in collaboration with Dr. Miroslav Ovečka and Dr. Anna Kuchařová.

zone, the mean nuclear fluorescence intensity of EB1c-GFP was steeply decreased. This decline in EB1c-GFP fluorescence intensity continued in the elongation zone while the nuclear area progressively increased (**Fig. 12**). Cross-correlation of nuclear EB1c-GFP mean signal intensity of some individual nuclei with their size and shape at certain position within the cell file revealed negative correlation between nuclear size and mean EB1c-GFP signal intensity in the meristematic zone (numbered insets in **Fig. 12A-C**). This negative correlation trend was stabilized in the transition zone and the elongation zone of all measured cell files in all evaluated tissue layers (**Fig. 12**) as evidenced by the continuous decrease in EB1c-GFP fluorescence intensity with the progressive increase in nuclear size.

Further, we quantified collectively measured data from several individual cell files of two independent roots. Data were evaluated separately for epidermis, cortex and endodermis. Quantitative evaluation of nuclear surface area values revealed rather stable distribution of this parameter in the meristematic zone of the epidermis. It increased slightly only in meristematic cells at gradually increasing distances from the stem cell region, surpassing slightly even the average reference value for the size of G2 nuclei (**Fig. 13A**). Further recognizable increase in the nucleus size took place within the transition zone, and dramatic increase in the elongation zone of epidermis (**Fig. 13A**). Mean fluorescence intensity of EB1c-GFP in interphase nuclei of epidermis fluctuated considerably; however, it was high in the meristematic cells. In nuclei of cells entering the transition zone mean fluorescence intensity of EB1c-GFP dropped considerably and in nuclei of elongating cells this drop in mean fluorescence intensity was dramatic, reflecting the inversely proportional increase in the nucleus size (**Fig. 13A**).

A similar tendency of stable nuclear size in the meristematic zone, a gradual increase in the transition zone and a considerable increase in the elongation zone was recorded also in cell files of the cortex layer (**Fig. 13B**). Nuclear size in the meristematic zone did not exceed the reference value for the size of G2 nuclei (**Fig. 13B**). Mean fluorescence intensity of EB1c-GFP in interphase nuclei of cortex cells was highest in the meristematic zone. However, it decreased dramatically in the transition zone, keeping further decreasing in the elongation zone as well (**Fig. 13B**).

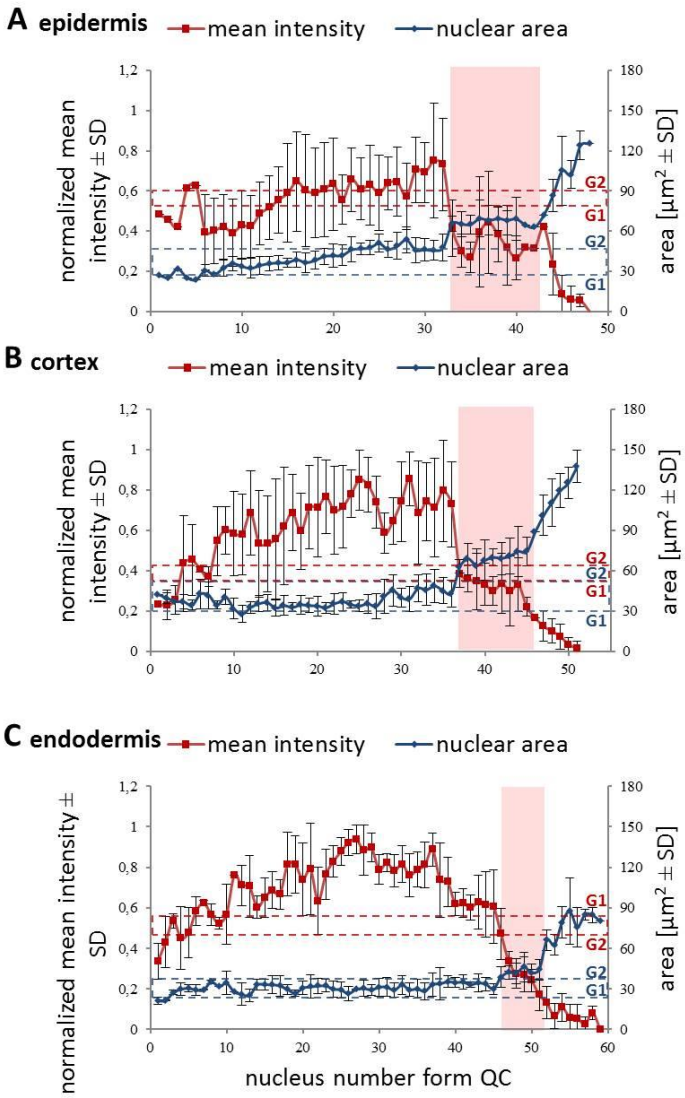

Fig. 13 Nuclear surface area and nuclear EB1c-GFP mean signal intensity in cells of different tissues along diverse developmental root zones. Average values of nuclear surface area (blue line) and EB1c-GFP mean signal intensity (red line) plotted against cell position counted from the stem cells surrounding quiescence center (QC). Data from 4 individual cell files were collected and evaluated separately for epidermis (**A**), cortex (**B**), and endodermis (**C**) from two independent roots. The transition zone is highlighted in pink colour. Dashed red lines for average mean intensity and dashed blue lines for average nuclear area of G1 and G2 nuclei are indicated as reference values. Major vertical axis (on the left) represents the values for the normalized mean intensity and minor vertical axis (on the right) represents values for area measurements. Horizontal axis represents the actual cell position counted from the stem cells surrounding quiescence center (QC). Because number of cells in cell files is not the same, data from individual cell files in average graphs were aligned according to their meristem-to-transition zone borders. Graphs were created by Dr. Miroslav Ovečka and Dr. Anna Kuchařová.

Size of nuclei of endodermal cells in the meristematic zone was constant, not exceeding the reference value of size measured for G2 nuclei, showing increase only after passage of meristematic cells into the transition zone. Size distribution of nuclei in the transition

zone and the elongation zone of endodermis was wider as in cortex and epidermis, but the general tendency of gradual nuclear size increase from meristem through transition zone to elongation zone was maintained also in endodermis (**Fig. 13C**).

Quantitative comparison of nuclear surface area and nuclear EB1c-GFP mean signal intensity in cell developmental zones of the root apex thus showed that the expression of EB1c-GFP decreased along the longitudinal axis of the root apex in all three measured tissue layers. Highest intensity was measured in the meristematic zone where cells are actively dividing, while in the transition zone and further in the elongation zone, expression levels of EB1c-GFP decreased inversely in relation to the nuclear area which progressively increased before entering the differentiation zone.

Reference values for comparison of nuclear surface area and nuclear EB1c-GFP mean signal intensity in all types of measured cells from the root apex were recorded from typical cells of the root meristematic zone, which were present in G1 and G2 stages of mitotic cell division. For safe identification of nuclei in G1 and G2 stages, we took advantage of long-term time-lapse imaging of growing root apex in the light-sheet microscope. Using play-back function we identified and picked cells just before mitotic division and marked them as G2 cells. Daughter cells derived from mitotic division of these cells were marked as G1 cells (**Fig. 10E**). We compared obtained average values of G1 and G2 nuclei with average values of all measured nuclei from non-dividing cells of meristematic zone, and all cells of transition and elongation zones for nuclear surface area (**Fig. 14A**) and nuclear EB1c-GFP mean signal intensity (**Fig. 14B**). This comparison was done separately for epidermis, cortex and endodermis. Average values of nuclear surface area of meristematic cells corresponded well with reference values from G1 and G2 nuclei. Most importantly, the average size of nuclei in the meristematic zone did not exceed the size of G2 nuclei (**Fig. 14A**). Size of nuclei in transition zone as well as in elongation zone was significantly higher. Significant differences in size of nuclei were also observed between transition zone and elongation zone (**Fig. 14A, C**). Similarly, average values of nuclear EB1c-GFP mean signal intensity of meristematic cells corresponded well with reference values from G1 and G2 nuclei, and there were found significantly lower values of nuclear EB1c-GFP mean signal intensity in cells of transition zone and elongation zone in comparison to cells of meristematic zone and reference G1 and G2 nuclei (**Fig. 14B, C**). From these data we can conclude that both nuclear size and EB1c-GFP fluorescence intensity showed significant differences

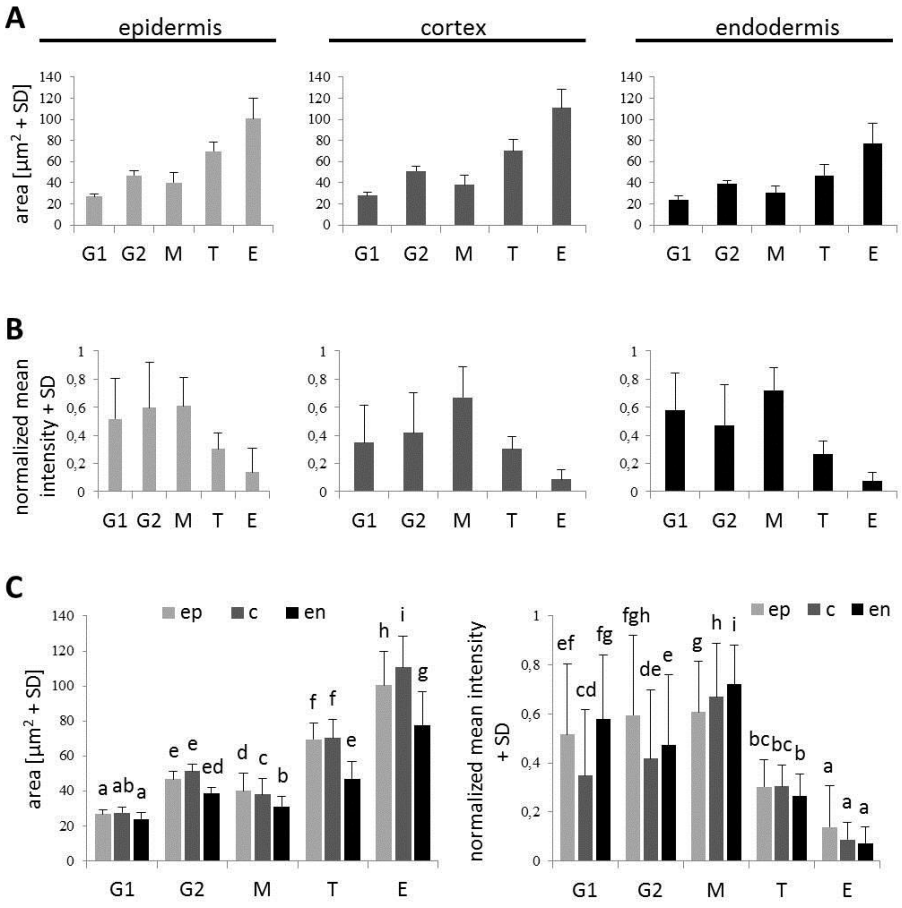

Fig. 14 Reference values of nuclear area and nuclear EB1c-GFP mean signal intensity in G1 and G2 stage meristematic cells as compared to post-meristematic cells. Average nuclear surface area (**A**) and average nuclear EB1c-GFP mean signal intensity (**B**) in G1 and G2 stage of cell cycle were compared with average values of the same parameters of non-dividing cells from meristem (M), transition zone (T) and elongation (E) zone in epidermis, cortex and endodermis. Comparison of average nuclear surface area and average nuclear EB1c-GFP mean signal intensity values in individual cell developmental zones among individual tissue layers (**C**). Different letters represent statistical significance according to one-way ANOVA test at $P<0.05$. Graphs were created by Dr. Anna Kuchařová.

between cells of meristematic zone, transition zone and elongation zone, and supported the correct classification of cells of the root apex into three distinct developmental zones.

From the data presented above it is apparent that there might be a high degree of correlation, positive or negative, between nuclear size and EB1c-GFP expression levels. We pursued this idea by quantitative correlation analysis plotting nuclear surface area, mean signal intensity (mean values per object area) and integrated signal intensity (sum values per object area) to clarify, whether the decrease of EB1c-GFP mean signal intensity during passage of root cells through cell developmental zones corresponds to

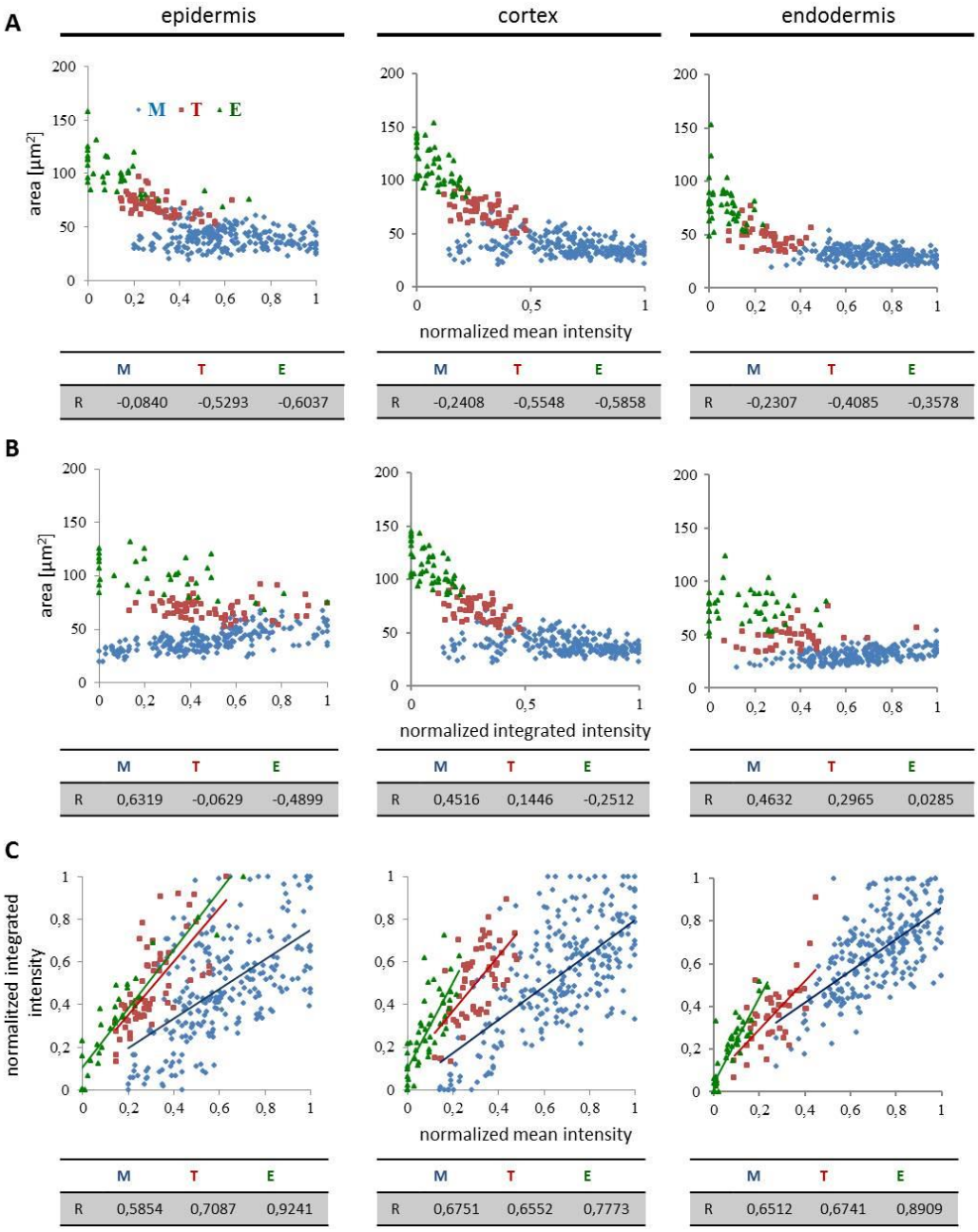

Fig. 15 Quantitative correlation analysis of nuclear surface area, nuclear EB1c-GFP mean signal intensity, and nuclear EB1c-GFP integrated signal intensity in diverse tissues and developmental root zones. Separate graphs presenting correlation between nuclear surface area and nuclear EB1c-GFP mean signal intensity (**A**), nuclear surface area and nuclear EB1c-GFP integrated signal intensity (**B**), and nuclear EB1c-GFP mean signal intensity and nuclear EB1c-GFP integrated signal intensity (**C**). Data from 4 individual cell files were collected and evaluated separately for epidermis, cortex and endodermis from two independent roots. Data are plotted separately for meristem (M, blue dots), transition zone (T, red dots) and elongation zone (E, green dots). Pearson´s correlation coefficients (R) are shown for each individual cell developmental zone of the root apex. Graphs were created in collaboration with Dr. Miroslav Ovečka and Dr. Anna Kuchařová.

the increase of nuclear surface area or not. This comparison was done separately for epidermal, cortical and endodermal cells. In the meristematic zone, we observed the highest variability of the nuclear EB1c-GFP mean fluorescence signal intensity (**Fig. 12, 13**) and thus not surprisingly, this zone exhibited the lowest correlation between nuclear surface area and nuclear EB1c-GFP mean signal intensity (**Fig. 15A**). Measurements from transition zone and elongation zone were better correlated with prevalent negative values indicating that the decrease of EB1c-GFP mean signal intensity in the transition zone and the elongation zone corresponded mainly to increase of nuclear surface area and not to decline of EB1c-GFP expression levels. This suggests prior regulation of EB1c protein in the meristematic zone where cells are actively dividing. Most importantly, values from these three cell developmental zones were separated, albeit partially overlapping at their borders in the respective correlation scatter plots (**Fig. 15A**). This observation proves the regular passage of cells from one developmental zone to another. Similar correlation analysis between nuclear surface area and nuclear EB1c-GFP integrated signal intensity revealed again the partial separation of measurements from meristematic zone, transition zone and elongation zone in all three measured tissue layers, although lower correlation coefficients and higher variability, especially in epidermis and endodermis, were apparent (**Fig. 15B**). The highest intensity of EB1c-GFP fluorescence signal was measured in the meristematic zone, however, it was largely fluctuating (**Fig. 13**). In accordance with this fact, the correlation between nuclear EB1c-GFP mean signal intensity and nuclear EB1c-GFP integrated signal intensity was lowest in the meristematic zone (**Fig. 15C**). It could reflect cell cycle-dependent regulation of EB1c in the zone of mitotically-active root cells. In the transition zone and the elongation zone expression of EB1c-GFP decreased opposite to the increased nuclear area, observation which was corroborated by the higher positive correlation coefficients for comparing nuclear EB1c-GFP mean signal intensity and nuclear EB1c-GFP integrated signal intensity (**Fig. 15C**).

Discussion

Development of environmental imaging in light-sheet microscope

The growing plant root system is physically challenged in its natural environment, the soil. As previously shown, natural root growth is strongly affected by the mechanical properties of the soil causing direct changes in root cell length and width compared to experimentally grown plants (Bengough et al., 2006; Panteris et al., 2013). It may also

indirectly affect the shoot growth (Jin et al., 2015). Conversely, in the conventional experimental setup, seedlings are mostly cultivated on air - solid medium interface which is significantly differing from the physical properties of the soil. Such a setting may cause the misinterpretation of the results, however, these cultivation methods are widely used and therefore widely accepted. Mimicking of the soil conditions in experimental environment is a challenging task (Okamoto et al., 2008). In the light-sheet microscopic setup, the seedling root is growing embedded in a solid agarose matrix and thus root growth is challenged by the rigidity of the medium, as happens during growth in the soil.

Another advantage of the light-sheet microscope is the ability to carry out long-term experiments at near-physiological conditions allowing root recordings with minimal stress (Maizel et al., 2011; Ovečka et al., 2015). By performing live cell imaging of 2 d old Arabidopsis seedlings for 2-5 h inside the light-sheet microscope, we demonstrate that by using light-sheet microscopy, plants grow in healthy conditions and thus they might be studied at the subcellular level with minimal limitations. Additionally, the light-sheet setup allowed for fast and up to some extent aberration free imaging at a considerable depth of the root, providing the opportunity to quantify nuclear levels of EB1-GFP not only for epidermis, but also for cortex and endodermis.

Nuclear localization of EB1c

EB1c, the distinct subtype from EB1 family, is specifically present in vascular plants. It contains at its unique C-terminal sequence two composite motifs that serve as NLS (Komaki et al., 2010). Besides, our *in silico* search showed putative nuclear export signals at positions 213L, 215I, 217S and 218L for EB1c. These findings suggest that EB1c is not tightly enclosed in the nucleus and that it may follow a canonical routine of active nucleocytoplasmic shuttling. Thus, EB1c cytoplasmic localization during mitosis and cytokinesis might be independent to nuclear envelope breakdown. The observation of EB1c localization in nuclei of post-mitotic, non-dividing cells such as those of the transition zone and the elongation zone, suggests that it might have a nuclear function. Thus, the visualization of nuclear EB1c-GFP in cells up to the differentiation zone suggests that EB1c might not be exclusively necessary for mitotic progression but rather have a broader role.

EB1c localization and function was previously documented in dividing cells of *Arabidopsis thaliana* (Dixit et al., 2006; Bisgrove et al., 2008; Komaki et al., 2010; Ho et al., 2011). In all the above studies, EB1c was studied in the context of cell division and studies were focused on the localization of EB1c at the microtubule plus ends with special emphasis on phragmoplast.

However, the evident interphase nuclear localization and function of EB1c was not systematically addressed in these former studies. For this reason we surveyed the nuclear occurrence of EB1c not only in the interphase cells of the meristematic zone, but also in post-mitotic non-dividing cells of the root transition and elongation zones. Measuring nuclear parameters revealed clear distinction among root developmental zones and correlated them with specific patterns of EB1c accumulation in the nuclei of different tissues and in both meristematic and post-meristematic root zones. Thus, EB1c-GFP can be considered a reliable physiological nuclear marker for root developmental studies including post-meristematic cells. With the help of previously published data about longitudinal root zonation (Dello Ioio et al., 2007; Baluška and Mancuso, 2013; Panteris et al., 2013), we identified particular zones in Arabidopsis plants expressing EB1c-GFP. As expected, EB1c-GFP signal was present in all nuclei across the studied root zones and tissues. We thus employed correlative quantitative studies monitoring developmental fluctuations in EB1c-GFP expression levels with the trend of nuclear size increase which is observed in the shoot-ward root growth gradient. Inversely to the nuclear area increase, expression of EB1c-GFP showed root-ward trend within all tissues along the longitudinal root axis with the highest intensity peak in the meristematic zone. The highest expression level and the lowest correlation between EB1c-GFP mean intensity and nuclear surface area in the meristematic zone are in accordance to previously published data about the role of EB1c in the cell division progression. *eb1c* mutants showed defects in spindle pole alignment, chromosomal segregation and phragmoplast orientation, however, the organization of the preprophase band was not impaired (Komaki et al., 2010). Nevertheless, EB1c might have a dual function in meristematic cells, depending on its subcellular localization (one on microtubule plus ends during mitosis and another one in nuclei during interphase).

More importantly we demonstrate for the first time, an evident persistent localization of EB1c in the nuclei of post-meristematic, non-dividing root cells residing within the transition and the elongation zones. As such this is the first study using quantitative

advanced light-sheet microscopy to follow nuclear changes in correlation to the nuclear accumulation of a native cytoskeletal protein (EB1c was expressed under its native promoter) during development of the primary root. In the transition zone, where division is ceased while differentiation and endoreduplication goes on, it seems to be a turning point for the expression of EB1c protein. From this point more than genetically regulated, expression of EB1c seems to be mechanistically related to increase in cell nucleus size which is carried out by endoreduplication. What exactly happens at the transition point and how switch from mitotic division to endoreduplication occurs is not well documented (del Pozo et al., 2006; Ishida et al., 2009; Ishida et al., 2010; Adachi et al., 2011; Heyman et al., 2011; Doskočilová et al., 2013). Our analyses highlight the nuclear localization of EB1c, opening in this way the hitherto unexplored field with several possible questions. One matter that needs to be resolved concerns whether nuclear recruitment of EB1c has a functional sense as well as the nature of its putative nuclear functional role(s). It is also opening the question on the mechanism of EB1c nuclear transport and export as it was not deciphered before.

Cloning, transformation and superresolution microscopy of DRONPA-tagged EB1c

Novák D, Komis G.

Material and Methods

Cloning of *proEB1c::EB1c:DRONPA*

All polymerase chain reaction (PCR) fragments were generated using Phusion High-Fidelity DNA Polymerase (Thermo Fisher Scientific, USA). Gene open reading frame (ORFs) were amplified from Col-0 genomic DNA (gDNA) and recombined using MultiSite Gateway® technology (Invitrogen, USA). The coding sequence of wild type *EB1c* excluding stop codon was amplified by PCR with *attB1* and *attB2* primers (Fw-EB1c_attB15′-GGGGACAAGTTTGTACAAAAAAGCAGGCTGCATGGCTACGAA CATTGGGATGATGG-3′; Rev-EB1c_attB2 5′-GGGGACCACTTTGTACAAGAA AGCTGGGTCGCAGGTCAAGAGAGGAGATGAACC-3′) for recombination reaction. By BP recombination reaction entry clone pDONR221:*EB1c* was prepared. 663 bp upstream sequence of the initiation codon ATG of *EB1c* was amplified by PCR with *attB4* and *attB1* primers (Fw-proEB1c_attB4 5′-GGGGACAACTTTGTATAG AAAAGTTGTGTTGGACAGGTTAATGGGCTTGTG-3′; Rev-proEB1c_attB1 5′-GG GGACTGCTTTTTTGTACAAACTTGGCTTCGATTTTCTCAGGTTTCTCTC-3′) for recombination. Using BP recombination reaction, construct for native promotor pDONRP4P1R:*proEB1c* was prepared. Both constructs were confirmed by sequencing. By LR recombination reaction of destination vector pH7m34GW with entry clones pDONRP4P1R:*proEB1c*, pDONR221:*EB1c* and pDONRP2RP3:*DRONPA* (kindly provided by Dr. Amparo Rosero), expression construct pH7m34GW *proEB1c::EB1c:DRONPA* was prepared. *Agrobacterium tumefaciens* GV3101 was transformed with this expression clone.

Transient transformation of *Nicotiana benthamiana* leaves

YEB medium (5 ml) including appropriate selection antibiotics was inoculated with *Agrobacterium tumefaciens* GV3101 previously transformed with binary vectors coding EB1c-DRONPA protein. Culture grown at 28 °C, 220 rpm to OD_{600} 0,4 was pelleted at 3000 g, 4 °C for 10 min. Pellet was resuspended in 5 ml buffer including 10 mM $MgCl_2$, 10 mM MES (pH 5,6) and 150 µM acetosyringone and subsequently incubated at room temperature for 2 h. Bacterial culture containing EB1c construct was infiltrated into 6 week old *Nicotiana benthamiana* leaves using syringe. After agroinfiltration, plants were covered with transparent plastic bags and maintained in fytotron for 24 h, than were uncovered. After 48 h, transformed epidermal cells were observed with

CLSM (LSM 710, Axio Imager 2, Carl Zeiss) equipped with Plan-Apochromat 20x/0.8 objective (Carl Zeiss, Germany). Cells were imaged with excitation lasers 488 nm and 405 nm and with emission filter 493 – 598 nm.

Stable transformation of *Arabidopsis thaliana* plants

Transformed Agrobacteria were used for transformation of Arabidopsis Col-0 plants (Clough and Bent, 1998; Davis et al., 2009). Seedlings were selected on hygromycin B (50 mg/ml) selection medium to identify T1 transgenic plants. T1 transformants carrying *proEB1c::EB1c:DRONPA* constructs were checked for DRONPA fluorescence signal with Leica stereomicroscope M165 FC, equipped with PLANAPO 1.6x objective, (Leica, Germany) and for phenotype in comparison to control plants. No phenotypes were discerned and thus the T2 generation of Arabidopsis plants expressing pH7m34GW *proEB1c::EB1c:DRONPA* was harvested and used for further experiments.

PALM and SIM microscopy

For imaging of EB1c-DRONPA, seedlings were sandwiched between coverslip and glass slide and mounted on the piezo stage of the Elyra PS.1 microscope (Carl Zeiss, Germany). Since DRONPA is leaky, seedlings were imaged with 488 nm excitation line, until dark state was reinstated. Subsequently the 405 nm activator laser line was switched on. Photoswitching of DRONPA molecules was recorded as a time series for a period of 30-45 min until they were irreversibly bleached. For imaging, we used a 63x/1.40 NA oil immersion objective (Carl Zeiss, Germany), a bandpass filter between 490 and 550 nm and an Andor iXon 897 Ultra EM CCD camera. After acquisition images were reconstructed using photoactivation localization microscopy (PALM) algorithm of Zen software (Black Version).

Results

Transient expression of EB1c-DRONPA in *Nicotiana benthamiana* leaves

Transient transformation of *Nicotiana benthamiana* leaves was performed in order to test *proEB1c::EB1c:DRONPA* construct (**Fig. 16A**). This experiment preliminarily proved fluorescent properties of EB1c-DRONPA construct.

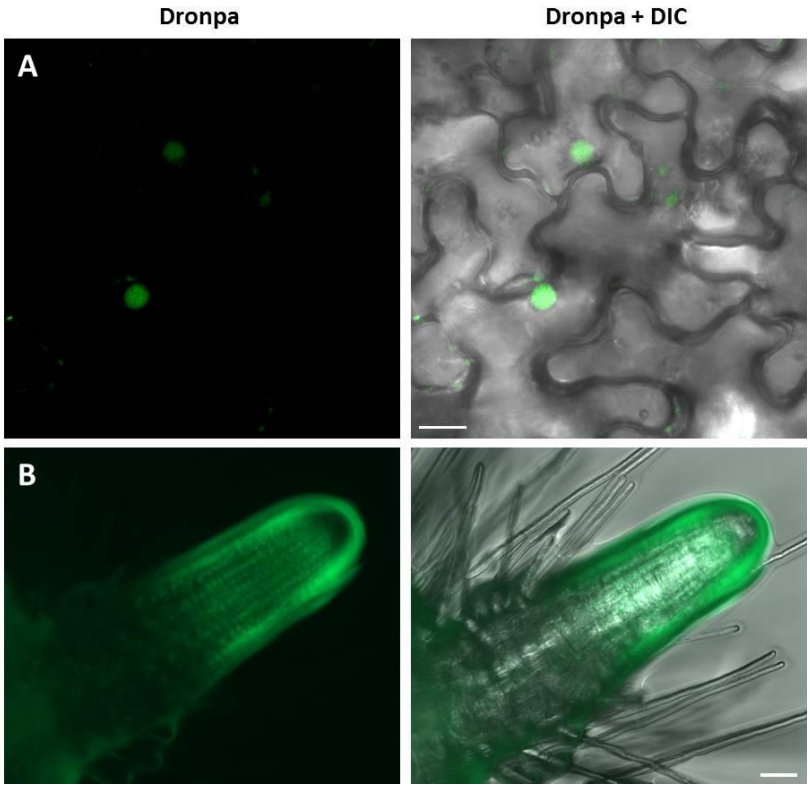

Fig. 16 Transient transformation of *N. benthamiana* leaves using *proEB1c::EB1c:DRONPA* construct in pH7m34GW expression vector showing nuclear localization (**A**). Representative images of *A. thaliana* lateral root stably transformed with *proEB1c::EB1c:DRONPA* construct (**B**). DIC - differential interference contrast. Scale bar = 20 µm in (A) and 50 µm in (B).

Stable transformation of EB1c-DRONPA to *Arabidopsis thaliana* Col-0

Stable transformation of *DRONPA*-fused *EB1c* gene driven under its own promoter into *Arabidopsis thaliana* Col-0 plants was performed using floral dip method. T1 transformants were selected on hygromycin B and checked for DRONPA fluorescence signal (**Fig. 16B**). T2 generation was harvested and used for microscopy experiments.

PALM imaging of root epidermal cells showed the nuclear spot-like distribution of DRONPA-tagged EB1c protein in comparison with diffuse nuclear signal observed by widefield epifluorescence microscopy (**Fig. 17A-B**). Moreover, PALM localization was more effective then structured illumination microscopy (SIM) in deciphering EB1c nuclear distribution (**Fig. 17C-D**).

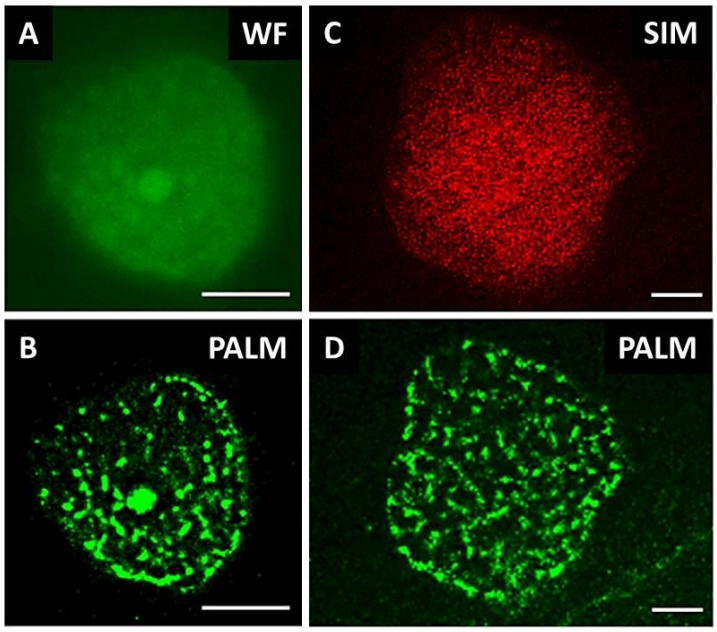

Fig. 17 Comparison of diffuse nuclear signal of DRONPA-tagged EB1c protein by widefield microscopy (WF) (**A**), photoactivation localization microscopy (PALM) (**B, D**) and structured illumination microscopy (SIM) (**C**). Images were performed by Dr. George Komis. Scale bar = 2 μm.

Discussion

Several fluorescence-based microscopy methods have been applied to visualize different organelles and subcellular compartments in living plant cells. For quantitative approaches widefield microscopy, spinning disk microscopy or CLSM are good workhorses. Advanced superresolution microscopy has provided new dimensions and perspectives for better imaging of living plant cells (Komis et al., 2018). Superresolution methods like PALM help uncover details of subcellular structures and molecular architecture.

Since EB1c contains two NLS motives at C-terminal part (Komaki et al., 2010) and also putative NES at positions 213L, 215I, 217S and 218L (Novák et al., 2016) it suggests that this protein is not tightly enclosed in the nucleus (it might undergo nucleo-cytoplasmic shuttling) and localization might be independent on nuclear envelope breakdown. During mitosis and cytokinesis EB1c localizes in cytoplasm. In non-dividing cells EB1c localizes in the nucleus, which is correspondencing to previously published data (Dixit et al., 2006; Komaki et al., 2010; Van Damme et al., 2004). Results from superresolution PALM microscopy showed the nuclear spot-like

distribution of EB1c-DRONPA. This suggests that EB1c might play an additional unknown role in the nucleus.

Gene Expression Pattern and Protein Localization of Arabidopsis Phospholipase D Alpha 1 Revealed by Advanced Light-Sheet and Super-Resolution Microscopy

---

Novák D, Vadovič P, Ovečka M, Šamajová O, Komis G, Colcombet J, Šamaj J.

Material and Methods

Plant Material, Mutant Screens

Seedlings were grown vertically on half-strength MS media (Murashige and Skoog, 1962) supplemented with 0.5% (w/v) gellan gum for 14 d in controlled environmental conditions with 21°C and a 16h/8h (light/dark) photoperiod. The illumination intensity was 150 µmol m^{-2} s^{-1}. Plants 12 to 15 days old were transferred to soil and cultivated in growth chamber in controlled environmental conditions with 21°C and a 16h/8h (light/dark) photoperiod and with the illumination intensity of 150 µmol m^{-2} s^{-1}.

We have used transfer DNA (T-DNA) insertion lines *pldα1-1* (SALK_067533) and *pldα1-2* (SALK_053785) described previously by Bargmann et al., 2009b and Zhang et al., 2004. The primers to check the T-DNA insertions were designed by the SIGnAL iSect tool (http://signal.salk.edu/tdnaprimers.2.html), and PCR was performed using genomic DNA from seedlings. *Arabidopsis thaliana* ecotype Columbia-0 (Col-0) was used as the control in the complementation assay (stomatal aperture measurement).

Preparation of complemented PLDα1-YFP

To generate the complementation transgenic lines, the coding sequence of wild type *PLDα1*(AT3G15730) under the control the native *PLDα1* promoter (1,944 bp upstream of the initiation codon ATG of *PLDα1*) was introduced into pGreen0229-YFP-Tnos vector using *Bam*HI-*Kpn*I restriction digest to generate *proPLDα1::PLDα1:YFP* construct. The constructs were confirmed by sequencing and transformed by floral dipping (Clough and Bent, 1998; Davis et al., 2009) to Arabidopsis wild type Col-0 as well as to *pldα1-1* and *pldα1-2* mutants using *Agrobacterium tumefaciens* strain GV 3101. In T1 generation we have selected 3 independent transgenic lines with the same fluorescent properties. One line was chosen and T2 or T3 progeny of BASTA-resistant transformants, carrying a single homozygous insertion, were used for experiments.

Preparation of transgenic line carrying PLDα1-YFP and mRFP-TUB6

Arabidopsis *pldα1-2* stably expressing *proPLDα1::PLDα1:YFP* in T2 generation were crossed with Col-0 plants stably expressing *pUBQ1:mRFP::TUB6* kindly provided by Geoffrey O. Wasteneys (Ambrose et al., 2011). F1 generation plants with PLDα1-YFP and mRFP-TUB6 (mRFP = red fluorescent protein, TUB6 = β-TUBULIN 6) expression

were selected based on fluorescence signal in the epifluorescence microscope (Axio Imager.M2, Carl Zeiss, Germany).

Immunoblotting analysis

Seedlings of 5 days old *pldα1-1* PLDα1-YFP and *pldα1-2* PLDα1-YFP complemented plants, a progeny from one selected T2 plant from each independent transgenic SALK line, were used for immunoblotting analysis. Roots from approximately 50 seedlings of 14 days old plants of *Arabidopsis thaliana*, ecotype Col-0, *pldα1-1* and *pldα1-2* single mutants as well as *pldα1-1* PLDα1-YFP and *pldα1-2* PLDα1-YFP complemented lines were homogenized in liquid nitrogen to fine powder and the proteins were extracted in E-buffer (50 mM HEPES (pH 7.5), 75 mM NaCl, 1 mM EGTA, 1 mM $MgCl_2$, 1 mM NaF, 10% (v/v) glycerol, Complete™ EDTA-free protease inhibitor and PhosSTOP™ phosphatase inhibitor cocktails (both from Roche, Basel, Switzerland). Following centrifugation at 13000g in 4°C for 15 min, supernatants were mixed with 4 fold concentrated Laemmli buffer (final concentration 62.5 mM Tris-HCl (pH 6.8), 2% (w/v) SDS, 10% (v/v) glycerol, 300 mM 2-mercaptoethanol) and boiled at 95 °C for 5 minutes. Protein extracts were separated on 12% TGX Stain-Free™ (Bio-Rad) gels (Biorad). Equal protein amounts were loaded for each sample. Proteins were transferred to PVDF membranes in a wet tank unit (Bio-Rad) overnight at 24 V and 4°C using the Tris-glycin-methanol transfer buffer. For immuno-detection of proteins, membranes were blocked in a mixture of 4% w/v low-fat dry milk and 4% w/v bovine serum albumin in Tris-buffered-saline (TBS, 100 mM Tris-HCl; 150 mM NaCl; pH 7.4) at 4 °C overnight. After washing with TBS-T (TBS, 0.1% Tween 20) membranes were incubated with polyclonal anti-phospholipase D alpha 1/2 antibody (Agrisera, Sweden) diluted 1:5000 in TBS-T containing 1% w/v bovine serum albumin (BSA) or with anti-GFP monoclonal antibody (Sigma-Aldrich, Merck, USA) diluted 1:1000 in TBS-T containing 1% w/v BSA at room temperature for 1.5 h. To validate the protein transfer, membranes were incubated with anti-beta-tubulin monoclonal antibody (Sigma-Aldrich, Merck, USA) diluted 1:2000 in TBS-T containing 1% w/v BSA at room temperature for 1.5 h. Following five washing steps in TBS-T, membranes were incubated 1.5h at RT with a horseradish peroxidase (HRP) conjugated goat anti-rabbit IgG secondary antibody (diluted 1:5000) in the case of anti-phospholipase D alpha 1/2 primary antibody, and with a HRP conjugated goat anti-mouse IgG secondary antibody (diluted 1:5000; both from Santa Cruz Biotechnology, Santa Cruz, CA, USA) in the case of anti-

GFP and anti-beta-tubulin primary monoclonal antibody. After washing in TBS-T, the signals were developed using Clarity Western ECL substrate (Biorad, Hercules, CA, USA). Luminescence was detected on Chemidoc MP documentation system (Biorad). Immunoblot analyses were performed in three biological replicates.

Stomatal aperture measurement after ABA treatment

Cotyledons of 7 days-old plants of various genotypes were used for stomatal closure analysis. Dissected cotyledons were floated on stomatal opening buffer [10 mM 2-(N-morpholino) ethanesulfonic acid (MES-KOH), pH = 6.15 and 30 mM KCl] under light for 2 hrs to fully open the stomata. Then they were treated with ABA (10 μM) in stomatal opening buffer for indicated period of time. ABA stock solution was prepared in ethanol. Ethanol in stomatal opening buffer was used as a negative control. Final concentration of ethanol in experimental solutions did not exceeded 0.01%. Stomatal aperture was documented using epifluorescence microscope AxioImager.M2 (Carl Zeiss, Germany) equipped with EC Plan-Neofluar 10x/0.30 objective (Carl Zeiss, Germany) using transmission light in single focal plane and quantitatively analyzed using Fiji (ImageJ) software (Schindelin et al., 2012).

Whole mount immunofluorescence labelling

Immunolocalization of microtubules, PLDα1, PLDα1-YFP and clathrin in root wholemounts was done as described previously (Šamajová et al., 2014). Samples were immunolabeled with rat anti-α-tubulin (clone YOL1/34; ABD Serotec), rabbit anti-phospholipase D alpha 1/2 (Agrisera, Sweden), mouse monoclonal anti-clathrin LC (Sigma-Aldrich) or mouse anti-GFP (Abcam) primary antibodies diluted 1:300, 1:300, 1:300 and 1:100, respectively in 3% (w/v) BSA in PBS at 4 °C overnight. In the case of double or triple co-immunolocalization a sequential immunolabeling was performed. Secondary antibodies included Alexa-Fluor 488 goat anti-rat, Alexa-Fluor 488 goat anti-mouse or Alexa-Fluor 546 goat anti-rat IgGs were diluted 1:500 in PBS containing 3% (w/v) BSA for 3 h (1.5 h at 37 °C and 1.5 h at room temperature). Where necessary, nuclei were counterstained with 4′,6-diamidino-2-phenylindole (DAPI). Microscopic analysis of immunolabeled samples was performed with a Zeiss 710 CLSM platform (Carl Zeiss, Germany), using excitation lines at 405, 488 and 561 nm from argon, HeNe, diode and diode pumped solid-state lasers.

Light-Sheet Fluorescence Microscopy

Developmental live cell imaging of 2-3 days old Arabidopsis plants with PLDα1-YFP expression was done with the light-sheet Z.1 fluorescence microscope (Carl Zeiss, Germany) equipped with W Plan-Apochromat 20x/1.0 NA detection objective (Carl Zeiss, Germany) and two LSFM 10x/0.2 NA illumination objectives (Carl Zeiss, Germany). Seedlings were prepared in FEP tubes with an inner diameter of 2.8 mm and wall thickness of 0.2 mm (Wolf-Technik, Germany) according to the "open system" protocol for long-term live-cell imaging of *Arabidopsis thaliana* seedlings described by Ovečka et al. (2015). Root was growing in the block of the culture medium inside of the FEP tube and upper green part of the seedling developed in an open space of the FEP tube with the access to air. Sample holder with the sample was placed into observation chamber of the light-sheet microscope tempered to 22°C using Peltier heating/cooling system. Before insertion of the sample to the microscope plants were ejected slightly out of the FEP tube allowing imaging of the root in the block of solidified culture medium, but without the FEP tube. Before the imaging, liquid medium filling the observation chamber was filter-sterilized using a sterile syringe filter. Roots were imaged using dual-side light-sheet illumination with excitation laser line 514 nm, beam splitter LP 580 and with emission filter BP525-565. Images were recorded with the PCO.Edge sCMOS camera (PCO AG, Germany) with the exposure time 30 ms and the imaging frequency of every 5 min in z-stack mode for 5-20 hours. Scaling of recorded images in x, y and z dimensions was 0.228 x 0.228 x 0.499 μm.

Spinning disk and Confocal laser scanning microscopy

Hypocotyls, leaves with pavement cells, stomata and trichomes of 5-8 days after germination Arabidopsis plants with PLDα1-YFP expression were documented with spinning disk microscope (Cell Observer SD, Carl Zeiss, Germany) equipped with Plan-Apochromat 20x/0.8 (Carl Zeiss, Germany) and Plan-Apochromat 63x/1.40 Oil (Carl Zeiss, Germany) objectives. Cells were imaged with excitation laser 514 nm and with emission filter BP535/30 for YFP. Cotyledons, petioles and guard cells were documented with confocal laser scanning microscope LSM 710 (Carl Zeiss, Germany) equipped with Plan-Apochromat 20x/0.8 (Carl Zeiss, Germany) and alpha Plan-Apochromat 63x/1.46 Oil (Carl Zeiss, Germany) objectives. Plants of 6 days after germination were stained with 4 μM FM4-64 (styryl dye for plasma membrane

visualisation, Invitrogen, USA) diluted in half-strength liquid MS medium for 90 min before imaging. Samples were imaged with excitation lasers 514 nm for YFP and 561 nm for mRFP and FM4-64, beam splitters MBS 458/514 for YFP, MBS 458/561 for mRFP and MBS 488/561 for FM4-64. Emission filters used were 519 – 550 nm for YFP, 590 – 610 nm for mRFP and 651 – 759 nm for FM4-64.

Structured Illumination Microscopy

The same immunolabeled wholemount samples examined with CLSM were also analyzed via a Zeiss SIM platform coupled with a PCO.Edge 5.5 sCMOS camera (Elyra PS.1, Carl Zeiss, Germany). Fluorophores were excited with the 405, 488, 561 and 647 nm laser lines. For acquisition with a 63x/1.40 oil immersion objective, the grating pattern was set to 5 rotations with 5 standard phase shifts per angular position. In case of z-stacks, Nyquist sampling was selected to be the smallest one (corresponding to DAPI channel with 91 nm section thickness), leading to oversampling of the rest of the channels. Image reconstruction was done according to previously published procedure (Komis et al., 2015).

Image processing

The post-processing, default deconvolution and profile measurement of all fluorescence images in this study, including 3D reconstruction or maximum intensity projection from individual z-stacks and creating subsets was done using ZEN 2010 software. All images exported from ZEN 2010 software were assembled and captioned in Microsoft PowerPoint to final pictures.

Results

Expression patterns of PLDα1-YFP in Arabidopsis plants

In order to characterize roles of PLDα1 in the plant development, we performed *in vivo* cell- and tissue-specific expression analysis of the PLDα1-YFP driven by native *PLDα1* promoter in two stably transformed *pldα1* mutants of *Arabidopsis thaliana*. Thus, both *pldα1-1* and *pldα1-2* mutants were stably transformed with *proPLDα1::PLDα1:YFP* construct using the floral dip method (Clough and Bent, 1998). Comparison of *proPLDα1::PLDα1:YFP* expression patterns in different aerial organs and tissues of *pldα1-1* and *pldα1-2* mutants stably expressing PLDα1-YFP is presented in **Fig. 18**. In order to prove the expression of PLDα1-YFP fusion protein in experimental plants

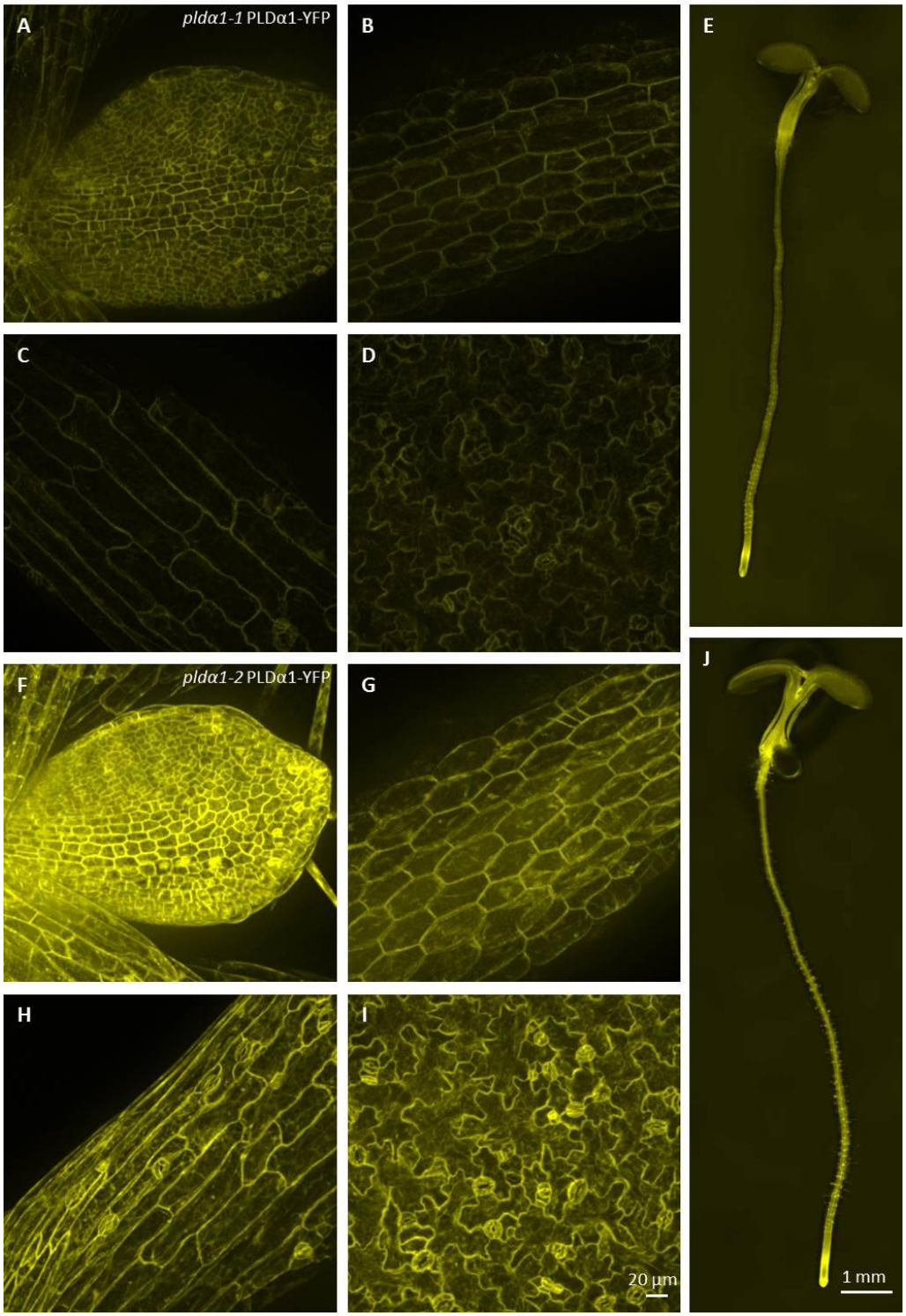

Fig. 18 Comparison of PLDα1-YFP localization in different aerial organs and tissues of *pldα1-1* (**A-E**) and *pldα1-2* (**F-J**) mutants stably expressing PLDα1-YFP driven by its own promoter: epidermis of first true leaf (**A, F**), epidermal cells of hypocotyl (**B, G**), epidermal cells of cotyledon petiole (**C, H**), epidermal cells of cotyledon (**D, I**) and entire 5 days-old seedling (**E, J**).

(*pldα1-1* and *pldα1-2* mutant plants stably transformed with *proPLDα1::PLDα1:YFP* construct), we performed SDS-PAGE with immunoblot analysis using

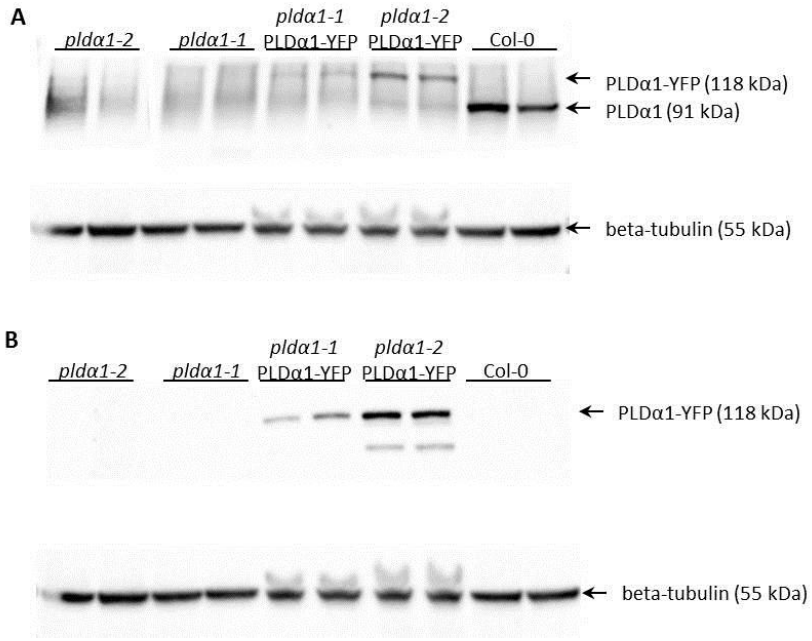

Fig. 19 Detection of PLDα1 in roots of *pldα1* mutants and in rescued *pldα1* mutants stably transformed with *proPLDα1::PLDα1:YFP* construct. (**A**) Immunoblots of *pldα1* mutants and in rescued *pldα1* mutants probed with anti-PLDα1/2 antibody. (**B**) Immunoblots of *pldα1* mutants and in rescued *pldα1* mutants probed with anti GFP antibody. PVDF membranes (BioRad) were probed with anti-beta tubulin as a loading control. Imunoblots were performed by Dr. Pavol Vadovič.

anti-phospholipase D alpha 1/2 and anti-GFP antibodies. This analysis confirmed the presence of PLDα1-YFP fusion protein with the expected molecular mass of 118 kDa,using both anti-PLDα1 and anti-GFP antibodies (**Fig. 19A-B**). In Col-0, which was used as a control, anti-PLDα1 antibody showed a protein band with a molecular weight of 91.8 kDa corresponding to PLDα1. We also confirmed the absence of PLDα1 protein in both *pldα1-1* and *pldα1-2* mutant plants. In addition, Col-0, *pldα1-1* and *pldα1-2* mutant plants were used as negative controls for the use of the anti-GFP antibody and we did not observe any band in these lines (**Fig. 19B**).

Functional complementation of *pldα1-1 and pldα1-2* mutants with PLDα1-YFP expression driven under its own promoter

Cellular levels of ABA increase in responses to drought and salt stresses, which promotes stomatal closure in order to prevent water loss. Although PLDα1 is the most predominant PLD in plants, *pldα1* KO mutants do not exhibit significant phenotypical changes (Fan et al., 1997; Zhang et al., 2012). Nevertheless PLDα1 controls proper water balance in plants responding to ABA by stomatal closure and this response is impaired in the *pldα1* KO mutants (Jiang et al., 2014; Pleskot et al., 2014; Zhang et al.,

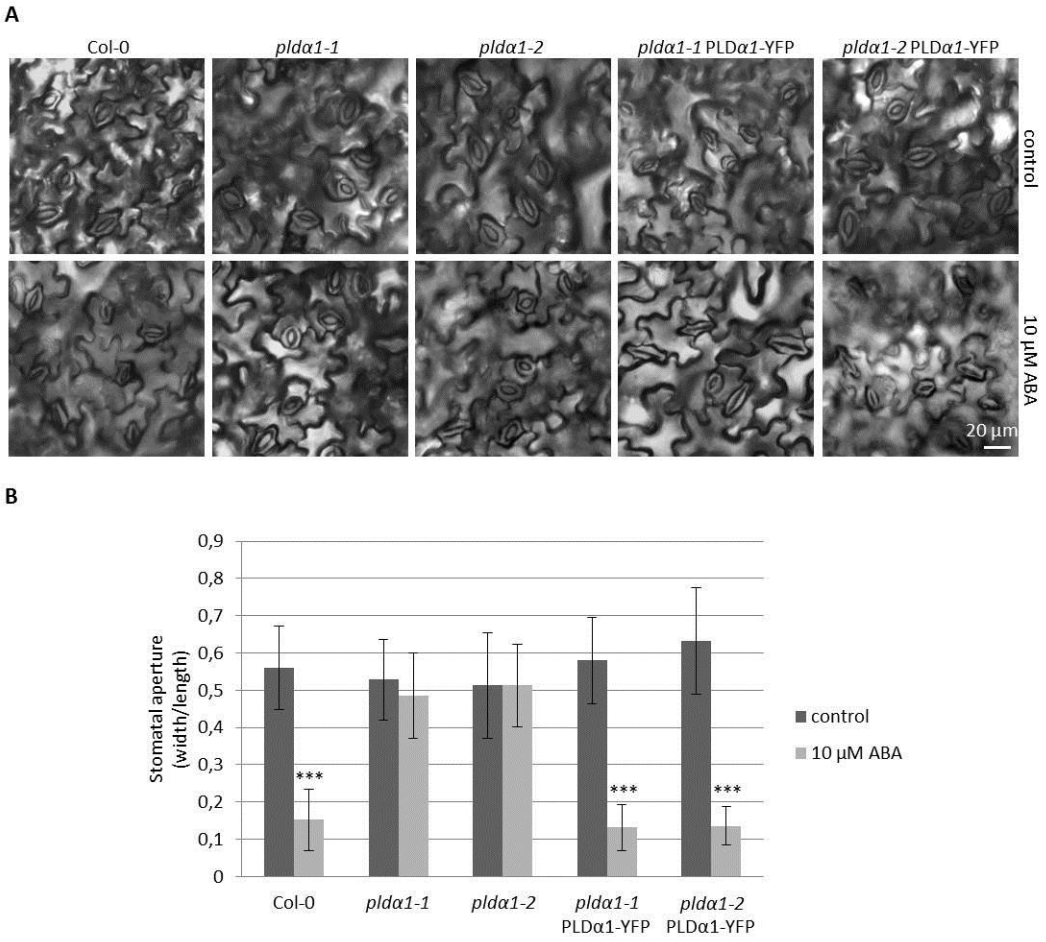

Fig. 20 ABA-induced stomatal closure in *pldα1* mutants and rescued plants. (**A**) Cotyledon epidermis of 7 days old Col-0, *pldα1-1*, *pldα1-2, pldα1-1* PLDα1-YFP and *pldα1-2* PLDα1-YFP plants showing opening of stomata in control condition and after 2 hours treatment with 10 µM ABA. (**B**) Aperture of cotyledon stomata guard cells of Col-0, *pldα1-1*, *pldα1-2, pldα1-1* PLDα1-YFP and *pldα1-2* PLDα1-YFP (measured as a ratio of aperture width and length, which is reduced upon its closure) in control condition and after 2 hours treatment with 10 µM ABA. Bar charts represent the mean ± SD for n = 40. Three asterisks indicate statistically significant differences (two-tailed paired *t*-test, $P < 0.001$) in stomatal closure. Images were performed in collaboration with Dr. Pavol Vadovič.

2017a). To verify that *pldα1-1* and *pldα1-2* mutants were complemented with *proPLDα1::PLDα1:YFP* construct and show wild type-like behaviour, we examined stomatal closure ability of these revertants by measuring stomatal aperture in cotyledons of 7 days old plants after treatment with 10 µM ABA. We have observed significantly increased stomatal closure after ABA treatment of wild type plants in comparison to *pldα1-1* and *pldα1-2* mutants, which were ABA-insensitive and showed no change in stomatal apertures (**Fig. 20**). These results were consistent with published data (Zhang et al., 2004; Jiang et al., 2014). Importantly, *pldα1-1* and *pldα1-2* mutant plants genetically complemented with *proPLDα1::PLDα1:YFP* construct reacted to ABA

treatment by substantial decrease of stomatal aperture, similarly to the wild type plants (**Fig. 20**). These results confirmed the phenotypical complementation of *pldα1-1* and *pldα1-2* mutants with *proPLDα1::PLDα1:YFP* construct which can be considered as a functional one for further expression and localization studies.

Developmental expression pattern and localization of PLDα1-YFP in Arabidopsis plants

Observation of developmental expression pattern and localization of PLDα1-YFP fusion protein has been done in *pldα1-1* mutant stably expressing a *proPLDα1::PLDα1:YFP* construct at cell-, tissue- and organ-specific levels using light-sheet fluorescence microscopy. Subcellular localization was performed using confocal and spinning disk microscopy. Developmental LSFM has been performed with 2- to 3-days old seedlings that were growing inside of the microscope imaging chamber in time periods ranging from 5 to 20 h. During these imaging periods, roots of experimental plants exhibited continuous growth at constant root growth rates. LSFM offered the possibility not only to localize PLDα1-YFP at the cellular level in root surface tissues (**Fig. 21A**), but it also allowed deep root imaging and tissue-specific visualization and localization of PLDα1-YFP in internal root tissues (**Fig. 21B**).

Imaging of tissue-specific expression of PLDα1-YFP in roots using LSFM revealed developmental regulation of PLDα1-YFP amount in the root apex. The expression levels of PLDα1-YFP in the root meristematic zone including rhizodermis, cortex and procambium were relatively low (**Fig. 21B**). On the other hand, particularly strong expression levels were revealed in the apical and lateral root cap cells (**Fig. 21C**). Remarkably strong expression was observed in central columella cells and particularly in cells of the third columella layer (**Fig. 21B-C**). Semi quantitative evaluation of the PLDα1-YFP amount in different cell layers of root apex (**Fig. 21D**) revealed a steep gradient between third and fourth outermost layers of the central root cap (**Fig. 21D-F**; profiles 1-2). There was a relatively low amount of PLDα1-YFP in the primary meristems at the position of the stem cell niche in comparison to the lateral root cap cells (**Fig. 21D-F**; profile 3). Proximally to the region of initial cells there was a clear gradient in the PLDα1-YFP amount within the radial organization of the root meristem with the highest level in the lateral root cap cells, much lower level in the rhizodermis, cortex and endodermis, and the lowest level in central cylinder tissues (**Fig. 21D-F**; profile 4). Different expression levels among lateral root cap cells, dermal tissues

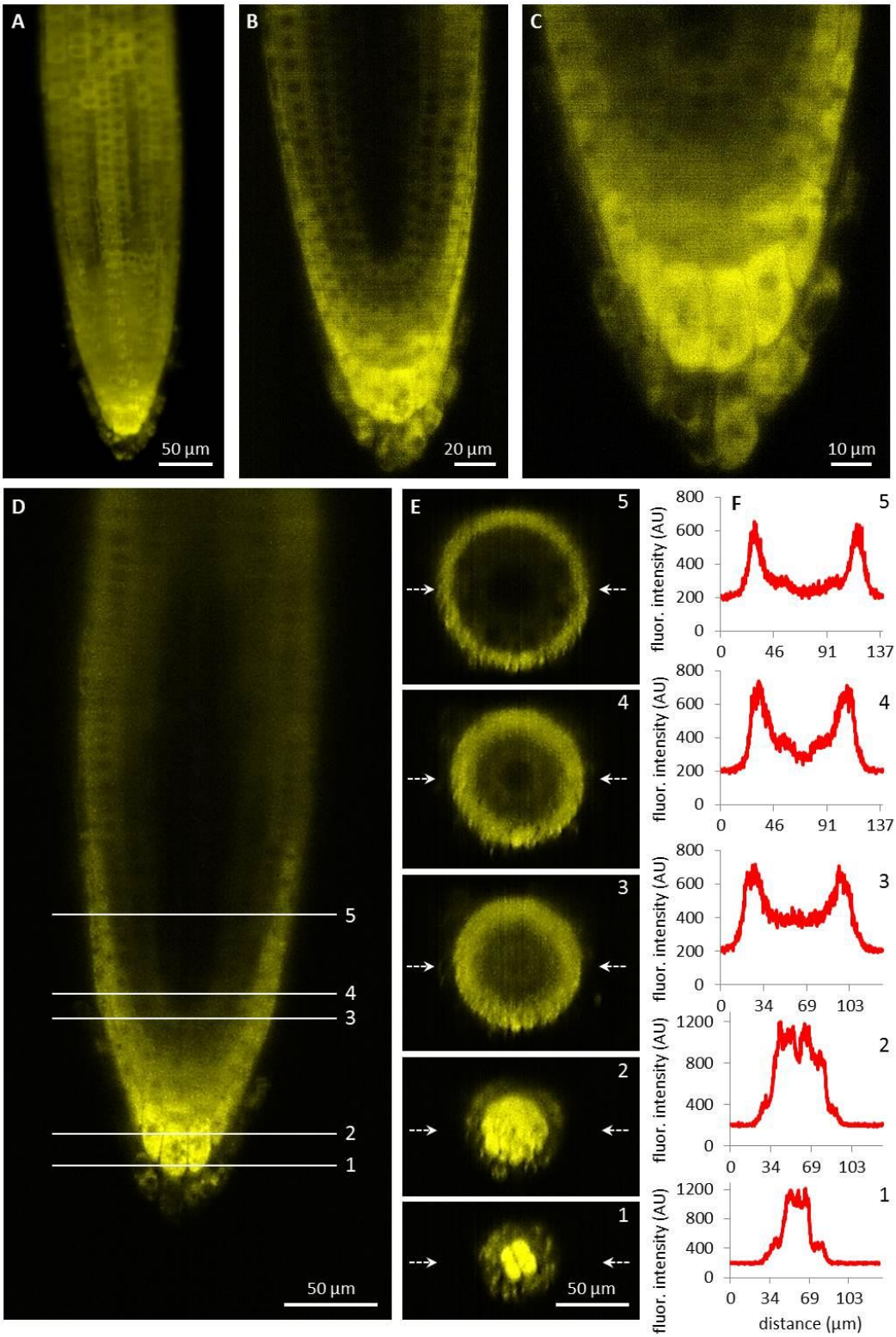

Fig. 21 Light-sheet fluorescence microscopy localization of PLDα1-YFP driven by *PLDα1* own promoter in *Arabidopsis thaliana* roots. (**A**) Overview of PLDα1-YFP localization in different tissues of the root tip constructed from maximum intensity projection of 330 optical sections (with thickness of 0.5 µm each). Amount of PLDα1-YFP fluctuated in root rhizodermal cells while the highest localization was visible in the root cap cells. (**B**) Median optical section of the root tip revealed differential distribution of PLDα1-YFP with the strongest expression in the root cap and lateral root cap cells and with much lower production of PLDα1-YFP in

rhizodermal, cortical and endodermal cell layers and with very low production in procambial cells. (**C**) Detail of the root cap showing the strongest expression level of PLDα1-YFP in central columella cells and particularly in cells of the third root cap layer. (**D-F**) Qualitative and semi-quantitative evaluation of the relative PLDα1-YFP distribution in longitudinal and radial zonation of the root tip. Five profiles at different positions of the root tip (**D**) were visualized into orthogonal projections of radial root sections (**E**) and profiles in the median positions of the radial root sections (indicated by arrows) were quantitatively displayed (**F**). Images were taken from *pldα1-1* and *pldα1-2* mutant plants stably expressing PLDα1-YFP. LSFM images were performed by Dr. Miroslav Ovečka.

(rhizodermis, cortex and endodermis) and central cylinder tissues were clearly visible in the central part of the root meristematic zone (**Fig. 21D-F**; profile 5).

In comparison to the relatively low expression level of the PLDα1-YFP in the root meristem, a dramatic enhancement was detected in the root transition zone, particularly in the rhizodermis (**Fig. 22A**). Rhizodermal cells showed much stronger expression levels in the trichoblast cell files compared to the atrichoblast ones (**Fig. 22B-E**). Relatively strong expression of PLDα1-YFP in trichoblast cells of the transition root zone revealed one additional aspect of particular interest. It was the strongly polarized localization of PLDα1-YFP at the cell corner of the trichoblasts facing the cleft contact with two underlying cortical cells (**Fig. 22A, C**). Thereon, the strong expression level of PLDα1-YFP in trichoblast cell files was also maintained later in the development of root hairs during bulge formation (**Fig. 22B**) and in tip-growing root hairs (**Fig. 22F-H**). Time-course semi quantitative evaluation of PLDα1-YFP distribution clearly revealed its accumulation in growing tips of root hairs (**Fig. 22G, H**). The PLDα1-YFP expression pattern in growing roots thus reflected the tissue-specific and developmentally-regulated transition from low PLDα1-YFP protein levels in actively dividing cells of the root apical meristem to much enhanced protein accumulation in the root transition zone harbouring post-mitotic cells preparing for cell elongation (**Fig. 21D-F**). Cell differentiation in root tissues led to localized accumulation of PLDα1-YFP, particularly in the developing rhizodermis, where PLDα1-YFP accumulated preferentially in trichoblasts (**Fig. 22B-E**), especially during the process of root hair formation (**Fig. 22F-H**). In all root tissues expressing moderate levels of PLDα1-YFP (root cap cells, root transition zone, trichoblast cell files and tip growing root hairs) we observed cytoplasmic localization of the fusion protein.

Expression pattern and localization of PLDα1-YFP in different cell types of aerial parts of 6 days old seedlings were documented with confocal and spinning disk microscopy.

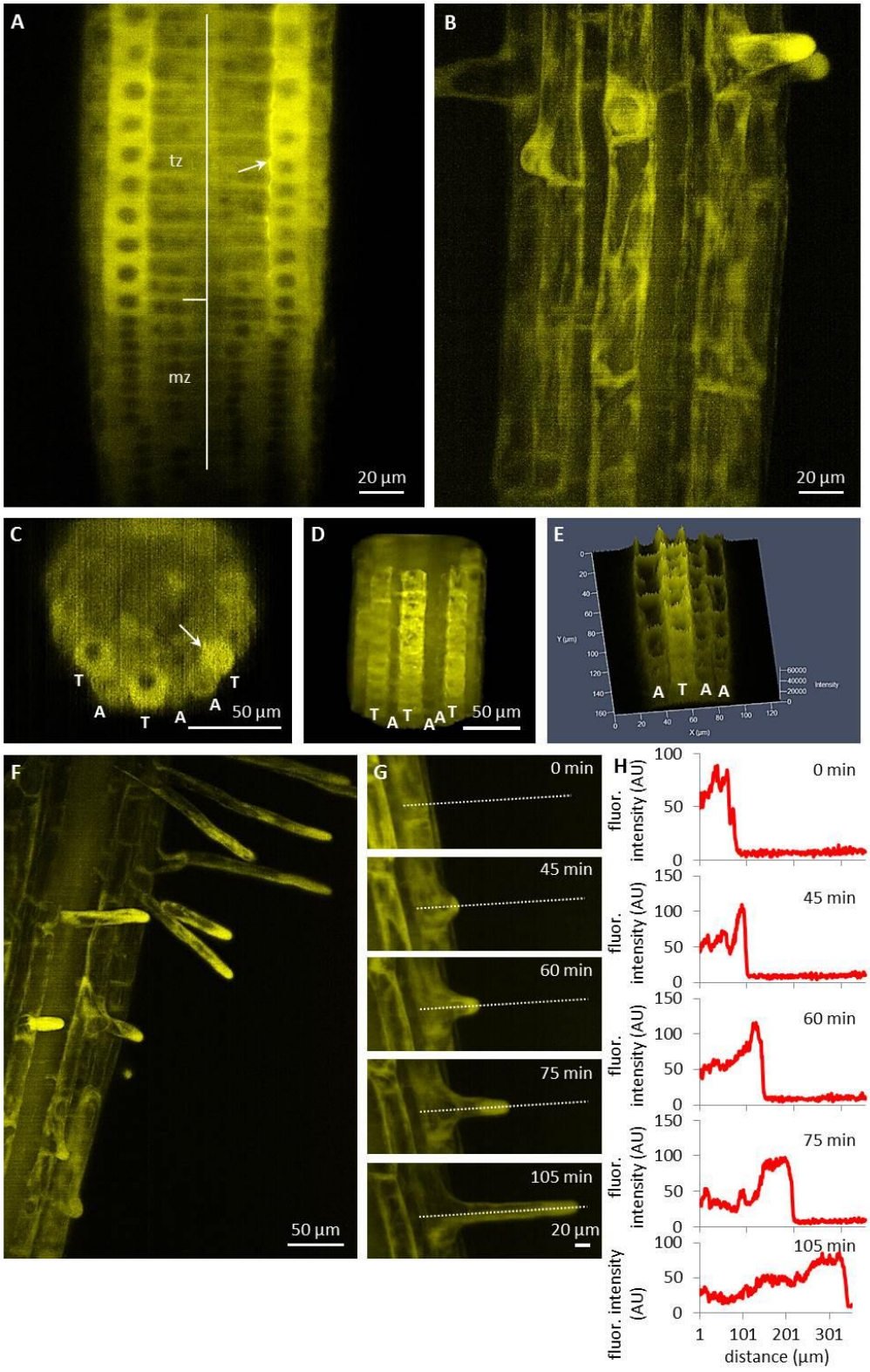

Fig. 22 Tissue- and cell-specific localization of PLDα1-YFP driven by its own native promoter in the root of *Arabidopsis thaliana* by light-sheet fluorescence microscopy. (**A**) Distribution of PLDα1-YFP in meristematic zone (mz) with relatively low expression and in transition zone (tz) with enhanced expression. (**B**) Differentiation zone of the root with stronger expression level of PLDα1-YFP in trichoblasts and bulges of emerging root hairs and lover expression level in atrichoblast cell files. (**C-E**) Orthogonal projection (**C**), 3D-rendering (**D**) and intensity-based

3D visualization (**E**) of root differentiation zone showing higher expression level of PLDα1-YFP in rhizodermal trichoblast cell files (labelled as T) and lover expression level in atrichoblast cell files (labelled as A). Arrows in A and C point local accumulation of PLDα1-YFP at the cell corner of the trichoblasts in the contact with two underlying cortical cells. (**F**) Enhanced localization of PLDα1-YFP in trichoblast cells at the stage of root hair formation and apparent accumulation of PLDα1-YFP in growing root hairs. (**G**) Time-course recording of accumulation and relocation of PLDα1-YFP during the root hair outgrowth in trichoblast root cell. Time frames of individual developmental stages are indicated in min. Dotted lines along the median longitudinal axis of the root hair indicate the position of fluorescence intensity profile measurement. (**H**) Fluorescence intensity profiles of PLDα1-YFP distribution corresponding to particular developmental stages of the root hair formation from the trichoblast root cell in (**G**). Images were taken from *pldα1-1* and *pldα1-2* mutant plants stably expressing PLDα1-YFP using light-sheet microscopy. LSFM images were performed by Dr. Miroslav Ovečka.

Relatively high expression level of PLDα1-YFP was observed in hypocotyl epidermal cells (**Fig. 23A**), in pavement cells and stomata guard cells of cotyledons (**Fig. 23B**), in leaf epidermis and stomata guard cells of leaves (**Fig. 23D**). Consistently with strong expression level of PLDα1-YFP in root rhizodermis and in developing root hairs we observed also strong expression of PLDα1-YFP in leaf trichomes (**Fig. 23E**). In more detail, high amounts of PLDα1-YFP were found at tips of trichome branches (**Fig. 23E**). A high level of PLDα1-YFP was observed also in epidermal cells of leaf petioles (**Fig. 23F**).

In cells of all examined aerial tissues, PLDα1-YFP was localized in the cytosol and predominantly at the cell cortex in the vicinity of the plasma membrane. Additionally, PLDα1-YFP was localized in cytoplasmic strands of interphase cells (**Fig. 23F**).

Accumulation of PLDα1-YFP in growing root hairs (**Fig. 22F-H**) suggested its role in actively growing cell domains. To test this possible scenario in leaf trichomes, we identified individual stages of trichome development in the first true leaf and we performed semiquantitative evaluation of PLDα1-YFP distribution along single profiles in individual trichome branches. To quantify PLDα1-YFP developmental redistribution during trichome formation, we measured profiles of PLDα1-YFP fluorescence in young trichome primordia without branches (**Fig. 24A**), in each individual branch of growing trichomes during later developmental stages (**Fig. 24B-D**) up to final stage of fully developed three-branched trichomes (**Fig. 24E**). Profiling of fluorescence intensity along individual trichome branches clearly revealed higher accumulation of PLDα1-YFP at the tip of actually growing branch during trichome development (**Fig. 24F**).

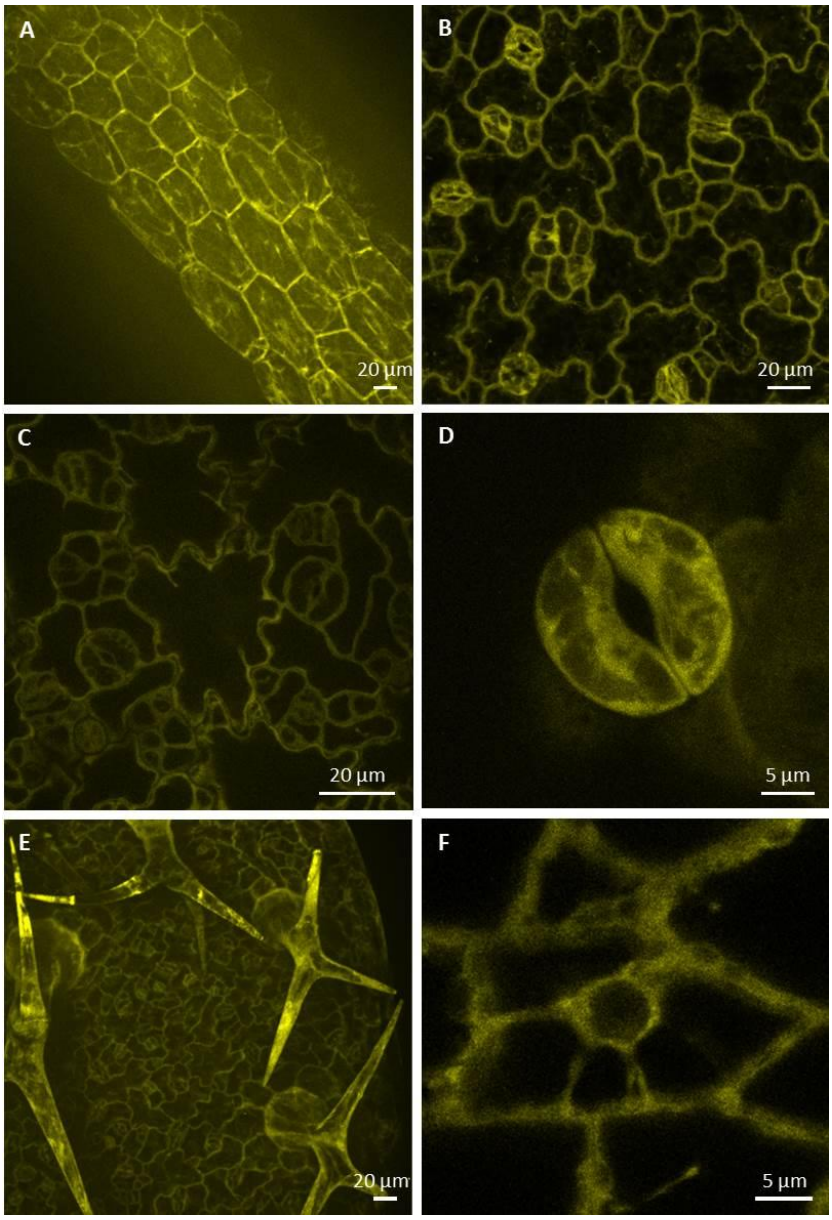

Fig. 23 Localization of PLDα1-YFP driven by *PLDα1* own promoter in different aerial organs and tissues of *Arabidopsis thaliana* seedlings. Images were taken from different cell types of aerial tissues of living *pldα1-2* mutants stably expressing PLDα1-YFP driven by its own promoter using confocal and spinning disk microscopy. Localization of PLDα1-YFP in hypocotyl epidermal cells (**A**), cotyledon epidermal cells and stomata (**B**), leaf epidermal pavement cells and stomata guard cells (**C**), leaf stoma guard cells (**D**), leaf epidermal cells and trichomes (**E**), and petiole epidermal cell (**F**). Spinning disk microscopy (A, C, D), confocal microscopy (B, E, F).

Association of PLDα1-YFP with microtubules

In order to investigate the localization pattern of PLDα1-YFP in respect to cortical and mitotic microtubules we crossed *pldα-1-2* mutant plants stably expressing *proPLDα1::PLDα1:YFP* construct with Col-0 plants stably expressing p*UBQ1::mRFP:TUB6* construct (red fluorescent protein fused to Arabidopsis alfa-

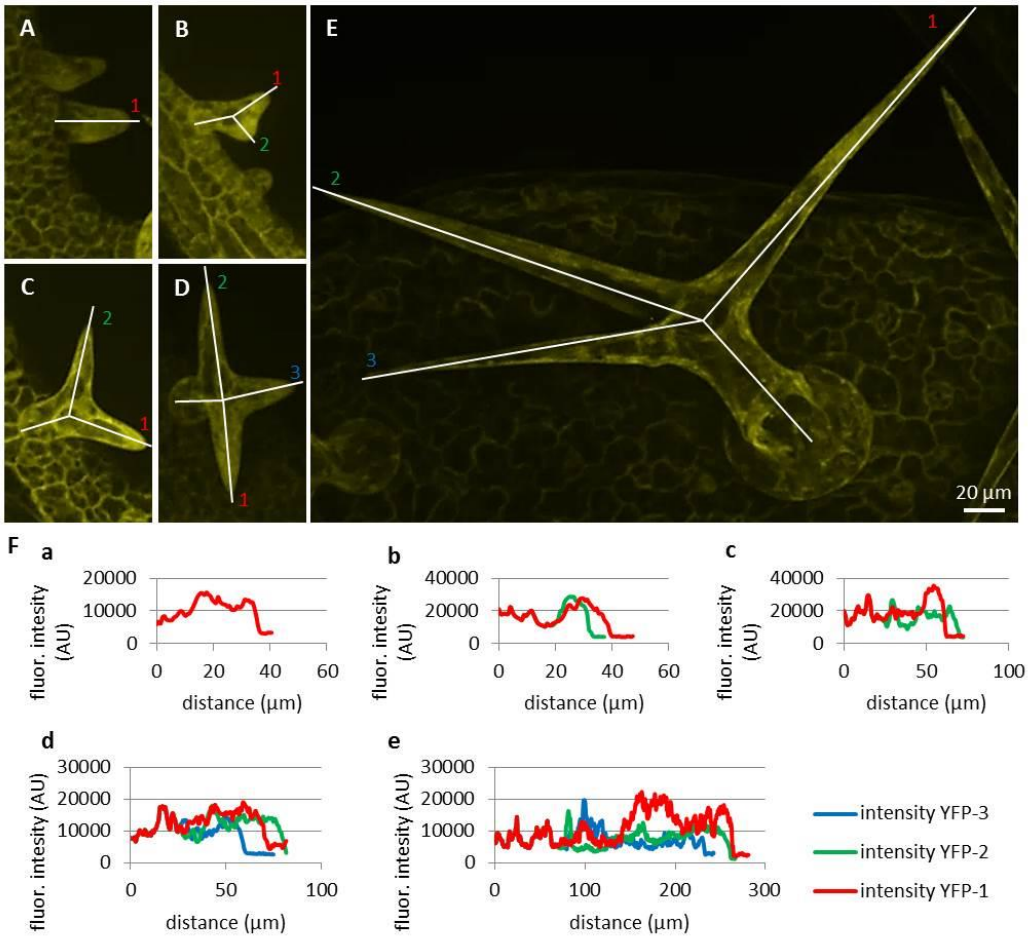

Fig. 24 Localization and accumulation of PLDα1-YFP in developing leaf trichomes in *pldα1-2* mutant plants stably expressing PLDα1-YFP driven by *PLDα1* own promoter. Images of maximum intensity projection were reconstructed from individual optical sections taken at the same live cell imaging condition from first (**B, D, E**) and second (**A, C**) true leaves of *pldα1-2* mutants stably expressing PLDα1-YFP. Developing trichomes are displayed from early developing stages with no branches (**A**), with progressing two branches (**B, C**), growing three branches (**D**) to maturating three branches (**E**). (**F**) Profiles of fluorescence intensity of YFP distribution in individual trichome branches indicated by lines in (**A-E**).

tubulin 6 isoform, Ambrose et al., 2011). Labelling of the plasma membrane in cells of such crossed line was performed with FM4-64. The co-localization experiments were done in non-dividing leaf petiole epidermal cells using confocal laser scanning microscopy (**Fig. 25**). 3-D rendering and orthogonal projections showed very close association of cortical microtubules with the plasma membrane and predominant localization of PLDα1-YFP in the cortical cytoplasm (**Fig. 25A**). Merge image of all three markers (**Fig. 25A**) and semi-quantitative measurement of fluorescence intensities along transversal profile in the cell cortex (**Fig. 25B**) revealed only poor co-localization, but rather association of PLDα1-YFP with cortical microtubules. This was

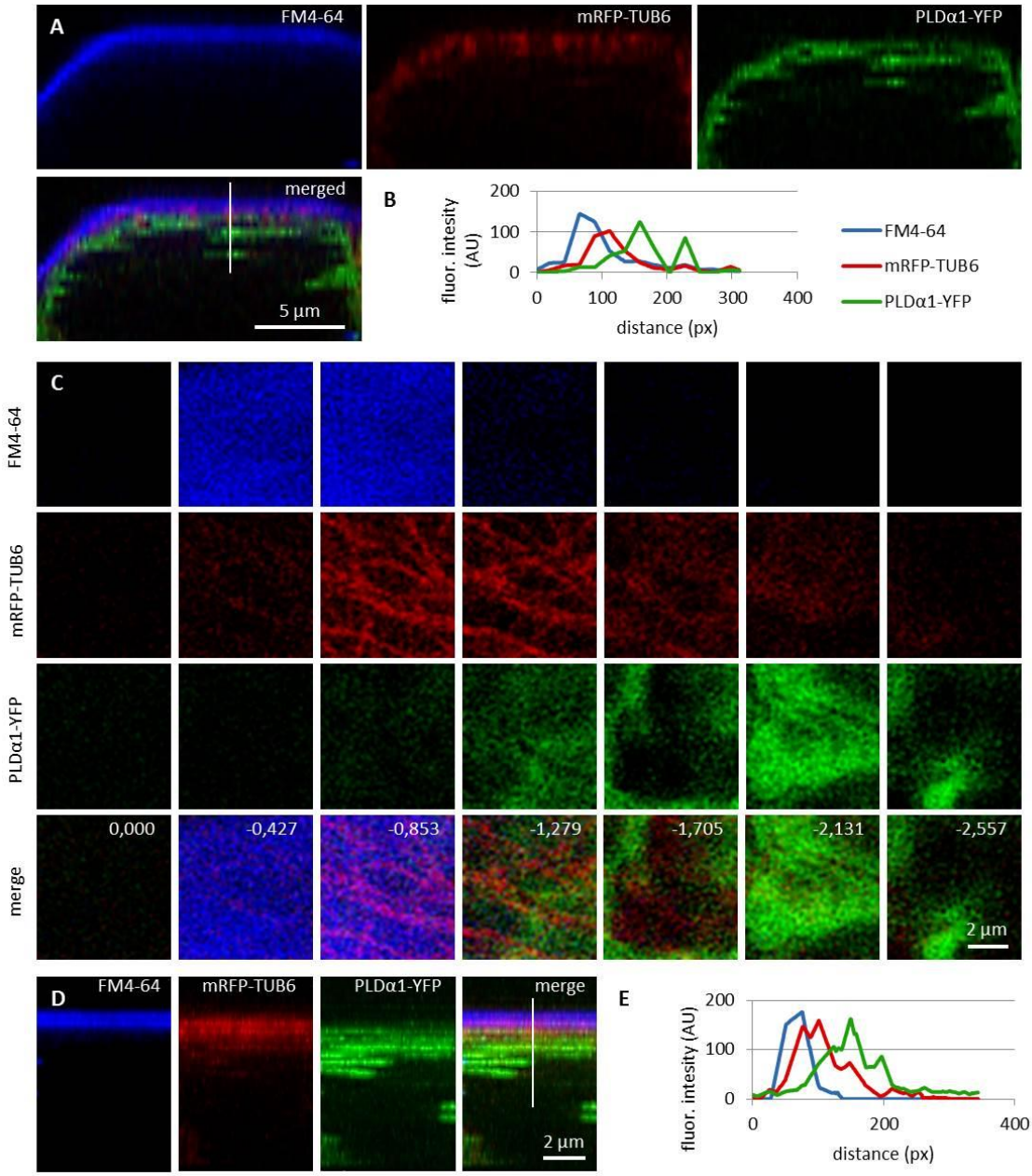

Fig. 25 Subcellular localization of PLDα1-YFP and cortical microtubules in respect to the plasma membrane in leaf petiole epidermal cells. Living interphase petiole cells with the expression of PLDα1-YFP (in green) and mRFP-TUB6 (in red) were counterstained with FM4-64 for delineation of the plasma membrane (in blue). (**A**) Orthogonal view of the 3D-reconstructed petiole cell from the z-stack imaging showing localization of plasma membrane, cortical microtubules and PLDα1. Line in merged image indicates position of measured profile. (**B**) Profile intensity of fluorescence distribution of the plasma membrane (blue), cortical microtubules (red) and PLDα1 (green) based on the distance from the cell surface. (**C**) Frontal view reconstructed from the individual z-stacks starting from the cell surface of the petiole cell to the cortical cytoplasm in steps indicating thickness of individual optical sections in µm. Individual channels are shown separately for the plasma membrane (labelled in blue), cortical microtubules (labelled in red) and PLDα1 (labelled in green), while the merge image shows the overlay of all three channels with the depth annotation. (**D**) Maximum intensity projection of the same image as in C from the side view (orthogonal projection) with the line indicating position of measured profile. (**E**) Profile intensity of fluorescence distribution of the plasma membrane

(blue), cortical microtubules (red) and PLDα1 (green) from D based on the distance from the cell surface. Analysis made in confocal microscope.

evident also from spatial separation of individual optical sections from 3-D scans of the cell cortex starting from the cell surface. By taking individual optical sections of 420 nm thickness (**Fig. 25C**), we observed uppermost signal of the FM4-64 related to the plasma membrane first, followed by mRFP signal corresponding to cortical microtubules located beneath the plasma membrane, and only then first appearance of the YFP signal related to the PLDα1. In merge image, the plasma membrane signal was enriched in second and third optical section (0.000 to -0.853 μm from the cell surface), network of cortical microtubules was present in third to fifth optical section (-0.853 to -1.705 μm from the cell surface), while PLDα1-YFP signal was enriched only in fourth to sixth optical section (-1.279 to -2.131 μm from the cell surface). Association and partial colocalization of PLDα1-YFP with cortical microtubules (detected as yellow spots in merge images) is visible only on the cytoplasmic face (**Fig. 25C**, optical section -1.279), but not on the membrane face (**Fig. 25C**, optical section -0.853) of the cortical microtubule network. Sandwich-like arrangement of the plasma membrane, cortical microtubule network and PLDα1-YFP was evident also from orthogonal view of the examined cell cortex area (**Fig. 25D**), proven also by semiquantitative fluorescence profile intensity measurement (**Fig. 25E**). These experiments revealed predominantly cytoplasmic localization of PLDα1-YFP.

Colocalization of PLDα1-YFP with microtubules in dividing cells

Colocalization of PLDα1-YFP with mitotic microtubule arrays was observed in dividing epidermal cells of leaf petioles using spinning disk microscopy (**Fig. 26A-E**). Association of PLDα1-YFP with PPB was evident in the pre-prophase and prophase stage (**Fig. 26A**), with mitotic spindle during metaphase to anaphase (**Fig. 26B-D**) and with progressing phragmoplast during cytokinesis (**Fig. 26E**). In the pre-prophase and prophase stage PLDα1-YFP accumulated in the cell cortex in a ring-like structure that was broader as PPB. This indicates that PLDα1-YFP, in addition of colocalization with microtubules inside PPB, also surrounded PPB in the cortical cytoplasm (**Fig. 26A, 26A**). Additionally, PLDα1-YFP was enriched also in cytoplasmic disk radiating from the nuclear surface to the cell cortex at the PPB plane (**Fig. 26A**, Video S1). Later on, PLDα1-YFP was strongly accumulated in microtubule arrays of the mitotic spindle which was surrounded by

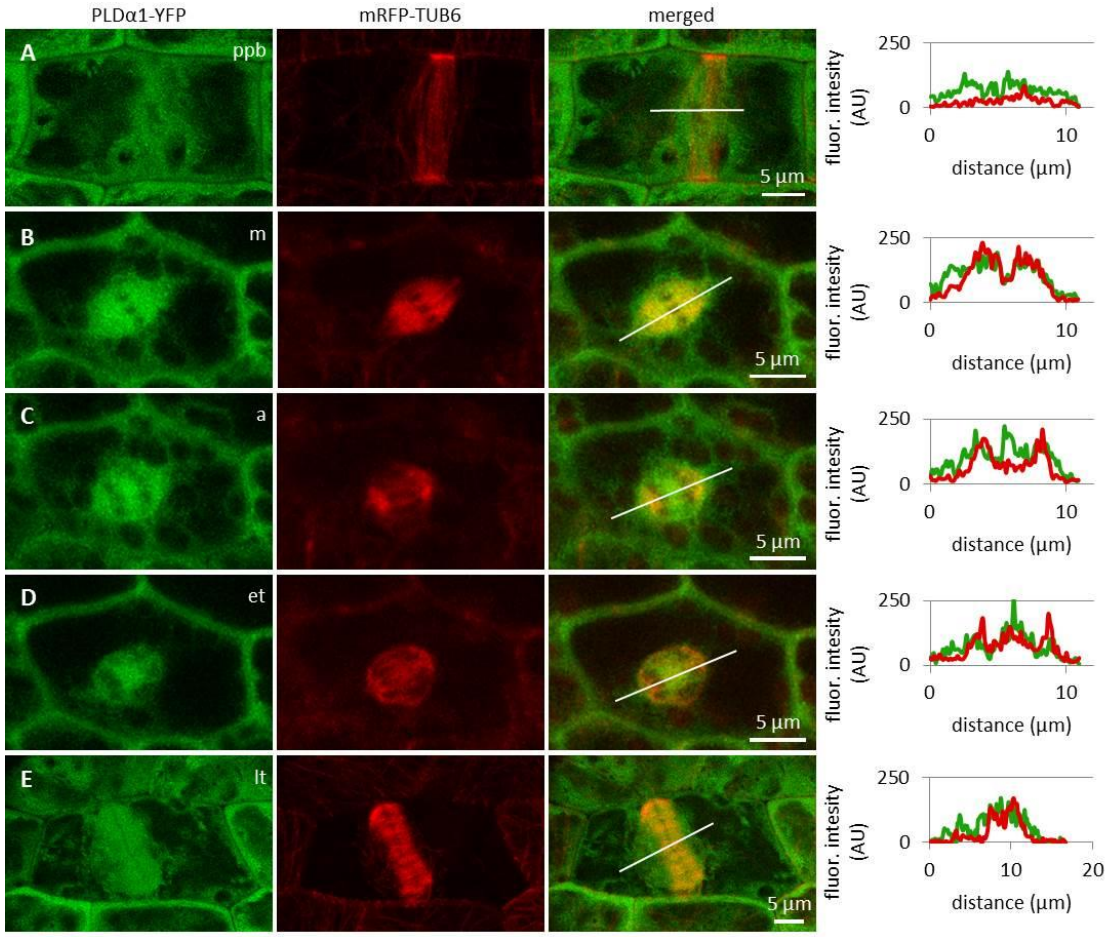

Fig. 26 Subcellular localization of PLDα1-YFP during cell division. Live cell imaging of PLDα1-YFP (green) and mRFP-TUB6 (red) in dividing leaf petiole epidermal cell. PLDα1-YFP was enriched at the location of preprophase band of microtubules (PPB) (**A**), while it strongly associated with the mitotic spindle (**B, C, D**), early (**D**) and late (**E**) phragmoplast. Profiles of fluorescent intensity of YFP and mRFP distribution measured at individual cell division stages are indicated by lines (**A-E**). ppb – preprophase band of microtubules, m – metaphase, a – anaphase, et – early telophase, lt – late telophase.

cytoplasmic layer enriched with PLDα1-YFP (**Fig. 26B-C**). Association of PLDα1-YFP with microtubules was documented by missing signal in the mitotic spindle occupied by chromosomes during metaphase and anaphase (**Fig. 26B-D**). Starting with the segregation of sister chromatids and their pulling to the opposite spindle poles, PLDα1-YFP accumulated also in the central zone of the anaphase spindle (**Fig. 26C-D**). Appearance of the early phragmoplast was connected with accumulation of PLDα1-YFP (**Fig. 26D**). However, PLDα1-YFP was absent in the late phragmoplast mid-zone during cell plate formation in cytokinesis (**Fig. 26E**). In addition, PLDα1-YFP was accumulated also in surrounding cytoplasm (phragmosome) enclosing cytokinetic apparatus in the centre of partially vacuolated cells (**Fig. 26E, 27B**, Video S2). As the

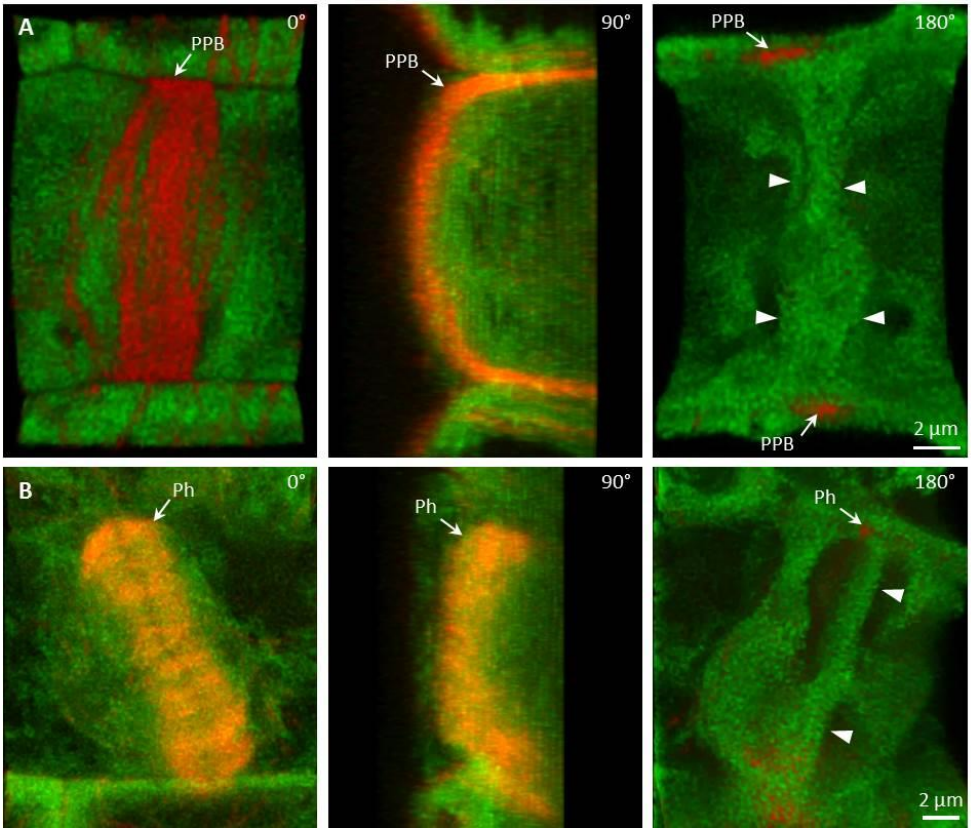

Fig. 27 Association of PLDα1-YFP with microtubules during cell division. Live cell imaging of dividing leaf epidermal petiole cells of complemented *pldα1-1 mutant* seedlings expressing PLDα1-YFP and mRFP-TUB6. (**A**) Rotation of 3-D reconstructed pre-prophase cell with established PPB (arrows) showing localization of PLDα1-YFP in cytoplasmic disk between cell nucleus and cortical PPB zone (arrowheads). Individual positions of rotating orthogonal projection correspond to Video S1. (**B**) Rotation of 3-D reconstructed cytokinetic cell with ring phragmoplast (arrows) showing localization of PLDα1-YFP among phragmoplast microtubules, in cytoplasm around the phragmoplast and in emerging cell plate in the central zone of the ring phragmoplast (arrowheads). Individual positions of rotating orthogonal projection correspond to Video S2.

late phragmoplast reached the cell periphery, PLDα1-YFP was associated with emerging cell plate in the central zone of the ring phragmoplast (**Fig. 27B**, Video S2). Visual comparison of PLDα1-YFP protein level in cortical cytoplasm between dividing cells and neighbouring non-dividing cells (**Fig. 26A, E**) clearly indicated intracellular relocation and accumulation of PLDα1-YFP within and around mitotic microtubule arrays. It indicates potential cell cycle-dependent cooperation of PLDα1-YFP with microtubules in proliferating cells.

Association of PLDα1-YFP with mitotic microtubule arrays was confirmed using immunofluorescence colocalization of PLDα1-YFP and microtubules in root meristem cells of complemented *pldα1-1* mutant seedlings expressing *proPLDα1::PLDα1:YFP*

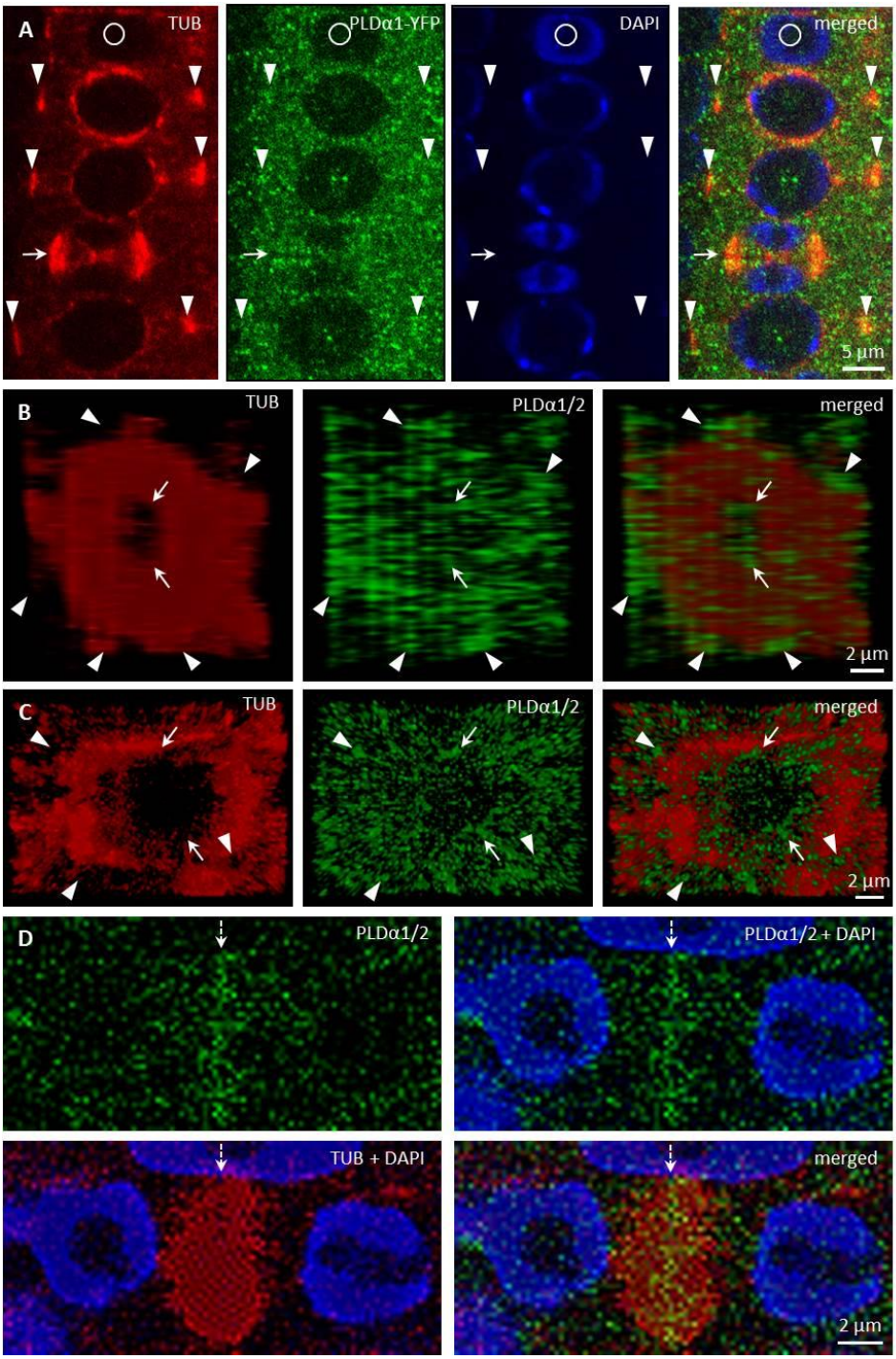

Fig. 28 Immunofluorescence colocalization of microtubules and PLDα1–YFP during cell division in Arabidopsis root meristem cells of complemented *pldα1-1* mutant seedlings expressing PLDα1-YFP. (**A**) Colocalization of PLDα1-YFP with microtubules of PPB (arrowheads) and late phragmoplast (arrow). Note that circle indicates non-dividing cell. (**B**) Orthogonal projection of disk phragmoplast stage with the distribution of PLDα1-YFP at the leading (outer) edge (arrowheads) as well as at the trailing (inner) edge in the central part (arrows) of the phragmoplast. Steel image of the orthogonal projection correspond to Video S3. (**C**) Orthogonal projection of more advanced ring phragmoplast showing association of PLDα1-YFP with the leading edge (arrowheads) and the trailing edge (arrows) of the phragmoplast. Steel image of the orthogonal projection correspond to Video S4. (**D**) Accumulation of PLDα1-YFP in central part of the phragmoplast at later stages of cytokinesis. Immunofluorescence images were performed by Dr. Olga Šamajová and Dr. Miroslav Ovečka.

construct. In non-dividing interphase or pre-mitotic cells PLDα1-YFP protein was localized in the cytoplasm, showing rather homogenous distribution (**Fig. 28A**). However, accumulation as well as partial association of PLDα1-YFP signal with microtubules of PPB, spindle and both early and late phragmoplast was observed in mitotic root cells (**Fig. 28A**). Detailed analysis of PLDα1-YFP distribution during cytokinesis revealed its specific association with progressing phragmoplast. 3-D reconstruction, orthogonal projection and rotation of disk phragmoplast with initiated depolymerisation of microtubules in the central part showed predominant association of PLDα1-YFP with leading (outer) edge of the phragmoplast as well as with the trailing (inner) edge, which was created in the central part of the phragmoplast (**Fig. 28B**, Video S3). Accumulation of PLDα1-YFP at the trailing edge of the late ring phragmoplast was more evident at later stages of the phragmoplast expansion (**Fig. 28C**, Video S4). During phragmoplast enlargement to the cell edges and consolidation of newly formed daughter nuclei, PLDα1-YFP appeared to be more accumulated in the developing cell plate (**Fig. 28D**). These results are consistent with PLDα1-YFP accumulation within and around mitotic microtubule arrays during cell division observed by live cell imaging (**Fig. 26**).

Next, we employed immunofluorescence localization of tubulin in dividing and non-dividing interphase cells of primary roots of *pldα1-1* mutant to characterize possible involvement of PLDα1 on general microtubule organization. However, no obvious differences in the microtubule organization were observed during mitosis, cytokinesis or in non-dividing interphase cells of *pldα1-1* mutant in comparison to wild type Col-0 plants.

Association of PLDα1-YFP with microtubules and CCVs and CCPs

In order to address the functional relationship between mitotic microtubules and PLDα1 in vesicular trafficking, we performed immunofluorescence localization of PLDα1-YFP with microtubules and clathrin-coated vesicles (CCVs) and clathrin-coated pits (CCPs) in dividing and non-dividing root rhizodermal cells of complemented *pldα1-1* mutant seedlings expressing *proPLDα1::PLDα1:YFP* construct (**Fig. 29**). In cytokinetic cells, PLDα1-YFP was associated with microtubules of the ring phragmoplast, while signal was less abundant in the phragmoplast central part. The distribution of clathrin signal in this zone was complementary to PLDα1-YFP distribution, with increased abundance in

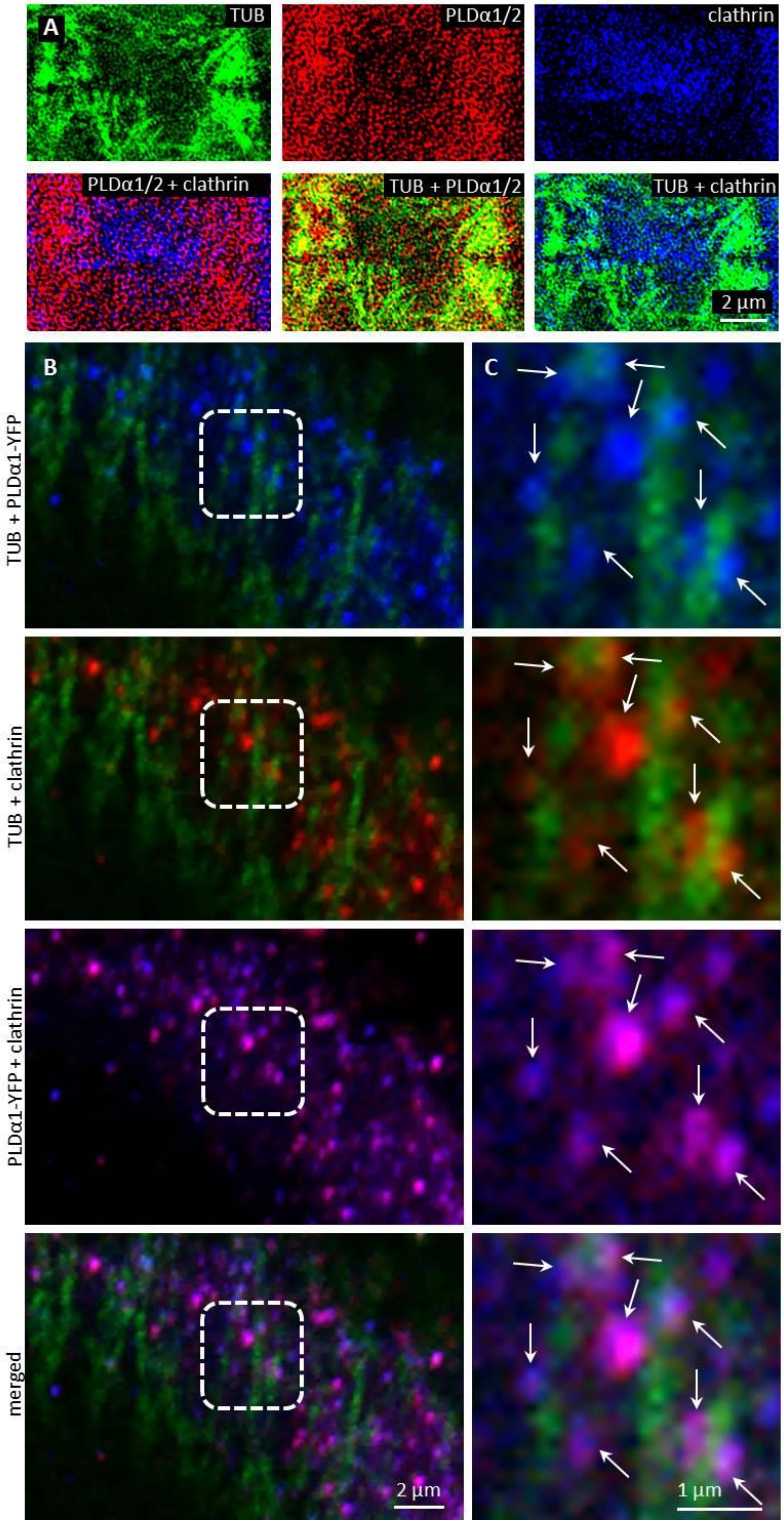

Fig. 29 Immunofluorescence colocalization of microtubules with PLDα1–YFP and clathrin in Arabidopsis root cells of complemented *pldα1-1* mutant expressing PLDα1–YFP. (**A**) Colocalization of microtubules (green), PLDα1–YFP (red) and clathrin (blue) in late phragmoplast of root meristematic cell during the cytokinesis. (**B**) Colocalization of cortical microtubules (green), PLDα1–YFP (blue) and clathrin (red) in interphase root cell. Boxed areas in (**B**) are magnified in (**C**). Arrows indicate colocalization of PLDα1–YFP with clathrin in association with cortical microtubules. Immunofluorescence images were performed by Dr. Olga Šamajová.

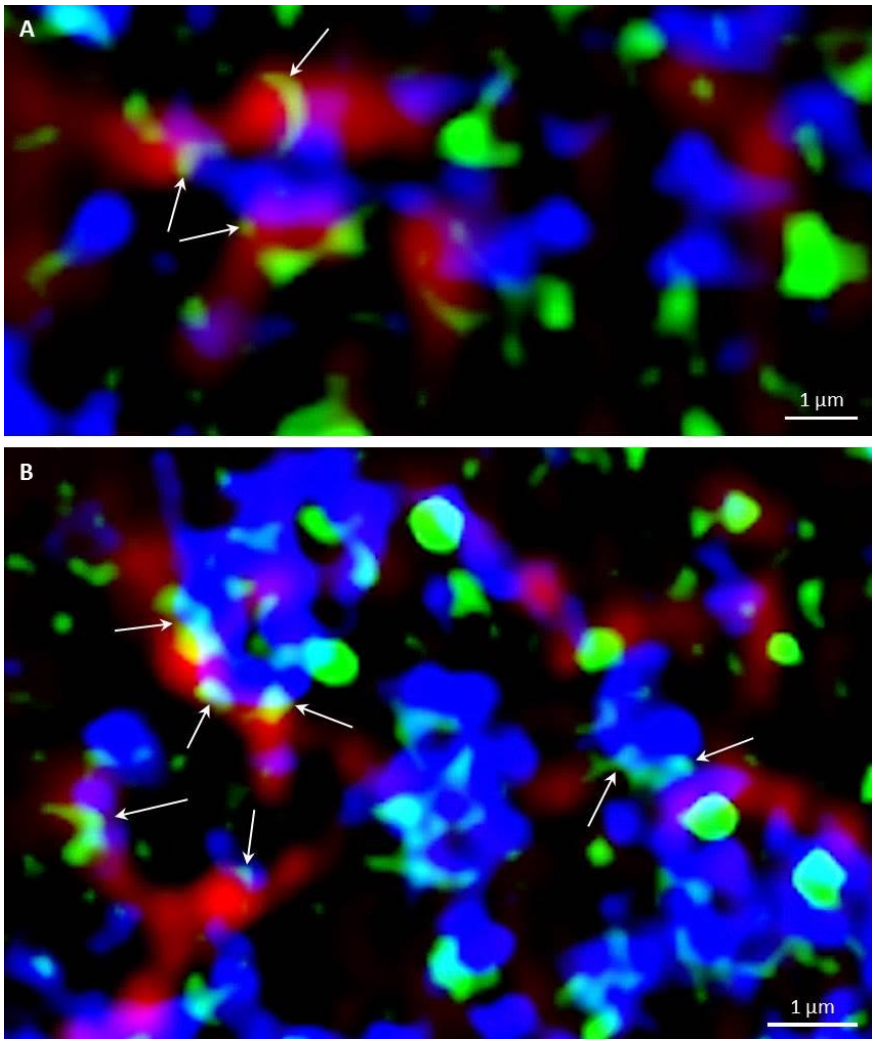

Fig. 30 Super-resolved SIM immunofluorescence colocalization of cortical microtubules (red), PLDα1–YFP (green) and clathrin (blue) in Arabidopsis root cells of complemented *pldα1-1* mutant expressing PLDα1–YFP. Arrows indicate spot-like and ring-like structures of PLDα1–YFP in close contact with cortical microtubules and individual CCVs and CCPs (**A**), or CCVs and CCPs arranged in clusters (**B**). Immunofluorescence images were performed by Dr. Olga Šamajová and Dr. George Komis.

the central part and decreased abundance at the zone of phragmoplast microtubules (**Fig. 29A**). Thus, the highest overlap of the clathrin and the PLDα1-YFP signal was observed at the trailing (inner) edge of the enlarging phragmoplast (**Fig. 29A**).

In non-dividing root rhizodermal cells cortical microtubules were bedecked with PLDα1-YFP closely associated or partially colocalized with CCVs. PLDα1-YFP was localized in spot-like structures decorating surface of microtubules in close association or partial colocalization with CCVs (**Fig. 29B**). For more detailed subcellular study of PLDα1 and microtubules involvement in vesicular trafficking we used super-resolved SIM. This analysis revealed association and partial colocalization of PLDα1-YFP with

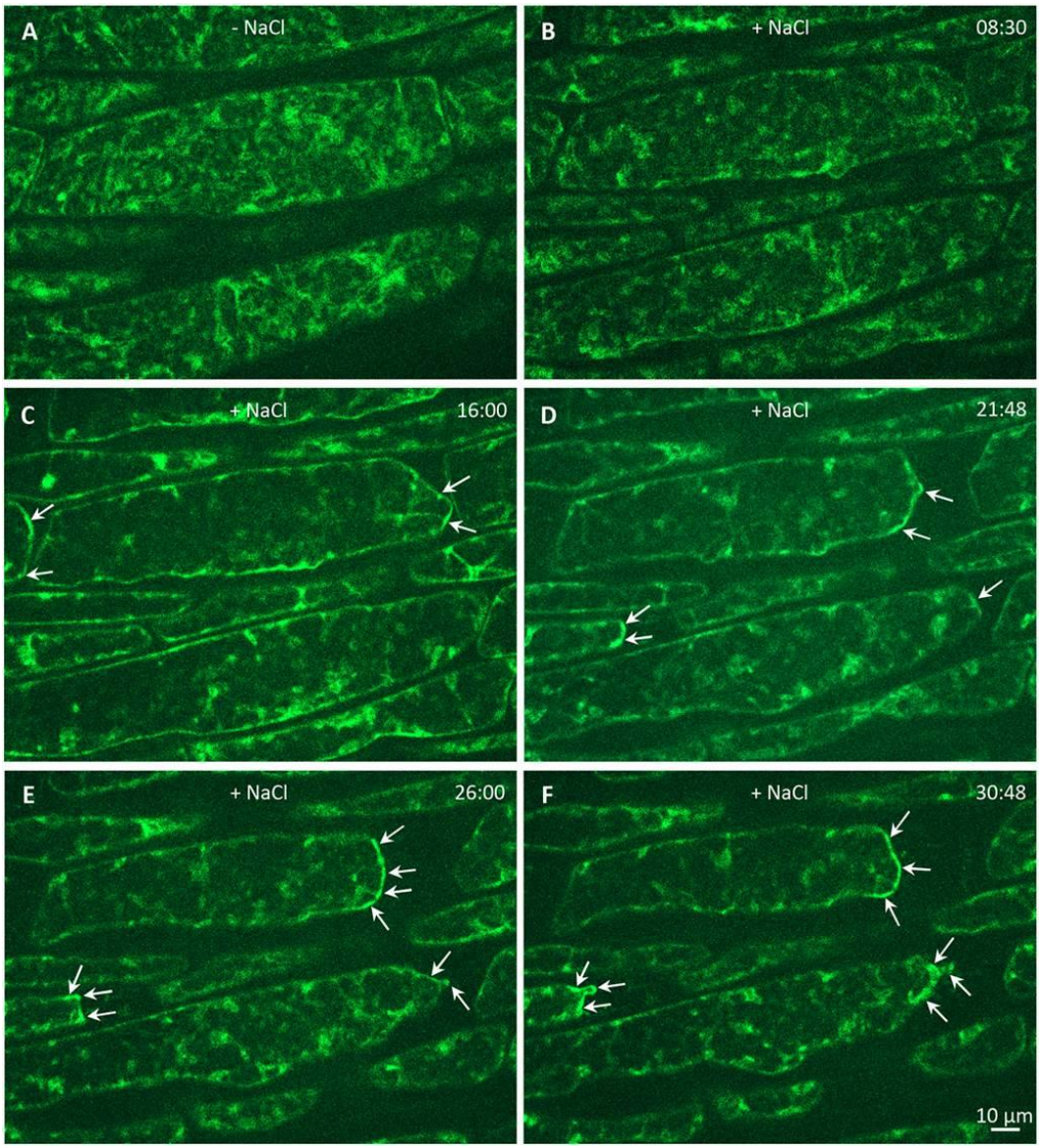

Fig. 31 Effect of salt stress on relocalization of PLDα1-YFP (shown in artificial green colour) driven by its native promoter in hypocotyl epidermal cells of complemented *pldα1-2* mutant. (**A**) Time-lapse imaging of PLDα1-YFP in hypocotyl epidermal cells under control conditions without salt and (**B-F**) during plasmolysis induced by 500 mM NaCl. The dynamic relocation and accumulation of PLDα1-YFP in plasmolyzed surface areas of detaching protoplasts is depicted by arrows. Time is indicated in min:sec. Images were performed by Dr. Olga Šamajová.

CCVs and CCPs in the close vicinity of cortical microtubules, in some cases creating spots and ring-like structures on their surface (**Fig. 30A**).

Association of PLDα1-YFP with CCVs and CCPs in the cytoplasm between cortical microtubules was observed in clathrin-rich clusters that were in close contact with cortical microtubules (**Fig. 30B**). Quantitative analysis of the above colocalization studies of clathrin and microtubules following either SIM or CLSM documentation,

showed positive colocalization in Col-0 root rhizodermal cells (Pearson's coefficient R=0,62) and no colocalization in *pldα1* mutant (Pearson's coefficient R=0). In conclusion, these data document a complex pattern of PLDα1 subcellular localization and its functional relationship to microtubule arrays in both non-dividing and dividing cells of Arabidopsis plants. Combination of different advanced microscopy methods provided data supporting a possible mechanism of interactions between clathrin-dependent endocytosis and cortical (as well as mitotic) microtubules, through the stabilization function of the PLDα1.

Finally, we wanted to test whether stress factors such as high salinity can induce subcellular relocation of PLDα1-YFP in Arabidopsis cells. Indeed, PLDα1-YFP was relocated and accumulated in curved surface areas of plasmolysed hypocotyl cells treated with 500mM NaCl (**Fig. 31**). These data might suggest a possible protective role of PLDα1 in these curved areas of retracting protoplasts detached from the cell wall during plasmolysis.

Discussion

PLD is a major family of membrane phospholipid-hydrolyzing enzymes in plants. *A. thaliana* PLDα1 and its product PA are involved in a variety of cellular and physiological processes, such as regulation of stomatal closure and opening, biotic and abiotic stress signalling, and regulation of cytoskeletal organization (Qin et al., 1997; Zhang et al., 2004; Bargmann and Munnik, 2006; Pleskot et al., 2013; Hong et al., 2016). Here we employed advanced microscopic methods to reveal precise developmental expression pattern and subcellular localization of PLDα1 in two rescued *pldα1* mutant lines.

ABA is an important hormone that regulates the adaptation of plants to various abiotic stresses (Danquah et al., 2014). It was shown by previous studies that *pldα1* mutant plants did not exhibit significant differences in morphological and developmental characteristics as compared to wild type plants (Fan et al., 1997; Zhang et al., 2012). However, PLDα1 controls proper water balance in plant responding to ABA hormone by stomatal closure which was impaired in *pldα1* KO mutants (Zhang et al., 2004; Guo et al., 2012; Jiang et al., 2014). Here we transformed *pldα1-1* and *pldα1-2* mutant plants with *proPLDα::PLDα1-YFP* construct and we observed stomatal closure after ABA

treatment similar to the wild type, suggesting functional complementation of both mutants by this construct.

Developmental expression pattern and localization of PLDα1-YFP

A previous study assessing organ distribution of PLDα1 protein in Arabidopsis plants by immunoblotting analysis showed higher amounts of this protein in flowers, stems, roots and siliques rather than in other organs. Moreover, the highest activity of PLDα1 was found in soluble fractions isolated from roots, flowers and siliques (Fan et al., 1999). This study, however, lacked cellular resolution within these organs. In contrast, advanced microscopy imaging used in our experiments revealed high expression levels of PLDα1-YFP in the apical and lateral root cap cells. These findings were in agreement with absolute expression levels of PLDα1 transcript from Genevestigator transcriptomic data (Brady et al., 2007). High expression levels of PLDα1-YFP were found also in trichoblast cell files and in developing roots hairs suggesting its role during root hair development. These results are supported by work of Potocký et al. (2014) reporting PA localization in the plasma membrane of tip-growing pollen tubes. In the aerial part of the plant we observed high PLDα1-YFP protein signal in pavement and stomata guard cells, which is again in accordance to Genevestigator transcriptomic data (Yang et al., 2008). On the other hand, and in contrary to Genevestigator transcriptomic data, we observed high expression levels of PLDα1-YFP in developing trichomes (Marks et al., 2009). These results support the role of PLDα1 protein in cell developmental processes and polar cell growth.

Cytoplasmic localization of PLDα1-YFP

The subcellular distribution of PLDα1 based on immunoblotting analyses of fractionated extracts of Arabidopsis leaves revealed the highest content at the plasma membrane, CCVs, intracellular membranes and mitochondria while only a small amount of protein was detected in nuclei (Fan et al., 1999).

Previously, PLD was implicated to link cortical microtubules to the plasma membrane (Dhonukshe et al., 2003). Later it was shown that PLDδ is the cortical microtubule-binding protein (Ho et al., 2009; Andreeva et al., 2009). Moreover, a current study showed colocalization of the PLDδ with cortical microtubules near to the plasma membrane in Arabidopsis hypocotyl cells (Zhang et al., 2017b). Many microtubule-dependent processes, e.g. mitosis, cytokinesis, cell elongation and signal transduction

are controlled by microtubule dynamics (Wymer and Lloyd, 1996; Hashimoto and Kato, 2006; Jiang et al., 2014). Under normal conditions, *pldα1* plants showed no changes in microtubule organization and density as compared to wild type plants (Zhang et al., 2012). However, PLDα1 KO in Arabidopsis leads to more severe disruption of cortical microtubules by inhibitors (Zhang et al., 2017a) or under salt stress conditions (Zhang et al., 2012). Furthermore, PA produced by activated PLDα1 directs AtMAP65-1 to the plasma membrane and enhances its microtubule stabilizing activity, thus microtubules are stabilized and cell survival is enhanced under the salt stress conditions (Zhang et al., 2012; Pleskot et al., 2014).

PLDα1 is the most abundant PLD present in both soluble and membrane fractions. It translocates from cytosolic to membrane fractions to hydrolyze membrane lipids under stress conditions (Wang et al., 2000; Hong et al., 2016). In our study we observed mainly cytoplasmic localization of PLDα1-YFP, sometimes in the vicinity of cortical microtubules, in non-dividing cells. By contrast, the localization of PLDδ which interacts with cortical microtubules was primarily restricted to the plasma membrane (Zhang et al., 2017b). With the entering of the cell to the mitosis PLDα1-YFP was enriched at mitotic microtubule arrays, namely PPB, microtubules of mitotic spindle in prophase, metaphase and anaphase, as well as to microtubules of the phragmoplast during cytokinesis. Although, colocalization between PLDα1 protein and microtubules was not previously observed in non-dividing protoplasts (Zhang et al., 2012), we detected accumulation of PLDα1-YFP at microtubule arrays during mitotic progression. These results were further confirmed using immunofluorescence colocalization of PLDα1-YFP and microtubules. PLDα1-YFP protein was slightly accumulated and partially colocalized with microtubules of preprophase band, spindle and both early and late phragmoplast.

Multiple PLDs have been implicated to have redundant roles in the same physiological processes, such as hyperosmotic stress and ABA signalling. However, their mechanisms of action might be different. KO of either PLDα1 or PLDδ cause the inhibition of ABA-induced stomatal closure while loss of both genes renders the stomata almost completely insensitive to ABA (Zhang et al., 2004; Guo et al., 2012; Uraji et al., 2012; Hong et al., 2016). Moreover, PLDα1, through PA as an intermediate, promotes H_2O_2 production, whereas PLDδ mediates the response to H_2O_2 in the ABA signalling pathway. In this scenario PLDα1 can indirectly regulate PLDδ activity through ROS

production (Guo et al., 2012; Hong et al., 2016). GhPLDα1 and H_2O_2 in the upland cotton (*Gossypium hirsutum*) are important components during the onset of the secondary cell wall thickening suggesting a putative role of PLDα1 in the vesicle trafficking (Tang and Liu, 2017). Furthermore, PLDα1 produced PA directs AtMAP65-1 to the plasma membrane and enhances its microtubule stabilizing activity, thus microtubules are stabilized and cell survival is enhanced under salt stress conditions (Zhang et al., 2012; Pleskot et al., 2014). Based on these findings, the question is posed whether PLDα1 can regulate mitotic progress alone or through PA, e.g. through the interaction with e.g. MAP65 proteins and/or PLDδ protein. More experiments should be performed to clarify the molecular mechanism by which PLDα1 affects mitotic microtubule arrays.

The mammalian PLD–PA signalling complex mediates protein–membrane interactions and membrane–cytoskeleton interfaces, and is involved in vesicle trafficking processes, such as exocytosis, endocytosis, membrane delivery and vesicle budding (McMahon and Gallop, 2005; Donaldson, 2009). Vesicle coating proteins, ARFs, Rho GTPases and soluble N-ethylmaleimide-sensitive factor attachment receptor (SNARE) proteins, facilitate vesicle formation, transport and fusion with the target organelle through PLD activators or as PA-binding or recruiting proteins (Chernomordik and Kozlov, 2003; Donaldson, 2009). In plants, there is some evidence that ARFs, Rho GTPases and SNARE proteins are involved in vesicle targeting to the cell division plane, vesicle fusion and cell plate biogenesis, although the exact roles of particular signalling proteins remains elusive (El Kasmi et al., 2013; Smertenko et al., 2017).

SPO14 is phospholipase D in *Saccharomyces cerevisiae*, which specifically hydrolyzes phosphatidylcholine to generate choline and PA. In vegetative cells, SPO14p localizes to the cytoplasm and is not required for normal growth. However, during sporulation, SPO14p localizes to the spindle pole bodies and prospore membrane where it is required for sporulation (Rudge et al., 1998; Liu et al., 2007). One function of SPO14p generated PA is to localize t-SNARE protein Spo20p to the prospore membrane (Nakanishi et al., 2006; Liu et al., 2007). As mentioned above, PLDα1 was enriched in the CCVs which predicts its role in vesicular trafficking (Fan et al., 1999). Furthermore, clathrin heavy chain isoforms and AP180 N-terminal homology domain clathrin-assembly proteins were identified as a PA binding proteins in a previous proteomic study (McLoughlin et al., 2013). Similarly, epsin-like clathrin adaptor 1 binds PA under

the negative membrane curvature stress in Arabidopsis (Putta et al., 2016). Furthermore, PLDα1 coimmunoprecipitates with Arabidopsis AP-2 complex and clathrin (Yamaoka et al., 2013), indicating that PLDα1 contributes to clathrin-mediated endocytosis. These data indicate that proteins involved in the clathrin-dependent endocytosis are potential targets of PLDα1-generated PA. Here we provide evidence for close associations of PLDα1-YFP with cortical and mitotic microtubules during cell division. It has been shown previously that the PPB region at the cell cortex possess a large number of CCPs and CCVs. Expected role of clathrin-mediated endocytosis in the PPB region is related to the regulated modification of the cell cortex by controlled removal of particular membrane proteins by endocytosis, being part of the cell division plane memory establishment (Karahara et al., 2009). Centrifugal expansion of the phragmoplast during cytokinesis is driven by microtubule polymerization with substantial microtubule stabilization by bundling at the leading edge of the phragmoplast (Murata et al., 2013). Phragmoplast microtubules are responsible for delivery of vesicles creating cell plate in the mid-zone region. Cell plate formation, however, is also based on removal of excess membrane and cell wall material. Endocytosis and membrane recycling thus play an indispensable role during cell plate expansion (van Oostende-Triplet et al., 2017). Endocytosis was implicated in the spatial restriction of syntaxin protein KNOLLE to the cell plate (Boutté et al., 2010) and in the removal of the cellulose synthase enzymes from the central part and their recycling to the peripheral growth zone of the cell plate (Miart et al., 2014). Consistently with these observations electron tomography analysis revealed a high density of CCPs and CCVs during the transformation of the tubulo-vesicular network to a planar fenestrated sheet during cell plate formation (Seguí-Simarro et al., 2004). CCPs and CCVs were mostly localized at the trailing (inner) edge of the enlarging phragmoplast. Internalization and recycling of material from the central part and its delivery to the leading edges of maturing cell plate were thus definitely connected to clathrin-dependent endocytosis (Boutté et al., 2010; Ito et al., 2012; Teh et al., 2013; Miart et al., 2014). Based on these findings and on our results we suggest that PLDα1 and its product PA might participate in the complex signalling network involved in the vesicle trafficking and membrane assembly during plant cytokinesis. Although the precise mechanism by which PLDα1 or PA are involved in these processes is unknown. Our results indicate that PLDα1 localized on microtubule surface can potentially functions as molecular glue for CCPs and CCVs associated with

microtubules. This is further corroborated by the observation that microtubule-colocalized clathrin structures are quantitatively absent in the *pldα1* mutant.

In animal literature it is suggested that PLD and PA regulate vesicle formation from cellular membranes. One possible mechanism is that physiochemical properties of PLD and PA as well as their protein-protein and lipid-protein interactions (e.g. with dynamin, COPI, kinesin, ARF, small GTPases, phosphatases, kinases and phosphoinositols) might regulate such vesicle formation (Manifava et al., 2001; Roth, 2008; Brito de Souza et al., 2014). More physiological and functional studies will be needed to prove this concept experimentally. But complex pattern of PLDα1 developmental expression, subcellular localization and its close association with cortical and mitotic microtubules in Arabidopsis documented here by advanced microscopy methods substantially contribute to this scenario and will promote further research in this topic.

Conclusions

First part of this thesis briefly summarizes current knowledge on plant microtubules and microtubule end-binding protein family, focused on EB1c protein. Further it introduces phospholipases, especially PLDα1 protein and potential connection of EB1c and PLDα1 to mitogen activated protein kinases. Likewise, conventional and advanced microscopy techniques are briefly explained.

Experimental part of this work describes developmental localization of microtubule EB1c protein in Arabidopsis root using advanced LSFM. Construct *proEB1c::EB1c:GFP* was stably transformed to *Arabidopsis thaliana*. Presence of chimeric EB1c-GFP protein was confirmed in T2 generation by protein extraction followed by SDS-PAGE and immunoblot analysis using anti-GFP antibody. Arabidopsis seedlings showing EB1c-GFP expression were observed using minimally invasive and phototoxic LSFM. We were able to address and quantify nuclear localization of EB1c in meristematic, transition and elongation root zones in three important root tissues such as epidermis, cortex and endodermis. Moreover, we correlated nuclear sizes with EB1c expression levels. Results demonstrate high potential of LSFM for 4-D live fluorescent imaging of plant samples such as growing roots. One indisputable advantage of LSFM is capacity to visualize proteins in deeper cell layers (e.g. endodermis) with minimal optical aberrations. Our results supported the unique role of the transition root zone in the cell reprogramming during their developmental transition from proliferation to differentiation in the developing root apex. We also cloned *EB1c* gene under control of native *EB1c* promotor and fused with *DRONPA*. Expression of chimeric EB1c-DRONPA protein was checked using transient transformation of *Nicotiana benthamina* before stable transformation of *A.thaliana*. This chimeric protein was localized to nuclear subdomains using super-resolution PALM microscopy.

Subsequently, we utilized advanced microscopy, namely LSFM, for developmental imaging of PLDα1 under natural conditions to explore cell-type specific expression patterns of this protein. KO *pldα1* mutants were complemented with *PLDα1* under control of native *PLDα1* promotor and fused with *YFP*. Stomata of cotyledons from wild type plants and plants complemented with PLDα1-YFP responded by closing to ABA treatment, in contrast to *pldα1* mutants insensitive to ABA in this respect. Microscopic observations revealed high accumulation of PLDα1-YFP in the root cap,

trichoblasts and tips of root hairs. A relatively high expression of PLDα1-YFP was observed in hypocotyl epidermal cells, pavement and stomatal guard cells of cotyledons, and in leaf epidermis, stomata guard cells, trichomes and petioles. PLDα1-YFP was colocalized with microtubules visualized by *pUBQ1:mRFP::TUB6* construct in both dividing and non-dividing cells. This experiment showed accumulation of PLDα1-YFP on mitotic spindles and phragmoplasts. Thus, we provided a high-resolution subcellular localization of PLDα1 in both dividing and non-dividing Arabidopsis cells in the root meristem and leaf petioles.

References

Adachi S, Minamisawa K, Okushima Y, Inagaki S, Yoshiyama K, Kondou Y, Kaminuma E, Kawashima M, Toyoda T, Matsui M, Kurihara D, Matsunaga S, Umeda M. (2011) Programmed induction of endoreduplication by DNA double-strand breaks in Arabidopsis. *Proc Natl Acad Sci U S A*. 108: 10004–10009. doi: 10.1073/pnas.1103584108

Akhmanova A, Steinmetz MO. (2008) Tracking the ends: a dynamic protein network controls the fate of microtubule tips. *Nat Rev Mol Cell Biol*. 9: 309–322. doi: 10.1038/nrm2369

Aloulou A, Ali YB, Bezzine S, Gargouri Y, Gelb MH. (2012) Phospholipases: an overview. *Methods Mol Biol*. 861: 63–85. doi: 10.1007/978-1-61779-600-5_4

Ambrose C, Allard JF, Cytrynbaum EN, Wasteneys GO. (2011) A CLASP-modulated cell edge barrier mechanism drives cell-wide cortical microtubule organization in Arabidopsis. *Nat Commun*. 2: 430. doi: 10.1038/ncomms1444

Andersson MX, Larsson KE, Tjellström H, Liljenberg C, Sandelius AS. (2005) Phosphate-limited oat. The plasma membrane and the tonoplast as major targets for phospholipid-to-glycolipid replacement and stimulation of phospholipases in the plasma membrane. *J Biol Chem*. 280: 27578–27586. doi: 10.1074/jbc.M503273200

Andreasson E, Ellis B. (2010) Convergence and specificity in the Arabidopsis MAPK nexus. *Trends Plant Sci*. 15: 106–113. doi: 10.1016/j.tplants.2009.12.001

Andreeva Z, Ho AYY, Barthet MM, Potocký M, Bezvoda R, Žárský V, Marc J. (2009) Phospholipase D family interactions with the cytoskeleton: isoform δ promotes plasma membrane anchoring of cortical microtubules. *Funct Plant Biol*. 36: 600–612. doi: 10.1071/FP09024

Arisz SA, Testerink C, Munnik T. (2009) Plant PA signaling via diacylglycerol kinase. *Biochim Biophys Acta*. 1791: 869–875. doi: 10.1016/j.bbalip.2009.04.006

Austin-Brown SL, Chapman KD. (2002) Inhibition of phospholipase D alpha by N-acylethanolamines. *Plant Physiol*. 129: 1892–1898. doi: 10.1104/pp.001974

Baluska F, Jasik J, Edelmann HG, Salajová T, Volkmann D. (2001) Latrunculin B-induced plant dwarfism: Plant cell elongation is F-actin-dependent. *Dev Biol*. 231: 113–124. doi: 10.1006/dbio.2000.0115

Baluška F, Kubica S, Hauskrecht M. (1990) Postmitotic 'isodiametric' cell growth in the maize root apex. *Planta*. 181: 269–274. doi: 10.1007/BF00195876

Baluška F, Mancuso S. (2013) Root apex transition zone as oscillatory zone. *Front Plant Sci*. 4: 354. doi: 10.3389/fpls.2013.00354

Baluska F, Salaj J, Mathur J, Braun M, Jasper F, Samaj J, Chua NH, Barlow PW, Volkmann D. (2000) Root hair formation: F-actin-dependent tip growth is initiated by local assembly of profilin-supported F-actin meshworks accumulated within expansin-enriched bulges. *Dev Biol*. 227: 618–632. doi: 10.1006/dbio.2000.9908

Bardwell AJ, Frankson E, Bardwell L. (2009) Selectivity of docking sites in MAPK kinases. *J Biol Chem*. 284: 13165–13173. doi: 10.1074/jbc.M900080200

Bargmann BO, Laxalt AM, ter Riet B, Testerink C, Merquiol E, Mosblech A, Leon-Reyes A, Pieterse CM, Haring MA, Heilmann I, Bartels D, Munnik T. (2009a) Reassessing the role of phospholipase D in the Arabidopsis wounding response. *Plant Cell Environ*. 32: 837–50. doi: 10.1111/j.1365-3040.2009.01962.x

Bargmann BO, Laxalt AM, ter Riet B, van Schooten B, Merquiol E, Testerink C, Haring MA, Bartels D, Munnik T. (2009b) Multiple PLDs required for high salinity and water deficit tolerance in plants. *Plant Cell Physiol*. 50: 78–89. doi: 10.1093/pcp/pcn173

Bargmann BO, Munnik T. (2006) The role of phospholipase D in plant stress responses. *Curr Opin Plant Biol*. 9: 515–522. doi: 10.1016/j.pbi.2006.07.011

Baskin TI, Cande WZ. (1990) The Structure and Function of the Mitotic Spindle in Flowering Plants. *Annu Rev Plant Physiol Plant Mol Biol* 41: 277–315. doi: https://doi.org/10.1146/annurev.pp.41.060190.001425

Beck M, Komis G, Müller J, Menzel D, Samaj J. (2010) Arabidopsis homologs of nucleus- and phragmoplast-localized kinase 2 and 3 and mitogen-activated protein kinase 4 are essential for microtubule organization. *Plant Cell*. 22: 755–771. doi: 10.1105/tpc.109.071746

Bengough AG, Bransby MF, Hans J, McKenna SJ, Roberts TJ, Valentine TA. (2006) Root responses to soil physical conditions; growth dynamics from field to cell. *J Exp Bot*. 57: 437–447. doi: 10.1093/jxb/erj003

Benková E, Hejátko J. (2009) Hormone interactions at the root apical meristem. *Plant Mol Biol*. 69: 383–396. doi: 10.1007/s11103-008-9393-6

Bisgrove SR, Lee YR, Liu B, Peters NT, Kropf DL. (2008) The microtubule plus-end binding protein EB1 functions in root responses to touch and gravity signals in Arabidopsis. *Plant Cell*. 20: 396–410. doi: 10.1105/tpc.107.056846

Boutté Y, Frescatada-Rosa M, Men S, Chow CM, Ebine K, Gustavsson A, Johansson L, Ueda T, Moore I, Jürgens G, Grebe M. (2010) Endocytosis restricts Arabidopsis KNOLLE syntaxin to the cell division plane during late cytokinesis. *EMBO J*. 29: 546–558. doi: 10.1038/emboj.2009.363

Brady SM, Orlando DA, Lee JY, Wang JY, Koch J, Dinneny JR, Mace D, Ohler U, Benfey PN. (2007) A high-resolution root spatiotemporal map reveals dominant expression patterns. *Science*. 318: 801–806. doi: 10.1126/science.1146265

Brito de Souza L, Pinto da Silva LL, Jamur MC, Oliver C. (2014) Phospholipase D is involved in the formation of Golgi associated clathrin coated vesicles in human parotid duct cells. *PLoS One*. 9: e91868. doi: 10.1371/journal.pone.0091868

Brown SS, Spudich JA. (1979) Cytochalasin inhibits the rate of elongation of actin filament fragments. *J Cell Biol*. 83: 657–662. doi: 10.1083/jcb.83.3.657

Camehl I, Drzewiecki C, Vadassery J, Shahollari B, Sherameti I, Forzani C, Munnik T, Hirt H, Oelmüller R. (2011) The OXI1 kinase pathway mediates Piriformospora indica-induced growth promotion in Arabidopsis. *PLoS Pathog*. 7: e1002051. doi: 10.1371/journal.ppat.1002051

Carpenter AE, Jones TR, Lamprecht MR, Clarke C, Kang IH, Friman O, Guertin DA, Chang JH, Lindquist RA, Moffat J, Golland P, Sabatini DM. (2006) CellProfiler: image analysis software for identifying and quantifying cell phenotypes. *Genome Biol*. 7: R100. doi: 10.1186/gb-2006-7-10-r100

Casas-Godoy L, Duquesne S, Bordes F, Sandoval G, Marty A. (2012) Lipases: an overview. *Methods Mol Biol*. 861: 3–30. doi: 10.1007/978-1-61779-600-5_1

Chan J, Calder GM, Doonan JH, Lloyd CW. (2003) EB1 reveals mobile microtubule nucleation sites in Arabidopsis. *Nat Cell Biol*. 5: 967–971. doi: 10.1038/ncb1057

Chernomordik LV, Kozlov MM. (2003) Protein-lipid interplay in fusion and fission of biological membranes. *Annu Rev Biochem*. 72: 175–207. doi: 10.1146/annurev.biochem.72.121801.161504

Clough SJ, Bent AF. (1998) Floral dip: a simplified method for Agrobacterium-mediated transformation of Arabidopsis thaliana. *Plant J*. 16: 735–743. doi: 10.1046/j.1365-313x.1998.00343.x

Colcombet J, Hirt H. (2008) Arabidopsis MAPKs: a complex signalling network involved in multiple biological processes. *Biochem J*. 413: 217–226. doi: 10.1042/BJ20080625

Cox G. (2002) Biological confocal microscopy. *Materials Today*. 5: 34–41. doi: https://doi.org/10.1016/S1369-7021(02)05329-4

Cruz-Ramírez A, Oropeza-Aburto A, Razo-Hernández F, Ramírez-Chávez E, Herrera-Estrella L. (2006) Phospholipase DZ2 plays an important role in extraplastidic galactolipid biosynthesis and phosphate recycling in Arabidopsis roots. *Proc Natl Acad Sci U S A*. 103: 6765–6770. doi: 10.1073/pnas.0600863103

Danquah A, de Zelicourt A, Colcombet J, Hirt H. (2014) The role of ABA and MAPK signaling pathways in plant abiotic stress responses. *Biotechnol Adv*. 32: 40–52. doi: 10.1016/j.biotechadv.2013.09.006

Davis AM, Hall A, Millar AJ, Darrah C, Davis SJ. (2009) Protocol: Streamlined sub-protocols for floral-dip transformation and selection of transformants in Arabidopsis thaliana. *Plant Methods*. 5: 3. doi: 10.1186/1746-4811-5-3

De Smet S, Cuypers A, Vangronsveld J, Remans T. (2015) Gene Networks Involved in Hormonal Control of Root Development in Arabidopsis thaliana: A Framework for Studying Its Disturbance by Metal Stress. *Int J Mol Sci*. 16: 19195–19224. doi: 10.3390/ijms160819195

del Pozo JC, Diaz-Trivino S, Cisneros N, Gutierrez C. (2006) The balance between cell division and endoreplication depends on E2FC-DPB, transcription factors regulated by the ubiquitin-SCFSKP2A pathway in Arabidopsis. *Plant Cell*. 18: 2224–2235. doi: 10.1105/tpc.105.039651

Dello Ioio R, Linhares FS, Scacchi E, Casamitjana-Martinez E, Heidstra R, Costantino P, Sabatini S. (2007) Cytokinins determine Arabidopsis root-meristem size by controlling cell differentiation. *Curr Biol*. 17: 678–682. doi: 10.1016/j.cub.2007.02.047

Dhonukshe P, Laxalt AM, Goedhart J, Gadella TW, Munnik T. (2003) Phospholipase d activation correlates with microtubule reorganization in living plant cells. *Plant Cell*. 15: 2666–2679. doi: 10.1105/tpc.014977

Dixit R, Chang E, Cyr R. (2006) Establishment of polarity during organization of the acentrosomal plant cortical microtubule array. *Mol Biol Cell*. 17: 1298–1305. doi: 10.1091/mbc.E05-09-0864

Donaldson JG. (2009) Phospholipase D in endocytosis and endosomal recycling pathways. *Biochim Biophys Acta*. 1791: 845–984. doi: 10.1016/j.bbalip.2009.05.011

dos Remedios CG, Chhabra D, Kekic M, Dedova IV, Tsubakihara M, Berry DA, Nosworthy NJ. (2003) Actin binding proteins: regulation of cytoskeletal microfilaments. *Physiol Rev*. 83: 433–473. doi: 10.1152/physrev.00026.2002

Doskočilová A, Kohoutová L, Volc J, Kourová H, Benada O, Chumová J, Plíhal O, Petrovská B, Halada P, Bögre L, Binarová P. (2013) NITRILASE1 regulates the exit from proliferation, genome stability and plant development. *New Phytol*. 198: 685–698. doi: 10.1111/nph.12185

Draviam VM, Shapiro I, Aldridge B, Sorger PK. (2006) Misorientation and reduced stretching of aligned sister kinetochores promote chromosome missegregation in EB1- or APC-depleted cells. *EMBO J*. 25: 2814–2827. doi: 10.1038/sj.emboj.7601168

Durek P, Schmidt R, Heazlewood JL, Jones A, MacLean D, Nagel A, Kersten B, Schulze WX. (2010) PhosPhAt: the Arabidopsis thaliana phosphorylation site database. An update. *Nucleic Acids Res*. 38: 828–834. doi: 10.1093/nar/gkp810

El Kasmi F, Krause C, Hiller U, Stierhof YD, Mayer U, Conner L, Kong L, Reichardt I, Sanderfoot AA, Jürgens G. (2013) SNARE complexes of different composition jointly mediate membrane fusion in Arabidopsis cytokinesis. *Mol Biol Cell*. 24: 1593–601. doi: 10.1091/mbc.E13-02-0074

Eliáš M, Potocký M, Cvrčková F, Žárský V. (2002) Molecular diversity of phospholipase D in angiosperms. *BMC Genomics*. 3: 2. doi: 10.1186/1471-2164-3-2

Era A, Tominaga M, Ebine K, Awai C, Saito C, Ishizaki K, Yamato KT, Kohchi T, Nakano A, Ueda T. (2009) Application of Lifeact reveals F-actin dynamics in Arabidopsis thaliana and the liverwort, Marchantia polymorpha. *Plant Cell Physiol*. 50: 1041–1048. doi: 10.1093/pcp/pcp055

Fan L, Zheng S, Cui D, Wang X. (1999) Subcellular distribution and tissue expression of phospholipase Dalpha, Dbeta, and Dgamma in Arabidopsis. *Plant Physiol*. 119: 1371–1378. doi: https://doi.org/10.1104/pp.119.4.1371

Fan L, Zheng S, Wang X. (1997) Antisense suppression of phospholipase D alpha retards abscisic acid- and ethylene-promoted senescence of postharvest

Arabidopsis leaves. *Plant Cell*. 9: 2183–2196. doi: https://doi.org/10.1105/tpc.9.12.2183

Feilner T, Hultschig C, Lee J, Meyer S, Immink RG, Koenig A, Possling A, Seitz H, Beveridge A, Scheel D, Cahill DJ, Lehrach H, Kreutzberger J, Kersten B. (2005) High throughput identification of potential Arabidopsis mitogen-activated protein kinases substrates. *Mol Cell Proteomics*. 4: 1558–1568. doi: 10.1074/mcp.M500007-MCP200

Gottlin EB, Rudolph AE, Zhao Y, Matthews HR, Dixon JE. (1998) Catalytic mechanism of the phospholipase D superfamily proceeds via a covalent phosphohistidine intermediate. *Proc Natl Acad Sci U S A*. 95: 9202–9207. doi: https://doi.org/10.1073/pnas.95.16.9202

Gräf R, Rietdorf J, Zimmermann T. (2005) Live cell spinning disk microscopy. *Adv Biochem Eng Biotechnol*. 95: 57–75. doi 10.1007/b102210

Guo L, Mishra G, Markham JE, Li M, Tawfall A, Welti R, Wang X. (2012) Connections between sphingosine kinase and phospholipase D in the abscisic acid signaling pathway in Arabidopsis. *J Biol Chem*. 287: 8286–8296. doi: 10.1074/jbc.M111.274274

Hasezawa S, Ueda K, Kumagai F. (2000) Time-sequence observations of microtubule dynamics throughout mitosis in living cell suspensions of stable transgenic Arabidopsis--direct evidence for the origin of cortical microtubules at M/G1 interface. *Plant Cell Physiol*. 4: 244–250. doi: https://doi.org/10.1093/pcp/41.2.244

Hashimoto T, Kato T. (2006) Cortical control of plant microtubules. *Curr Opin Plant Biol*. 9: 5–11. doi: 10.1016/j.pbi.2005.11.005

Hayashi I, Wilde A, Mal TK, Ikura M. (2005) Structural basis for the activation of microtubule assembly by the EB1 and p150Glued complex. *Mol Cell*. 19: 449–460. doi: 10.1016/j.molcel.2005.06.034

Hayashi K, Hasegawa J, Matsunaga S. (2013) The boundary of the meristematic and elongation zones in roots: endoreduplication precedes rapid cell expansion. *Sci Rep*. 3: 2723. doi: 10.1038/srep02723

Heller M (1978) Phospholipase D. *Adv Lipid Res* 16: 267–326. doi: https://doi.org/10.1016/B978-0-12-024916-9.50011-1

Heyman J, Van den Daele H, De Wit K, Boudolf V, Berckmans B, Verkest A, Alvim Kamei CL, De Jaeger G, Koncz C, De Veylder L. (2011) Arabidopsis

ULTRAVIOLET-B-INSENSITIVE4 maintains cell division activity by temporal inhibition of the anaphase-promoting complex/cyclosome. *Plant Cell*. 23: 4394–4410. doi: 10.1105/tpc.111.091793

Ho AYY, Day DA, Brown MH, Marc J. (2009) Arabidopsis phospholipase Dd as an initiator of cytoskeleton-mediated signalling to fundamental cellular processes. *Functional Plant Biology*. 36: 190–198. doi: https://doi.org/10.1071/FP08222

Ho CM, Hotta T, Guo F, Roberson RW, Lee YR, Liu B. (2011) Interaction of antiparallel microtubules in the phragmoplast is mediated by the microtubule-associated protein MAP65-3 in Arabidopsis. *Plant Cell*. 23: 2909–2923. doi: 10.1105/tpc.110.078204

Hoffmann C, Moes D, Dieterle M, Neumann K, Moreau F, Tavares Furtado A, Dumas D, Steinmetz A, Thomas C. (2014) Live cell imaging reveals actin-cytoskeleton-induced self-association of the actin-bundling protein WLIM1. *J Cell Sci*. 127: 583–598. doi: 10.1242/jcs.134536

Hong Y, Devaiah SP, Bahn SC, Thamasandra BN, Li M, Welti R, Wang X. (2009) Phospholipase D epsilon and phosphatidic acid enhance Arabidopsis nitrogen signaling and growth. *Plant J*. 58: 376–87. doi: 10.1111/j.1365-313X.2009.03788.x

Hong Y, Pan X, Welti R, Wang X. (2008) The effect of phospholipase Dalpha3 on Arabidopsis response to hyperosmotic stress and glucose. *Plant Signal Behav*. 3: 1099–1100. doi: 10.1105/tpc.107.056390

Hong Y, Zhang W, Wang X. (2010) Phospholipase D and phosphatidic acid signalling in plant response to drought and salinity. *Plant Cell Environ*. 33: 627–635. doi: 10.1111/j.1365-3040.2009.02087.x

Hong Y, Zhao J, Guo L, Kim SC, Deng X, Wang G, Zhang G, Li M, Wang X. (2016) Plant phospholipases D and C and their diverse functions in stress responses. *Prog Lipid Res*. 62: 55–74. doi: 10.1016/j.plipres.2016.01.002

Hussey PJ, Ketelaar T, Deeks MJ. (2006) Control of the actin cytoskeleton in plant cell growth. *Annu Rev Plant Biol*. 57: 109–115. doi: 10.1146/annurev.arplant.57.032905.105206

Ishida T, Adachi S, Yoshimura M, Shimizu K, Umeda M, Sugimoto K. (2010) Auxin modulates the transition from the mitotic cycle to the endocycle in Arabidopsis. *Development*. 137: 63–71. doi: 10.1242/dev.035840

Ishida T, Fujiwara S, Miura K, Stacey N, Yoshimura M, Schneider K, Adachi S, Minamisawa K, Umeda M, Sugimoto K. (2009) SUMO E3 ligase HIGH PLOIDY2 regulates endocycle onset and meristem maintenance in Arabidopsis. *Plant Cell*. 21: 2284–2297. doi: 10.1105/tpc.109.068072

Ishihama N, Yoshioka H. (2012) Post-translational regulation of WRKY transcription factors in plant immunity. *Curr Opin Plant Biol*. 15:431–437. doi: 10.1016/j.pbi.2012.02.003

Ito E, Fujimoto M, Ebine K, Uemura T, Ueda T, Nakano A. (2012) Dynamic behavior of clathrin in Arabidopsis thaliana unveiled by live imaging. *Plant J*. 69: 204–216. doi: 10.1111/j.1365-313X.2011.04782.x

Jiang K, Akhmanova A. (2011) Microtubule tip-interacting proteins: a view from both ends. *Curr Opin Cell Biol*. 23: 94–101. doi: 10.1016/j.ceb.2010.08.008

Jiang Y, Wu K, Lin F, Qu Y, Liu X, Zhang Q. (2014) Phosphatidic acid integrates calcium signaling and microtubule dynamics into regulating ABA-induced stomatal closure in Arabidopsis. *Planta*. 239: 565–575. doi: 10.1007/s00425-013-1999-5

Jin K, Shen J, Ashton RW, White RP, Dodd IC, Phillips AL, Parry MA, Whalley WR. (2015) The effect of impedance to root growth on plant architecture in wheat. *Plant Soil*. 392: 323–332. doi: 10.1007/s11104-015-2462-0

Jonak C, Okrész L, Bögre L, Hirt H. (2002) Complexity, cross talk and integration of plant MAP kinase signalling. *Curr Opin Plant Biol*. 5: 415–424. doi: https://doi.org/10.1016/S1369-5266(02)00285-6

Kalachova T, Iakovenko O, Kretinin S, Kravets V. (2013) Involvement of phospholipase D and NADPH-oxidase in salicylic acid signaling cascade. *Plant Physiol Biochem*. 66: 127–133. doi: 10.1016/j.plaphy.2013.02.006

Karahara I, Suda J, Tahara H, Yokota E, Shimmen T, Misaki K, Yonemura S, Staehelin LA, Mineyuki Y. (2009) The preprophase band is a localized center of clathrin-mediated endocytosis in late prophase cells of the onion cotyledon epidermis. *Plant J*. 57: 819–831. doi: 10.1111/j.1365-313X.2008.03725.x

Keshet Y, Seger R. (2010) The MAP kinase signaling cascades: a system of hundreds of components regulates a diverse array of physiological functions. *Methods Mol Biol*. 661: 3–38. doi: 10.1007/978-1-60761-795-2_1

Kim SC, Guo L, Wang X. (2013) Phosphatidic acid binds to cytosolic glyceraldehyde-3-phosphate dehydrogenase and promotes its cleavage in Arabidopsis. *J Biol Chem*. 288: 11834–11844. doi: 10.1074/jbc.M112.427229

Kohoutová L, Kourová H, Nagy SK, Volc J, Halada P, Mészáros T, Meskiene I, Bögre L, Binarová P. (2015) The Arabidopsis mitogen-activated protein kinase 6 is associated with γ-tubulin on microtubules, phosphorylates EB1c and maintains spindle orientation under nitrosative stress. *New Phytol*. 207: 1061–1074. doi: 10.1111/nph.13501

Komaki S, Abe T, Coutuer S, Inzé D, Russinova E, Hashimoto T. (2010) Nuclear-localized subtype of end-binding 1 protein regulates spindle organization in Arabidopsis. *J Cell Sci*. 123: 451–459. doi: 10.1242/jcs.062703

Komarova Y, De Groot CO, Grigoriev I, Gouveia SM, Munteanu EL, Schober JM, Honnappa S, Buey RM, Hoogenraad CC, Dogterom M, Borisy GG, Steinmetz MO, Akhmanova A. (2009) Mammalian end binding proteins control persistent microtubule growth. *J Cell Biol*. 184: 691–706. doi: 10.1083/jcb.200807179

Komis G, Mistrik M, Šamajová O, Ovečka M, Bartek J, Šamaj J. (2015) Superresolution live imaging of plant cells using structured illumination microscopy. *Nat Protoc*. 10: 1248–63. doi: 10.1038/nprot.2015.083

Komis G, Novák D, Ovečka M, Šamajová O, Šamaj J. (2018) Advances in Imaging Plant Cell Dynamics. *Plant Physiol*. 176: 80–93. doi: 10.1104/pp.17.00962

Kooijman EE, Chupin V, de Kruijff B, Burger KN. (2003) Modulation of membrane curvature by phosphatidic acid and lysophosphatidic acid. *Traffic*. 4: 162–174. doi: https://doi.org/10.1034/j.1600-0854.2003.00086.x

Kopczak SD, Haas NA, Hussey PJ, Silflow CD, Snustad DP. (1992) The small genome of Arabidopsis contains at least six expressed alpha-tubulin genes. *Plant Cell*. 4: 539–547. doi: 10.1105/tpc.4.5.539

Kost B, Spielhofer P, Chua NH. (1998) A GFP-mouse talin fusion protein labels plant actin filaments in vivo and visualizes the actin cytoskeleton in growing pollen tubes. *Plant J*. 16: 393–401. doi: https://doi.org/10.1046/j.1365-313x.1998.00304.x

Krinke O, Flemr M, Vergnolle C, Collin S, Renou JP, Taconnat L, Yu A, Burketová L, Valentová O, Zachowski A, Ruelland E. (2009) Phospholipase D activation is an early component of the salicylic acid signaling pathway in Arabidopsis cell suspensions. *Plant Physiol*. 150: 424–436. doi: 10.1104/pp.108.133595

Kusner DJ, Barton JA, Qin C, Wang X, Iyer SS. (2003) Evolutionary conservation of physical and functional interactions between phospholipase D and actin. *Arch Biochem Biophys*. 412: 231–241. doi: https://doi.org/10.1016/S0003-9861(03)00052-3

Kusner DJ, Barton JA, Wen KK, Wang X, Rubenstein PA, Iyer SS. (2002) Regulation of phospholipase D activity by actin. Actin exerts bidirectional modulation of Mammalian phospholipase D activity in a polymerization-dependent, isoform-specific manner. *J Biol Chem*. 277: 50683–50692. doi: 10.1074/jbc.M209221200

la Cour T, Kiemer L, Mølgaard A, Gupta R, Skriver K, Brunak S. (2004) Analysis and prediction of leucine-rich nuclear export signals. *Protein Eng Des Sel*. 17: 527–536. doi: 10.1093/protein/gzh062

Lamprecht MR, Sabatini DM, Carpenter AE. (2007) CellProfiler: free, versatile software for automated biological image analysis. *Biotechniques*. 42: 71–75. doi: 10.2144/000112257

Ledbetter MC, Porter KR. (1963) A "MICROTUBULE" IN PLANT CELL FINE STRUCTURE. *J Cell Biol*. 19: 239–250. doi: 10.1083/jcb.19.1.239

Lee JS, Huh KW, Bhargava A, Ellis BE. (2008) Comprehensive analysis of protein-protein interactions between Arabidopsis MAPKs and MAPK kinases helps define potential MAPK signalling modules. *Plant Signal Behav*. 3: 1037–1041. doi: 10.4161/psb.3.12.6848

Lein W, Saalbach G. (2001) Cloning and direct G-protein regulation of phospholipase D from tobacco. *Biochim Biophys Acta*. 1530: 172–183. doi: https://doi.org/10.1016/S1388-1981(00)00182-7

Li M, Hong Y, Wang X. (2009) Phospholipase D- and phosphatidic acid-mediated signaling in plants. *Biochim Biophys Acta*. 1791: 927–935. doi: 10.1016/j.bbalip.2009.02.017

Li M, Qin C, Welti R, Wang X. (2006) Double knockouts of phospholipases Dzeta1 and Dzeta2 in Arabidopsis affect root elongation during phosphate-limited growth but do not affect root hair patterning. *Plant Physiol*. 140: 761–770. doi: 10.1104/pp.105.070995

Li R, Gundersen GG. (2008) Beyond polymer polarity: how the cytoskeleton builds a polarized cell. *Nat Rev Mol Cell Biol*. 9: 860–873. doi: 10.1038/nrm2522

Liu S, Wilson KA, Rice-Stitt T, Neiman AM, McNew JA. (2007) In vitro fusion catalyzed by the sporulation-specific t-SNARE light-chain Spo20p is stimulated by phosphatidic acid. *Traffic*. 8: 1630–1643. doi: 10.1111/j.1600-0854.2007.00628.x

Maizel A, von Wangenheim D, Federici F, Haseloff J, Stelzer EH. (2011) High-resolution live imaging of plant growth in near physiological bright conditions using light sheet fluorescence microscopy. *Plant J*. 68: 377–385. doi: 10.1111/j.1365-313X.2011.04692.x

Manifava M, Thuring JW, Lim ZY, Packman L, Holmes AB, Ktistakis NT. (2001) Differential binding of traffic-related proteins to phosphatidic acid- or phosphatidylinositol (4,5)- bisphosphate-coupled affinity reagents. *J Biol Chem*. 276: 8987-8994. doi: 10.1074/jbc.M010308200

Marc J, Granger CL, Brincat J, Fisher DD, Kao Th, McCubbin AG, Cyr RJ. (1998) A GFP-MAP4 reporter gene for visualizing cortical microtubule rearrangements in living epidermal cells. *Plant Cell*. 10: 1927–1940. doi: https://doi.org/10.1105/tpc.10.11.1927

Marks MD, Wenger JP, Gilding E, Jilk R, Dixon RA. (2009) Transcriptome analysis of Arabidopsis wild-type and gl3-sst sim trichomes identifies four additional genes required for trichome development. *Mol Plant*. 2: 803–822. doi: 10.1093/mp/ssp037

Mathur J, Mathur N, Kernebeck B, Srinivas BP, Hülskamp M. (2003) A novel localization pattern for an EB1-like protein links microtubule dynamics to endomembrane organization. *Curr Biol*. 13: 1991–1997. doi: https://doi.org/10.1016/j.cub.2003.10.033

Mathur J, Spielhofer P, Kost B, Chua N. (1999) The actin cytoskeleton is required to elaborate and maintain spatial patterning during trichome cell morphogenesis in Arabidopsis thaliana. *Development*. 126: 5559–5568. doi: http://dev.biologists.org/content/126/24/5559.long

McLamore ES, Diggs A, Calvo Marzal P, Shi J, Blakeslee JJ, Peer WA, Murphy AS, Porterfield DM. (2010) Non-invasive quantification of endogenous root auxin transport using an integrated flux microsensor technique. *Plant J*. 63: 1004–1016. doi: 10.1111/j.1365-313X.2010.04300.x

McLoughlin F, Arisz SA, Dekker HL, Kramer G, de Koster CG, Haring MA, Munnik T, Testerink C. (2013) Identification of novel candidate phosphatidic acid-

binding proteins involved in the salt-stress response of Arabidopsis thaliana roots. *Biochem J*. 450: 573–581. doi: 10.1042/BJ20121639

McMahon HT, Gallop JL. (2005) Membrane curvature and mechanisms of dynamic cell membrane remodelling. *Nature*. 438: 590–596. doi: 10.1038/nature04396

Meijer HJ, Munnik T. (2003) Phospholipid-based signaling in plants. *Annu Rev Plant Biol*. 54: 265–306. doi: 10.1146/annurev.arplant.54.031902.134748

Miart F, Desprez T, Biot E, Morin H, Belcram K, Höfte H, Gonneau M, Vernhettes S. (2014) Spatio-temporal analysis of cellulose synthesis during cell plate formation in Arabidopsis. *Plant J*. 77: 71–84. doi: 10.1111/tpj.12362

Mishra G, Zhang W, Deng F, Zhao J, Wang X. (2006) A bifurcating pathway directs abscisic acid effects on stomatal closure and opening in Arabidopsis. *Science*. 312: 264–266. doi: 10.1126/science.1123769

Morton WM, Ayscough KR, McLaughlin PJ. (2000) Latrunculin alters the actin-monomer subunit interface to prevent polymerization. *Nat Cell Biol*. 2: 376–378. doi: 10.1038/35014075

Motes CM, Pechter P, Yoo CM, Wang YS, Chapman KD, Blancaflor EB. (2005) Differential effects of two phospholipase D inhibitors, 1-butanol and N-acylethanolamine, on in vivo cytoskeletal organization and Arabidopsis seedling growth. *Protoplasma*. 226: 109–123. doi: 10.1007/s00709-005-0124-4

Munnik T, Musgrave A. (2001) Phospholipid Signaling in Plants: Holding On to Phospholipase D. *Sci STKE.* 2001: 42. doi: 10.1126/stke.2001.111.pe42

Murashige T, Skoog F. (1962) A revised medium for rapid growth and bioassays with tobacco tissue cultures. *Physiol. Plant*. 15: 473–497. doi: 10.1111/j.1399-3054.1962.tb08052.x

Murata T, Sano T, Sasabe M, Nonaka S, Higashiyama T, Hasezawa S, Machida Y, Hasebe M. (2013) Mechanism of microtubule array expansion in the cytokinetic phragmoplast. *Nat Commun*. 4: 1967. doi: 10.1038/ncomms2967

Nakagawa T, Suzuki T, Murata S, Nakamura S, Hino T, Maeo K, Tabata R, Kawai T, Tanaka K, Niwa Y, Watanabe Y, Nakamura K, Kimura T, Ishiguro S. (2007) Improved Gateway binary vectors: high-performance vectors for creation of fusion constructs in transgenic analysis of plants. *Biosci Biotechnol Biochem*. 71: 2095–2100. doi: 10.1271/bbb.70216

Nakamura M, Naoi K, Shoji T, Hashimoto T. (2004) Low concentrations of propyzamide and oryzalin alter microtubule dynamics in Arabidopsis epidermal cells. *Plant Cell Physiol*. 45: 1330–1334. doi: 10.1093/pcp/pch300

Nakamura Y, Awai K, Masuda T, Yoshioka Y, Takamiya K, Ohta H. (2005) A novel phosphatidylcholine-hydrolyzing phospholipase C induced by phosphate starvation in Arabidopsis. *J Biol Chem*. 280: 7469–7476. doi: 10.1074/jbc.M408799200

Nakanishi H, Morishita M, Schwartz CL, Coluccio A, Engebrecht J, Neiman AM. (2006) Phospholipase D and the SNARE Sso1p are necessary for vesicle fusion during sporulation in yeast. *J Cell Sci*. 119: 1406–1415. doi: 10.1242/jcs.02841

Novák D, Kuchařová A, Ovečka M, Komis G, Šamaj J. (2016) Developmental Nuclear Localization and Quantification of GFP-Tagged EB1c in Arabidopsis Root Using Light-Sheet Microscopy. *Front Plant Sci*. 6: 1187. doi: 10.3389/fpls.2015.01187

Novák D, Vadovič P, Ovečka M, Šamajová O, Komis G, Colcombet J, Šamaj J. (2018) Gene Expression Pattern and Protein Localization of Arabidopsis Phospholipase D Alpha 1 Revealed by Advanced Light-Sheet and Super-Resolution Microscopy. *Front Plant Sci*. 9: 371. doi: 10.3389/fpls.2018.00371

Okamoto T, Tsurumi S, Shibasaki K, Obana Y, Takaji H, Oono Y, Rahman A. (2008) Genetic dissection of hormonal responses in the roots of Arabidopsis grown under continuous mechanical impedance. *Plant Physiol*. 146: 1651–1662. doi: 10.1104/pp.107.115519

Ovečka M, Vaškebová L, Komis G, Luptovčiak I, Smertenko A, Šamaj J. (2015) Preparation of plants for developmental and cellular imaging by light-sheet microscopy. *Nat Protoc*. 10: 1234–1247. doi: 10.1038/nprot.2015.081

Panteris E, Adamakis ID, Daras G, Hatzopoulos P, Rigas S. (2013) Differential responsiveness of cortical microtubule orientation to suppression of cell expansion among the developmental zones of Arabidopsis thaliana root apex. *PLoS One*. 8: e82442. doi: 10.1371/journal.pone.0082442

Pappan K, Austin-Brown S, Chapman KD, Wang X. (1998) Substrate selectivities and lipid modulation of plant phospholipase D alpha, -beta, and -gamma. *Arch Biochem Biophys*. 353: 131–140. doi: 10.1006/abbi.1998.0640

Peters C, Li M, Narasimhan R, Roth M, Welti R, Wang X. (2010) Nonspecific phospholipase C NPC4 promotes responses to abscisic acid and tolerance to

hyperosmotic stress in Arabidopsis. *Plant Cell*. 22: 2642–3659. doi: 10.1105/tpc.109.071720

Pleskot R, Li J, Zárský V, Potocký M, Staiger CJ. (2013) Regulation of cytoskeletal dynamics by phospholipase D and phosphatidic acid. *Trends Plant Sci*. 18: 496–504. doi: 10.1016/j.tplants.2013.04.005

Pleskot R, Pejchar P, Staiger CJ, Potocký M. (2014) When fat is not bad: the regulation of actin dynamics by phospholipid signaling molecules. *Front Plant Sci*. 5: 5. doi: 10.3389/fpls.2014.00005

Potocký M, Pleskot R, Pejchar P, Vitale N, Kost B, Zárský V. (2014) Live-cell imaging of phosphatidic acid dynamics in pollen tubes visualized by Spo20p-derived biosensor. *New Phytol*. 203: 483–494. doi: 10.1111/nph.12814

Putta P, Rankenberg J, Korver RA, van Wijk R, Munnik T, Testerink C, Kooijman EE. (2016) Phosphatidic acid binding proteins display differential binding as a function of membrane curvature stress and chemical properties. *Biochim Biophys Acta*. 1858: 2709–2716. doi: 10.1016/j.bbamem.2016.07.014

Qin C, Wang C, Wang X (2002) Kinetic analysis of Arabidopsis phospholipase D delta. Substrate preference and mechanism of activation by Ca2+ and phosphatidylinositol 4,5-biphosphate. *J Biol Chem*. 277: 49685–49690. doi: 10.1074/jbc.M209598200

Qin C, Wang X. (2002) The Arabidopsis phospholipase D family. Characterization of a calcium-independent and phosphatidylcholine-selective PLD zeta 1 with distinct regulatory domains. *Plant Physiol.* 128: 1057–1068. doi: 10.1104/pp.010928

Qin W1, Pappan K, Wang X. (1997) Molecular heterogeneity of phospholipase D (PLD). Cloning of PLDgamma and regulation of plant PLDgamma, -beta, and -alpha by polyphosphoinositides and calcium. *J Biol Chem*. 272: 28267–28273. doi: 10.1016/j.tplants.2013.04.005

Quarles RH, Dawson RM. (1969) The distribution of phospholipase D in developing and mature plants. *Biochem J.* 112: 787–794. doi: 10.1042/bj1120787

Ren J, Longping W, Xinjiao G, Changjiang J, Yu X, Xuebiao Y. (2009) DOG1.0: illustrator of protein domain structures. *Cell Res*. 19: 271–273. doi: 10.1038/cr.2009.6

Riedl J, Crevenna AH, Kessenbrock K, Yu JH, Neukirchen D, Bista M, Bradke F, Jenne D, Holak TA, Werb Z, Sixt M, Wedlich-Soldner R. (2008) Lifeact: a versatile marker to visualize F-actin. *Nat Methods*. 5: 605–607. doi: 10.1038/nmeth.1220

Roth MG. (2008) Molecular mechanisms of PLD function in membrane traffic. *Traffic*. 9: 1233–1239. doi: 10.1111/j.1600-0854.2008.00742.x

Rudge SA, Morris AJ, Engebrecht J. (1998) Relocalization of phospholipase D activity mediates membrane formation during meiosis. *J Cell Biol*. 140: 81–90. doi: 10.1083/jcb.140.1.81

Ryu SB (2004) Phospholipid-derived signaling mediated by phospholipase A in plants. *Trends Plant Sci*. 9: 229–235. doi: 10.1016/j.tplants.2004.03.004

Šamajová O, Komis G, Šamaj J. (2013) Emerging topics in the cell biology of mitogen-activated protein kinases. *Trends Plant Sci*. 18: 140–148. doi: 10.1016/j.tplants.2012.11.004

Šamajová O, Komis G, Šamaj J. (2014) Immunofluorescent localization of MAPKs and colocalization with microtubules in Arabidopsis seedling whole-mount probes. *Methods Mol Biol*. 1171: 107–115. doi: 10.1007/978-1-4939-0922-3_9

Sang Y, Zheng S, Li W, Huang B, Wang X. (2001) Regulation of plant water loss by manipulating the expression of phospholipase D alpha. *Plant J*. 28:135–44. doi: https://doi.org/10.1046/j.1365-313X.2001.01138.x

Sasabe M, Kosetsu K, Hidaka M, Murase A, Machida Y. (2011) Arabidopsis thaliana MAP65-1 and MAP65-2 function redundantly with MAP65-3/PLEIADE in cytokinesis downstream of MPK4. *Plant Signal Behav*. 6: 743–747. doi: 10.4161/psb.6.5.15146

Schindelin J, Arganda-Carreras I, Frise E, Kaynig V, Longair M, Pietzsch T, Preibisch S, Rueden C, Saalfeld S, Schmid B, Tinevez JY, White DJ, Hartenstein V, Eliceiri K, Tomancak P, Cardona A. (2012) Fiji: an open-source platform for biological-image analysis. *Nat Methods*. 9: 676–682. doi: 10.1038/nmeth.2019

Seguí-Simarro JM, Austin JR 2nd, White EA, Staehelin LA. (2004) Electron tomographic analysis of somatic cell plate formation in meristematic cells of Arabidopsis preserved by high-pressure freezing. *Plant Cell*. 16: 836–856. doi: 10.1105/tpc.017749

Sheahan MB, Staiger CJ, Rose RJ, McCurdy DW. (2004) A green fluorescent protein fusion to actin-binding domain 2 of Arabidopsis fimbrin highlights new features of a dynamic actin cytoskeleton in live plant cells. *Plant Physiol*. 136: 3968–3978. doi: 10.1104/pp.104.049411

Smékalová V, Doskočilová A, Komis G, Samaj J. (2014) Crosstalk between secondary messengers, hormones and MAPK modules during abiotic stress signalling in plants. *Biotechnol Adv*. 32: 2–11. doi: 10.1016/j.biotechadv.2013.07.009

Smertenko A, Assaad F, Baluška F, Bezanilla M, Buschmann H, Drakakaki G, Hauser MT, Janson M, Mineyuki Y, Moore I, Müller S, Murata T, Otegui MS, Panteris E, Rasmussen C, Schmit AC, Šamaj J, Samuels L, Staehelin LA, Van Damme D, Wasteneys G, Žárský V. (2017) Plant Cytokinesis: Terminology for Structures and Processes. *Trends Cell Biol*. 27: 885–894. doi: 10.1016/j.tcb.2017.08.008

Smertenko A, Franklin-Tong VE. (2011) Organisation and regulation of the cytoskeleton in plant programmed cell death. *Cell Death Differ*. 18: 1263–1270. doi: 10.1038/cdd.2011.39

Smertenko AP, Chang HY, Sonobe S, Fenyk SI, Weingartner M, Bögre L, Hussey PJ. (2006) Control of the AtMAP65-1 interaction with microtubules through the cell cycle. *J Cell Sci*. 119: 3227–3237. doi: 10.1242/jcs.03051

Smertenko AP, Chang HY, Wagner V, Kaloriti D, Fenyk S, Sonobe S, Lloyd C, Hauser MT, Hussey PJ. (2004) The Arabidopsis microtubule-associated protein AtMAP65-1: molecular analysis of its microtubule bundling activity. *Plant Cell*. 16: 2035–2047. doi: 10.1105/tpc.104.023937

Smertenko AP, Kaloriti D, Chang HY, Fiserova J, Opatrny Z, Hussey PJ. (2008) The C-terminal variable region specifies the dynamic properties of Arabidopsis microtubule-associated protein MAP65 isotypes. *Plant Cell*. 20: 3346–3358. doi: 10.1105/tpc.108.063362

Stuckey JA, Dixon JE. (1999) Crystal structure of a phospholipase D family member. *Nat Struct Biol*. 6: 278–284. doi: 10.1038/6716

Sung TC, Altshuller YM, Morris AJ, Frohman MA. (1999a) Molecular analysis of mammalian phospholipase D2. *J Biol Chem*. 274: 494–502. doi: 10.1074/jbc.274.1.494

Sung TC, Zhang Y, Morris AJ, Frohman MA. (1999b) Structural analysis of human phospholipase D1. *J Biol Chem*. 274: 3659–3666. doi: 10.1074/jbc.274.6.3659

Takáč T, Pechan T, Samajová O, Ovečka M, Richter H, Eck C, Niehaus K, Samaj J. (2012) Wortmannin treatment induces changes in Arabidopsis root proteome and post-Golgi compartments. *J Proteome Res*. 11: 3127–3142. doi: 10.1021/pr201111n

Tamura N, Draviam VM. (2012) Microtubule plus-ends within a mitotic cell are 'moving platforms' with anchoring, signalling and force-coupling roles. *Open Biol*. 2: 120132. doi: 10.1098/rsob.120132

Tang K, Liu JY. (2017) Molecular characterization of GhPLDα1 and its relationship with secondary cell wall thickening in cotton fibers. *Acta Biochim Biophys Sin (Shanghai)*. 49: 33–43. doi: 10.1093/abbs/gmw113

Tanoue T, Nishida E. (2003) Molecular recognitions in the MAP kinase cascades. *Cell Signal*. 15: 455–462. doi: 10.1016/S0898-6568(02)00112-2

Teh OK, Shimono Y, Shirakawa M, Fukao Y, Tamura K, Shimada T, Hara-Nishimura I. (2013) The AP-1 μ adaptin is required for KNOLLE localization at the cell plate to mediate cytokinesis in Arabidopsis. *Plant Cell Physiol*. 54: 838–847. doi: 10.1093/pcp/pct048

Testerink C, Munnik T. (2005) Phosphatidic acid: a multifunctional stress signaling lipid in plants. *Trends Plant Sci*. 10: 368–375. doi: 10.1016/j.tplants.2005.06.002

Testerink C, Munnik T. (2011) Molecular, cellular, and physiological responses to phosphatidic acid formation in plants. *J Exp Bot*. 62: 2349–2361. doi: 10.1093/jxb/err079

Thomas C, Tholl S, Moes D, Dieterle M, Papuga J, Moreau F, Steinmetz A. (2009) Actin bundling in plants. *Cell Motil Cytoskeleton*. 66: 940–957. doi: 10.1002/cm.20389

Tilney LG, Bryan J, Bush DJ, Fujiwara K, Mooseker MS, Murphy DB, Snyder DH. (1973) Microtubules: evidence for 13 protofilaments. *J Cell Biol*. 59: 267–275. doi: 10.1083/jcb.59.2.267

Tirnauer JS, Canman JC, Salmon ED, Mitchison TJ. (2002) EB1 targets to kinetochores with attached, polymerizing microtubules. *Mol Biol Cell*. 13: 4308–4316. doi: 10.1091/mbc.E02-04-0236

Uraji M, Katagiri T, Okuma E, Ye W, Hossain MA, Masuda C, Miura A, Nakamura Y, Mori IC, Shinozaki K, Murata Y. (2012) Cooperative function of PLDδ and PLDα1 in abscisic acid-induced stomatal closure in Arabidopsis. *Plant Physiol*. 159: 450–460. doi: 10.1104/pp.112.195578

Van Damme D, Van Poucke K, Boutant E, Ritzenthaler C, Inzé D, Geelen D. (2004) In vivo dynamics and differential microtubule-binding activities of MAP65 proteins. *Plant Physiol*. 136: 3956–3967. doi: 10.1104/pp.104.051623

van der Weele CM, Jiang HS, Palaniappan KK, Ivanov VB, Palaniappan K, Baskin TI. (2003) A new algorithm for computational image analysis of deformable motion at high spatial and temporal resolution applied to root growth. Roughly uniform elongation in the meristem and also, after an abrupt acceleration, in the elongation zone. *Plant Physiol*. 132: 1138–1148. doi: 10.1104/pp.103.021345

van Leeuwen W, Okrész L, Bögre L, Munnik T. (2004) Learning the lipid language of plant signalling. *Trends Plant Sci*. 9: 378–384. doi: 10.1016/j.tplants.2004.06.008

van Oostende-Triplet C, Guillet D, Triplet T, Pandzic E, Wiseman PW, Geitmann A. (2017) Vesicle Dynamics during Plant Cell Cytokinesis Reveals Distinct Developmental Phases. *Plant Physiol*. 174: 1544–1558. doi: 10.1104/pp.17.00343

van Schooten B, Testerink C, Munnik T. (2006) Signalling diacylglycerol pyrophosphate, a new phosphatidic acid metabolite. *Biochim Biophys Acta*. 1761: 151–159. doi: 10.1016/j.bbalip.2005.12.010

Verbelen JP, De Cnodder T, Le J, Vissenberg K, Baluska F. (2006) The Root Apex of Arabidopsis thaliana Consists of Four Distinct Zones of Growth Activities: Meristematic Zone, Transition Zone, Fast Elongation Zone and Growth Terminating Zone. *Plant Signal Behav*. 1: 296–304. doi: 10.4161/psb.1.6.3511

Voigt B, Timmers AC, Samaj J, Hlavacka A, Ueda T, Preuss M, Nielsen E, Mathur J, Emans N, Stenmark H, Nakano A, Baluska F, Menzel D. (2005a) Actin-based motility of endosomes is linked to the polar tip growth of root hairs. *Eur J Cell Biol*. 84: 609–621. doi: 10.1016/j.ejcb.2004.12.029

Voigt B, Timmers AC, Samaj J, Müller J, Baluska F, Menzel D. (2005b) GFP-FABD2 fusion construct allows in vivo visualization of the dynamic actin cytoskeleton in all cells of Arabidopsis seedlings. *Eur J Cell Biol*. 84: 595–608. doi: 10.1016/j.ejcb.2004.11.011

Wang C, Wang X. (2001) A novel phospholipase D of Arabidopsis that is activated by oleic acid and associated with the plasma membrane. *Plant Physiol*. 127: 1102–1112. doi: https://doi.org/10.1104/pp.010444

Wang C, Zien CA, Afitlhile M, Welti R, Hildebrand DF, Wang X. (2000) Involvement of phospholipase D in wound-induced accumulation of jasmonic acid in arabidopsis. *Plant Cell*. 12: 2237–2246. doi: https://doi.org/10.1105/tpc.12.11.2237

Wang G, Ryu S, Wang X. (2012) Plant phospholipases: an overview. *Methods Mol Biol*. 861: 123–137. doi: 10.1007/978-1-61779-600-5_8

Wang X. (2000) Multiple forms of phospholipase D in plants: the gene family, catalytic and regulatory properties, and cellular functions. *Prog Lipid Res*. 39: 109–149. doi: https://doi.org/10.1016/S0163-7827(00)00002-3

Wang X. (2001) PLANT PHOSPHOLIPASES. *Annu Rev Plant Physiol Plant Mol Biol*. 52: 211–231. doi: 10.1146/annurev.arplant.52.1.211

Wang X. (2004) Lipid signaling. *Curr Opin Plant Biol*. 7: 329–36, doi: 10.1016/j.pbi.2004.03.012

Wasteneys GO. (2002) Microtubule organization in the green kingdom: chaos or self-order? *J Cell Sci*. 115: 1345–1354. doi: http://jcs.biologists.org/content/115/7/1345.long

Weber M, Huisken J. (2011) Light sheet microscopy for real-time developmental biology. *Curr Opin Genet Dev*. 21: 566–572. doi: 10.1016/j.gde.2011.09.009

Weigel D, Jürgens G. (2002) Stem cells that make stems. *Nature*. 415: 751–754. doi: 10.1038/415751a

Winder SJ, Ayscough KR. (2005) Actin-binding proteins. *J Cell Sci*. 118: 651–654. doi: 10.1242/jcs.01670

Wymer C, Lloyd C. (1996) Dynamic microtubules: implications for cell wall patterns. *Trends Plant Sci*. 7: 222–228. doi: 10.1016/1360-1385(96)86899-3

Xue Y, Liu Z, Cao J, Ma Q, Gao X, Wang Q, Jin C, Zhou Y, Wen L, Ren J. (2011) GPS 2.1: enhanced prediction of kinase-specific phosphorylation sites with an algorithm of motif length selection. *Protein Eng Des Sel*. 24: 255–260. doi: 10.1093/protein/gzq094

Yamaoka S, Shimono Y, Shirakawa M, Fukao Y, Kawase T, Hatsugai N, Tamura K, Shimada T, Hara-Nishimura I. (2013) Identification and dynamics of Arabidopsis adaptor protein-2 complex and its involvement in floral organ development. *Plant Cell*. 25: 2958–2969. doi: 10.1105/tpc.113.114082

Yamaryo Y, Dubots E, Albrieux C, Baldan B, Block MA. (2008) Phosphate availability affects the tonoplast localization of PLDzeta2, an Arabidopsis thaliana phospholipase D. *FEBS Lett*. 582: 685–690. doi: 10.1016/j.febslet.2008.01.039

Yang Y, Costa A, Leonhardt N, Siegel RS, Schroeder JI. (2008) Isolation of a strong Arabidopsis guard cell promoter and its potential as a research tool. *Plant Methods*. 4: 6. doi: 10.1186/1746-4811-4-6

Young SA, Wang X, Leach JE. (1996) Changes in the Plasma Membrane Distribution of Rice Phospholipase D during Resistant Interactions with Xanthomonas oryzae pv oryzae. *Plant Cell*. 8: 1079–1090. doi: 10.1105/tpc.8.6.1079

Yu L, Nie J, Cao C, Jin Y, Yan M, Wang F, Liu J, Xiao Y, Liang Y, Zhang W. (2010) Phosphatidic acid mediates salt stress response by regulation of MPK6 in Arabidopsis thaliana. *New Phytol*. 188: 762–773. doi: 10.1111/j.1469-8137.2010.03422.x

Zhang H, Dawe RK. (2011) Mechanisms of plant spindle formation. *Chromosome Res*. 19: 335–344. doi: 10.1007/s10577-011-9190-y

Zhang Q, Berkey R, Blakeslee JJ, Lin J, Ma X, King H, Liddle A, Guo L, Munnik T, Wang X, Xiao S. (2018) Arabidopsis Phospholipase Dα1 and Dδ Oppositely Modulate EDS1- and SA-independent Basal Resistance Against Adapted Powdery Mildew. *Journal of Experimental Botany*, ery146, doi: https://doi.org/10.1093/jxb/ery146

Zhang Q, Lin F, Mao T, Nie J, Yan M, Yuan M, Zhang W. (2012) Phosphatidic acid regulates microtubule organization by interacting with MAP65-1 in response to salt stress in Arabidopsis. *Plant Cell*. 24: 4555–4576. doi: 10.1105/tpc.112.104182

Zhang Q, Qu Y, Wang Q, Song P, Wang P, Jia Q, Guo J. (2017a) Arabidopsis phospholipase D alpha 1-derived phosphatidic acid regulates microtubule organization and cell development under microtubule-interacting drugs treatment. *J Plant Res*. 130: 193–202. doi: 10.1007/s10265-016-0870-8

Zhang Q, Song P, Qu Y, Wang P, Jia Q, Guo L, Zhang C, Mao T, Yuan M, Wang X, Zhang W. (2017b) Phospholipase Dδ negatively regulates plant thermotolerance by destabilizing cortical microtubules in Arabidopsis. *Plant Cell Environ*. 40: 2220–2235. doi: 10.1111/pce.13023

Zhang W, Qin C, Zhao J, Wang X. (2004) Phospholipase D alpha 1-derived phosphatidic acid interacts with ABI1 phosphatase 2C and regulates abscisic acid signaling. *Proc Natl Acad Sci U S A*. 101: 9508–9513. doi: 10.1073/pnas.0402112101

Zhang W, Wang C, Qin C, Wood T, Olafsdottir G, Welti R, Wang X. (2003) The oleate-stimulated phospholipase D, PLDdelta, and phosphatidic acid decrease H2O2-induced cell death in Arabidopsis. *Plant Cell*. 15: 2285–2295. doi: 10.1105/tpc.013961

Zhang Y, Zhu H, Zhang Q, Li M, Yan M, Wang R, Wang L, Welti R, Zhang W, Wang X. (2009) Phospholipase dalpha1 and phosphatidic acid regulate NADPH oxidase activity and production of reactive oxygen species in ABA-mediated stomatal closure in Arabidopsis. *Plant Cell*. 21: 2357–2377. doi: 10.1105/tpc.108.062992

Zhao J, Wang X. (2004) Arabidopsis phospholipase Dalpha1 interacts with the heterotrimeric G-protein alpha-subunit through a motif analogous to the DRY motif in G-protein-coupled receptors. *J Biol Chem*. 279: 1794–1800. doi: 10.1074/jbc.M309529200

Abbreviations

+TIPs	microtubule plus-end tracking proteins
AA	amino acid
ABA	abscisic acid
ABPs	actin-binding proteins
AFs	actin filaments
ATP	adenosine triphosphate
AU	arbitrary unit
bp	base pair
BSA	bovine serum albumin
C2	calcium-dependent phospholipid -binding domain
C2-PLDs	calcium-dependent phospholipid binding domain-containing PLDs
CCD	coupled with charge-coupled device
CCP	clathrin-coated pits
CCV	clathrin-coated vesicles
CDK	cyclin-dependent kinase
CH	calponin-homology domain
CLSM	confocal laser scanning microscopy
Col-0	*Arabidopsis thaliana* ecotype Columbia-0
C-terminal	carboxy-terminal
DAG	diacylglycerol
DAPI	4′,6-diamidino-2-phenylindole
D-domain	docking domain
DGK	diacylglycerolkinase
DIC	differential interference contrast
DNA	deoxyribonucleic acid
EB1	End-binding 1
eb1a eb1b	double knock-out mutant of END-BINDING 1 a and END-BINDING 1 b
EB1a	END-BINDING 1 a
EB1b	END-BINDING 1 b
EB1c	END-BINDING 1 c

eb1c	knock-out mutant of END-BINDING 1 c
EBH	EB1 unique homology domain
ECL	enhanced chemiluminescence
EM	electron microscope
ER	endoplasmic reticulum
fABD2	actin-binding domain 2 of Arabidopsis fimbrin
F-actin	filamentous actin
FEP	fluorinated ethylene propylene
FM4-64	styryl dye for plasma membrane visualization
Fw	forward primer
g	gravity of Earth
G-actin	globular actin
gDNA	genomic DNA
GFP	GREEN FLUORESCENT PROTEIN
GPI-PLC	glycosylphosphatidylinositol PLC
HKD	HxKxxxxD domain
HRP	horseradish peroxidase
JA	jasmonic acid
kDa	kilodaltons
KO	knock-out
LSFM	light-sheet fluorescence microscopy
MAP4	MICROTUBULE-ASSOCIATED PROTEIN 4
MAP65	microtubule-associated proteins 65
MAP65-1	MICROTUBULE ASSOCIATED PROTEIN 65-1
MAPKK or MAP2K	mitogen-activated protein kinase kinase
MAPKKK or MAP3K	mitogen-activated protein kinase kinase kinase
MAPKKKKs or MAP4Ks	MAPKKK kinases
MAPKs	mitogen-activated protein kinases
MAPs	microtubule-associated proteins
MPK3	MITOGEN-ACTIVATED PROTEIN KINASE 3
MPK4	MITOGEN-ACTIVATED PROTEIN KINASE 4
MPK6	MITOGEN-ACTIVATED PROTEIN KINASE 6
mRFP	RED FLUORESCENT PROTEIN
MS	Murashige & Skoog

MTB1	microtubule binding domain 1
MTB2	microtubule binding domain 2
MTs	microtubules
NA	numerical aperture
NAEs	N-acylethanolamines
NLS	nuclear localization sequence
NPC	nonspecific PLC
N-terminal	amino-terminal
OD_{600}	optical density measured at a wavelength of 600 nm
OE	overexpressing
ORF	open reading frame
PA	phosphatidic acid
PALM	photoactivation localization microscopy
PC	phophatidylcholine
PCR	polymerase chain reaction
PE	phosphatidylethanolamine
PG	phosphatidylglycerol
PH	Pleckstrin homology domain
PIP_2	phosphatidylinositolbisphosphate
PI-PLC	phosphoinositide-specific PLC
PL	phospholipase
PLA	phospholipase A
PLB	phospholipase B
PLC	phospholipase C
PLD	phospholipase D
pldα1 x map65-1	double knock-out mutant of PHOSPHOLIPASE D ALPHA 1 and MICROTUBULE ASSOCIATED PROTEIN 65-1
PLDα1	PHOSPHOLIPASE D ALPHA 1
pldα1	knock-out mutant of PHOSPHOLIPASE D ALPHA 1
pldα1/δ	double knock-out mutant of PHOSPHOLIPASE D ALPHA 1 and PHOSPHOLIPASE D DELTA
PLDα2	PHOSPHOLIPASE D ALPHA 2
PLDα3	PHOSPHOLIPASE D ALPHA 3

pldα3	knock-out mutant of PHOSPHOLIPASE D ALPHA 3
PLDβ	PHOSPHOLIPASE D BETA
PLDβ1	PHOSPHOLIPASE D BETA 1
PLDβ2	PHOSPHOLIPASE D BETA 2
PLDγ	PHOSPHOLIPASE D GAMMA
PLDγ1	PHOSPHOLIPASE D GAMMA 1
PLDγ2	PHOSPHOLIPASE D GAMMA 2
PLDγ3	PHOSPHOLIPASE D GAMMA 3
pldδ	knock-out mutant of PHOSPHOLIPASE D DELTA
PLDδ	PHOSPHOLIPASE D DELTA
pldε	knock-out mutant of PHOSPHOLIPASE D EPSILON
PLDε	PHOSPHOLIPASE D EPSILON
PLDζ	PHOSPHOLIPASE D ZETA
PLDζ1	PHOSPHOLIPASE D ZETA 1
PLDζ2	PHOSPHOLIPASE D ZETA 2
PM	plasma membrane
PPB	preprophase band
PS	phosphatidylserine
PVDF	polyvinylidene difluoride
PX	Phox homology
PX/PH-PLDs	Pleckstrin homology and Phox homology domain-containing PLDs
Rev	reverse primer
RNA	ribonucleic acid
R-OH	primary alcohol
ROS	reactive oxygen species
rpm	revolutions per minute
SA	salicylic acid
SD	standard deviation
SDS-PAGE	sodium dodecyl sulphate-polyacrylamide gel electrophoresis
sCMOS	complementary metal–oxide–semiconductor
SIM	structured illumination microscopy

SNARE	soluble N-ethylmaleimide-sensitive factor attachment receptor
SNR	signal-to-noise ratio
SP-motif	Pro directed Ser/Thr motif
SPO14	phospholipase D in *Saccharomyces cerevisiae*
TBS	Tris-buffered-saline
TBS-T	TBS, 0.1% Tween 20
T-DNA	transfer DNA
TUB6	β-TUBULIN 6
UV	ultra violet
WLIM1	Widely-expressed LIM protein 1
YFP	YELLOW FLUORESCENT PROTEIN

Curriculum vitae

Mgr. Dominik Novák

Address:	Na Hradě 246/2, Olomouc, 779 00, Czech Republic
Date of birth:	19th October 1988
Place of birth:	Uherské Hradiště
E-mail:	dominik.novak@upol.cz
	dominik.filip.novak@gmail.com
Phone:	+420 732 178 001

Education

Ph.D. study in Biochemistry 2014 – present

Palacký University Olomouc

Title of Ph.D. thesis: Developmental expression and localization of END-BINDING 1 c and PHOSPHOLIPASE D ALPHA 1 proteins

Master's program in Biochemistry 2012 – 2014

Palacký University Olomouc

Title of Master's thesis: Studying of selected cytoskeletal proteins-cloning and microscopical observation

Bachelor's programme in Biochemistry 2008 – 2012

Masaryk University Brno

Title of Bachelor's thesis: Study of ethylene receptor ETR1 and its influence on cytokinin signalling pathway in plants

Employment

Ph.D. student / academic researcher 09/2016 – present

Centre of the Region Haná for Biotechnological and Agricultural Research, Department of Cell Biology, Faculty of Science, Palacký University Olomouc

A scientist in biological sciences 01/2016 – 08/2016

Centre of the Region Haná for Biotechnological and Agricultural Research, Department of Cell Biology, Faculty of Science, Palacký University Olomouc

Research Internships abroad

Universiteit van Amsterdam 02/2018 – 04/2018

Faculty of Science, Swammerdam Institute for Life Sciences, Plant Cell Biology department, prof. Munnik´s lab

Project participation

- Mitogen-activated protein kinase-dependent phosphorylation and functional regulation of cytoskeletal End binding 1c protein. Czech Science Foundation GAČR, project Nr. 14-27598P
- Proteomic analysis of Arabidopsis MAPK mutants. IGA 2013 PrF_2013_011
- Biological and molecular analysis of selected MAPKs during abiotic stress. IGA 2014 PrF_2014033
- Microscopy study of MAPKs and cytoskeleton in Arabidopsis and Medicago. IGA 2015 PřF 2015_015
- Application of proteomics to study microtubule cleavage using katanin in Arabidopsis. IGA_PrF_2016_012
- Regulation of phospholipase D alpha 1 function by MPK3-dependent phosphorylation. Czech Science Foundation GAČR, project Nr. 16-22044S

Teaching Experience

CRH / GFP	GFP technologies and confocal microscopy	2014
		2015
		2016
CRH / MM	Microscopic methods and their application in biotechnology	2015
		2016

International conferences

- 7th EPSO 2013, Porto Heli, Greece
- Komis G, Mistrik M, Šamajová O, Ovečka M, Kuchařová A, Novák D, Bartek J, Šamaj J. (2015) Live cell structured illumination microscopy imaging. Plant Biotechnology: Green for Good III 2015, Olomouc, Czech Republic
- Novák D, Kuchařová A, Ovečka M, Komis G, Šamaj J. (2016) Developmental nuclear localization of *Arabidopsis* EB1c protein in the root apex using light-

sheet microscopy. 17th European Congress on Biotechnology 2016, Krakow, Poland

- Novák D, Kuchařová A, Ovečka M, Perničková K, Komis G, Šamaj J. (2017) Developmental nuclear localization of End Binding 1c protein in *Arabidopsis* root. Biotechnology of plant products: Green for Good IV 2017, Olomouc, Czech Republic

Fields of interest

Microscopy (light microscopy, CLSM, spinning disk microscopy, Light-sheet microscopy), molecular biology methods (DNA and RNA isolation, PCR based techniques, GATEWAY cloning, recombinant GFP technology), biochemical methods (protein extraction, SDS-PAGE, western blotting), cytological techniques (whole mount immunolabelling), plant transformation (transient in *Nicotiana benthamiana* and stable in *Arabidopsis thaliana*), genetics (phenotype studies and backcrosses).

List of publications

Sum of Times Cited (Web of Science, 06/2018):	8
h-index:	2

Novák D, Kuchařová A, Ovečka M, KomisG, Šamaj J. (2016) Developmental Nuclear Localization and Quantification of GFP-Tagged EB1c in *Arabidopsis* Root Using Light-Sheet Microscopy. *Front. Plant Sci*. 6: 1187. doi: 10.3389/fpls.2015.01187

Komis G, Novák D, Ovečka M, Šamajová O, Šamaj J. (2018) Advances in Imaging Plant Cell Dynamics. *Plant Physiol*. 176: 80–93. doi: 10.1104/pp.17.00962

Novák D, Vadovič P, Ovečka M, Šamajová O, Komis G, Colcombet J, Šamaj J. (2018) Gene Expression Pattern and Protein Localization of Arabidopsis Phospholipase D Alpha 1 Revealed by Advanced Light-Sheet and Super-Resolution Microscopy. *Front. Plant Sci*. 9: 371. doi: 10.3389/fpls.2018.00371

Supplements

Supplement I

Research article

Developmental Nuclear Localization and Quantification of GFP-Tagged EB1c in *Arabidopsis* Root Using Light-Sheet Microscopy

Novák D*, Kuchařová A*, Ovečka M*, KomisG, Šamaj J. (2016) *Front. Plant Sci*. 6: 1187. doi: 10.3389/fpls.2015.01187

* joined first authors

frontiers in Plant Science

ORIGINAL RESEARCH
published: 05 January 2016
doi: 10.3389/fpls.2015.01187

Developmental Nuclear Localization and Quantification of GFP-Tagged EB1c in *Arabidopsis* Root Using Light-Sheet Microscopy

*Dominik Novák †, Anna Kuchařová †, Miroslav Ovečka †, George Komis and Jozef Šamaj **

Department of Cell Biology, Centre of the Region Haná for Biotechnological and Agricultural Research, Palacký University Olomouc, Olomouc, Czech Republic

The development of the root apex is determined by progress of cells from the meristematic region to the successive post-mitotic developmental zones for transition, cell elongation and final cell differentiation. We addressed root development, tissue architecture and root developmental zonation by means of light-sheet microscopic imaging of *Arabidopsis thaliana* seedlings expressing END BINDING protein 1c (EB1c) fused to green fluorescent protein (GFP) under control of native *EB1c* promoter. Unlike the other two members of the EB1 family, plant-specific EB1c shows prominent nuclear localization in non-dividing cells in all developmental zones of the root apex. The nuclear localization of EB1c was previously mentioned solely in meristematic cells, but not further addressed. With the help of advanced light-sheet microscopy, we report quantitative evaluations of developmentally-regulated nuclear levels of the EB1c protein tagged with GFP relatively to the nuclear size in diverse root tissues (epidermis, cortex, and endodermis) and root developmental zones (meristem, transition, and elongation zones). Our results demonstrate a high potential of light-sheet microscopy for 4D live imaging of fluorescently-labeled nuclei in complex samples such as developing roots, showing capacity to quantify parameters at deeper cell layers (e.g., endodermis) with minimal aberrations. The data presented herein further signify the unique role of developmental cell reprogramming in the transition from cell proliferation to cell differentiation in developing root apex.

Keywords: end-binding 1c (EB1c), nucleus, root apex, development, transition zone, light-sheet microscopy

OPEN ACCESS

Edited by:
Stefano Mancuso, Università degli Studi di Firenze, Italy

Reviewed by:
Ken Yokawa, University of Bonn, Germany
Emmanuel Panteris, Aristotle University of Thessaloniki, Greece

****Correspondence:***
Jozef Šamaj
jozef.samaj@upol.cz

† These authors have contributed equally to this work.

Specialty section:
This article was submitted to Plant Evolution and Development, a section of the journal Frontiers in Plant Science

Received: *27 October 2015*
Accepted: *10 December 2015*
Published: *05 January 2016*

Citation:
Novák D, Kuchařová A, Ovečka M, Komis G and Šamaj J (2016) Developmental Nuclear Localization and Quantification of GFP-Tagged EB1c in Arabidopsis Root Using Light-Sheet Microscopy. Front. Plant Sci. 6:1187. doi: 10.3389/fpls.2015.01187

INTRODUCTION

Root development in higher plants is early defined in the developing embryo as soon as root meristem initials appear (Scheres and Berleth, 1998). Thereon, the further growth of the primary root as exemplified in the model dicot *Arabidopsis thaliana* progresses through formative periclinal and proliferative anticlinal divisions in the root meristem and through post-mitotic cell elongation. In this way the root can be anatomically defined laterally by the existence of distinct cell files and longitudinally by the formation of distinct root zones.

In a center wise fashion, root cell files can be discerned to the central cylinder formed by protoxylem and protophloem, surrounded by the pericycle, and followed by the endodermis, the

cortex and finally the epidermis that forms the outer root layer. All different root cell types strictly originate from stem cells surrounding the quiescent center at the very root tip (Weigel and Jurgens, 2002). During the growth of the root apex, cells within certain cell files progress through different growth stages in a highly regulated manner. They undergo proliferative anticlinal divisions which are followed by elongation and finally by terminal differentiation in a relatively short time period. In this respect, the root apex is longitudinally divided into four distinguishable zones—meristematic, transition, elongation, and differentiation (Verbelen et al., 2006; Baluška and Mancuso, 2013). The meristematic zone, is characterized by successive cell divisions of non- or minimally elongating cells (van der Weele et al., 2003). In the elongation zone, cell length increases and cell divisions are suppressed. In many classical anatomical studies, the boundary region between meristematic and elongation zone is often neglected. Nevertheless, previous studies demonstrated a population of nearly isodiametric cells within all cell files, with particular characteristics in intracellular architecture such as actin organization (Baluska et al., 1997) or cellular functions such as fluid phase endocytosis (Samaj et al., 2004). This cell population forms a distinct post-mitotic zone in dicots and monocots and it is called transition zone. The transition zone (or otherwise called distal elongation zone; DEZ; Baluška et al., 1990; Ishikawa and Evans, 1993) is considered to form an important link between the meristematic and elongation zone.

The transition zone is interpolated between the meristematic and the elongation zone while cells in this zone are also polarized. The transition zone is sensitive to a variety of stimuli, including plant hormones, effects of cytoskeletal disrupting drugs, gravity, light, oxygen or heavy metal exposure (Illés et al., 2006; Dello Ioio et al., 2007, 2008; Ruzicka et al., 2009; Baluška and Mancuso, 2013; Eleftheriou et al., 2015). Moreover, cells of the root transition zone exhibit unique physiological behaviors including oscillations of ion and hormone fluxes and also of gene expression (Benková and Hejatko, 2009; McLamore et al., 2010; Baluška and Mancuso, 2013).

During cell remodeling in the elongating root, nucleus shape and position undergo dramatic changes (Chytilova et al., 2000; Ketelaar et al., 2002; Sliwinska et al., 2012). While cell expansion proceeds in the elongation zone, DNA amount (C value) increases by switching from mitotic to endoreduplication cycles (Hayashi et al., 2013). The switch from the mitosis to endoreduplication is accompanied by suppression of mitotic entry by inactivation of mitotic cyclin-dependent kinases (Adachi et al., 2011). Endoreduplication causes nuclear enlargement and reshaping.

Microtubule plus-end-tracking proteins are mostly conserved proteins throughout eukaryotes (Jiang and Akhmanova, 2011). They regulate MT plus-end dynamics (Bisgrove et al., 2004; Hamada, 2007; Akhmanova and Steinmetz, 2008). Proteins from End-binding 1 (EB1) family were first identified as +TIPs in plants and are highly conserved both evolutionary and structurally throughout kingdoms (Chan et al., 2003; Mathur et al., 2003; Bisgrove et al., 2008). Significant influence of the microtubule plus-end dynamics refers them as key players in the cell expansion and cell division (Tirnauer et al., 2002a,b; Draviam et al., 2006; Akhmanova and Steinmetz, 2008). They are composed of N-terminal microtubule-interacting calponin-homology (CH) domain and C-terminal EB1 unique homology domain which mediates EB1 protein dimerization and interaction with other proteins (Komarova et al., 2009). The *Arabidopsis* genome encodes for three EB1 isoforms (Bisgrove et al., 2008), EB1a (At3g47690), EB1b (At5g62500), and EB1c (At5g67270). EB1a and EB1b share 78% aminoacid identity and they are typical members of microtubule plus-end-tracking proteins. Fused with GFP protein, EB1a and EB1b distinctly decorate the plus end of cortical and mitotic microtubules (Chan et al., 2003; Mathur et al., 2003). In contrast, EB1c shows different localization and seems to have different functions (Bisgrove et al., 2008; Komaki et al., 2010). It shares only 49% aminoacid identity with EB1a and EB1b and it is considered to be plant-specific (Bisgrove et al., 2008). Its aminoacid sequence differs remarkably at its C-terminal part. EB1a and b possess acidic aminoacid residues in the C terminal region, while C terminal part of EB1c contains basic residues encompassing a nuclear localization sequence. This is consistent with the nuclear localization of EB1c in interphase and post-cytokinetic cells (Komaki et al., 2010). Furthermore, the primary sequence of EB1c, unlike EB1a and EB1b, contains five unique SP motifs and one D-domain motif suggesting its targeting by protein kinases implicated in the cell cycle including cyclin-dependent kinases and mitogen-activated protein kinases (MAPKs) (Samajova et al., 2013). In animal kingdom, proteins from EB1 family were shown to be regulated by phosphorylation (Tamura and Draviam, 2012). A putative interaction between EB1c and MAPKs was recently shown also in plants (Kohoutová et al., 2015). All plant EB1 proteins decorate mitotic microtubules (Chan et al., 2003; Dixit et al., 2006), however, solely EB1c becomes actively transported to the nucleus at the end of cytokinesis (Bisgrove et al., 2008; Komaki et al., 2010). Single *eb1c* mutants showed collapsed spindles and fragmented phragmoplasts (Komaki et al., 2010) and they exhibited hypersensitivity to microtubule-disrupting drugs (Bisgrove et al., 2008).

Since EB1 proteins are typical microtubule plus-end-tracking proteins, all previous studies were focused on the possible function of EB1c during the cell division where EB1c decorates mitotic microtubules (Bisgrove et al., 2008; Komaki et al., 2010; Ho et al., 2011). However, accumulation of EB1c in the mitotic interphase and post-mitotic nuclei was undermined. Consequently, we extend the localization studies of EB1c protein to demonstrate its occurrence and accumulation in the nuclei of non-dividing mitotic cells but especially in cells of post-mitotic transition and elongation root zones. Moreover, we present the first quantitative study of EB1c nuclear content in non-dividing and post-mitotic cells of different root tissues at different developmental root zones with special emphasis on transition zone.

Most of the studies which dissected root anatomy and its developmental establishment so far were based on roots growing on the interface of solidified nutrient media under conditions of uniform seedling illumination (e.g., Ruzicka et al., 2009; Sliwinska et al., 2012) and only few studies elaborated root architecture and subcellular organization of soil grown roots

(e.g., Panteris et al., 2013). Moreover, the microscopic elucidation of root cellular and tissue architecture was vastly established with microscopes equipped with horizontal working stages and spherical aberration-limited working distances (Petricka et al., 2012). Therefore, experimental conditions which documented root development in the laboratory setup have been largely deviating from the natural environment. For this reason we employed light-sheet microscopy as an excellent tool for near-physiological, live cell imaging in long-term with the potential to study dynamic developmental processes using firmly established protocol for sample preparation and imaging (Maizel et al., 2011; Sena et al., 2011; Ovecka et al., 2015). With the setup of the light-sheet microscope used herein it is possible: (a) to mount seedlings vertically allowing the root to grow along the gravity vector, (b) to achieve minimal illumination of the root as happens under natural conditions, and (c) to grow root embedded in solid medium closely resembling conditions in the soil.

From the technical point of view, the light-sheet microscope allows minimal exposure of roots carrying GFP-tagged proteins to phototoxic irradiation while importantly provides the means for fast and adequate resolution in the three spatial dimensions (Maizel et al., 2011; Ovecka et al., 2015). This is made possible by the low excitation laser powers and the relatively high numerical aperture objectives used for excitation of the sample and acquisition of the image (Ovecka et al., 2015).

The purpose of the present study is to follow the developmental correlation between nuclear levels of EB1c and the organization of the root of *Arabidopsis thaliana* in distinct zones and cell files. We did so in living plants which were imaged under minimally invasive light-sheet microscopy. Thus, we were able to address and quantify nuclear localization of EB1c in meristematic, transition and elongation zones and we extend the observations to three important root tissue layers in all zones: the epidermis, the cortex and the endodermis, correlating nuclear size with EB1c expression levels.

MATERIALS AND METHODS

Molecular Methods

Genomic DNA isolated from fresh leaves of 7-days-old *Arabidopsis thaliana* (L.) Heynh. (ecotype Columbia) seedlings was used for amplification of the complete coding region of *EB1c* gene together with its upstream promoter region. *EB1c* promoter region was identified according to previously published data (Komaki et al., 2010) and designed using *Arabidopsis* Sequence Viewer (http://arabidopsis.org). The promoter sequence *pEB1c* was suggested to comprise of 663 base pairs upstream of the start codon of the *EB1c* gene. For the cloning, we used Gateway® technology. Primers were designed according to manufacturer's instructions. Whole genomic fragment was recombined into pDONR207 Gateway® vector and subsequently transferred by LR recombination reaction into the Gateway® destination vector pGWB450 designed for C-terminal GFP fusion with kanamycin resistance for plant selection. All recombinations were confirmed by sequencing. Expression vector pGWB450::pEB1c::EB1c:GFP was transformed into *Agrobacterium tumefaciens*, strain GV3101. Transformed Agrobacteria were used for several independent transformations of *Arabidopsis* plants (Clough and Bent, 1998; Davis et al., 2009). Seedlings were selected on kanamycin (50 mg/ml) selection medium to identify T1 transgenic plants. T1 transformants carrying pEB1c::EB1c:GFP constructs were checked for phenotype in comparison to control plants. No phenotypes were discerned and thus the T2 generation of *Arabidopsis* plants expressing pGWB450::pEB1c::EB1c:GFP was harvested and used for further experiments.

Protein Extraction, SDS-PAGE and Immunoblotting

Twelve-days old *Arabidopsis* plants expressing EB1c-GFP were analyzed on fluorescent stereomicroscope Leica MZ FLIII (Leica Microsystems, Germany) for EB1c-GFP signal. Protein extraction was carried out from roots of plants expressing EB1c-GFP and from wild type *Arabidopsis thaliana* (L.) Heynh. (ecotype Columbia). Roots were harvested, weighted, flesh frozen and immediately ground in the liquid nitrogen. Powder was extracted in extraction buffer (1:1, w/v) (50 mM Na-HEPES pH 7.5, 150 mM NaCl, 1 mM $MgCl_2.6H_2O$, 1 mM EGTA, 1 mM DTT, 1 mM NaF) supplemented with protease inhibitors Complete (Roche, Germany) and phosphatase inhibitors PhosStop (Roche, Germany). Crude extract was centrifuged 10 min, 8000 g at 4°C. Resulting supernatant was used for SDS-PAGE and subsequent western blot analysis. 15 µg of total protein was loaded on 8% SDS-PAGE gels followed by immunoblotting with PVDF membrane and Western blotted with antibody against GFP (anti GFP rabbit ABCAM AB290) in dilution of 1:2000. Secondary antibody (goat anti-rabbit, Santa Cruz Biotechnology) was used in dilution of 1:5000. After incubation in ECL reagents (according to manufacturer instructions), immunoreactive bands were documented using the BioRad ChemiDoc™ MP System.

Plant Material and Sample Preparation for Light-Sheet Imaging

Seeds of *Arabidopsis thaliana* (L.) Heynh. (ecotype Columbia) transgenic line expressing *pEB1::cEB1c:GFP* were surface sterilized, plated onto solidified ½ MS medium and kept in 4°C for 4 days. After this period seeds were transferred to round 90 × 25 mm Petri dishes filled with 80 ml of ½MS medium solidified with 0.6% w/v Phytagel, and placed into small depressions facilitating gravitropic root growth inside solidified culture medium. Plates were cultivated in culture chamber horizontally for 2 days at 22°C, 50% humidity, 16/8-h light/dark cycle. After germination of seedlings when they were 1-days-old, they were enclosed by fluorinated ethylene propylene (FEP) tube with an inner diameter of 1.1 mm and wall thickness of 0.2 mm (Wolf-Technik, Germany). FEP tubes were carefully inserted into culture medium to enclose individual seedling inside. After 24 h seedlings in FEP tubes were removed from the plate, transferred to the microscope and prepared for imaging according to established protocol (Ovecka et al., 2015). Seedlings in FEP tubes were prepared according to an "open system," where root is growing in the original Phytagel-solidified culture medium in the lower part of FEP tube and shoot is growing in the

upper aerated part of the FEP tube. This approach provides green parts of seedlings with continuous access to oxygen and allows growth and development of roots and shoots in the microscope chamber during long-term imaging experiments (Ovecka et al., 2015). All experiments and measurements were done on 2-days old seedlings.

Light-Sheet Microscopy

Developmental live cell imaging was done with the light-sheet Z.1 fluorescence microscope (Carl Zeiss, Germany), equipped with W Plan-Apochromat 20×/1.0 NA water immersion detection objective (Carl Zeiss, Germany) and LSFM 10x/0.2 NA illumination objective (Carl Zeiss, Germany). Seedlings were imaged using dual-side illumination by a light-sheet modulated into a pivot scan mode, with excitation laser line 488 nm and with emission filter BP505-545. Image acquisition was done every 2 min in Z-stack mode for a time period of 2–5 h. Scaling of images in x, y, and z dimensions was 0.228 × 0.228 × 0.477 μm. To prevent the movement of the growing root apex out of the field of view, images were acquired in two subsequent views coordinated to each other in y coordinate. Images were recorded with the PCO.Edge sCMOS camera (PCO AG, Germany) with the exposure time 25 ms.

Measurements, Statistical Analyses, and *in silico* Predictions

From images of the whole root acquired using Zen 2014 software (Carl Zeiss, Germany) subsets of data were created, with defined x−, y−, and z− dimensions comprising whole volume of several nuclei from one particular cell file. Several subsets were created in order to segment nuclei of all cells of particular cell file in ordered positions from the stem cells surrounding quiescence center of the root up to visible cell differentiation at the end of elongation zone. All subsets were transformed to 2D images using Maximum intensity projection function of the Zen 2014 software. In all images uniform correction of brightness and contrast was done before they were exported for image analysis. All quantitative data were produced with publicly available software CellProfiler 2.1.1 (http://www.cellprofiler.org; Carpenter et al., 2006; Lamprecht et al., 2007). Nuclear area from 2D images that represent surface projection of the nuclear volume (referred herein as nuclear surface area) was measured as the actual number of pixels in the manually defined region multiplied by the pixel area. Mean intensity values were calculated as the average pixel intensity in the defined region, integrated intensity values were calculated as the total pixel intensity in the defined region. Values were subsequently normalized to a 0–1 range using the following formula: $x_N = (x_i - x_{min})/x_{max} - x_{min}$ (where x_N = normalized intensity, x_i = absolute intensity, x_{min} = minimum absolute intensity and x_{max} = maximum absolute intensity). Thus, all biological variables within measured root tips were brought into the comparable proportions and plant—to—plant differences in the expression of EB1c-GFP were compensated. Data from 4 individual cell files were collected and evaluated separately for epidermis, cortex and endodermis from two independent experiments (two independent roots). Final statistical data evaluation and plot production was done with Microsoft Excel software.

Prediction of putative nuclear export sequences was performed using the NetNES 1.1 server with the accession numbers of the three *Arabidopsis thaliana* EB1 isoforms (EB1a, AT3G47690; EB1b, AT5G62500; and EB1c, AT5G67270) (la Cour et al., 2004). For protein domain structure illustration, DOG 1.0 illustrator was used (Ren et al., 2009).

RESULTS

We studied the *in vivo* subcellular nuclear localization of the EB1c protein during root development in stably transformed *Arabidopsis thaliana* plants. Beside the already published presence of nuclear localization sequence in EB1c protein sequence (Komaki et al., 2010), our *in silico* search using NetNES 1.1 prediction server (la Cour et al., 2004) revealed the occurrence of putative nuclear export signals at positions 213L, 215I, 217S, and 218L for EB1c (**Supplementary Figure 1**). At the same respect, we compared the other EB1 family members in *Arabidopsis*, EB1a and EB1b. NES was not predicted for EB1b, while for EB1a, there is one prediction at position 193I albeit with a low score over the threshold. We prepared *EB1c:GFP* construct driven by its own promoter. The 663 bp long promoter sequence and the complete coding region of *EB1c* gene were cloned using Gateway® technology into the binary vector and subsequently transformed into *A. thaliana* plants (ecotype Col-0) while T2 generation of plants was used for experiments. To prove the expression of EB1c-GFP fusion protein in the plants, we performed SDS-PAGE with subsequent Western-blot analysis using seedlings expressing EB1c-GFP and Col-0 as a negative control (**Figure 1A**). EB1c-GFP protein signal was clearly detected using anti-GFP antibody at the molecular mass corresponding to 64 kDa which is the predicted size of the fusion protein. As negative controls, we used extracts from untransformed wild-type plants as well as extracts from plants expressing EB1c-GFP treated only with secondary antibody (**Figure 1A**).

Root growth and development require passage of root cells through successive developmental zones. Large extend of this process from spatial and temporal point of view requires special microscopic applications for effective live cell imaging. Developmental light-sheet microscopy overcomes these limitations and allows real-time or time-lapse imaging of whole developing seedlings (Ovecka et al., 2015). We performed live cell imaging with seedlings growing over a period between 2 and 5 h inside the light-sheet microscope. EB1c-GFP was localized in nuclei of all non-dividing root cells within the root apex, with particularly strong expression level in cells of the root meristematic zone (**Figure 1B**). General overview of EB1c-GFP expressing roots revealed zonation of the root apex into different cell developmental zones, namely into meristematic, transition, elongation, and differentiation zones (**Figure 1B**). Seedlings were prepared and cultivated in cylinders of Phytagel-solidified culture medium. During imaging over a range of several hours, seedlings exhibited undisturbed continuous root growth inside of the microscope (**Figure 1C**, **Supplementary Movie 1**). Average root

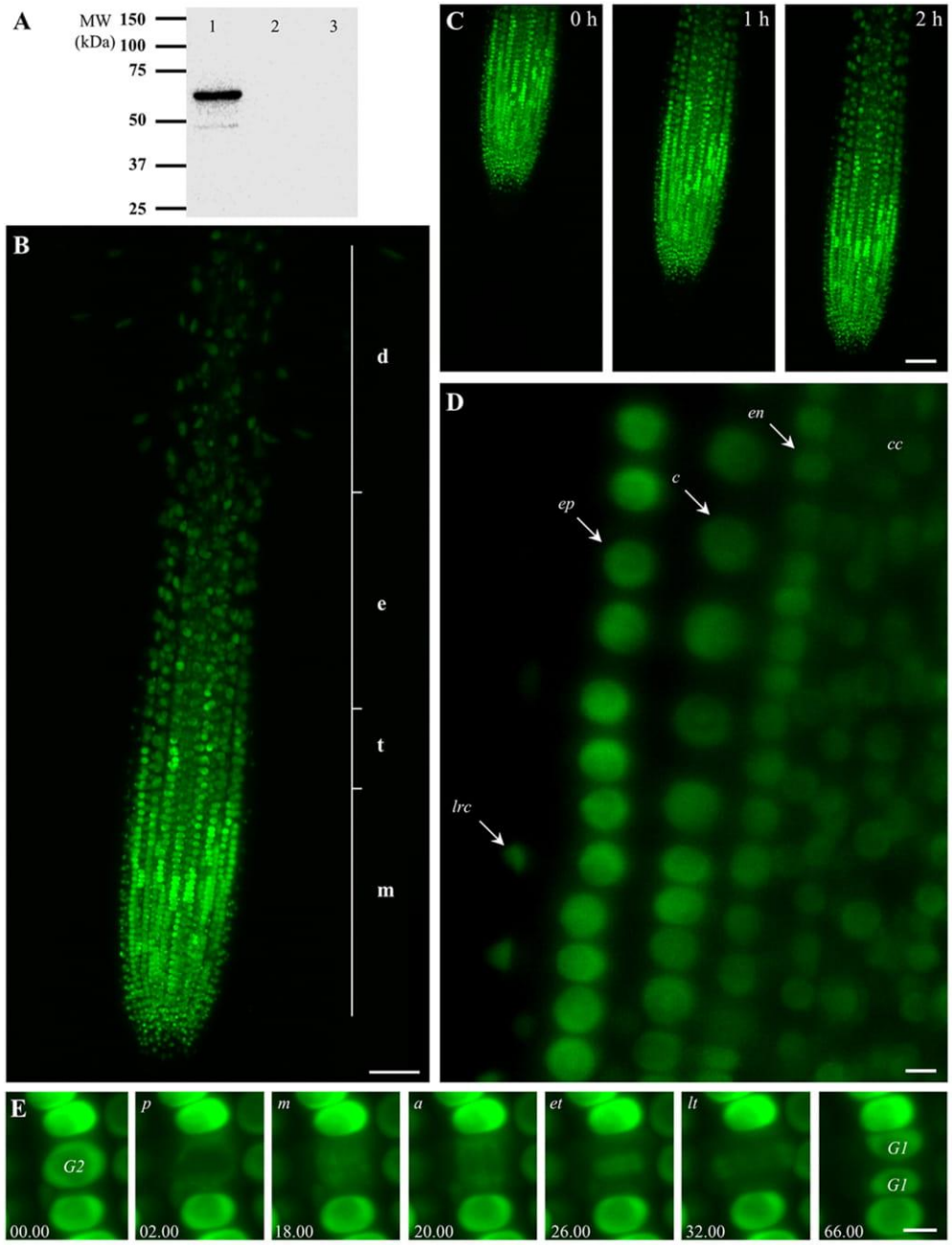

FIGURE 1 | Characterization of transgenic *Arabidopsis thaliana* plants expressing EB1c-GFP driven by EB1c own promoter and localization of EB1c-GFP. (A) SDS-PAGE followed by western blot analysis using anti-GFP antibody from protein extract of *A. thaliana* T2 plants expressing EB1c-GFP (lane 1), protein extract from untransformed Col-0 plants (lane 2), and protein extract from *Arabidopsis* plants expressing EB1c-GFP immunoblotted only with secondary antibody (lane 3). **(B)** General overview of the root tip of 2-days old *A. thaliana* seedling expressing EB1c-GFP. Average root zonation into individual cell developmental zones consisting meristematic zone (m), transition zone (t), elongation zone (e), and differentiation zone (d) is depicted. EB1c-GFP was localized in nuclei of root cells, with particularly strong expression level in cells of the root meristematic zone. **(C)** Live cell imaging of seedling growing inside of the light-sheet microscope over the period of 2 h. **(D)** Localization of EB1c-GFP by light-sheet microscopy in cells of individual root tissue layers, in epidermis (arrow, ep), cortex (arrow, c), endodermis (arrow, en), central cylinder (arrow, cc), and lateral root cap cells (arrow, lrc). In all imaged tissues, light-sheet microscopy revealed clearly nuclear localization of EB1c-GFP in root cells. **(E)** Localization of EB1c-GFP by light-sheet microscopy during mitotic cell division of root cells in the meristematic zone. EB1c-GFP relocated from G2 stage nuclei to spindle in prophase (p), metaphase (m), and anaphase (a), to phragmoplast at early and late telophase (et, lt), and redistributed back to reconstructed G1 stage nuclei after cell division. Time progression of the cell division is indicated in min. Scale bar = 50 μm in **(B,C)** and 5 μm in **(D,E)**.

growth rate of 2-days old seedlings expressing EB1c-GFP in the light-sheet microscope was 1.686 ($\pm$ 0.721) μm.min^{-1} ($\pm$SD, $n = 6$).

Light-sheet microscopy, in addition to time-lapse imaging of the entire root development, allowed localization of EB1c-GFP at the cellular and subcellular levels. At the level of cellular resolution, this method was suitable for visualization not only surface cells and tissues of the root, like lateral root cap cells and epidermis, but further allowed visualization of individual cells from inner tissues of the *Arabidopsis* root including the cortex, the endodermis and the central cylinder. In all imaged tissues, light-sheet microscopy revealed clearly nuclear localization of EB1c-GFP in root cells (**Figure 1D**). Subcellular resolution of the light-sheet microscopy was documented during mitotic cell division of root cells in the meristematic zone, where EB1c-GFP relocated from G2 stage nuclei to mitotic spindles and cytokinetic phragmoplasts during the respective cell division stages and finally was redistributed back to reconstituted G1 stage nuclei after completing cell division (**Figure 1E**).

The longitudinal developmental zonation of the root apex of plants expressing EB1c-GFP fusion protein into different developmental zones was determined in individual cell files of epidermis (**Figures 2A–D**, arrows in B and C denote the first cell of each consecutive zone), cortex (**Figures 2E–H**, arrows in F and G denote the first cell of each consecutive zone) and endodermis (**Figures 2I–L**, arrows in J and K denote the first cell of each consecutive zone). The cell arrangement in the meristematic zone of the epidermis was influenced by frequent cell divisions rather than by cell elongation (along longitudinal root axis). This leads to generation of tightly-packed wide but very short cells, with compressed nuclei (**Figure 2A**). Very similar cell and nuclear shapes were observed within the meristematic zone in the cortex layer (**Figure 2E**). In the endodermis nuclei of cells in the meristematic zone appeared smaller and due to different ratio between cell width and cell height their shape was not deformed to the same extent as in the epidermis and the cortex (c.f. **Figures 2A,E,I**). With termination of the mitotic activity in the meristematic zone, cell sizes, and shapes were changing. At the end of the meristematic zone, nuclei became round and larger in all three layers (**Figures 2B,F,J**). Before starting rapid cell elongation, however, there was a population of cells with short length, as indicated by short and similar distance between nuclei of individual cells (**Figures 2B,F,J**). In addition, they showed reduction in the EB1c-GFP fluorescence intensity. Based on these characteristics, an onset of the transition zone placed before rapid cell elongation could be identified in each cell file of epidermis (**Figure 2B**), cortex (**Figure 2F**), and endodermis (**Figure 2J**). Cells from the transition zone of each tissue layer entered subsequently cell elongation zone, which was indicated by further changes in the nucleus size, EB1c-GFP fluorescence intensity and apparent dilatation of distances between neighbor nuclei within the cell files (**Figures 2C,G,K**). Rapid cell elongation was connected with apparent enlargement of nuclei in epidermis (**Figure 2D**) and cortex (**Figure 2H**), changes in nuclear shape in all three tissue layers (**Figures 2D,H,L**) and further reduction in EB1c-GFP fluorescence intensity.

To characterize the distribution of EB1c-GFP in the apex of *Arabidopsis* root in detail, we quantified the intensity of EB1c-GFP nuclear fluorescence in the previously defined root cell developmental zones (meristem, transition zone, elongation zone and differentiation zone). The quantitative evaluation of the EB1c-GFP protein content in interphase nuclei of root cells was performed in light-sheet images acquired in 4D modes (encompassing x, y, z, and t dimensions). In individual cell files of the epidermis, the cortex and the endodermis all interphase nuclei in order were taken into account, starting from the stem cell niche region and progressing up to cell elongation before cells reached the zone of cell differentiation (i.e., as evidenced by root hair emergence in the root epidermis). In each cell file, the meristem—to—transition zone border (**Figures 2B,F,J**) and the transition zone—to—elongation zone border (**Figures 2C,G,K**) were identified. Parameters for identification of particular borders and range of individual cell developmental zones included the spatial extent of the cell division, size, and fluorescence intensity reference values from nuclei of cells in G1 and G2 stages, increase in the nuclear size after termination of the cell division, and increase in the distance between nuclei of individual cells in the elongation zone. Thus, all cells in each cell file were topologically divided into meristematic zone, transition zone, and elongation zone (**Figure 1B**).

Values of nuclear surface area and EB1c-GFP mean signal intensity for quantitative evaluation were plotted against cell position counted from the stem cells surrounding quiescence center. Both parameters were measured and evaluated separately for the epidermis, the cortex and the endodermis. We found that in all tissues, as cells proceeded from proliferation to the differentiation, the nuclear surface area increased while fluorescence intensity of EB1c-GFP signal decreased. This trend was apparent from quantification of individual cell files of the epidermis (**Figure 3A**), the cortex (**Figure 3B**) and the endodermis (**Figure 3C**). In the meristematic zone, actively dividing cells contained the smallest nuclei exhibiting the highest EB1c-GFP content. In the transition zone, the mean nuclear fluorescence intensity of EB1c-GFP was steeply decreased. This decline in EB1c-GFP fluorescence intensity continued in the elongation zone while the nuclear area progressively increased (**Figure 3**). Cross-correlation of nuclear EB1c-GFP mean signal intensity of some individual nuclei with their size and shape at certain position within the cell file revealed negative correlation between nuclear size and mean EB1c-GFP signal intensity in the meristematic zone (numbered insets in **Figures 3A–C**). This negative correlation trend was stabilized in the transition zone and the elongation zone of all measured cell files in all evaluated tissue layers (**Figure 3**) as evidenced by the continuous decrease in EB1c-GFP fluorescence intensity with the progressive increase in nuclear size.

Further, we quantified collectively measured data from several individual cell files of two independent roots. Data were evaluated separately for epidermis, cortex, and endodermis. Quantitative evaluation of nuclear surface area values revealed rather stable distribution of this parameter in the meristematic zone of the epidermis. It increased slightly only in meristematic cells at gradually increasing distances from the stem cell region,

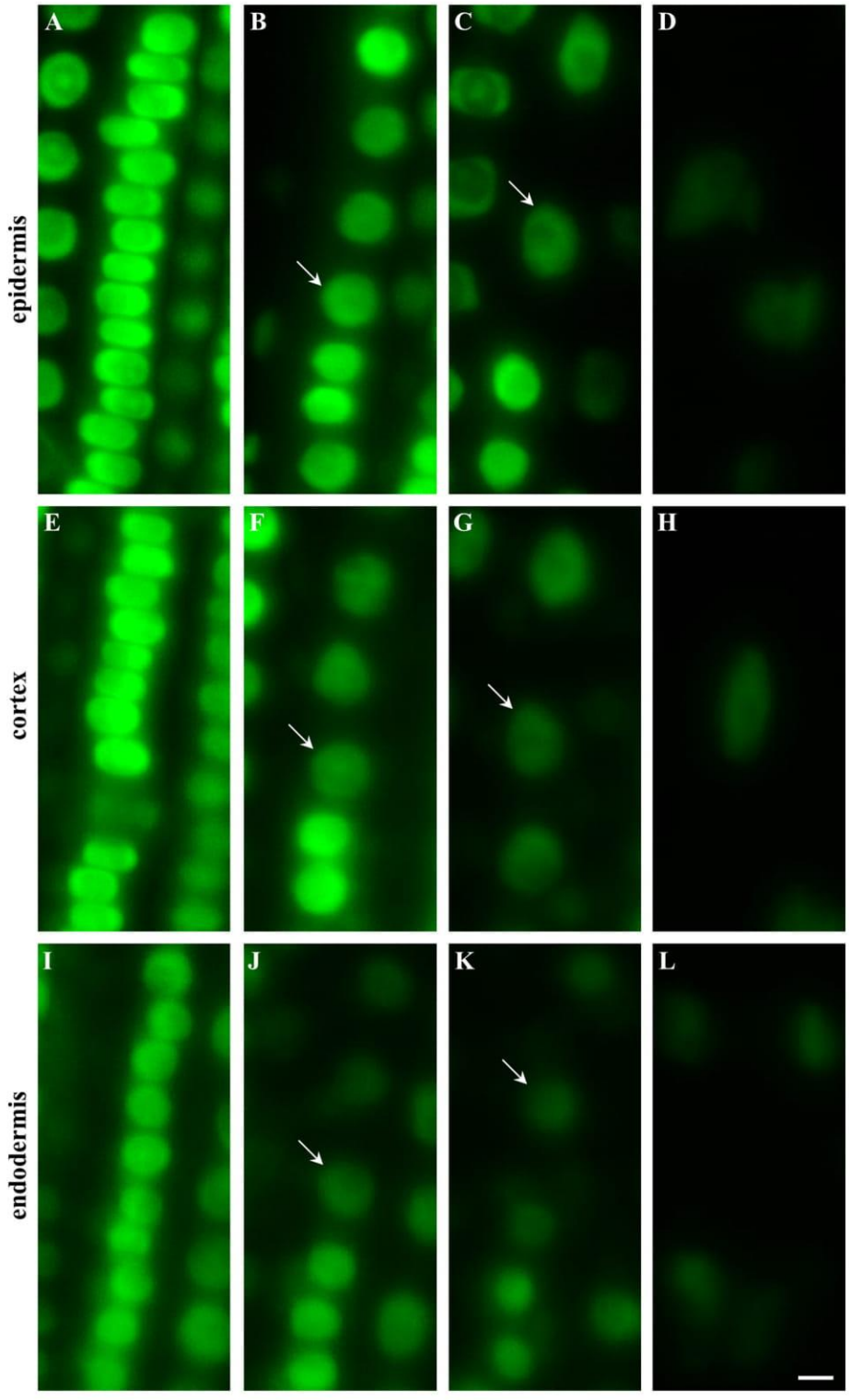

FIGURE 2 | Shoot-ward developmental zonation in the root apex of transgenic *Arabidopsis thaliana* plants expressing EB1c-GFP protein. Cell arrangement and position were assessed in individual cell files of epidermis **(A–D)**, cortex **(E–H)** and endodermis **(I–L)**. Typical appearance of cells in each tissue layer with nuclear localization of EB1c-GFP is shown for meristematic zone **(A,E,I)**, at the meristem-transition zone border **(B,F,J)**, at the transition zone-elongation zone border **(C,G,K)** and within the elongation zone **(D,H,L)**. Arrows define nuclei of first cell within the transition zone **(B,F,J)** and first cell within the elongation zone **(C,G,K)**. Fluorescence intensity of images is presented to the scale recorded during the acquisition of each individual cell type. Scale bar = 5 μm.

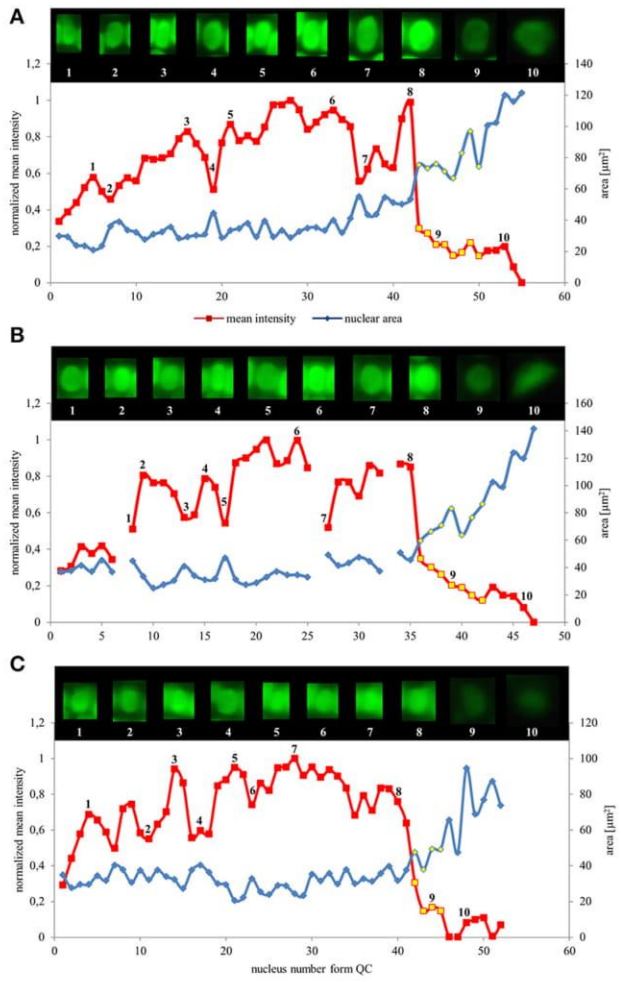

FIGURE 3 | Nuclear surface area and nuclear EB1c-GFP mean signal intensity distribution in root developmental zones of the root apex in individual cell files. Relationship between nuclear area (blue line) and nuclear EB1c-GFP mean signal intensity (red line) in respect to cell position counted from the stem cells surrounding quiescent center in individual cell file of epidermis **(A)**, cortex **(B)**, and endodermis **(C)**. Values for nuclei in the transition zone are highlighted by yellow points, which allow distinguishing also meristematic zone (appearing before the transition zone) and elongation zone (appearing after the transition zone). Inset images over the lines show individual nuclei of cells at the actual position, documenting changes in nuclear shape, size, and mean EB1c-GFP fluorescence intensity. Major vertical axis (on the left) represents the values for the normalized mean intensity and minor vertical axis (on the right) represents values for area measurements. Horizontal axis represents the actual cell position counted from the stem cells surrounding quiescent center. Data are shown for one representative cell file from each tissue layer. Interruptions of the curve in the cortex **(B)** are caused by presence of dividing cells within the file.

surpassing slightly even the average reference value for the size of G2 nuclei (**Figure 4A**). Further recognizable increase in the nucleus size took place within the transition zone, and dramatic increase in the elongation zone of epidermis (**Figure 4A**). Mean fluorescence intensity of EB1c-GFP in interphase nuclei of epidermis fluctuated considerably; however, it was high in the meristematic cells. In nuclei of cells entering the transition zone mean fluorescence intensity of EB1c-GFP dropped considerably and in nuclei of elongating cells this drop in mean fluorescence intensity was dramatic, reflecting the inversely proportional increase in the nucleus size (**Figure 4A**).

A similar tendency of stable nuclear size in the meristematic zone, a gradual increase in the transition zone and a considerable increase in the elongation zone was recorded also in cell files of the cortex layer (**Figure 4B**). Nuclear size in the meristematic zone did not exceed the reference value for the size of G2 nuclei (**Figure 4B**). Mean fluorescence intensity of EB1c-GFP in interphase nuclei of cortex cells was highest in the meristematic zone. However, it decreased dramatically in the transition zone, keeping further decreasing in the elongation zone as well (**Figure 4B**).

Size of nuclei of endodermal cells in the meristematic zone was constant, not exceeding the reference value of size measured for G2 nuclei, showing increase only after passage of meristematic cells into the transition zone. Size distribution of nuclei in the transition zone and the elongation zone of endodermis was wider as in cortex and epidermis, but the general tendency of gradual nuclear size increase from meristem through transition zone to elongation zone was maintained also in endodermis (**Figure 4C**).

Quantitative comparison of nuclear surface area and nuclear EB1c-GFP mean signal intensity in cell developmental zones of the root apex thus showed that the expression of EB1c-GFP decreased along the longitudinal axis of the root apex in all three measured tissue layers. Highest intensity was measured in the meristematic zone where cells are actively dividing, while in the transition zone and further in the elongation zone, expression levels of EB1c-GFP decreased inversely in relation to the nuclear area which progressively increased before entering the differentiation zone.

Reference values for comparison of nuclear surface area and nuclear EB1c-GFP mean signal intensity in all types of measured cells from the root apex were recorded from typical cells of the root meristematic zone, which were present in G1 and G2 stages of mitotic cell division. For safe identification of nuclei in G1 and G2 stages, we took advantage of long-term time-lapse imaging of growing root apex in the light-sheet microscope. Using play-back function we identified and picked cells just before mitotic division and marked them as G2 cells. Daughter cells derived from mitotic division of these cells were marked as G1 cells (**Figure 1E**). We compared obtained average values of G1 and G2 nuclei with average values of all measured nuclei from non-dividing cells of meristematic zone, and all cells of transition and elongation zones for nuclear surface area (**Figure 5A**) and nuclear EB1c-GFP mean signal intensity (**Figure 5B**). This comparison was done separately for epidermis, cortex and endodermis. Average values of nuclear surface area of meristematic cells corresponded well with reference values from G1 and G2 nuclei. Most importantly, the average size of nuclei in the meristematic zone did not exceed the size of G2 nuclei (**Figure 5A**). Size of nuclei in transition zone as well as in elongation zone was significantly higher. Significant differences in size of nuclei were also observed between transition zone and elongation zone (**Figures 5A,C**). Similarly, average values of nuclear EB1c-GFP mean signal intensity of meristematic

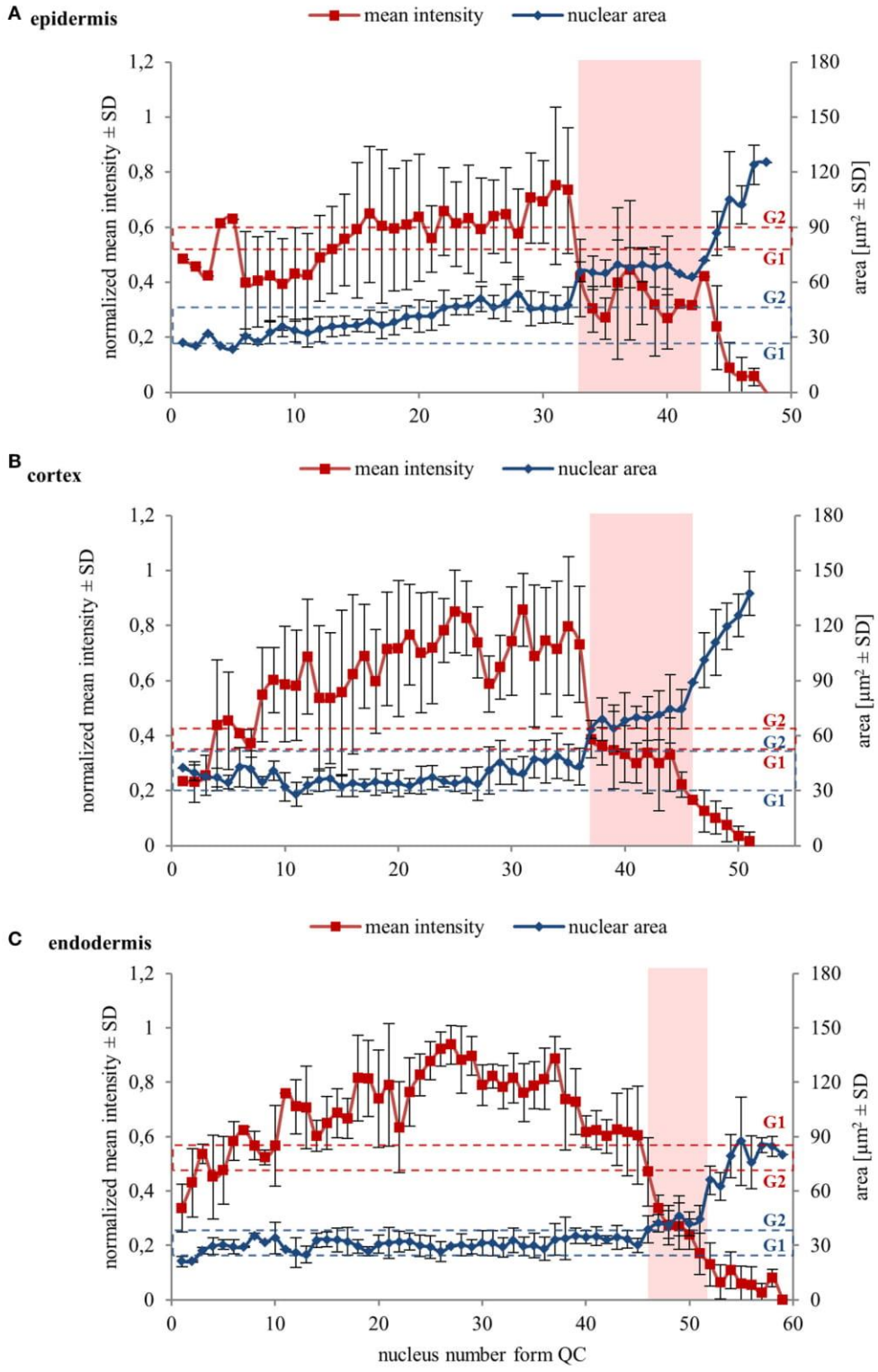

FIGURE 4 | Nuclear surface area and nuclear EB1c-GFP mean signal intensity in cells of different tissues along diverse developmental root zones. Average values of nuclear surface area (blue line) and EB1c-GFP mean signal intensity (red line) plotted against cell position counted from the stem cells surrounding quiescence center. Data from 4 individual cell files were collected and evaluated separately for epidermis **(A)**, cortex **(B)**, and endodermis **(C)** from two independent roots. The transition zone is highlighted in pink color. Dashed red lines for average mean intensity and dashed blue lines for average nuclear area of G1 and G2 nuclei are indicated as reference values. Major vertical axis (on the left) represents the values for the normalized mean intensity and minor vertical axis (on the right) represents values for area measurements. Horizontal axis represents the actual cell position counted from the stem cells surrounding quiescence center. Because number of cells in cell files is not the same, data from individual cell files in average graphs were aligned according to their meristem-to-transition zone borders.

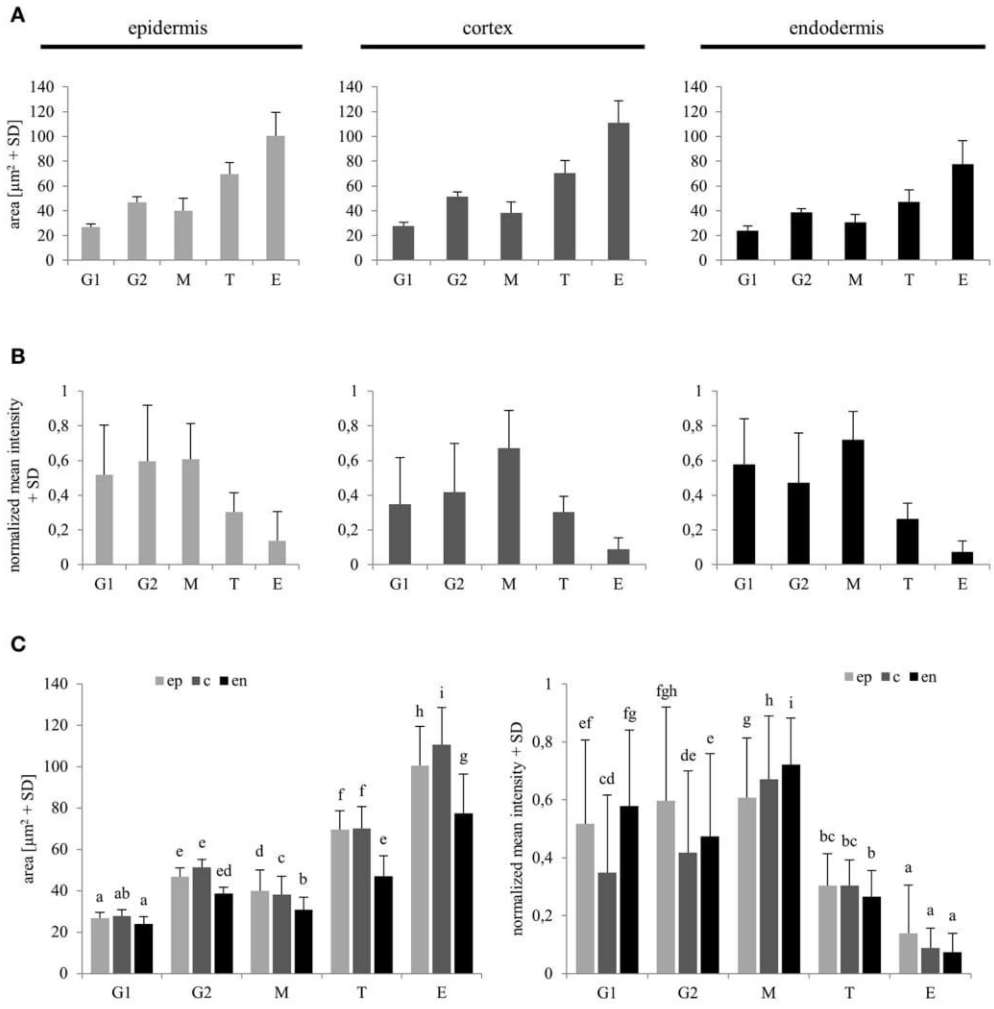

FIGURE 5 | Reference values of nuclear area and nuclear EB1c-GFP mean signal intensity in G1 and G2 stage meristematic cells as compared to post-meristematic cells. Average nuclear surface area **(A)** and average nuclear EB1c-GFP mean signal intensity **(B)** in G1 and G2 stage of cell cycle were compared with average values of the same parameters of non-dividing cells from meristem (M), transition zone (T), and elongation (E) zone in epidermis, cortex, and endodermis. Comparison of average nuclear surface area and average nuclear EB1c-GFP mean signal intensity values in individual cell developmental zones among individual tissue layers **(C)**. Different letters represent statistical significance according to One-way ANOVA test at $P < 0.05$.

cells corresponded well with reference values from G1 and G2 nuclei, and there were found significantly lower values of nuclear EB1c-GFP mean signal intensity in cells of transition zone and elongation zone in comparison to cells of meristematic zone and reference G1 and G2 nuclei (**Figures 5B,C**). From these data we can conclude that both nuclear size and EB1c-GFP fluorescence intensity showed significant differences between cells of meristematic zone, transition zone and elongation zone, and supported the correct classification of cells of the root apex into three distinct developmental zones.

From the data presented above it is apparent that there might be a high degree of correlation, positive or negative, between nuclear size and EB1c-GFP expression levels. We pursued this idea by quantitative correlation analysis plotting nuclear surface area, mean signal intensity (mean values per object area) and integrated signal intensity (sum values per object area) to clarify, whether the decrease of EB1c-GFP mean signal intensity during passage of root cells through cell developmental zones corresponds to the increase of nuclear surface area or not. This comparison was done separately for epidermal, cortical, and endodermal cells. In the meristematic zone, we observed the highest variability of the nuclear EB1c-GFP mean fluorescence signal intensity (**Figures 3**, **4**) and thus not surprisingly, this zone exhibited the lowest correlation between nuclear surface area and nuclear EB1c-GFP mean signal intensity (**Figure 6A**). Measurements from transition zone and elongation zone were better correlated with prevalent negative values indicating that the decrease of EB1c-GFP mean signal intensity in the transition zone and the elongation zone corresponded mainly to increase of nuclear surface area and not to decline of EB1c-GFP expression levels. This suggests prior regulation of EB1c protein in the meristematic zone where

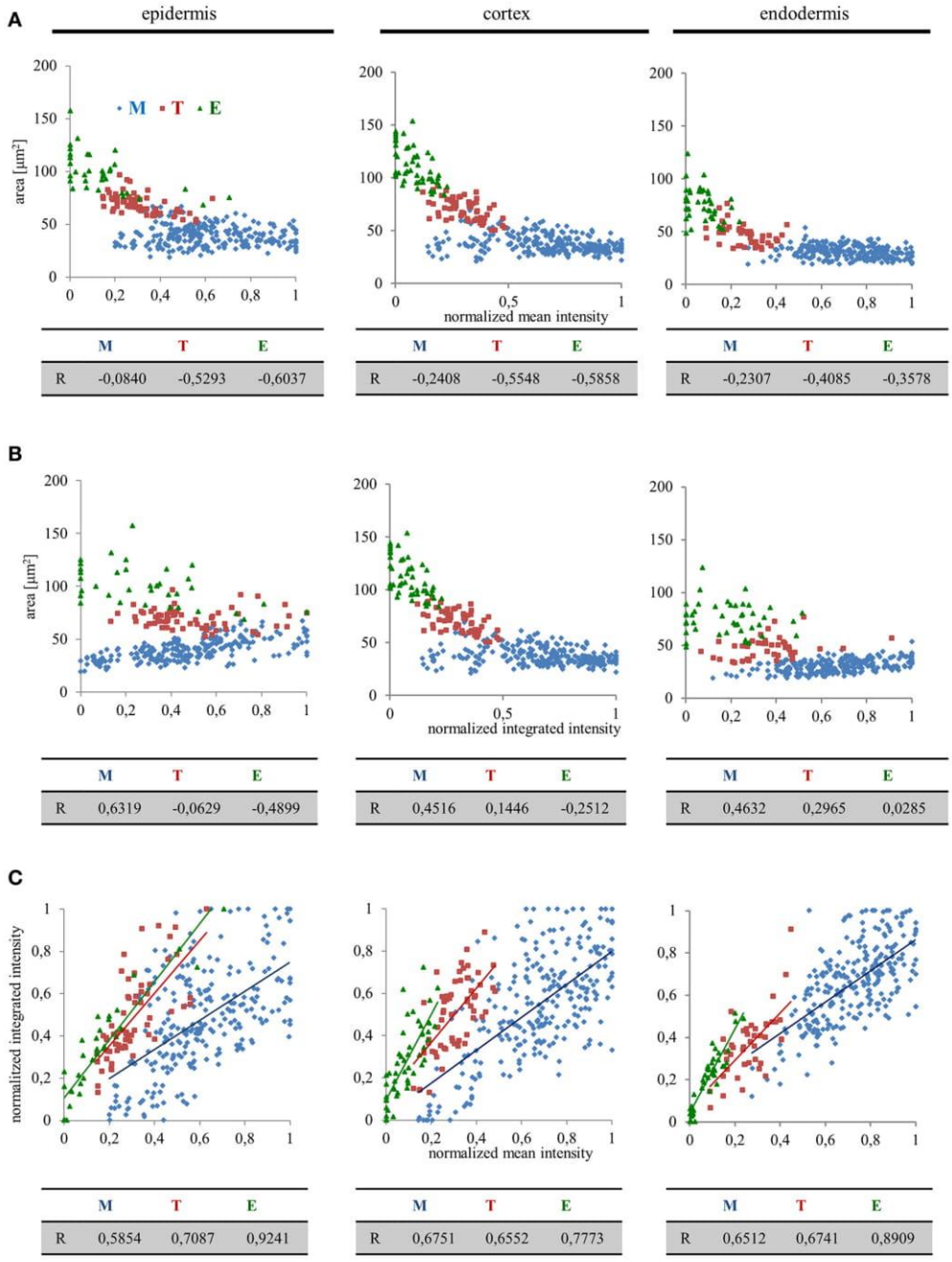

FIGURE 6 | Quantitative correlation analysis of nuclear surface area, nuclear EB1c-GFP mean signal intensity, and nuclear EB1c-GFP integrated signal intensity in diverse tissues and developmental root zones. Separate graphs presenting correlation between nuclear surface area and nuclear EB1c-GFP mean signal intensity **(A)**, nuclear surface area and nuclear EB1c-GFP integrated signal intensity **(B)**, and nuclear EB1c-GFP mean signal intensity and nuclear EB1c-GFP integrated signal intensity **(C)**. Data from 4 individual cell files were collected and evaluated separately for epidermis, cortex and endodermis from two independent roots. Data are plotted separately for meristem (M, blue dots), transition zone (T, red dots), and elongation zone (E, green dots). Pearson's correlation coefficients (R) are shown for each individual cell developmental zone of the root apex.

cells are actively dividing. Most importantly, values from these three cell developmental zones were separated, albeit partially overlapping at their borders in the respective correlation scatter plots (**Figure 6A**). This observation proves the regular passage of cells from one developmental zone to another. Similar correlation analysis between nuclear surface area and nuclear EB1c-GFP integrated signal intensity revealed again the partial separation of measurements from meristematic zone, transition zone and elongation zone in all three measured tissue layers, although lower correlation coefficients and higher variability, especially

in epidermis and endodermis, were apparent (**Figure 6B**). The highest intensity of EB1c-GFP fluorescence signal was measured in the meristematic zone, however, it was largely fluctuating (**Figure 4**). In accordance with this fact, the correlation between nuclear EB1c-GFP mean signal intensity and nuclear EB1c-GFP integrated signal intensity was lowest in the meristematic zone (**Figure 6C**). It could reflect cell cycle-dependent regulation of EB1c in the zone of mitotically-active root cells. In the transition zone and the elongation zone expression of EB1c-GFP decreased opposite to the increased nuclear area, observation which was corroborated by the higher positive correlation coefficients for comparing nuclear EB1c-GFP mean signal intensity and nuclear EB1c-GFP integrated signal intensity (**Figure 6C**).

DISCUSSION

Development of Environmental Imaging in Light-Sheet Microscope

The growing plant root system is physically challenged in its natural soil environment. Root growth is strongly affected by the mechanical properties of the soil causing direct changes in root cell length and width compared to experimentally grown plants (Bengough et al., 2006; Panteris et al., 2013). This may also indirectly affect the shoot growth (Jin et al., 2015). Conversely, in the conventional experimental setup, seedlings are mostly cultivated on air—solid medium interface which is significantly differing from the physical properties of the soil. Such a setting may cause the misinterpretation of the results, however, these cultivation methods are widely used and therefore widely accepted. Mimicking of the soil conditions in experimental environment is a challenging task (Okamoto et al., 2008). In the light-sheet microscopic setup, the seedling root is growing embedded in a solid agarose matrix and thus root growth is challenged by the rigidity of the medium, as happens during growth in the soil.

Another advantage of the light-sheet microscope is the ability to carry out long-term experiments at near-physiological conditions allowing root recordings with minimal stress (Maizel et al., 2011; Ovecka et al., 2015). By performing live cell imaging of 2-days old *Arabidopsis* seedlings for 2–5 h inside the light-sheet microscope, we demonstrate that by using light-sheet microscopy, plants grow in healthy conditions and thus they might be studied at the subcellular level with minimal limitations. Additionally, the light-sheet setup allowed for fast and up to some extent aberration free imaging at a considerable depth of the root, providing the opportunity to quantify nuclear levels of EB1-GFP not only for epidermis, but also for cortex and endodermis.

Nuclear Localization of EB1c

EB1c, the distinct subtype from EB1 family, is specifically present in vascular plants. It contains at its unique C-terminal sequence two composite motifs that serve as nuclear localization sequence (Komaki et al., 2010). Besides, our *in silico* search showed putative nuclear export signals at positions 213L, 215I, 217S, and 218L for EB1c. These findings suggest that EB1c is not tightly enclosed in the nucleus and that it may follow a canonical routine of active nucleocytoplasmic shuttling. Thus, EB1c cytoplasmic localization during mitosis and cytokinesis might be independent to nuclear envelope breakdown. The observation of EB1c localization in nuclei of post-mitotic, non-dividing cells such as those of the transition zone and the elongation zone, suggests that it might have a nuclear function. Thus, the visualization of nuclear EB1c-GFP in cells up to the differentiation zone suggests that EB1c might not be exclusively necessary for mitotic progression but rather have a broader role.

EB1c localization and function was previously documented in dividing cells of *Arabidopsis thaliana* (Dixit et al., 2006; Bisgrove et al., 2008; Komaki et al., 2010; Ho et al., 2011). In all the above studies, EB1c was studied in the context of cell division and studies were focused on the localization of EB1c at the microtubule plus ends with special emphasis on phragmoplast.

However, the evident interphase nuclear localization and function of EB1c was not systematically addressed in these former studies. For this reason we surveyed the nuclear occurrence of EB1c not only in the interphase cells of the meristematic zone, but also in post-mitotic non-dividing cells of the root transition and elongation zones. Measuring nuclear parameters revealed clear distinction among root developmental zones and correlated them with specific patterns of EB1c accumulation in the nuclei of different tissues and in both meristematic and post-meristematic root zones. Thus, EB1c-GFP can be considered a reliable physiological nuclear marker for root developmental studies including post-meristematic cells. With the help of previously published data about longitudinal root zonation (Dello Ioio et al., 2007; Baluška and Mancuso, 2013; Panteris et al., 2013), we identified particular zones in *Arabidopsis* plants expressing EB1c-GFP. As expected, EB1c-GFP signal was present in all nuclei across the studied root zones and tissues. We thus employed correlative quantitative studies monitoring developmental fluctuations in EB1c-GFP expression levels with the trend of nuclear size increase which is observed in the shoot-ward root growth gradient. Inversely to the nuclear area increase, expression of EB1c-GFP showed root-ward trend within all tissues along the longitudinal root axis with the highest intensity peak in the meristematic zone. The highest expression level and the lowest correlation between EB1c-GFP mean intensity and nuclear surface area in the meristematic zone are in accordance to previously published data about the role of EB1c in the cell division progression. *eb1c* mutants showed defects in spindle pole alignment, chromosomal segregation and phragmoplast orientation, however, the organization of the preprophase band was not impaired (Komaki et al., 2010). Nevertheless, EB1c might have a dual function in meristematic cells, depending on its subcellular localization (one on microtubule plus ends during mitosis and another one in nuclei during interphase).

More importantly we demonstrate for the first time, an evident persistent localization of EB1c in the nuclei of post-meristematic, non-dividing root cells residing within the transition and the elongation zones. As such this is the first study using quantitative advanced light-sheet microscopy to follow nuclear changes in correlation to the nuclear accumulation of a native cytoskeletal protein (EB1c was expressed under

its native promoter) during development of the primary root. There seems to be a turning point for the expression of EB1c protein in the transition zone, where division is ceased while differentiation and endoreduplication are progressing. From this developmental point, expression of EB1c seems to be mechanistically related to increase in cell nucleus size which is carried out by endoreduplication. What exactly happens at the transition point and how switch from mitotic division to endoreduplication occurs is not well documented (del Pozo et al., 2006; Ishida et al., 2009, 2010; Adachi et al., 2011; Heyman et al., 2011; Doskocilova et al., 2013).

Our analyses highlight the nuclear localization of EB1c, opening in this way the hitherto unexplored field with several possible questions. According to its size (37 kDa) native EB1c is within the limits of passive diffusion through the nuclear pore (Brandizzi et al., 2012). However, we have never observed cytoplasmic localization of GFP-tagged EB1c in interphase cells suggesting that somehow it is tethered to the interphase nucleus. Whether this tethering is of functional significance or it serves storage purposes extends beyond the scope of the present manuscript. Nevertheless, it was of interest to see that EB1c is strongly predicted to interact with essential cell cycle check point proteins with nuclear localization during interphase. Using the STRING v10 protein interaction database (Szklarczyk et al., 2015) with a high stringency cutoff (0.9) we found putative interactors of EB1c, that include MAD2 (spindle assembly checkpoint protein with nuclear localization during interphase and kinetochore localization during mitosis; Ding et al., 2012), BUB3 (cell cycle arrest protein; Paganelli et al., 2015), and BUBR1 (checkpoint serine/threonine-protein kinase; Paganelli et al., 2015). Whether EB1c interacts with the above checkpoint proteins and/or other nuclear proteins and whether the nuclear presence of EB1c is of any functional significance are matters under investigation.

AUTHOR CONTRIBUTIONS

DN and AK cloned constructs and transformed *Arabidopsis* plants. DN made immunoblot experiment. MO and DN performed live bioimaging using light-sheet microscopy. DN, MO, and AK performed image analysis and data evaluation. JŠ designed and coordinated all experiments and also participated on data interpretation. DN, AK, MO, GK, and JŠ wrote the manuscript. All authors approved the final manuscript.

ACKNOWLEDGMENTS

This work was supported by the Czech Science Foundation (GACR) grant 14-27598P and by student project IGA PrF_2015_015.

SUPPLEMENTARY MATERIAL

The Supplementary Material for this article can be found online at: http://journal.frontiersin.org/article/10.3389/fpls.2015.01187

Supplementary Figure1 | Predictions of putative nuclear export sequences in EB1a/EB1b (A) and EB1c (B) proteins using the NetNES 1.1 server (la Cour et al., 2004). (A) Analysis of EB1a and EB1b proteins showed one putative NES at the position 193I in EB1a protein; however, the score is low over the threshold. Main domains are marked at the DOG protein model (Ren et al., 2009). **(B)** Analysis of EB1c protein showed four putative NES at the positions 213L, 215I, 217S, 218L. Main domains, D-motif and putative nuclear localization sequence are marked at the DOG protein model of EB1c. NN, neural network algorithm; HMM, Hidden Markov Model algorithm; NES score, combination of NN and HMM algorithms; CH, calponin homology domain; EBH, end binding homology domain; D, D domain (serves as a platform for interaction with MAPK).

Supplementary Movie 1 | Root growth of *Arabidopsis thaliana* seedling, expressing EB1c-GFP, observed by light-sheet microscopy. Root of 2-days old plant was recorded for a time period of 5 h. Movie was produced from time-lapse image acquisition of every 2 min and is presented in the speed of 14 fps.

REFERENCES

Adachi, S., Minamisawa, K., Okushima, Y., Inagaki, S., Yoshiyama, K., Kondou, Y., et al. (2011). Programmed induction of endoreduplication by DNA double-strand breaks in *Arabidopsis*. *Proc. Natl. Acad. Sci. U.S.A.* 108, 10004–10009. doi: 10.1073/pnas.1103584108

Akhmanova, A., and Steinmetz, M. O. (2008). Tracking the ends: a dynamic protein network controls the fate of microtubule tips. *Nat. Rev. Mol. Cell Biol.* 9, 309–322. doi: 10.1038/nrm2369

Baluška, F., Kubica, S., and Hauskrecht, M. (1990). Postmitotic' isodiametric' cell growth in the maize root apex. *Planta* 181, 269–274. doi: 10.1007/BF00195876

Baluška, F., and Mancuso, S. (2013). Root apex transition zone as oscillatory zone. *Front. Plant Sci.* 4:354. doi: 10.3389/fpls.2013.00354

Baluska, F., Vitha, S., Barlow, P. W., and Volkmann, D. (1997). Rearrangements of F-actin arrays in growing cells of intact maize root apex tissues: a major developmental switch occurs in the postmitotic transition region. *Eur. J. Cell Biol.* 72, 113–121.

Bengough, A. G., Bransby, M. F., Hans, J., McKenna, S. J., Roberts, T. J., and Valentine, T. A. (2006). Root responses to soil physical conditions; growth dynamics from field to cell. *J. Exp. Bot.* 57, 437–447. doi: 10.1093/jxb/erj003

Benková, E., and Hejatko, J. (2009). Hormone interactions at the root apical meristem. *Plant Mol. Biol.* 69, 383–396. doi: 10.1007/s11103-008-9393-6

Bisgrove, S. R., Hable, W. E., and Kropf, D. L. (2004). +TIPs and microtubule regulation. The beginning of the plus end in plants. *Plant Physiol.* 136, 3855–3863. doi: 10.1104/pp.104.051037

Bisgrove, S. R., Lee, Y. R., Liu, B., Peters, N. T., and Kropf, D. L. (2008). The microtubule plus-end binding protein EB1 functions in root responses to touch and gravity signals in *Arabidopsis*. *Plant Cell* 20, 396–410. doi: 10.1105/tpc.107.056846

Brandizzi, F., Irons, S. L., and Evans, D. E. (2012). The plant nuclear envelope: new prospects for a poorly understood structure. *New Phytol.* 163, 227–246. doi: 10.1111/j.1469-8137.2004.01118.x

Carpenter, A. E., Jones, T. R., Lamprecht, M. R., Clarke, C., Kang, I. H., Friman, O., et al. (2006). CellProfiler: image analysis software for identifying and quantifying cell phenotypes. *Genome Biol.* 7:R100. doi: 10.1186/gb-2006-7-10-r100

Chan, J., Calder, G. M., Doonan, J. H., and Lloyd, C. W. (2003). EB1 reveals mobile microtubule nucleation sites in *Arabidopsis*. *Nat. Cell Biol.* 5, 967–971. doi: 10.1038/ncb1057

Chytilova, E., Macas, J., Sliwinska, E., Rafelski, S. M., Lambert, G. M., and Galbraith, D. W. (2000). Nuclear dynamics in *Arabidopsis thaliana*. *Mol. Biol. Cell* 11, 2733–2741. doi: 10.1091/mbc.11.8.2733

Clough, S. J., and Bent, A. F. (1998). Floral dip: a simplified method for Agrobacterium-mediated transformation of *Arabidopsis thaliana*. *Plant J.* 16, 735–743. doi: 10.1046/j.1365-313x.1998.00343.x

Davis, A. M., Hall, A., Millar, A. J., Darrah, C., and Davis, S. J. (2009). Protocol: Streamlined sub-protocols for floral-dip transformation and selection of transformants in *Arabidopsis thaliana*. *Plant Methods* 5:3. doi: 10.1186/1746-4811-5-3

Dello Ioio, R., Linhares, F. S., Scacchi, E., Casamitjana-Martinez, E., Heidstra, R., Costantino, P., et al. (2007). Cytokinins determine *Arabidopsis* root-meristem size by controlling cell differentiation. *Curr. Biol.* 17, 678–682. doi: 10.1016/j.cub.2007.02.047

Dello Ioio, R., Nakamura, K., Moubayidin, L., Perilli, S., Taniguchi, M., Morita, M. T., et al. (2008). A genetic framework for the control of cell division and differentiation in the root meristem. *Science* 322, 1380–1384. doi: 10.1126/science.1164147

del Pozo, J. C., Diaz-Trivino, S., Cisneros, N., and Gutierrez, C. (2006). The balance between cell division and endoreplication depends on E2FC-DPB, transcription factors regulated by the ubiquitin-SCFSKP2A pathway in *Arabidopsis*. *Plant Cell* 18, 2224–2235. doi: 10.1105/tpc.105.039651

Ding, D., Muthuswamy, S., and Meier, I. (2012). Functional interaction between the *Arabidopsis* orthologs of spindle assembly checkpoint proteins MAD1 and MAD2 and the nucleoporin NUA. *Plant Mol. Biol.* 79, 203–216 doi: 10.1007/s11103-012-9903-4

Dixit, R., Chang, E., and Cyr, R. (2006). Establishment of polarity during organization of the acentrosomal plant cortical microtubule array. *Mol. Biol. Cell* 17, 1298–1305. doi: 10.1091/mbc.E05-09-0864

Doskocilová, A., Kohoutová, L., Volc, J., Kourová, H., Benadá, O., Chumová, J., et al. (2013). NITRILASE1 regulates the exit from proliferation, genome stability and plant development. *New Phytol.* 198, 685–698. doi: 10.1111/nph.12185

Draviam, V. M., Shapiro, I., Aldridge, B., and Sorger, P. K. (2006). Misorientation and reduced stretching of aligned sister kinetochores promote chromosome missegregation in EB1- or APC-depleted cells. *EMBO J.* 25, 2814–2827. doi: 10.1038/sj.emboj.7601168

Eleftheriou, E. P., Adamakis, I. D., Panteris, E., and Fatsiou, M. (2015). Chromium-induced ultrastructural changes and oxidative stress in roots of *Arabidopsis thaliana*. *Int. J. Mol. Sci.* 16, 15852–15871. doi: 10.3390/ijms160715852

Hamada, T. (2007). Microtubule-associated proteins in higher plants. *J. Plant Res.* 120, 79–98. doi: 10.1007/s10265-006-0057-9

Hayashi, K., Hasegawa, J., and Matsunaga, S. (2013). The boundary of the meristematic and elongation zones in roots: endoreduplication precedes rapid cell expansion. *Sci. Rep.* 3, 2723. doi: 10.1038/srep02723

Heyman, J., Van den Daele, H., De Wit, K., Boudolf, V., Berckmans, B., Verkest, A., et al. (2011). *Arabidopsis* ULTRAVIOLET-B-INSENSITIVE4 maintains cell division activity by temporal inhibition of the anaphase-promoting complex/cyclosome. *Plant Cell* 23, 4394–4410. doi: 10.1105/tpc.111.091793

Ho, C. M., Hotta, T., Guo, F., Roberson, R. W., Lee, Y. R., and Liu, B. (2011). Interaction of antiparallel microtubules in the phragmoplast is mediated by the microtubule-associated protein MAP65-3 in *Arabidopsis*. *Plant Cell* 23, 2909–2923. doi: 10.1105/tpc.110.078204

Illés, P., Schlicht, M., Pavlovkin, J., Lichtscheidl, I., Baluska, F., and Ovecka, M. (2006). Aluminium toxicity in plants: internalization of aluminium into cells of the transition zone in *Arabidopsis* root apices related to changes in plasma membrane potential, endosomal behaviour, and nitric oxide production. *J. Exp. Bot.* 57, 4201–4213. doi: 10.1093/jxb/erl197

Ishida, T., Adachi, S., Yoshimura, M., Shimizu, K., Umeda, M., and Sugimoto, K. (2010). Auxin modulates the transition from the mitotic cycle to the endocycle in *Arabidopsis*. *Development* 137, 63–71. doi: 10.1242/dev.035840

Ishida, T., Fujiwara, S., Miura, K., Stacey, N., Yoshimura, M., Schneider, K., et al. (2009). SUMO E3 ligase HIGH PLOIDY2 regulates endocycle onset and meristem maintenance in *Arabidopsis*. *Plant Cell* 21, 2284–2297. doi: 10.1105/tpc.109.068072

Ishikawa, H., and Evans, M. L. (1993). The role of the distal elongation zone in the response of maize roots to auxin and gravity. *Plant Physiol.* 102, 1203–1210.

Jiang, K., and Akhmanova, A. (2011). Microtubule tip-interacting proteins: a view from both ends. *Curr. Opin. Cell Biol.* 23, 94–101. doi: 10.1016/j.ceb.2010.08.008

Jin, K., Shen, J., Ashton, R. W., White, R. P., Dodd, I. C., Phillips, A. L., et al. (2015). The effect of impedance to root growth on plant architecture in wheat. *Plant Soil* 392, 323–332. doi: 10.1007/s11104-015-2462-0

Ketelaar, T., Faivre-Moskalenko, C., Esseling, J. J., de Ruijter, N. C., Grierson, C. S., Dogterom, M., et al. (2002). Positioning of nuclei in *Arabidopsis* root hairs: an actin-regulated process of tip growth. *Plant Cell* 14, 2941–2955. doi: 10.1105/tpc.005892

Kohoutová, L., Kourová, H., Nagy, S. K., Volc, J., Halada, P., Mészáros, T., et al. (2015). The *Arabidopsis* mitogen-activated protein kinase 6 is associated with gamma-tubulin on microtubules, phosphorylates EB1c and maintains spindle orientation under nitrosative stress. *New Phytol.* 207, 1061–1074. doi: 10.1111/nph.13501

Komaki, S., Abe, T., Coutuer, S., Inzé, D., Russinova, E., and Hashimoto, T. (2010). Nuclear-localized subtype of end-binding 1 protein regulates spindle organization in *Arabidopsis*. *J. Cell Sci.* 123, 451–459. doi: 10.1242/jcs.062703

Komarova, Y., De Groot, C. O., Grigoriev, I., Gouveia, S. M., Munteanu, E. L., Schober, J. M., et al. (2009). Mammalian end binding proteins control persistent microtubule growth. *J. Cell Biol.* 184, 691–706. doi: 10.1083/jcb.200807179

la Cour, T., Kiemer, L., Molgaard, A., Gupta, R., Skriver, K., and Brunak, S. (2004). Analysis and prediction of leucine-rich nuclear export signals. *Protein Eng. Des. Sel.* 17, 527–536. doi: 10.1093/protein/gzh062

Lamprecht, M. R., Sabatini, D. M., and Carpenter, A. E. (2007). CellProfiler: free, versatile software for automated biological image analysis. *Biotechniques* 42, 71–75. doi: 10.2144/000112257

Maizel, A., von Wangenheim, D., Federici, F., Haseloff, J., and Stelzer, E. H. (2011). High-resolution live imaging of plant growth in near physiological bright conditions using light sheet fluorescence microscopy. *Plant J.* 68, 377–385. doi: 10.1111/j.1365-313X.2011.04692.x

Mathur, J., Mathur, N., Kernebeck, B., Srinivas, B. P., and Hulskamp, M. (2003). A novel localization pattern for an EB1-like protein links microtubule dynamics to endomembrane organization. *Curr. Biol.* 13, 1991–1997. doi: 10.1016/j.cub.2003.10.033

McLamore, E. S., Diggs, A., Calvo Marzal, P., Shi, J., Blakeslee, J. J., Peer, W. A., et al. (2010). Non-invasive quantification of endogenous root auxin transport using an integrated flux microsensor technique. *Plant J.* 63, 1004–1016. doi: 10.1111/j.1365-313X.2010.04300.x

Okamoto, T., Tsurumi, S., Shibasaki, K., Obana, Y., Takaji, H., Oono, Y., et al. (2008). Genetic dissection of hormonal responses in the roots of *Arabidopsis* grown under continuous mechanical impedance. *Plant Physiol.* 146, 1651–1662. doi: 10.1104/pp.107.115519

Ovecka, M., Vaskebova, L., Komis, G., Luptovciak, I., Smertenko, A., and Samaj, J. (2015). Preparation of plants for developmental and cellular imaging by light-sheet microscopy. *Nat. Protoc.* 10, 1234–1247. doi: 10.1038/nprot.2015.081

Paganelli, L., Caillaud, M. C., Quentin, M., Damiani, I., Govetto, B., Lecomte, P., et al. (2015). Three BUB1 and BUBR1/MAD3-related spindle assembly checkpoint proteins are required for accurate mitosis in *Arabidopsis*. *New Phytol.* 205, 202–215 doi: 10.1111/nph.13073

Panteris, E., Adamakis, I. D., Daras, G., Hatzopoulos, P., and Rigas, S. (2013). Differential responsiveness of cortical microtubule orientation to suppression of cell expansion among the developmental zones of *Arabidopsis thaliana* root apex. *PLoS ONE* 8:e82442. doi: 10.1371/journal.pone.0082442

Petricka, J. J., Schauer, M. A., Megraw, M., Breakfield, N. W., Thompson, J. W., Georgiev, S., et al. (2012). The protein expression landscape of the *Arabidopsis* root. *Proc. Natl. Acad. Sci. U.S.A.* 109, 6811–6818. doi: 10.1073/pnas.1202546109

Ren, J., Longping, W., Xinjiao, G., Changjiang, J., Yu, X., and Xuebiao, Y. (2009). DOG1.0: illustrator of protein domain structures. *Cell Res.* 19, 271–273. doi: 10.1038/cr.2009.6

Ruzicka, K., Simaskova, M., Duclercq, J., Petrasek, J., Zazimalova, E., Simon, S., et al. (2009). Cytokinin regulates root meristem activity via modulation of the polar auxin transport. *Proc. Natl. Acad. Sci. U.S.A.* 106, 4284–4289. doi: 10.1073/pnas.0900060106

Samaj, J., Baluska, F., Voigt, B., Schlicht, M., Volkmann, D., and Menzel, D. (2004). Endocytosis, actin cytoskeleton, and signaling. *Plant Physiol.* 135, 1150–1161. doi: 10.1104/pp.104.040683

Samajova, O., Komis, G., and Samaj, J. (2013). Emerging topics in the cell biology of mitogen-activated protein kinases. *Trends Plant Sci.* 18, 140–148. doi: 10.1016/j.tplants.2012.11.004

Scheres, B., and Berleth, T. (1998). Root development: new meanings for root canals? *Curr. Opin. Plant Biol.* 1, 32–36. doi: 10.1016/S1369-5266(98)80124-6

Sena, G., Frentz, Z., Birnbaum, K. D., and Leibler, S. (2011). Quantitation of cellular dynamics in growing *Arabidopsis* roots with light sheet microscopy. *PLoS ONE* 6:e21303. doi: 10.1371/journal.pone.0021303

Sliwinska, E., Mathur, J., and Bewley, J. D. (2012). Synchronously developing collet hairs in *Arabidopsis thaliana* provide an easily accessible system for studying nuclear movement and endoreduplication. *J. Exp. Bot.* 63, 4165–4178. doi: 10.1093/jxb/ers099

Szklarczyk, D., Franceschini, A., Wyder, S., Forslund, K., Heller, D., Huerta-Cepas, J., et al. (2015). STRING v10: protein-protein interaction networks, integrated over the tree of life. *Nucleic Acids Res.* 43, D447–D452. doi: 10.1093/nar/gku1003

Tamura, N., and Draviam, V. M. (2012). Microtubule plus-ends within a mitotic cell are moving platforms' with anchoring, signalling and force-coupling roles. *Open Biol.* 2:120132. doi: 10.1098/rsob.120132

Tirnauer, J. S., Canman, J. C., Salmon, E. D., and Mitchison, T. J. (2002a). EB1 targets to kinetochores with attached, polymerizing microtubules. *Mol. Biol. Cell* 13, 4308–4316. doi: 10.1091/mbc.E02-04-0236

Tirnauer, J. S., Grego, S., Salmon, E. D., and Mitchison, T. J. (2002b). EB1-microtubule interactions in Xenopus egg extracts: role of EB1 in microtubule stabilization and mechanisms of targeting to microtubules. *Mol. Biol. Cell* 13, 3614–3626. doi: 10.1091/mbc.02-04-0210

van der Weele, C. M., Jiang, H. S., Palaniappan, K. K., Ivanov, V. B., Palaniappan, K., and Baskin, T. I. (2003). A new algorithm for computational image analysis of deformable motion at high spatial and temporal resolution applied to root growth. Roughly uniform elongation in the meristem and also, after an abrupt acceleration, in the elongation zone. *Plant Physiol.* 132, 1138–1148. doi: 10.1104/pp.103.021345

Verbelen, J. P., De Cnodder, T., Le, J., Vissenberg, K., and Baluska, F. (2006). The root apex of *Arabidopsis thaliana* consists of four distinct zones of growth activities: meristematic zone, transition zone, fast elongation zone and growth terminating zone. *Plant Signal. Behav.* 1, 296–304. doi: 10.4161/psb.1.6.3511

Weigel, D., and Jurgens, G. (2002). Stem cells that make stems. *Nature* 415, 751–754. doi: 10.1038/415751a

Conflict of Interest Statement: The authors declare that the research was conducted in the absence of any commercial or financial relationships that could be construed as a potential conflict of interest.

Supplement II

Research article

Advances in Imaging Plant Cell Dynamics

Komis G, Novák D, Ovečka M, Šamajová O, Šamaj J. (2018) *Plant Physiol*. 176: 80–93. doi: 10.1104/pp.17.00962

Advances in Imaging Plant Cell Dynamics[1][OPEN]

George Komis, Dominik Novák, Miroslav Ovečka, Olga Šamajová, and Jozef Šamaj[2]

Centre of the Region Haná for Biotechnological and Agricultural Research, Faculty of Science, Palacký University Olomouc, 783 71 Olomouc, Czech Republic

ORCID IDs: 0000-0001-6121-7164 (O.Š.); 0000-0003-4750-2123 (J.Š.).

After the establishment of advanced fluorescence microscopy methods and the development of numerous fluorescent proteins, it is possible to follow the organization and dynamics of most organelles and subcellular compartments in cells of living plants. Nowadays, it is possible to address subcellular architecture at the nanoscale through the implementation of superresolution microscopy methods such as structured illumination microscopy, photoactivation localization microscopy, or stochastic optical reconstruction and stimulated emission depletion microscopy. In a developmental context, the dynamic cellular and subcellular changes can be monitored long term in whole plant organs by light-sheet fluorescence microscopy. This is a mesoscopic method offering high-speed imaging, very low phototoxicity, and bioimaging of vertically oriented plants. This Update aims to provide the principles, the current application range, and the expected potential of superresolution and light-sheet fluorescence microscopy methods as well as a brief description of the improvements of standard wide-field epifluorescence and confocal systems.

METHODS OF SUPERRESOLUTION MICROSCOPY

Superresolution microscopy is a term that collectively refers to various techniques that bend or overcome diffraction limitations that strictly define the resolution limit of classical far-field optical microscopy systems. Resolution in conventional far-field systems is proportional to the wavelength of excitation light and inversely proportional to the numerical aperture of the light-collecting lens.

One major category of superresolution microscopy includes techniques that illuminate the sample by means of patterned light, such as structured illumination microscopy (SIM; linear and nonlinear; Gustafsson, 2000; Rego et al., 2012) and stimulated emission depletion microscopy (STED; Dyba et al., 2003).

The second major category of superresolution techniques includes single-molecule localization strategies that interrogate the positioning of individual fluorophores with subdiffraction accuracy. Such techniques mainly include photoactivation localization microscopy (PALM; Betzig et al., 2006), stochastic optical reconstruction microscopy (STORM; Rust et al., 2006), and some related variants such as superresolution optical fluctuation microscopy (SOFI; Dertinger et al., 2010a, 2010b), Bayesian analysis of blinking and bleaching (3B), and superresolution radial fluctuations (Cox et al., 2011; Small and Parthasarathy, 2014; Gustafsson et al., 2016). These so-called pointillistic superresolution techniques exploit properties of specific fluorophores to undergo repeated transitions between on and off states under certain conditions (Dempsey et al., 2011; Vaughan and Zhuang, 2011).

SIM

SIM imposes a spatially modulated light pattern (generated by means of a grating with an effective spacing of $\lambda_{exc}/2$; Gustafsson, 2000) that combines with diffraction orders of the emitting sample to Moiré

ADVANCES

- Dynamic plant bioimaging requires compensation between speed of imaging and spatial resolution since subcellular structures can be restricted in a virtually two-dimensional space, such as the cortical cytoplasm, or they can occupy bigger volumes as is the case of nuclei or mitotic microtubules.
- Superresolution methods address the issue of resolution at the nanoscale while within limits can provide temporal resolution of dynamic processes.
- Volumetric imaging of developmental or physiological events can be done at the whole seedling level using light-sheet fluorescence microscopy and its variants.

[1] This work was supported by the Czech Science Foundation (GAČR), projects 15-19284 and 16-24313S.

[2] Address correspondence to jozef.samaj@upol.cz.

G.K., D.N., M.O., O.Š., and J.Š. conceived and wrote the article.

[OPEN] Articles can be viewed without a subscription.

www.plantphysiol.org/cgi/doi/10.1104/pp.17.00962

patterns. Such Moiré patterns are generated by rotations (either three or five rotations at 36° or 60° increments, respectively) and phase shifts (three or five at $2\pi/3$ increments) of the grating. Individual images from each position of the grating are then combined, deconvolved, and used to reconstruct an image, which by definition is twice resolved compared with the Abbe limit (Gustafsson, 2000). Since linear SIM can rescue up to two diffraction orders, it is still diffraction limited. However, by means of linear SIM combined with high numerical aperture objectives (Komis et al., 2014), microtubules that were simply visualized using GFP-labeled tags (GFP-MBD [Marc et al., 1998] and GFP-TUA6 [Shaw et al., 2003]) could be practically resolved to the theoretical 100-nm threshold of linear SIM (Komis et al., 2014, 2015). This is twice as good as the theoretical optimum of 200 nm predicted by Abbe's equation. The Z-resolution can be significantly better compared with confocal laser scanning microscopy (CLSM; Sahl et al., 2017, and refs. therein). The final spatial resolution achieved by SIM is dependent on the specifications of the platform used for image acquisition, since different commercial platforms employ different means to generate patterned light as well as different numbers of rotations and phase shifts (discussed by Komis et al. [2015]). The temporal resolution of SIM is limited by the mechanical rotations and phase shifts of the light pattern. Thus, reconstructed time series of highly dynamic structures can suffer from motion artifacts (Förster et al., 2016). However, the acquisition frame rate of any commercial SIM platform is sufficient to record moderately dynamic events such as end-wise length fluctuations of microtubules and tracking minor growth/shrinkage events with a length below 200 nm. On the basis of differences in the signal intensity, SIM allows one to discriminate the dynamics of very proximal or bundled microtubules even if these cannot be resolved optically (Komis et al., 2014). Although not as effective as STED (see below) or PALM/STORM in superresolving intracellular structures, linear SIM offers several advantages for cell imaging. It is fluorophore unlimited, moderately fast (with imaging speeds ranging from 100 ms for a single image with Deltavision OMX to 600 ms with Nikon NSIM or 1.2 s with Zeiss Elyra S.1), and well represented in the market (Komis et al., 2015).

Nonlinear SIM, whereby emission of the fluorophore is not linearly proportional to excitation illumination, is able to truly superresolve intracellular structures such as microtubules in a diffraction-unlimited manner (Rego et al., 2012). However, appropriate platforms are not yet widely accessible to the microscopy community.

SIM can be used to image living cells of variable sizes. Thus, live SIM studies have been conducted in bacteria (Bottomley et al., 2017), showing the subcellular distribution of RNA polymerase (Stracy et al., 2015) and the time-resolved assembly of the FtsZ ring during bacterial division (Strauss et al., 2012). 2D and 3D SIM can temporally resolve subcellular structures of small eukaryotic cells, such as the spindle pole body (Fig. 1, A–F) and mitotic spindle (Fig. 1, G and H), or the reorganization of the actin cytoskeleton during cell fusion in fission yeast (Dudin et al., 2015). In custom-built systems, 2D and 3D SIM has been reportedly used at video frame rates and documented the organization and dynamics of microtubules (Kner et al., 2009; Schvartz et al., 2017) and mitochondria (Shao et al., 2011) in mammalian cells.

Depending on the optics and, especially, the objective numerical aperture, intracellular structures can be dynamically visualized at significantly better resolution than 100 nm (Li et al., 2015). In cases where the optical

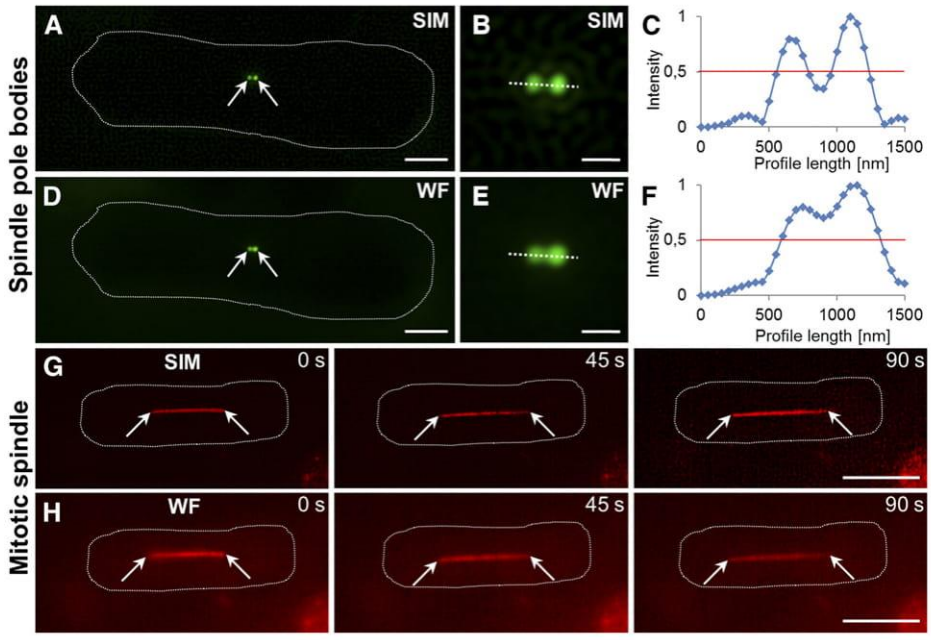

Figure 1. Comparative structured illumination and wide-field epifluorescence microscopy imaging of *Schizosaccharomyces pombe* cytoskeletal structures. A to C, Newly separated spindle pole bodies in a premitotic cell (A and B) and their clear discrimination based on normalized fluorescence intensity profiling (C) by means of SIM in *S. pombe* cells expressing the GFP-pcp1 spindle pole marker. D to F, Spindle bodies as visualized by wide-field epifluorescence (D and E) with less prominent resolution (F) compared with SIM. G and H, Mitotic spindle elongation visualized by SIM (G) and wide-field epifluorescence (H) in *S. pombe* cells expressing an mCherry-atb2 microtubule marker. Arrows indicate spindle pole bodies (A and D) and mitotic spindle poles (G and H). Bars = 2 μm (A and D), 1 μm (B and E), and 5 μm (G and H).

path can be split between two or more cameras, there is a possibility for dual or multiple-channel dynamic imaging of two or more subcellular compartments at the same time (for review, see Hirano et al., 2015; Li et al., 2015). Time-lapse 3D SIM imaging has been markedly improved by combining SIM and light-sheet fluorescence microscopy (LSFM) into a lattice light sheet with exceptional frame rates of acquisition (Chen et al., 2014).

In plants, 2D SIM can visualize various superresolved subcellular structures. These structures may include plasma membrane microdomains containing FLOTILIN1 (Flot1; Fig. 2A), actin filaments (Fig. 2, B and C), microtubules (Komis et al., 2014, 2015), and late endosomes (Fig. 2, E–H), providing quantitative information on the resolution improvement (Fig. 2D). Rare events such as vesicle fusion, which cannot be resolved by wide-field epifluorescence methods, can be captured by SIM (Fig. 2, I and J).

2D and 3D SIM also can elucidate the structures of organelles such as plastids (Fig. 3, A and B), mitochondria (Fig. 3, C and D), nuclei (Fig. 3, E–H), and the endoplasmic reticulum (Fig. 3, I and J). Moreover, 3D SIM was used successfully to decipher the architecture of plasmodesmata (Fitzgibbon et al., 2010; Knox et al., 2015), address the structure of virus replication complexes (Linnik et al., 2013), and localize the positions of viral movement proteins in plasmodesmata (Tilsner et al., 2013).

Nevertheless, time-lapse imaging using either 2D or 3D SIM is still very scarce in plant science. In the 2D mode, time-lapse SIM revealed superresolved cortical microtubule dynamics (Komis et al., 2014) and the dynamics of Flot1 under resting conditions or after flg22 treatment (Yu et al., 2017). In both cases, the subject of interest was confined at the cell periphery, being positioned close to the coverslip and, thus, facilitating image acquisition. In the same manner, other cortical structures, including the endoplasmic reticulum (Fig. 4, A and B) and the actin cytoskeleton (Fig. 4, C and D), can be tracked over time for relatively long periods.

SIM also can be used for more advanced quantitative studies, which may include the colocalization of different subcellular structures. Colocalization studies using SIM combined with single-particle averaging were used to map the positions of individual components of complex subcellular organelles such as the spindle pole body of fission yeast (Burns et al., 2015; Bestul et al., 2017). Finally, it was shown that fluorescence recovery after photobleaching (FRAP) analysis can be adopted by SIM to provide quantitative information on protein kinetics (Schneider et al., 2013).

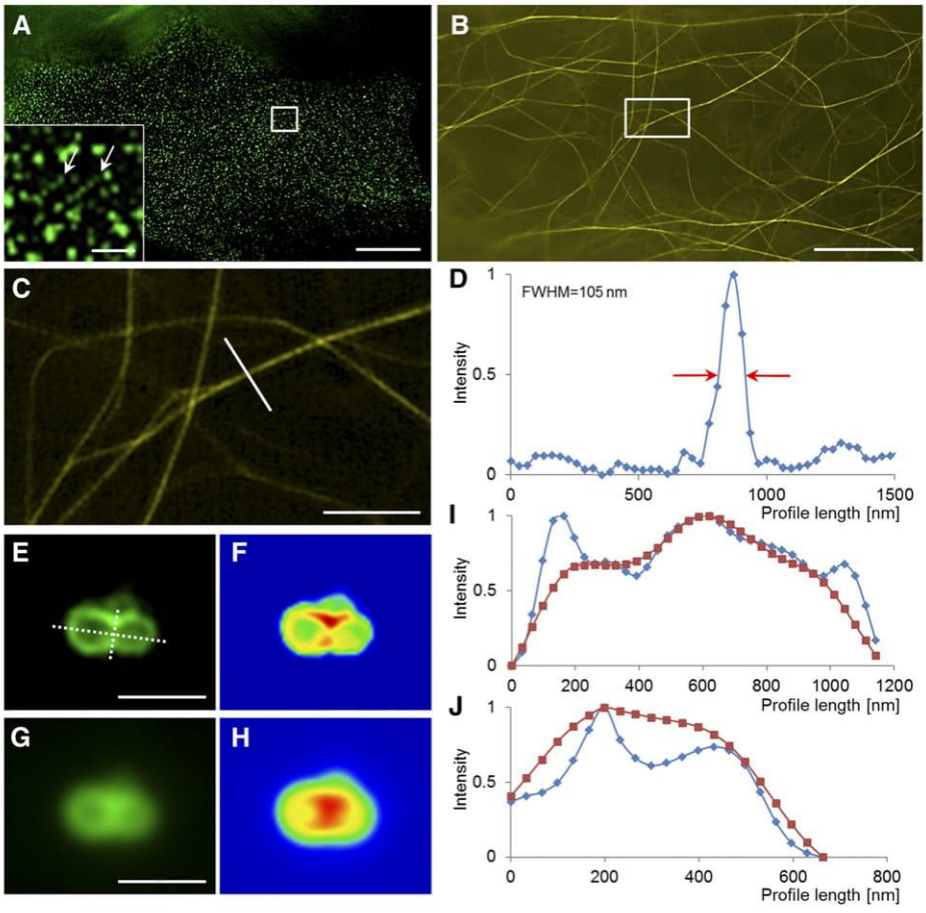

Figure 2. The superresolution potential of structured illumination microscopy applied to subcellular live imaging of plants. A, Imaging of Flot1 clusters at the plasma membrane of an Arabidopsis cotyledon pavement cell expressing a GFP-Flot1 marker. The inset shows two linear clusters of Flot1 particles (arrows). B to D, Imaging of the actin cytoskeleton in a hypocotyl epidermal cell expressing a YFP-FABD2-YFP actin marker (B; the boxed area is magnified in C) with the capacity to resolve fine actin bundles at approximately 100 nm at full width at half-maximum (FWHM) of the intensity profile (D) shown in C. E to J, Visualization of late endosome fusion with SIM imaging in root epidermal cells or Arabidopsis expressing a GFP-FYVE late endosomal reporter (E and F) as compared with wide-field epifluorescence (G and H). The graphic depiction of the longitudinal (I) and the transverse (J) profiles, drawn as dotted lines in E, highlights the potential of SIM to identify the area of fusion as an area of decreased fluorescence intensity. Bars = 10 μm (A and B), 2 μm (C), and 1 μm (E, G, and inset in A).

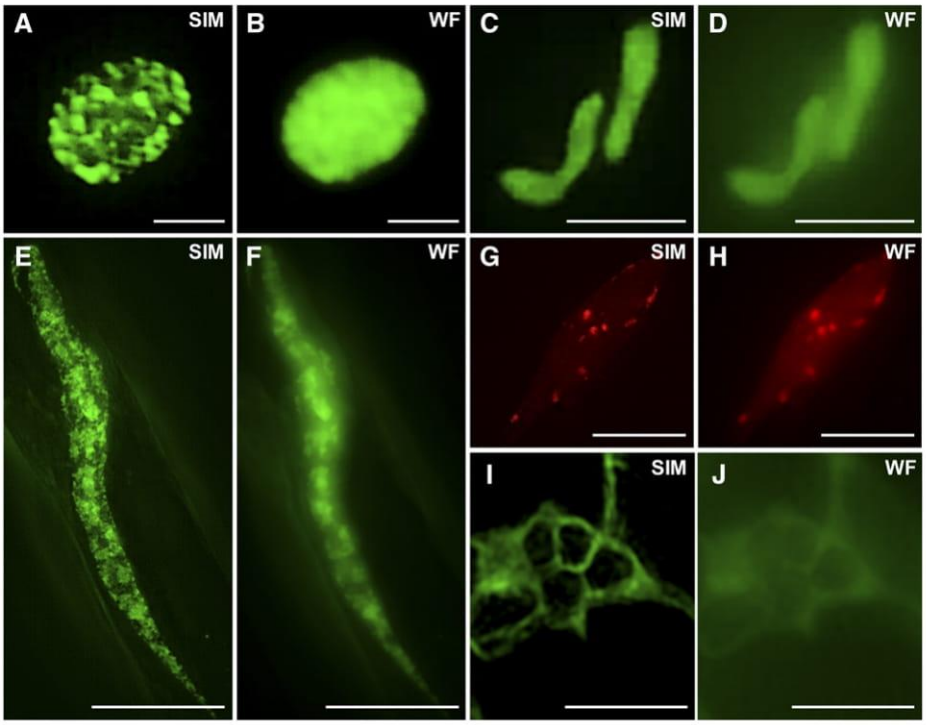

Figure 3. Structured illumination microscopy can deliver superresolved images of various plant organelles as compared with wide-field (WF) epifluorescence imaging. A and B, Plastids labeled by the marker ADP-sugar pyrophosphatase fused with GFP. C and D, Mitochondria labeled by the mitochondria-targeting sequence of the γ-subunit of the F1-ATPase fused with GFP. E and F, Nuclear structures of root epidermal cells expressing a nuclear localization signal-GFP marker. G and H, Nuclear structures of root epidermal cells expressing an HTB-mRFP marker. I and J, Structures of endoplasmic reticulum in root hairs stably expressing a GFP-HDEL marker. Bars = 2 μm (A–D, I, and J) and 10 μm (E–H).

SIM is prone to spherical aberrations due to refractive index mismatches. This may hamper the visualization of the subcellular architecture of plant samples not adequately coated by the observation medium. It can be avoided by mounting plants in an oxygen-saturated perfluorocarbon (Littlejohn et al., 2010, 2014; Littlejohn and Love, 2012; Chi and Ambrose, 2016). SIM also is prone to optical artifacts that may be caused by inaccurate grid movements (Langhorst et al., 2009), and resolving capacity depends on the labeling quality and the signal-to-noise ratio (SNR) of the sample. If the object in focus is dimly labeled and obscured by out-of-focus light or background fluorescence, the contrast of the grating pattern will be deteriorated and will not allow the calculation of the final image at the expected high resolution (Langhorst et al., 2009). Moreover, SIM is heavily dependent on postacquisition image reconstruction, while settings of the deconvolution algorithms may lead to artifacts in image reconstruction (for review, see Komis et al., 2015; Demmerle et al., 2017).

The principle of structured illumination can be combined with other microscopy methods, such as spinning disk to deliver superresolution images or wide-field epifluorescence to reduce out-of-focus readouts and provide optical sectioning of the sample. In the first case, the speed of imaging using the combination of SIM and spinning disk can achieve temporal resolutions between 30 and 100 frames per second (Hayashi and Okada, 2015). To our knowledge, a hybrid system of SIM-spinning disk is offered as an add-on for wide-field epifluorescence microscopes provided by Andor (DSD system; http://www.andor.com/learning-academy/revolution-dsd-principles-of-operation). The Zeiss Apotome system is a structured illumination add-on for wide-field microscopes that markedly improves image quality and allows for optical sectioning minimizing out-of-focus blur (https://applications.zeiss.com/C125792900358A3F/0/05BA0ED63B5E4CA2C1257E85004AB36A/$FILE/EN_41_011_081_ApoTome2.pdf).

Single-Molecule Localization Microscopy

Single-molecule localization microscopy (SMLM) includes all techniques that improve the precision of localization of single fluorophores based on their blinking (transition between emitting and dark states) under redox conditions (STORM; Rust et al., 2006; Dempsey et al., 2011) or on the localization of photoactivatable, photoswitchable, or photoconvertible fluorescent proteins (PALM; Nienhaus and Nienhaus, 2016). The precision of localization itself depends on the number of photons collected from a single molecule, the pixel size of the detector, the background signal, and the SD of the point-spread function. Therefore, it is important to acquire images at high SNR using cameras with low noise. Thus, PALM/STORM acquisitions are preferably performed using a total internal reflection microscopy (TIRF) illumination mode and electron microscopy CCD cameras.

The resolution of SMLM techniques can be optimally 10 times better than Abbe's limit (i.e. approximately 20 nm), but these techniques suffer from extreme limitations related to sample stability and fluorophore performance during acquisition. Since they investigate fluorophore localization at tens of nanometer precision,

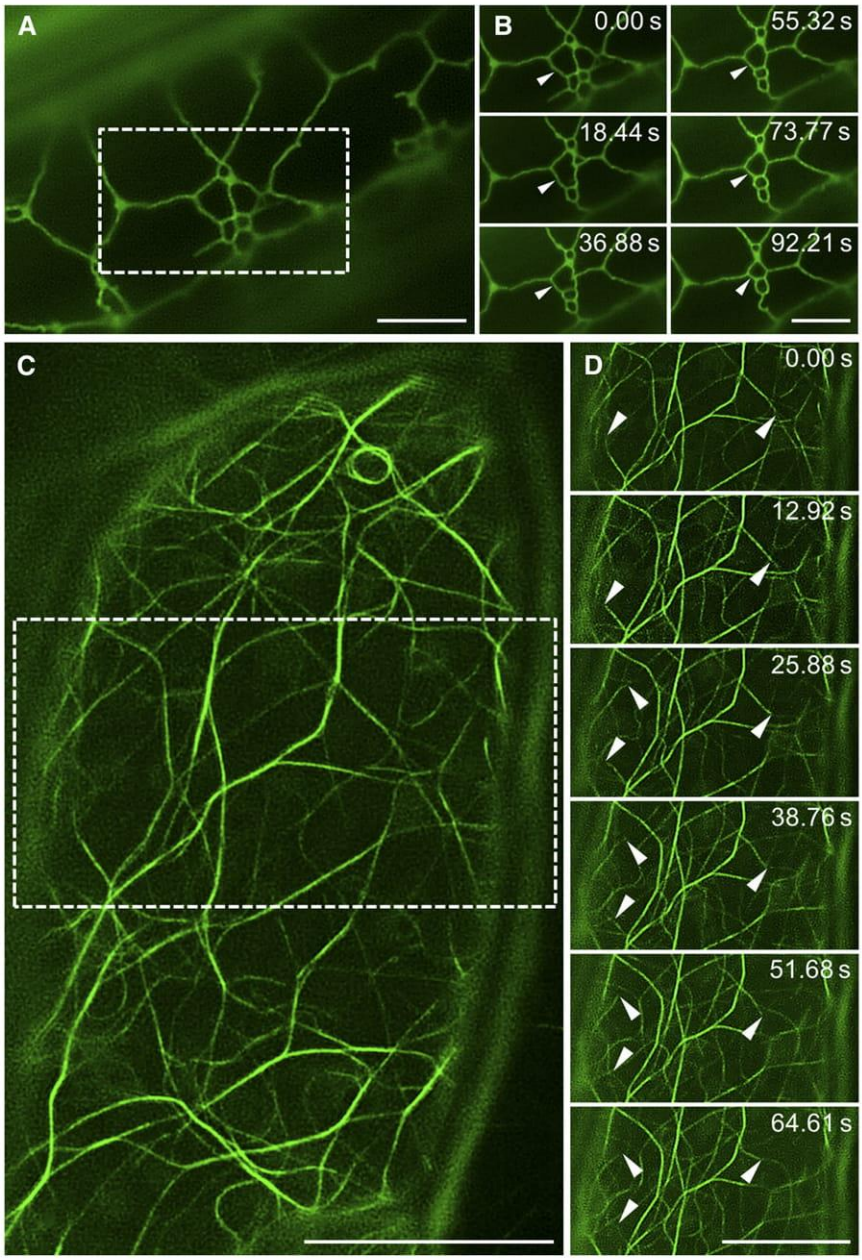

Figure 4. The potential for time-resolved structured illumination microscopy imaging. A and B, Overview (A) and time-lapse imaging (B) of cortical endoplasmic reticulum in a hypocotyl epidermal cell expressing a GFP-HDEL marker. The dynamic reorganization of the endoplasmic reticulum tubular structure is depicted by arrowheads (B). C and D, Overview (C) and time-lapse imaging (D) of actin filaments in a hypocotyl epidermal cell expressing a GFP-FABD2 marker. The dynamic reorganization of actin filaments is depicted by arrowheads (D). Bars = 5 μm (A and B) and 10 μm (C and D).

it is essential that the sample should be very firmly immobilized, and the examined structures must exhibit negligible dynamics during the thousands of time frames needed for image acquisition (Halpern et al., 2015). The two most important fluorophore properties affecting the performance of SMLM are the number of photons detected for every switching event (transition between on/off states) and the duty cycle of the fluorophore, which represents the fraction of time that the fluorophore spends in the on state. For optimal SMLM, a high photon yield and a low duty cycle of the fluorophore are desirable (Dempsey et al., 2011). Therefore, SMLM imaging is fluorophore limited, especially regarding genetically encoded fluorescent proteins. Although plant codon-optimized photoactivatable/photoswitchable proteins (Lummer et al., 2011, 2013) and photoconvertible proteins (Hosy et al., 2015) are available, these have been used very rarely for SMLM imaging of plant samples so far. One such study employed PALM to investigate the perinuclear organization of the actin cytoskeleton in living tobacco (*Nicotiana tabacum*) BY-2 suspension cells labeled with the tetrameric variant of photoswitchable EosFP (IrisFP) and achieved resolution of approximately 50 nm (Durst et al., 2014). Another study utilized fusions of the monomeric photoconvertible protein mEos3.2 with plasma membrane or tonoplast proteins to decipher the kinetics of their motility by means of single-particle tracking PALM (Hosy et al., 2015). Our provided example of PALM imaging shows the nuclear distribution of DRONPA-tagged

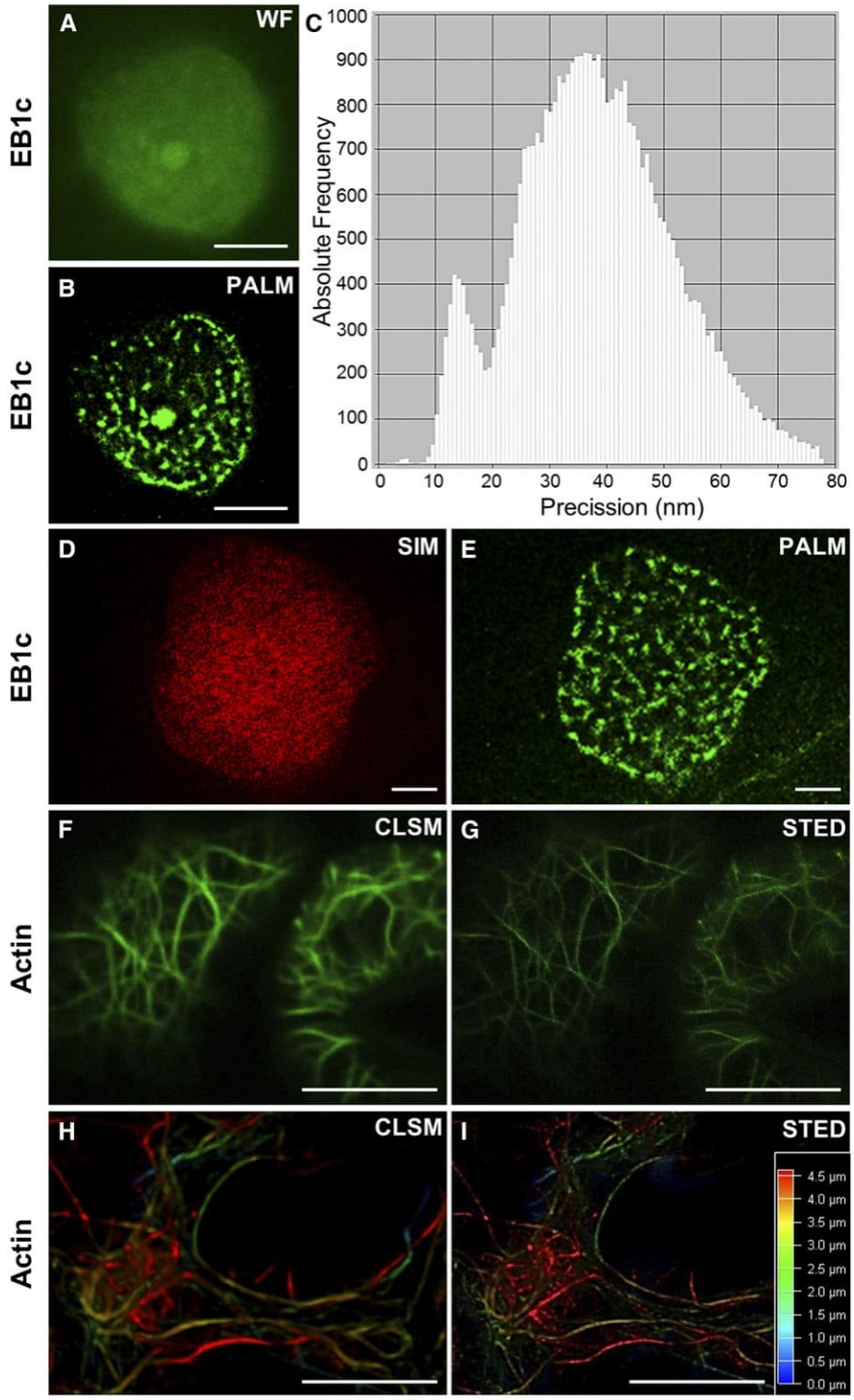

Figure 5. Photoactivation localization microscopy of EB1c protein in root epidermal cells of Arabidopsis expressing an EB1c-DRONPA marker and STED of actin filaments in Arabidopsis cotyledon epidermal cells expressing a GFP-FABD2 actin marker. A to C, Wide-field (WF) epifluorescence (A) and PALM (B) imaging and quantitative assessment (C) of the precision of localization of B at approximately 40 nm. D and E, Comparison of SIM (D) and PALM (E) localization of EB1c. F and G, Comparison of CLSM (F) and STED (G) imaging of actin filaments in Arabidopsis cotyledon epidermal cells. H and I, Volumetric CLSM (H) and STED (I) imaging of actin microfilament organization in Arabidopsis cotyledon epidermal cells. Bars = 2 μm (A, B, D, and E) and 10 μm (F–I).

plant-specific END BINDING1c (EB1c), a member of the microtubule plus end-binding protein family of Arabidopsis (*Arabidopsis thaliana*), in comparison with the diffuse nuclear signal observed by wide-field microscopy (Fig. 5, A–C). Moreover, PALM localization is more effective then SIM in deciphering EB1c nuclear distribution (Fig. 5, D and E).

STORM is heavily dependent on the photochemical properties of the fluorophores. This method is used preferentially for fixed and immunolabeled probes.

Moreover, the blinking of fluorophores suitable for STORM requires special buffer conditions, but with the appropriate fluorophore-buffer combination, the resolution can reach 5 nm (Dempsey et al., 2011). Efficient blinking of commonly used STORM fluorophores can be achieved in commercial mounting media, especially in Vectashield (Olivier et al., 2013). The introduction of *Escherichia coli* dihydrofolate reductase (eDHFR) as a protein tag of intracellular structures allows the labeling of eDHFR fusion proteins with fluorophore-conjugated trimethoprim primers used for live STORM applications (Wombacher et al., 2010).

STORM studies are very limited in plants and restricted to fixed probes. Such studies include the mapping of RNA polymerase II in interphase nuclei of Arabidopsis in fixed samples with Cy and AlexaFluor fluorophores (Schubert and Weisshart, 2015) and the visualization of cortical microtubules in fixed root cells immunolabeled with antibodies conjugated to the photoswitchable fluorophore AlexaFluor 647 at a resolution of approximately 50 nm (Dong et al., 2015).

STED

STED is a conceptually simple technique that projects two laser beams on the sample. The central Gaussian beam excites the sample while being surrounded by a doughnut-shaped eraser pulsed laser beam (Dyba and Hell, 2003). Superresolution in STED is achieved by the return in the ground state of nearly all excited fluorophores, except for those in the center of the excitation focus. Current STED beams include lasers at 592 nm, 660 nm (which corresponds to the second excitation maximum of chlorophyll), and 775 nm (https://www.leica-microsystems.com/fileadmin/downloads/Leica%20TCS%20SP8%20STED%203X/Brochures/Leica%20TCS%20SP8%20STED%203X-Brochure_EN.pdf). If compared with all other superresolution techniques, STED is based on scanning the sample with the combination of laser beams; in this way, it bears resemblance to CLSM. Since its development (Dyba and Hell, 2003; Dyba et al., 2003), STED has not found fertile ground in plant cell biology. There is only one study available (Kleine-Vehn et al., 2011). This might relate to the extreme output of the laser lines used, rendering STED quite phototoxic and unsuitable for mid- to long-term observations of living plant samples (for review, see Turkowyd et al., 2016). The original commercial STED designs used continuous-wave (CW) lasers (CW-STED), increasing the photon load and phototoxicity. An additional problem with CW lasers is that, for a short time, excited fluorophores outside the zero intensity center of the STED beam still emit photons before emission is suppressed. Such residual photons contribute to blurring of the resulting image when they are detected. This problem can be managed by so-called gated STED, detecting photons with a certain delay, in order to exclude the possibility that photons arising outside the center of the STED beam contribute to the image (Moffitt et al., 2011; Neupane et al., 2015; Castello et al., 2016). Another approach to improve the resolution of STED is the use of pulsed lasers. In this case, both lasers can be delivered as synchronous or asynchronous picosecond pulses, as in the original development of the method (Dyba and Hell, 2003). Moreover, image acquisition can be improved by resonant scanning, allowing very fast acquisition rates and high-rate volumetric imaging of actin filaments in living cotyledon epidermal cells at better resolution compared with CLSM (Fig. 5, F–I). A positive feature of STED is that, being a confocal microscopy-based technology, it can be used for superresolution in combination with quantitative imaging methods such as fluorescence correlation spectroscopy (FCS) either at the cell surface (Andrade et al., 2015) or in deeper parts of the cell (Lanzanò et al., 2017). Unlike SIM and PALM/STORM, which require postacquisition image processing to deliver the superresolved result, STED provides superresolution during acquisition.

Software-Based Superresolution for Live Cell Imaging

Software-based superresolution relies on optical fluctuations of fluorophores occurring under standard imaging conditions and the ability to record these fluctuations via single-photon-sensitive cameras. Such methods are described briefly here because they require a relatively cheap microscopic setup and represent an attractive option for the plant cell biologist.

One such example includes the acquisition of oversampled Z-stacks (i.e. smaller sample section thickness than what is defined by the Nyquist sampling rate; see https://svi.nl/NyquistRate) using a spinning disk microscope and subsequent 3D deconvolution based on commercially available software (Okamoto et al., 2012; Nakano, 2013). This approach was used in the study of cellulose synthase trafficking (Fujimoto et al., 2015).

Another software-based approach that can deliver superresolution results from any basic wide-field epifluorescence setup is called 3B (Cox et al., 2011). This method can be implemented as an ImageJ (https://imagej.nih.gov/ij/) plugin or a stand-alone platform (Cox et al., 2011; Rosten et al., 2013; both available from http://www.coxphysics.com/3b/). It is useful for time-lapse data sets of samples labeled with conventional fluorescent proteins. A big drawback of 3B is that it is extremely time consuming, which makes the processing of large data sets troublesome. However, cloud computing at affordable prices can overcome this drawback (Hu et al., 2013). A recently developed method called superresolution radial fluctuations (SRRF; Gustafsson et al., 2016; https://bitbucket.org/rhenriqueslab/nanoj-srrf/wiki/Home) is implemented as a plugin for Fiji image-analysis software (Schindelin et al., 2012; https://fiji.sc/) and can deliver superresolution information from both wide-field and confocal sources at a good temporal frame rate (1 s). In this respect, Andor has commercialized a much accelerated

SRRF stream live superresolution workflow (http://www.andor.com/srrf-stream).

SOFI is another postacquisition software-processing procedure (Dertinger et al., 2009). Like 3B and SRRF, SOFI processes data sets acquired by standard wide-field epifluorescence platforms with no specification on the fluorophore but with the requirement that the fluorophore must exhibit at least two detectable fluorescent states (a dark one and a bright one; Dertinger et al., 2009). SOFI can deliver superresolution images at a lower sample SNR compared with default PALM/STORM approaches (Geissbuehler et al., 2011). Importantly, SOFI postacquisition processing can be combined with spinning disk imaging (Hosny et al., 2013).

LSFM

LSFM is a fast mesoscopic imaging method combining advantages of wide-field fluorescence microscopy and 4D volumetric imaging. It is based on sample illumination by a thin sheet of light (with controllable thickness in the range of micrometers). The light sheet can be generated in either a unilateral or, ideally, a bilateral fashion. Such an adjustable sheet of light enables optical sectioning of the sample and excitation of the fluorophores only within the thin illuminated volume. This illuminated sample volume is well adjusted to the focal plane of the detection objective, thus eliminating out-of-focus fluorophore excitation and light emission. Thus, LSFM prevents the photobleaching of fluorophores outside of the light sheet volume. Because the detection path is oriented orthogonally to the illumination, the system is capable of spherical aberration-free acquisition (Weber and Huisken, 2011). To allow optical sectioning, it is possible to either move the light sheet through the sample (Kumar et al., 2014) or, alternatively, to move the sample with respect to a stationary light sheet (Huisken et al., 2004; Chen et al., 2014; Reynaud et al., 2015; Kumar et al., 2016). With the high speed of sample movement through the light sheet, the fluorophore photobleaching as well as phototoxicity in the sample are reduced considerably. The above setup is supported by the currently existing LSFM platforms, as it allows very fast optical sectioning and rapid image acquisition. Therefore, the total effective excitation energy absorbed by the sample in LSFM can be several orders of magnitude lower in comparison with the epifluorescence wide-field or confocal laser scanning systems (Ichikawa et al., 2014; Stelzer, 2015). The sample mounted on a rotor can be rotated during multiangular acquisition, allowing precise postacquisition rendering for 4D (x, y, z, and t) image reconstruction. Although LSFM is a mesoscopic imaging method not even reaching resolution close to the diffraction limit, it became the most advanced approach for long-term developmental live cell imaging at the subcellular, cellular, tissue, organ, and whole-organism levels.

A great potential of LSFM in developmental studies is provided by its ability to maintain biological samples under almost natural conditions. The standard approach of animal sample preparation is full embedding and immobilization of the sample in transparent gel-like agarose (Kaufmann et al., 2012). Immobilization of plants in agarose ensures their stabilization in the vertical orientation. However, embedding of plant aerial parts is not compatible with proper physiological conditions, which are necessary for long-term imaging. Recently developed open systems for plant preparation and maintenance during LSFM long-term imaging (Ovečka et al., 2015; von Wangenheim et al., 2017) ensure that plants are maintained in the microscope vertically oriented (according to the gravity vector). Simultaneously, continuous root growth is supported by appropriate culture medium, and the aerial part grows freely in the air. Controllable illumination devices maintain desirable photoperiod protocols; thus, imaging experiments can be performed over a period of several days. Altogether, LSFM is a forefront method for long-term developmental imaging of plants in a natural vertical orientation maintaining their undisturbed growth in near-environmental conditions.

The most common type of LSFM devices is based on a classical selective-plane illumination microscopy (SPIM) principle with a horizontal setup for both illumination and detection objectives, where the sample is introduced to the field of view vertically from above. Microscopy modalities based on this hardware arrangement are either commercially available (Lightsheet Z.1 from Carl Zeiss) or can be constructed in place directly according to the OpenSPIM concept (http://openspim.org). The OpenSPIM concept was developed to adapt modular SPIM systems to the particular requirements of end users (Gualda et al., 2013; Pitrone et al., 2013). The concept is well supported by the community and provides a broad range of biological applications (Girstmair et al., 2016). By means of the vertical placement of the sample, both commercially available and custom-made LSFM/SPIM systems are suitable and already have been used successfully for long-term developmental imaging of plants. An alternative LSFM system based on the inclined optical arrangement, like dual-view inverted SPIM, might be designed for the imaging of animal living samples at subcellular resolution (Kumar et al., 2014, 2016). Such a system is optimal for the horizontal placement of rather thin and transparent samples mounted in a standard glass slide format (Kumar et al., 2014); therefore, it has no practical application on living plants so far.

Applications of LFSM in plant biology are dynamically evolving, while studies on growing Arabidopsis roots provided long-term observations of cell division progression in cells carrying the microtubule markers GFP-MBD (Maizel et al., 2011) and GFP-TUA5 (Ovečka et al., 2015; Fig. 6A). However, the spatial and temporal resolutions of LSFM also allow characterizing the redistributions of actin filaments in the phragmoplast during cytokinesis of Arabidopsis root cells carrying the actin marker YFP-FABD2-YFP (Fig. 6B) or tobacco BY-2 suspension cells carrying another actin marker,

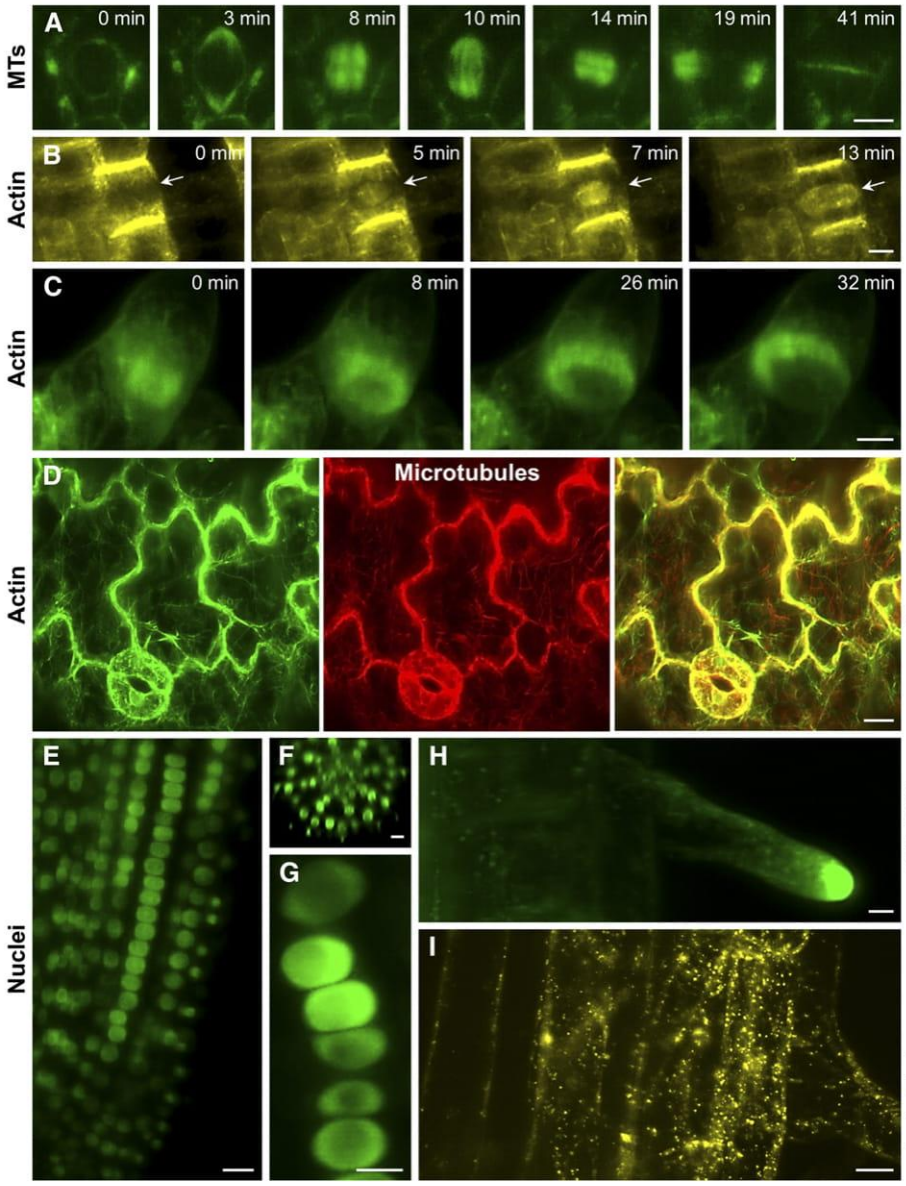

Figure 6. Advances of LSFM imaging of dynamic cellular and developmental processes in plants. A, Imaging of microtubules (MTs) in a time-course recording of a dividing Arabidopsis root epidermal cell as visualized using a GFP-TUA5 marker. B, Time-course imaging of actin in phragmoplast of a dividing Arabidopsis root epidermal cell (arrows) as visualized using a YFP-FABD2-YFP marker. C, Time-course imaging of actin in phragmoplast of a dividing BY-2 suspension cell as visualized using a GFP-Lifeact marker. D, Covisualization of actin using GFP-FABD2 and microtubules using mCherry-TUA5 in cotyledon stomata and pavement cells of Arabidopsis. E to G, Localization of EB1c in nuclei of Arabidopsis root as visualized using an EB1c-GFP marker. The high potential of LSFM for deep tissue imaging provides insight into EB1c-GFP nuclear localization in cells of different developmental zones (E), different root cell layers (F), as well as in individual cell files (G). H, Localization of the small Rab GTPase RabA1d in early endosomal-trans-Golgi network (EE-TGN) compartments accumulating at the tip of growing root hairs as visualized using a GFP-RabA1d marker. I, Imaging of late endosomes in Arabidopsis cortical and epidermal root cells as visualized using a YFP-RabF2a marker. Bars = 5 μm (A, B, and G–I) and 10 μm (C–F).

GFP-Lifeact (Fig. 6C). Owing to the high speed of imaging, LSFM can track the dynamics of more than one subcellular structure (Fig. 6D). Thus, Ovečka et al. (2015) showed live coimaging of actin filaments and microtubules in the cotyledon epidermal cells, while von Wangenheim et al. (2016) tracked cell fate by simultaneous imaging of plasma membrane and nuclear markers during lateral root formation. LSFM, unlike other live cell-imaging techniques, was able to successfully localize signaling protein such as mitogen-activated protein kinase 6 (MPK6) to the preprophase band of Arabidopsis root meristematic cells (Smékalová et al., 2014). One possible target of MPK6 is plant-specific EB1c. This protein is localized in the nucleus of nondividing cells. Long-term developmental imaging by LSFM revealed the correlation between nuclear size and EB1c content in diverse root tissues (epidermis, cortex, and endodermis) and in different developmental zones (meristematic, transition, and elongation zones) of the Arabidopsis root (Fig. 6, E–G; Novák et al., 2016). LSFM also allowed the precise characterization of cell division patterns during the formation and growth of Arabidopsis lateral roots (von Wangenheim et al., 2016). Another important advantage of LSFM for dynamic developmental studies of plants is deep imaging of nuclei (Novák et al., 2016) and endosomes (Berson et al., 2014) in inner root tissues and the undisturbed development of root hairs (Fig. 6, E–I). The good spatial and excellent temporal resolutions of LSFM also facilitate the simultaneous monitoring of mitotic microtubules in several tissue layers of the root meristem of the crop species *Medicago sativa* that is significantly thicker in comparison with Arabidopsis (Vyplelová et al., 2017). Recently, it was demonstrated

that developmental imaging can be scaled up in existing commercial platforms by customized sample imaging chambers, allowing high-throughput imaging of developmental processes such as root growth (de Luis Balaguer et al., 2016).

LSFM also can track physiological processes such as calcium fluxes by using ratiometric calcium indicators in the intact and freely moving nematode *Caenorhabditis elegans* (Ardiel et al., 2017) or during the neuronal activity of zebrafish larvae (Barykina et al., 2017). In the first case, fast exposure (2.5–4.5 ms) was translated to a 5-Hz volumetric acquisition frame rate, allowing imaging of the entire animal. Along with advancing volumetric image acquisition by paralleled illumination with more than one light sheet (Dean et al., 2017), such results exemplify the potential of LSFM to monitor fast physiological events with subcellular resolution in whole organisms, organs, or tissues.

The growth of sensitive cells such as root hairs may be compromised under standard conditions of sample preparation and imaging with conventional microscopes (Ovečka et al., 2005). By using LSFM, it is possible to monitor the growth of root hairs from their initiation to full differentiation but also to track fast-moving organelles such as endosomes and correlate their dynamics to the pattern of root hair elongation (Fig. 6, H and I; Berson et al., 2014). Moreover, LSFM was combined recently with Förster resonance energy transfer (FRET) to address the respiration rates of root hairs using a FRET sensor for MgATP production (De Col et al., 2017). A similar FRET-based sensor was used to follow cytosolic calcium oscillations during root (Costa et al., 2013) and root hair (Candeo et al., 2017) growth.

Of considerable importance for the implementation of LSFM in any laboratory is the fact that LSFM data sets are very big and routinely exceed terabyte sizes. This makes the postacquisition storage, processing (e.g. multiview registration and fusion), and analysis of such data sets quite demanding. At present, there are software solutions that efficiently address the problem of data access and postacquisition processing, including BigDataViewer (Pietzsch et al., 2015) and TeraFly (Bria et al., 2016).

Obviously, LSFM is not able to compete with superresolution methods providing nanotracking of structures and organelles at the subcellular level. However, LSFM significantly advanced the developmental imaging of plants, providing near-environmental conditions. In the near future, the functional combination of LSFM and superresolution concepts (Chen et al., 2014) might provide a new platform for very powerful spatiotemporal imaging of living plants.

SHORT UPDATE ON WIDE-FIELD AND CONFOCAL MICROSCOPY SYSTEMS

Research-grade wide-field epifluorescence microscopes and single-photon CLSM devices are in the standard setup of any cell biology research unit, and there have been numerous studies employing such microscopes. Especially CLSM has been in the forefront of qualitative and quantitative studies, such as the assessment of protein-protein interactions through FRET, recording of protein dynamics with fluorescence lifetime imaging (FLIM), and interactions with FLIM/FRET (Hoffmann et al., 2014; Garagounis et al., 2017; Lv et al., 2017), or the recording and the quantification of diffusion/mobility of single molecular species through FCS (Li et al., 2016). Especially in CLSM, speed, sensitivity, and the spectral range of image acquisition have been improved by resonant scanning approaches and the implementation of gallium arsenide phosphide alloy-based multispectral or hybrid detectors using sensitive avalanche photodiodes combined with the high dynamic range of PMTs (for review, see Jonkman and Brown, 2015).

For more specialized applications, platforms are expanding to include TIRF, particularly suitable for in vitro microscopic assays, variable-angle emission microscopy, with increased depth of excitation compared with TIRF, and finally, spinning disk microscopy, which is ideal for fast 3D time-lapse imaging of demanding events such as mitosis (Komis et al., 2017) but with reduced resolution capacity compared with CLSM (Wang et al., 2005). Detailed descriptions of these modalities are beyond the scope of this Update, and the reader is referred to relevant reviews (Henty-Ridilla et al., 2013; Shaw and Ehrhardt, 2013; Li et al., 2015).

Airyscan CLSM

A recent advancement of CLSM with improved resolution is Airyscan CLSM. The Airyscan detector has 32 subAiry (0.25 AU each) gallium arsenide phosphide alloy-based elements that are geometrically fitted to acquire the entire Airy pattern of emitted light and assign it to the correct position by software reconstruction (Weisshart, 2014; Huff et al., 2015). The averaged image from the detector elements can have improved xy resolution by a factor of 1.7 (resulting in a theoretical value of 140 nm). This corresponds to a CLSM device with the pinhole adjusted to approximately 0.2 AU but with much improved SNR (Weisshart, 2014). At the fast imaging mode, Airyscan frame rates approximate resonant scanning, being able to reach 27 frames per second but with compromise in resolution. Airyscan CLSM is a very recent advancement of microscopy technologies, and its applications have been limited. By taking advantage of high-speed acquisition at improved resolution, it was possible to capture microtubule-buckling events during the contraction of cardiomyocytes at high resolution (Robison et al., 2016). Very recently, Airyscan CLSM was used to capture mitotic spindle and phragmoplast dynamics in Arabidopsis *ktn1-2* mutants devoid of the KATANIN1 protein (Komis et al., 2017).

OUTSTANDING QUESTIONS

- Can hybrid microscopy methods like lattice light-sheet or computational superresolution methods be applied for dynamic plant cell imaging?
- Will the most recent designs of time gated- and pulsed STED circumvent the problems of phototoxicity and allow time recordings of intracellular dynamics in plants?
- Can pointillistic methods of superresolution track molecular events such as the assembly and the function of cellulose synthases in vivo?
- Will the recent designs of light-sheet microscopes allow the monitoring of challenging processes such as embryogenesis in model plants?

CONCLUSION AND OUTLOOK

A survey of the available literature can show the importance of microscopy in plant live imaging. All the existing fluorescence-based microscopy methods have been applied to visualize different organelles and subcellular compartments. For quantitative approaches such as FRAP, FRET, FLIM, and FCS, the CLSM apparatus remains the workhorse, although other methods may be used instead (i.e. SIM can be combined with FRAP [Conduit et al., 2015] and STED can be used for FCS [Lanzanò et al., 2017]). With no doubt, recently developed advanced superresolution methods (such as SIM, PALM, STORM, and STED, software-based superresolution approaches, and Airyscan CLSM) and methods for long-term developmental imaging (such as LSFM and SPIM) have provided new dimensions and perspectives for better imaging of plant cells, especially in terms of significantly improved spatial and temporal resolution.

The field of microscopy is vigorously advancing toward hybrid methods, including Bessel or Airy beam illumination and lattice light-sheet microscopy. These were developed to compensate for speed, spatial resolution, and physiological imaging in just one microscope (Fahrbach and Rohrbach, 2012; Chen et al., 2014; Vettenburg et al., 2014). In the near future, they will possibly be applicable to the cumbersome plant specimens (Meinert et al., 2016). Such platforms will allow subcellular tracking of complex structures like the mitotic spindle in plant cells with unprecedented spatiotemporal resolution and with developmental connotations, similar to already published lattice light-sheet imaging of animal cells (Yamashita et al., 2015).

Integration of the precision of localization-based superresolution methods in plant cell imaging (including PALM and STORM) is expected to expand and help us uncover details of the molecular architecture and intermolecular associations within complex subcellular structures in the near future.

ACKNOWLEDGMENTS

We thank Jinxing Lin (Key Laboratory of Photosynthesis and Molecular Environmental Physiology, Institute of Botany, Chinese Academy of Sciences) for Arabidopsis seeds carrying the *proFlot1::FLOT1:GFP* marker, Dr. Juraj Gregan (Department of Genetics, Faculty of Natural Sciences, Comenius University) for *Schizosaccharomyces pombe* strains carrying GFP-pcp1 and mCherry-atb2 spindle pole body and microtubule markers, Dr. Yoshihisa Oda (Department of Biological Sciences, Graduate School of Science, University of Tokyo) for the HTB-mRFP chromatin marker, Dr. Javier Pozueta (Instituto de Agrobiotecnología, Universidad Pública de Navarra) for Arabidopsis seeds carrying ADP-sugar pyrophosphatase fused with GFP, Dr. Yasuo Niwa (Laboratory of Plant Cell Technology, Graduate School of Nutritional and Environmental Sciences, University of Shizuoka) for Arabidopsis seeds carrying GFP-tagged mitochondria-targeting presequence of the N terminus of the γ-subunit of F1-ATPase, Dr. Jim Haseloff (Division of Cell Biology, Medical Research Council Laboratory of Molecular Biology, United Kingdom) for Arabidopsis seeds carrying GFP fused to the HDEL endoplasmic reticulum retention sequence mGFP5, Dr. Jiří Macas (Institute of Plant Molecular Biology, Czech Republic) for Arabidopsis seeds carrying GFP fused to a nuclear localization signal and to the complete coding region of GUS, Dr. Arun Sampathkumar (Max Planck Institute of Molecular Plant Physiology) for Arabidopsis seeds carrying the double markers GFP-FABD2 and mCherry-TUA5, and Dr. Andrei Smertenko (Institute of Biological Chemistry, Washington State University) for BY-2 cultures expressing GFP-Lifeact.

Received August 3, 2017; accepted November 20, 2017; published November 22, 2017.

LITERATURE CITED

Andrade DM, Clausen MP, Keller J, Mueller V, Wu C, Bear JE, Hell SW, Lagerholm BC, Eggeling C (2015) Cortical actin networks induce spatiotemporal confinement of phospholipids in the plasma membrane: a minimally invasive investigation by STED-FCS. Sci Rep **5:** 11454

Ardiel EL, Kumar A, Marbach J, Christensen R, Gupta R, Duncan W, Daniels JS, Stuurman N, Colón-Ramos D, Shroff H (2017) Visualizing calcium flux in freely moving nematode embryos. Biophys J **112:** 1975–1983

Barykina NV, Subach OM, Piatkevich KD, Jung EE, Malyshev AY, Smirnov IV, Bogorodskiy AO, Borshchevskiy VI, Varizhuk AM, Pozmogova GE, et al (2017) Green fluorescent genetically encoded calcium indicator based on calmodulin/M13-peptide from fungi. PLoS ONE **12:** e0183757

Berson T, von Wangenheim D, Takáč T, Šamajová O, Rosero A, Ovečka M, Komis G, Stelzer EH, Šamaj J (2014) Trans-Golgi network localized small GTPase RabA1d is involved in cell plate formation and oscillatory root hair growth. BMC Plant Biol **14:** 252

Bestul AJ, Yu Z, Unruh JR, Jaspersen SL (2017) Molecular model of fission yeast centrosome assembly determined by superresolution imaging. J Cell Biol **216:** 2409–2424

Betzig E, Patterson GH, Sougrat R, Lindwasser OW, Olenych S, Bonifacino JS, Davidson MW, Lippincott-Schwartz J, Hess HF (2006) Imaging intracellular fluorescent proteins at nanometer resolution. Science **313:** 1642–1645

Bottomley AL, Turnbull L, Whitchurch CB, Harry EJ (2017) Immobilization techniques of bacteria for live super-resolution imaging using structured illumination microscopy. Methods Mol Biol **1535:** 197–209

Bria A, Iannello G, Onofri L, Peng H (2016) TeraFly: real-time three-dimensional visualization and annotation of terabytes of multidimensional volumetric images. Nat Methods **13:** 192–194

Burns S, Avena JS, Unruh JR, Yu Z, Smith SE, Slaughter BD, Winey M, Jaspersen SL (2015) Structured illumination with particle averaging reveals novel roles for yeast centrosome components during duplication. eLife **4:** 08586

Candeo A, Doccula FG, Valentini G, Bassi A, Costa A (2017) Light sheet fluorescence microscopy quantifies calcium oscillations in root hairs of Arabidopsis thaliana. Plant Cell Physiol **58:** 1161–1172

Castello M, Tortarolo G, Hernández IC, Bianchini P, Buttafava M, Boso G, Tosi A, Diaspro A, Vicidomini G (2016) Gated-STED microscopy

with subnanosecond pulsed fiber laser for reducing photobleaching. Microsc Res Tech **79:** 785–791

Chen BC, Legant WR, Wang K, Shao L, Milkie DE, Davidson MW, Janetopoulos C, Wu XS, Hammer JA III, Liu Z, et al (2014) Lattice light-sheet microscopy: imaging molecules to embryos at high spatiotemporal resolution. Science **346:** 1257998

Chi Z, Ambrose C (2016) Microtubule encounter-based catastrophe in Arabidopsis cortical microtubule arrays. BMC Plant Biol **16:** 18

Conduit PT, Wainman A, Novak ZA, Weil TT, Raff JW (2015) Re-examining the role of Drosophila Sas-4 in centrosome assembly using two-colour-3D-SIM FRAP. eLife **4:** 08483

Costa A, Candeo A, Fieramonti L, Valentini G, Bassi A (2013) Calcium dynamics in root cells of *Arabidopsis thaliana* visualized with selective plane illumination microscopy. PLoS ONE **8:** e75646

Cox S, Rosten E, Monypenny J, Jovanovic-Talisman T, Burnette DT, Lippincott-Schwartz J, Jones GE, Heintzmann R (2011) Bayesian localization microscopy reveals nanoscale podosome dynamics. Nat Methods **9:** 195–200

Dean KM, Roudot P, Welf ES, Pohlkamp T, Garrelts G, Herz J, Fiolka R (2017) Imaging subcellular dynamics with fast and light-efficient volumetrically parallelized microscopy. Optica **4:** 263–271

De Col V, Fuchs P, Nietzel T, Elsässer M, Voon CP, Candeo A, Seeliger I, Fricker MD, Grefen C, Møller IM, et al (2017) ATP sensing in living plant cells reveals tissue gradients and stress dynamics of energy physiology. eLife **6:** 26770

de Luis Balaguer MA, Ramos-Pezzotti M, Rahhal MB, Melvin CE, Johannes E, Horn TJ, Sozzani R (2016) Multi-sample Arabidopsis Growth and Imaging Chamber (MAGIC) for long term imaging in the ZEISS Lightsheet Z.1. Dev Biol **419:** 19–25

Demmerle J, Innocent C, North AJ, Ball G, Müller M, Miron E, Matsuda A, Dobbie IM, Markaki Y, Schermelleh L (2017) Strategic and practical guidelines for successful structured illumination microscopy. Nat Protoc **12:** 988–1010

Dempsey GT, Vaughan JC, Chen KH, Bates M, Zhuang X (2011) Evaluation of fluorophores for optimal performance in localization-based super-resolution imaging. Nat Methods **8:** 1027–1036

Dertinger T, Colyer R, Iyer G, Weiss S, Enderlein J (2009) Fast, background-free, 3D super-resolution optical fluctuation imaging (SOFI). Proc Natl Acad Sci USA **106:** 22287–22292

Dertinger T, Colyer R, Vogel R, Enderlein J, Weiss S (2010a) Achieving increased resolution and more pixels with superresolution optical fluctuation imaging (SOFI). Opt Express **18:** 18875–18885

Dertinger T, Heilemann M, Vogel R, Sauer M, Weiss S (2010b) Super-resolution optical fluctuation imaging with organic dyes. Angew Chem Int Ed Engl **49:** 9441–9443

Dong B, Yang X, Zhu S, Bassham DC, Fang N (2015) Stochastic optical reconstruction microscopy imaging of microtubule arrays in intact *Arabidopsis thaliana* seedling roots. Sci Rep **5:** 15694

Dudin O, Bendezú FO, Groux R, Laroche T, Seitz A, Martin SG (2015) A formin-nucleated actin aster concentrates cell wall hydrolases for cell fusion in fission yeast. J Cell Biol **208:** 897–911

Durst S, Hedde PN, Brochhausen L, Nick P, Nienhaus GU, Maisch J (2014) Organization of perinuclear actin in live tobacco cells observed by PALM with optical sectioning. J Plant Physiol **171:** 97–108

Dyba M, Hell SW (2003) Photostability of a fluorescent marker under pulsed excited-state depletion through stimulated emission. Appl Opt **42:** 5123–5129

Dyba M, Jakobs S, Hell SW (2003) Immunofluorescence stimulated emission depletion microscopy. Nat Biotechnol **21:** 1303–1304

Fahrbach FO, Rohrbach A (2012) Propagation stability of self-reconstructing Bessel beams enables contrast-enhanced imaging in thick media. Nat Commun **3:** 632

Fitzgibbon J, Bell K, King E, Oparka K (2010) Super-resolution imaging of plasmodesmata using three-dimensional structured illumination microscopy. Plant Physiol **153:** 1453–1463

Förster R, Wicker K, Müller W, Jost A, Heintzmann R (2016) Motion artefact detection in structured illumination microscopy for live cell imaging. Opt Express **24:** 22121–22134

Fujimoto M, Suda Y, Vernhettes S, Nakano A, Ueda T (2015) Phosphatidylinositol 3-kinase and 4-kinase have distinct roles in intracellular trafficking of cellulose synthase complexes in Arabidopsis thaliana. Plant Cell Physiol **56:** 287–298

Garagounis C, Kostaki KI, Hawkins TJ, Cummins I, Fricker MD, Hussey PJ, Hetherington AM, Sweetlove LJ (2017) Microcompartmentation of cytosolic aldolase by interaction with the actin cytoskeleton in Arabidopsis. J Exp Bot **68:** 885–898

Geissbuehler S, Dellagiacoma C, Lasser T (2011) Comparison between SOFI and STORM. Biomed Opt Express **2:** 408–420

Girstmair J, Zakrzewski A, Lapraz F, Handberg-Thorsager M, Tomancak P, Pitrone PG, Simpson F, Telford MJ (2016) Light-sheet microscopy for everyone? Experience of building an OpenSPIM to study flatworm development. BMC Dev Biol **16:** 22

Gualda EJ, Vale T, Almada P, Feijó JA, Martins GG, Moreno N (2013) OpenSpinMicroscopy: an open-source integrated microscopy platform. Nat Methods **10:** 599–600

Gustafsson MG (2000) Surpassing the lateral resolution limit by a factor of two using structured illumination microscopy. J Microsc **198:** 82–87

Gustafsson N, Culley S, Ashdown G, Owen DM, Pereira PM, Henriques R (2016) Fast live-cell conventional fluorophore nanoscopy with ImageJ through super-resolution radial fluctuations. Nat Commun **7:** 12471

Halpern AR, Howard MD, Vaughan JC (2015) Point by point: an introductory guide to sample preparation for single-molecule, super-resolution fluorescence microscopy. Curr Protoc Chem Biol **7:** 103–120

Hayashi S, Okada Y (2015) Ultrafast superresolution fluorescence imaging with spinning disk confocal microscope optics. Mol Biol Cell **26:** 1743–1751

Henty-Ridilla JL, Li J, Blanchoin L, Staiger CJ (2013) Actin dynamics in the cortical array of plant cells. Curr Opin Plant Biol **16:** 678–687

Hirano Y, Matsuda A, Hiraoka Y (2015) Recent advancements in structured-illumination microscopy toward live-cell imaging. Microscopy (Oxf) **64:** 237–249

Hoffmann C, Moes D, Dieterle M, Neumann K, Moreau F, Tavares Furtado A, Dumas D, Steinmetz A, Thomas C (2014) Live cell imaging reveals actin-cytoskeleton-induced self-association of the actin-bundling protein WLIM1. J Cell Sci **127:** 583–598

Hosny NA, Song M, Connelly JT, Ameer-Beg S, Knight MM, Wheeler AP (2013) Super-resolution imaging strategies for cell biologists using a spinning disk microscope. PLoS ONE **8:** e74604

Hosy E, Martinière A, Choquet D, Maurel C, Luu DT (2015) Super-resolved and dynamic imaging of membrane proteins in plant cells reveal contrasting kinetic profiles and multiple confinement mechanisms. Mol Plant **8:** 339–342

Hu YS, Nan X, Sengupta P, Lippincott-Schwartz J, Cang H (2013) Accelerating 3B single-molecule super-resolution microscopy with cloud computing. Nat Methods **10:** 96–97

Huff J, Bathe W, Netz R, Anhut T, Weisshart K (2015) The Airyscan detector from ZEISS: confocal imaging with improved signal-to-noise ratio and super-resolution. Nat Methods **12:** http://dx.doi.org/10.1038/nmeth.f.388

Huisken J, Swoger J, Del Bene F, Wittbrodt J, Stelzer EHK (2004) Optical sectioning deep inside live embryos by selective plane illumination microscopy. Science **305:** 1007–1009

Ichikawa T, Nakazato K, Keller PJ, Kajiura-Kobayashi H, Stelzer EHK, Mochizuki A, Nonaka S (2014) Live imaging and quantitative analysis of gastrulation in mouse embryos using light-sheet microscopy and 3D tracking tools. Nat Protoc **9:** 575–585

Jonkman J, Brown CM (2015) Any way you slice it: a comparison of confocal microscopy techniques. J Biomol Tech **26:** 54–65

Kaufmann A, Mickoleit M, Weber M, Huisken J (2012) Multilayer mounting enables long-term imaging of zebrafish development in a light sheet microscope. Development **139:** 3242–3247

Kleine-Vehn J, Wabnik K, Martinière A, Łangowski Ł, Willig K, Naramoto S, Leitner J, Tanaka H, Jakobs S, Robert S, et al (2011) Recycling, clustering, and endocytosis jointly maintain PIN auxin carrier polarity at the plasma membrane. Mol Syst Biol **7:** 540

Kner P, Chhun BB, Griffis ER, Winoto L, Gustafsson MG (2009) Super-resolution video microscopy of live cells by structured illumination. Nat Methods **6:** 339–342

Knox K, Wang P, Kriechbaumer V, Tilsner J, Frigerio L, Sparkes I, Hawes C, Oparka K (2015) Putting the squeeze on plasmodesmata: a role for reticulons in primary plasmodesmata formation. Plant Physiol **168:** 1563–1572

Komis G, Luptovčiak I, Ovečka M, Samakovli D, Šamajová O, Šamaj J (2017) Katanin effects on dynamics of cortical microtubules and mitotic

arrays in Arabidopsis thaliana revealed by advanced live-cell imaging. Front Plant Sci **8:** 866

Komis G, Mistrik M, Šamajová O, Doskočilová A, Ovečka M, Illés P, Bartek J, Šamaj J (2014) Dynamics and organization of cortical microtubules as revealed by superresolution structured illumination microscopy. Plant Physiol **165:** 129–148

Komis G, Mistrik M, Šamajová O, Ovečka M, Bartek J, Šamaj J (2015) Superresolution live imaging of plant cells using structured illumination microscopy. Nat Protoc **10:** 1248–1263

Kumar A, Christensen R, Guo M, Chandris P, Duncan W, Wu Y, Santella A, Moyle M, Winter PW, Colón-Ramos D, et al (2016) Using stage- and slit-scanning to improve contrast and optical sectioning in dual-view inverted light sheet microscopy (diSPIM). Biol Bull **231:** 26–39

Kumar A, Wu Y, Christensen R, Chandris P, Gandler W, McCreedy E, Bokinsky A, Colón-Ramos DA, Bao Z, McAuliffe M, et al (2014) Dual-view plane illumination microscopy for rapid and spatially isotropic imaging. Nat Protoc **9:** 2555–2573

Langhorst MF, Schaffer J, Goetze B (2009) Structure brings clarity: structured illumination microscopy in cell biology. Biotechnol J **4:** 858–865

Lanzanò L, Scipioni L, Di Bona M, Bianchini P, Bizzarri R, Cardarelli F, Diaspro A, Vicidomini G (2017) Measurement of nanoscale three-dimensional diffusion in the interior of living cells by STED-FCS. Nat Commun **8:** 65

Li D, Shao L, Chen BC, Zhang X, Zhang M, Moses B, Milkie DE, Beach JR, Hammer JA III, Pasham M, et al (2015) Extended-resolution structured illumination imaging of endocytic and cytoskeletal dynamics. Science **349:** aab3500

Li X, Xing J, Qiu Z, He Q, Lin J (2016) Quantification of membrane protein dynamics and interactions in plant cells by fluorescence correlation spectroscopy. Mol Plant **9:** 1229–1239

Linnik O, Liesche J, Tilsner J, Oparka KJ (2013) Unraveling the structure of viral replication complexes at super-resolution. Front Plant Sci **4:** 6

Littlejohn GR, Gouveia JD, Edner C, Smirnoff N, Love J (2010) Perfluorodecalin enhances *in vivo* confocal microscopy resolution of *Arabidopsis thaliana* mesophyll. New Phytol **186:** 1018–1025

Littlejohn GR, Love J (2012) A simple method for imaging *Arabidopsis* leaves using perfluorodecalin as an infiltrative imaging medium. J Vis Exp **59:** 3394

Littlejohn GR, Mansfield JC, Christmas JT, Witterick E, Fricker MD, Grant MR, Smirnoff N, Everson RM, Moger J, Love J (2014) An update: improvements in imaging perfluorocarbon-mounted plant leaves with implications for studies of plant pathology, physiology, development and cell biology. Front Plant Sci **5:** 140

Lummer M, Humpert F, Steuwe C, Caesar K, Schüttpelz M, Sauer M, Staiger D (2011) Reversible photoswitchable DRONPA-s monitors nucleocytoplasmic transport of an RNA-binding protein in transgenic plants. Traffic **12:** 693–702

Lummer M, Humpert F, Wiedenlübbert M, Sauer M, Schüttpelz M, Staiger D (2013) A new set of reversibly photoswitchable fluorescent proteins for use in transgenic plants. Mol Plant **6:** 1518–1530

Lv X, Jing Y, Xiao J, Zhang Y, Zhu Y, Julian R, Lin J (2017) Membrane microdomains and the cytoskeleton constrain AtHIR1 dynamics and facilitate the formation of an AtHIR1-associated immune complex. Plant J **90:** 3–16

Maizel A, von Wangenheim D, Federici F, Haseloff J, Stelzer EH (2011) High-resolution live imaging of plant growth in near physiological bright conditions using light sheet fluorescence microscopy. Plant J **68:** 377–385

Marc J, Granger CL, Brincat J, Fisher DD, Kao T, McCubbin AG, Cyr RJ (1998) A *GFP-MAP4* reporter gene for visualizing cortical microtubule rearrangements in living epidermal cells. Plant Cell **10:** 1927–1940

Meinert T, Tietz O, Palme KJ, Rohrbach A (2016) Separation of ballistic and diffusive fluorescence photons in confocal light-sheet microscopy of Arabidopsis roots. Sci Rep **6:** 30378

Moffitt JR, Osseforth C, Michaelis J (2011) Time-gating improves the spatial resolution of STED microscopy. Opt Express **19:** 4242–4254

Nakano A (2013) Super-resolution confocal live imaging microscopy (SCLIM): cutting-edge technology in cell biology. Conf Proc IEEE Eng Med Biol Soc **2013:** 133–135

Neupane B, Jin T, Mellor LF, Loboa EG, Ligler FS, Wang G (2015) Continuous-wave stimulated emission depletion microscope for imaging actin cytoskeleton in fixed and live cells. Sensors (Basel) **15:** 24178–24190

Nienhaus K, Nienhaus GU (2016) Chromophore photophysics and dynamics in fluorescent proteins of the GFP family. J Phys Condens Matter **28:** 443001

Novák D, Kuchařová A, Ovečka M, Komis G, Šamaj J (2016) Developmental nuclear localization and quantification of GFP-tagged EB1c in *Arabidopsis* root using light-sheet microscopy. Front Plant Sci **6:** 1187

Okamoto M, Kurokawa K, Matsuura-Tokita K, Saito C, Hirata R, Nakano A (2012) High-curvature domains of the ER are important for the organization of ER exit sites in Saccharomyces cerevisiae. J Cell Sci **125:** 3412–3420

Olivier N, Keller D, Rajan VS, Gönczy P, Manley S (2013) Simple buffers for 3D STORM microscopy. Biomed Opt Express **4:** 885–899

Ovečka M, Lang I, Baluška F, Ismail A, Illeš P, Lichtscheidl IK (2005) Endocytosis and vesicle trafficking during tip growth of root hairs. Protoplasma **226:** 39–54

Ovečka M, Vaškebová L, Komis G, Luptovčiak I, Smertenko A, Šamaj J (2015) Preparation of plants for developmental and cellular imaging by light-sheet microscopy. Nat Protoc **10:** 1234–1247

Pietzsch T, Saalfeld S, Preibisch S, Tomancak P (2015) BigDataViewer: visualization and processing for large image data sets. Nat Methods **12:** 481–483

Pitrone PG, Schindelin J, Stuyvenberg L, Preibisch S, Weber M, Eliceiri KW, Huisken J, Tomancak P (2013) OpenSPIM: an open-access light-sheet microscopy platform. Nat Methods **10:** 598–599

Rego EH, Shao L, Macklin JJ, Winoto L, Johansson GA, Kamps-Hughes N, Davidson MW, Gustafsson MG (2012) Nonlinear structured-illumination microscopy with a photoswitchable protein reveals cellular structures at 50-nm resolution. Proc Natl Acad Sci USA **109:** E135–E143

Reynaud EG, Peychl J, Huisken J, Tomancak P (2015) Guide to light-sheet microscopy for adventurous biologists. Nat Methods **12:** 30–34

Robison P, Caporizzo MA, Ahmadzadeh H, Bogush AI, Chen CY, Margulies KB, Shenoy VB, Prosser BL (2016) Detyrosinated microtubules buckle and bear load in contracting cardiomyocytes. Science **352:** 0659

Rosten E, Jones GE, Cox S (2013) ImageJ plug-in for Bayesian analysis of blinking and bleaching. Nat Methods **10:** 97–98

Rust MJ, Bates M, Zhuang X (2006) Sub-diffraction-limit imaging by stochastic optical reconstruction microscopy (STORM). Nat Methods **3:** 793–795

Sahl SJ, Hell SW, Jakobs S (2017) Fluorescence nanoscopy in cell biology. Nat Rev Mol Cell Biol **18:** 685–701

Schindelin J, Arganda-Carreras I, Frise E, Kaynig V, Longair M, Pietzsch T, Preibisch S, Rueden C, Saalfeld S, Schmid B, et al (2012) Fiji: an open-source platform for biological-image analysis. Nat Methods **9:** 676–682

Schneider K, Fuchs C, Dobay A, Rottach A, Qin W, Wolf P, Álvarez-Castro JM, Nalaskowski MM, Kremmer E, Schmid V, et al (2013) Dissection of cell cycle-dependent dynamics of Dnmt1 by FRAP and diffusion-coupled modeling. Nucleic Acids Res **41:** 4860–4876

Schubert V, Weisshart K (2015) Abundance and distribution of RNA polymerase II in *Arabidopsis* interphase nuclei. J Exp Bot **66:** 1687–1698

Schvartz T, Aloush N, Goliand I, Segal I, Nachmias D, Arbely E, Elia N (2017) Direct fluorescent-dye labeling of α-tubulin in mammalian cells for live cell and superresolution imaging. Mol Biol Cell **28:** 2747–2756

Shao L, Kner P, Rego EH, Gustafsson MG (2011) Super-resolution 3D microscopy of live whole cells using structured illumination. Nat Methods **8:** 1044–1046

Shaw SL, Ehrhardt DW (2013) Smaller, faster, brighter: advances in optical imaging of living plant cells. Annu Rev Plant Biol **64:** 351–375

Shaw SL, Kamyar R, Ehrhardt DW (2003) Sustained microtubule treadmilling in *Arabidopsis* cortical arrays. Science **300:** 1715–1718

Small AR, Parthasarathy R (2014) Superresolution localization methods. Annu Rev Phys Chem **65:** 107–125

Smékalová V, Luptovčiak I, Komis G, Šamajová O, Ovečka M, Doskočilová A, Takáč T, Vadovič P, Novák O, Pechan T, et al (2014) Involvement of YODA and mitogen activated protein kinase 6 in Arabidopsis post-embryogenic root development through auxin up-regulation and cell division plane orientation. New Phytol **203:** 1175–1193

Stelzer EHK (2015) Light-sheet fluorescence microscopy for quantitative biology. Nat Methods **12:** 23–26

Stracy M, Lesterlin C, Garza de Leon F, Uphoff S, Zawadzki P, Kapanidis AN (2015) Live-cell superresolution microscopy reveals the organization of RNA polymerase in the bacterial nucleoid. Proc Natl Acad Sci USA **112:** E4390–E4399

Strauss MP, Liew AT, Turnbull L, Whitchurch CB, Monahan LG, Harry EJ (2012) 3D-SIM super resolution microscopy reveals a bead-like arrangement for FtsZ and the division machinery: implications for triggering cytokinesis. PLoS Biol **10:** e1001389

Tilsner J, Linnik O, Louveaux M, Roberts IM, Chapman SN, Oparka KJ (2013) Replication and trafficking of a plant virus are coupled at the entrances of plasmodesmata. J Cell Biol **201:** 981–995

Turkowyd B, Virant D, Endesfelder U (2016) From single molecules to life: microscopy at the nanoscale. Anal Bioanal Chem **408:** 6885–6911

Vaughan JC, Zhuang X (2011) New fluorescent probes for super-resolution imaging. Nat Biotechnol **29:** 880–881

Vettenburg T, Dalgarno HI, Nylk J, Coll-Lladó C, Ferrier DE, Čižmár T, Gunn-Moore FJ, Dholakia K (2014) Light-sheet microscopy using an Airy beam. Nat Methods **11:** 541–544

von Wangenheim D, Fangerau J, Schmitz A, Smith RS, Leitte H, Stelzer EH, Maizel A (2016) Rules and self-organizing properties of post-embryonic plant organ cell division patterns. Curr Biol **26:** 439–449

von Wangenheim D, Hauschild R, Friml J (2017) Light sheet fluorescence microscopy of plant roots growing on the surface of a gel. J Vis Exp **119:** 55044

Vyplelová P, Ovečka M, Šamaj J (2017) Alfalfa root growth rate correlates with progression of microtubules during mitosis and cytokinesis as revealed by environmental light-sheet microscopy. Front Plant Sci **8:** 1870

Wang E, Babbey CM, Dunn KW (2005) Performance comparison between the high-speed Yokogawa spinning disc confocal system and single-point scanning confocal systems. J Microsc **218:** 148–159

Weber M, Huisken J (2011) Light sheet microscopy for real-time developmental biology. Curr Opin Genet Dev **21:** 566–572

Weisshart K (2014) The basic principle of Airyscanning. Technology note. Carl Zeiss Microscopy GmbH, 07745 Jena, Germany

Wombacher R, Heidbreder M, van de Linde S, Sheetz MP, Heilemann M, Cornish VW, Sauer M (2010) Live-cell super-resolution imaging with trimethoprim conjugates. Nat Methods **7:** 717–719

Yamashita N, Morita M, Legant WR, Chen BC, Betzig E, Yokota H, Mimori-Kiyosue Y (2015) Three-dimensional tracking of plus-tips by lattice light-sheet microscopy permits the quantification of microtubule growth trajectories within the mitotic apparatus. J Biomed Opt **20:** 101206

Yu M, Liu H, Dong Z, Xiao J, Su B, Fan L, Komis G, Šamaj J, Lin J, Li R (2017) The dynamics and endocytosis of Flot1 protein in response to flg22 in Arabidopsis. J Plant Physiol **215:** 73–84

Supplement III

Research article

Gene Expression Pattern and Protein Localization of Arabidopsis Phospholipase D Alpha 1 Revealed by Advanced Light-Sheet and Super-Resolution Microscopy

Novák D*, Vadovič P*, Ovečka M, Šamajová O, Komis G, Colcombet J, Šamaj J. (2018) *Front. Plant Sci*. 9: 371. doi: 10.3389/fpls.2018.00371

* joined first authors

frontiers in Plant Science

ORIGINAL RESEARCH
published: 21 March 2018
doi: 10.3389/fpls.2018.00371

Gene Expression Pattern and Protein Localization of Arabidopsis Phospholipase D Alpha 1 Revealed by Advanced Light-Sheet and Super-Resolution Microscopy

Dominik Novák[1†], *Pavol Vadovič*[1†], *Miroslav Ovečka*[1], *Olga Šamajová*[1], *George Komis*[1], *Jean Colcombet*[2] *and Jozef Šamaj*[1*]

[1] *Department of Cell Biology, Centre of the Region Haná for Biotechnological and Agricultural Research, Palacký University Olomouc, Olomouc, Czechia,* [2] *UMR9213 Institut des Sciences des Plantes de Paris Saclay, Orsay, France*

OPEN ACCESS

Edited by:
Martin Huelskamp, Universität zu Köln, Germany

Reviewed by:
Qun Zhang, Nanjing Agricultural University, China
Fatima Cvrckova, Charles University, Czechia

***Correspondence:**
Jozef Šamaj
jozef.samaj@upol.cz

[†] *These authors have contributed equally to this work.*

Specialty section:
This article was submitted to Plant Cell Biology, a section of the journal Frontiers in Plant Science

Received: *15 January 2018*
Accepted: *06 March 2018*
Published: *21 March 2018*

Citation:
Novák D, Vadovič P, Ovečka M, Šamajová O, Komis G, Colcombet J and Šamaj J (2018) Gene Expression Pattern and Protein Localization of Arabidopsis Phospholipase D Alpha 1 Revealed by Advanced Light-Sheet and Super-Resolution Microscopy. Front. Plant Sci. 9:371. doi: 10.3389/fpls.2018.00371

Phospholipase D alpha 1 (PLDα1, At3g15730) and its product phosphatidic acid (PA) are involved in a variety of cellular and physiological processes, such as cytoskeletal remodeling, regulation of stomatal closure and opening, as well as biotic and abiotic stress signaling. Here we aimed to study developmental expression patterns and subcellular localization of PLDα1 in Arabidopsis using advanced microscopy methods such as light-sheet fluorescence microscopy (LSFM) and structured illumination microscopy (SIM). We complemented two knockout *pldα1* mutants with a YFP-tagged PLDα1 expressed under the *PLDα1* native promoter in order to study developmental expression pattern and subcellular localization of PLDα1 in *Arabidopsis thaliana* under natural conditions. Imaging of tissue-specific and developmentally-regulated localization of YFP-tagged PLDα1 by LSFM in roots of growing seedlings showed accumulation of PLDα1-YFP in the root cap and the rhizodermis. Expression of PLDα1-YFP in the rhizodermis was considerably higher in trichoblasts before and during root hair formation and growth. Thus, PLDα1-YFP accumulated in emerging root hairs and in the tips of growing root hairs. PLDα1-YFP showed cytoplasmic subcellular localization in root cap cells and in cells of the root transition zone. In aerial parts of plants PLDα1-YFP was also localized in the cytoplasm showing enhanced accumulation in the cortical cytoplasmic layer of epidermal non-dividing cells of hypocotyls, leaves, and leaf petioles. However, in dividing cells of root apical meristem and leaf petiole epidermis PLDα1-YFP was enriched in mitotic spindles and phragmoplasts, as revealed by co-visualization with microtubules. Finally, super-resolution SIM imaging revealed association of PLDα1-YFP with both microtubules and clathrin-coated vesicles (CCVs) and pits (CCPs). In conclusion, this study shows the developmentally-controlled expression and subcellular localization of PLDα1 in dividing and non-dividing Arabidopsis cells.

Keywords: *Arabidopsis thaliana*, development, localization, light-sheet fluorescence microscopy, microtubules, phospholipase D, At3g15730

INTRODUCTION

The major function of the phospholipase D (PLD) enzymes is to hydrolyse phospholipids such as phosphatidylcholine, resulting in the production of phosphatidic acid (PA) by transphosphatidylation of water and a free soluble head group, e.g., choline (Munnik and Musgrave, 2001). The *PLD* gene family shows significant expansion in plants, and it is represented by 12 *PLD* genes in *Arabidopsis thaliana*, by comparison to just two in animals and one in yeast (Wang et al., 2012). Plant PLDs are distributed in six subclasses: α-(with 3 members), β-(with 2 members), γ-(with 3 members), δ-, ε-, ζ-(all with 2 members), depending on the protein sequences and enzymatic properties of individual members (Qin and Wang, 2002; Wang, 2005; Bargmann and Munnik, 2006; Hong et al., 2016). All 12 phospholipase D (PLD) isoforms in Arabidopsis catalyze the transphosphatidylation of water, thus generating phosphatidic acid having variable signaling roles.

Previously, some PLDs were proposed to play a morphogenetic role linked to microtubules. The relation of PLDs with microtubule organization was directly shown in the case of a tobacco PLD isoform that specifically decorates cortical microtubules (Gardiner et al., 2001) leading to the assumption that PLDs may be a specific component linking cortical microtubules to the cell wall—plasma membrane—cortical cytoskeleton continuum. Later studies on transgenic Arabidopsis cell lines using pull-down assay with GFP tagged PLDδ identified PLDδ as a cortical microtubule-binding protein (Andreeva et al., 2009; Ho et al., 2009; Hong et al., 2016). Such regulatory interactions among microtubules and PLD isoforms (particularly the Arabidopsis PLDα1 isoform) proved to have functional consequences during plant responses to salt and hyperosmotic stress (Zhang et al., 2012), ABA-induced stomatal closure (Jiang et al., 2014), and drug-induced microtubule reorganization (Zhang et al., 2017a). One prominent target of PLDα1-produced phosphatidic acid is MAP65-1, a microtubule crosslinker which contains motifs for phosphatidic acid binding outside its carboxylterminal microtubule binding domain (Zhang et al., 2012). Interestingly, phosphatidic acid binding seems to occur at the self-association aminoterminus of MAP65-1. Known and expected new functions of PLDα1 in plants might link this enzyme to G proteins, cytoskeleton and vesicular trafficking (e.g., Choudhury and Pandey, 2016, 2017; Hong et al., 2016). However, overall regulation of developmental expression pattern in cell- and tissue-specific context and subcellular localization of PLDα1 in dividing cells is not known.

Dynamic cellular and subcellular changes can be monitored for long periods with light-sheet microscopy. Moreover, imaging can be done at near physiological conditions with minimal phototoxicity at high speed. The method is based on sample illumination with a thin layer of light, thus eliminating out-of-focus excitation and preventing photobleaching. The detection path is oriented orthogonally to the illumination while plant is growing vertically according to gravity vector (Ovečka et al., 2015). Super-resolution microscopy methods can bend or overcome diffraction limitations of conventional microscopes. One such method is structured illumination microscopy (SIM; Rego et al., 2012). SIM illuminates the sample with a light pattern which combines with diffraction orders of the emitting sample to Moiré patterns. Many such patterns are generated by rotation and phase shifting of the illumination pattern. Individual images taken through high-numerical aperture objectives are combined from each position of the light pattern to reconstruct the final image (Komis et al., 2015).

In this study, we utilized advanced microscopy method such as light-sheet microscopy for developmental imaging of PLDα1 under natural condition to explore cell-type specific expression. In addition, we provide a high-resolution subcellular localization of PLDα1 in both dividing and non-dividing Arabidopsis cells in the root meristem and leaf petioles.

MATERIALS AND METHODS

Plant Material, Mutant Screens

Seedlings were grown vertically on half-strength MS medium (Murashige and Skoog, 1962) supplemented with 0.5% (w/v) gellan gum for 14 d in Fytotron with 21°C and a 16/8 h (light/dark) photoperiod. The illumination intensity was 150 μmol m^{-2} s^{-1}. Plants 12–15 days old were transferred to soil and cultivated in Fytotron with 21°C and a 16/8 h (light/dark) photoperiod and with the illumination intensity of 150 μmol m^{-2} s^{-1}.

We have used T-DNA insertion lines *pldα1-1* (SALK_067533) and *pldα1-2* (SALK_053785) described previously by Bargmann et al. (2009) and Zhang et al. (2004). To check the T-DNA insertions primers were designed by the SIGnAL iSect tool (http://signal.salk.edu/tdnaprimers.2.html), and PCR was performed using genomic DNA from seedlings. *A. thaliana* ecotype Columbia-0 (Col-0) was used as the control in the complementation assay (stomatal aperture measurement).

Preparation of Complemented PLDα1-YFP

To genetically complement mutant lines, the coding sequence of wild-type *PLDα1*(At3g15730) along with the native *PLDα1* promoter (1,944 bp upstream of the initiation codon ATG of *PLDα1*) was cloned into pGreen0229-YFP-Tnos vector using *Bam*HI-*Kpn*I restriction digest to generate *proPLDα1::PLDα1:YFP* construct. The constructs were confirmed by sequencing and transformed by floral dip method (Clough and Bent, 1998; Davis et al., 2009) to Arabidopsis Col-0 ecotype (wild type) as well as to *pldα1-1* and *pldα1-2* mutants using *Agrobacterium tumefaciens* strain GV 3101. In T1 generation we have selected three independent transgenic lines with the same fluorescent properties. One line was chosen and T2 or T3 progeny of BASTA-resistant transformants, carrying a single homozygous insertion, were used for experiments.

Preparation of Transgenic Line Carrying PLDα1-YFP and mRFP-TUB6

Arabidopsis *pldα1-2* stably expressing *proPLDα1::PLDα1:YFP* in T2 generation were crossed with Col-0 plants stably expressing *pUBQ1:mRFP::TUB6* kindly provided by Geoffrey O. Wasteneys (Ambrose et al., 2011). F1 generation plants with PLDα1-YFP and mRFP-TUB6 expression were selected based on fluorescence

signal in the epifluorescence microscope (Axio Imager.M2, Carl Zeiss, Germany).

Immunoblotting Analysis

Immunoblotting analysis was performed as described previously (Takác et al., 2017). Seedlings of 5 days old *pldα1-1* PLDα1-YFP and *pldα1-2* PLDα1-YFP complemented plants, a progeny from one selected T2 plant from each independent transgenic SALK line, were used for immunoblotting analysis. Roots from ∼50 seedlings of 14 days old plants of *A. thaliana*, ecotype Col-0, *pldα1-1,* and *pldα1-2* single mutants as well as *pldα1-1* PLDα1-YFP and *pldα1-2* PLDα1-YFP complemented lines were homogenized using liquid nitrogen to fine powder and the proteins were extracted in E-buffer [50 mM HEPES (pH 7.5), 75 mM NaCl, 1 mM EGTA, 1 mM $MgCl_2$, 1 mM NaF, 10% (v/v) glycerol, Complete™ EDTA-free protease inhibitor and PhosSTOP™ phosphatase inhibitor cocktails (both from Roche, Basel, Switzerland]. After centrifugation at 13000 g in 4°C for 15 min, supernatants were mixed with 4-fold concentrated Laemmli buffer [final concentration 62.5 mM Tris-HCl (pH 6.8), 2% (w/v) SDS, 10% (v/v) glycerol, 300 mM 2-mercaptoethanol] and boiled for 5 min. Protein extracts were separated on 12% TGX Stain-Free™ (Bio-Rad) gels (Biorad). Equal protein amounts were loaded for each sample. Proteins were transferred to polyvinylidene difluoride (PVDF) membranes in a wet tank unit (Bio-Rad) overnight at 24 V and 4°C using the Tris-glycin-methanol transfer buffer. Membranes were blocked in a mixture of 4% (w/v) low-fat dry milk and 4% (w/v) bovine serum albumin in Tris-buffered-saline (TBS, 100 mM Tris-HCl; 150 mM NaCl; pH 7.4) at 4°C overnight. Following washing step with TBS-T (TBS, 0.1% Tween 20) membranes were incubated with polyclonal anti-phospholipase D alpha 1/2 antibody (Agrisera, Sweden) diluted 1:5000 in TBS-T containing 1% (w/v) BSA or with anti-GFP monoclonal antibody (Sigma-Aldrich, Merck, USA) diluted 1:1000 in TBS-T containing 1% (w/v) BSA at room temperature for 1.5 h. As a loading and protein transfer control, membranes were incubated with anti-beta-tubulin monoclonal antibody (Sigma-Aldrich, Merck, USA) diluted 1:2000 in TBS-T containing 1% (w/v) BSA at room temperature for 1.5 h. Following five washing steps in TBST, membranes were incubated 1.5 h at RT with a horseradish peroxidase (HRP) conjugated goat anti-rabbit IgG secondary antibody (diluted 1:5000) in the case of anti-phospholipase D alpha 1/2 primary antibody, and with a HRP conjugated goat anti-mouse IgG secondary antibody (diluted 1:5000; both from Santa Cruz Biotechnology, Santa Cruz, CA, USA) in the case of anti-GFP and anti-beta-tubulin primary monoclonal antibody. After washing in TBS-T, the signals were developed using Clarity Western ECL substrate (Biorad, Hercules, CA, USA). Luminescence was detected on Chemidoc MP documentation system (Biorad). Three biological replicates of immunoblot experiment were performed.

Stomatal Aperture Measurement

Cotyledons of 7 days-old plants of various genotypes were used for stomatal closure analysis as described previously (Jiang et al., 2014). Dissected cotyledons were floated on stomatal opening buffer [10 mM 2-(N-morpholino) ethanesulfonic acid (MES-KOH), pH = 6.15 and 30 mM KCl] under light for 2 h to fully open the stomata. Then they were treated with ABA (10 μM) in stomatal opening buffer for indicated period of time. ABA stock solution was prepared in ethanol. Ethanol in stomatal opening buffer was used as a negative control. Final concentration of ethanol in experimental solutions did not exceeded 0.01% (v/v). Stomatal aperture was documented using epifluorescence microscope AxioImager.M2 (Carl Zeiss, Germany) equipped with EC Plan-Neofluar 10x/0.30 objective (Carl Zeiss, Germany) using transmission light in single focal plane and quantitatively analyzed using Fiji (ImageJ) software.

Whole Mount Immunofluorescence Labeling

Immunolocalization of microtubules, PLDα1, PLDα1-YFP, and clathrin in root wholemounts was done as described previously (Šamajová et al., 2014). Samples were immunolabeled with rat anti-α-tubulin (clone YOL1/34; ABD Serotec), rabbit anti-phospholipase D alpha 1/2 (Agrisera, Sweden), mouse monoclonal anti-clathrin LC (Sigma-Aldrich) or mouse anti-GFP (Abcam) primary antibodies diluted 1:300, 1:300, 1:300 and 1:100, respectively, in 3% (w/v) BSA in PBS at 4°C overnight. In the case of double or triple co-immunolocalization a sequential immunolabeling was performed. Secondary antibodies included Alexa-Fluor 488 goat anti-rat, Alexa-Fluor 488 goat anti-mouse or Alexa-Fluor 546 goat anti-rat IgGs were diluted 1:500 in PBS containing 3% (w/v) BSA for 3 h (1.5 h at 37°C and 1.5 h at room temperature). Where necessary, nuclei were counterstained with DAPI. Microscopic analysis of immunolabeled samples was performed with a Zeiss 710 CLSM platform (Carl Zeiss, Jena, Germany), using excitation lines at 405, 488, and 561 nm from argon, HeNe, diode, and diode pumped solid-state lasers.

Light-Sheet Fluorescence Microscopy

Developmental live cell imaging of 2–3 days old Arabidopsis plants with PLDα1-YFP expression was done with the light-sheet Z.1 fluorescence microscope (Carl Zeiss, Germany) equipped with W Plan-Apochromat 20x/1.0 NA or W Plan-Apochromat 40x/1.0 NA objectives (Carl Zeiss, Germany) and two LSFM 10x/0.2 NA illumination objectives (Carl Zeiss, Germany). Seedlings were prepared in fluorinated ethylene propylene (FEP) tubes with an inner diameter of 2.8 mm and wall thickness of 0.2 mm (Wolf-Technik, Germany) according to the "open system" protocol for long-term live-cell imaging of *A. thaliana* seedlings described by Ovečka et al. (2015). Root was growing in the block of the culture medium inside of the FEP tube and upper green part of the seedling developed in an open space of the FEP tube with the access to air. Sample holder with the sample was placed into observation chamber of the light-sheet microscope tempered to 22°C using a Peltier heating/cooling system. Before insertion of the sample to the microscope plants were ejected slightly out of the FEP tube allowing imaging of the root in the block of solidified culture medium, but without the FEP tube. Before the imaging, liquid medium filling the observation chamber was filter-sterilized using a sterile syringe

filter. Roots were imaged using dual-side light-sheet illumination with excitation laser line 514 nm, beam splitter LP 580 and with emission filter BP525-565. Images were recorded with the PCO.Edge sCMOS camera (PCO AG, Germany) with the exposure time 30 ms and the imaging frequency of every 5 min in Z-stack mode for 5–20 h. Scaling of recorded images in x, y, and z dimensions was 0.228 × 0.228 × 0.499 μm. For counterstaining of plant cell walls with propidium iodide, seedlings were germinating and growing in blocks of the solidified culture medium containing 1 $\mu g.ml^{-1}$ of propidium iodide (Invitrogen, USA) before imaging. Seedlings (2 days old) growing directly in the solidified medium containing propidium iodide were transferred to the light-sheet microscope for root imaging.

Spinning Disk and Confocal Laser Scanning Microscopy

Hypocotyls, leaves with pavement cells, stomata, and trichomes of 5–8 DAG Arabidopsis plants with PLDα1-YFP expression were documented with spinning disk microscope (Cell Observer SD, Carl Zeiss, Germany) equipped with Plan-Apochromat 20x/0.8 (Carl Zeiss, Germany) and Plan-Apochromat 63x/1.40 Oil (Carl Zeiss, Germany) objectives. Cells were imaged with excitation laser 514 nm and with emission filter BP535/30 for YFP. Cotyledons, petioles and guard cells were documented with confocal laser scanning microscope LSM 710 (Carl Zeiss, Germany) equipped with Plan-Apochromat 20x/0.8 (Carl Zeiss, Germany) and alpha Plan-Apochromat 63x/1.46 Oil (Carl Zeiss, Germany) objectives. Plants of 6 DAG were stained with 4 μM FM4-64 (Invitrogen, USA) diluted in half-strength liquid MS medium for 90 min before imaging. Samples were imaged with excitation lasers 514 nm for YFP and 561 nm for mRFP and FM4-64, beam splitters MBS 458/514 for YFP, MBS 458/561 for mRFP and MBS 488/561for FM4-64. Emission spectrum used were 519–550 nm for YFP, 590–610 nm for mRFP and 651–759 nm for FM4-64.

Structured Illumination Microscopy

The same immunolabeled wholemount samples examined with CLSM were also analyzed via a Zeiss SIM platform coupled with a PCO.Edge 5.5 sCMOS camera (Elyra PS.1, Carl Zeiss, Germany). Fluorophores were excited with the 405, 488, 561, and 647 nm laser lines. For acquisition with a 63x/1.40 oil immersion objective, the grating pattern was set to 5 rotations with 5 standard phase shifts per angular position. In case of Z-stacks, Nyquist sampling was selected to be the smallest one (corresponding to DAPI channel with 91 nm section thickness), leading to oversampling of the rest of the channels. Image reconstruction was done according to previously published procedures (Komis et al., 2015).

Image Processing

The post-processing, default deconvolution using Nearest Neighbour or Constrained Iterative algorithms and profile measurement of all fluorescence images in this study, including 3D reconstruction or maximum intensity projection from individual z-stacks and creating subsets was done using ZEN 2010 software. All images exported from ZEN 2010 software were assembled and captioned in Microsoft PowerPoint to final figures.

RESULTS

Expression Patterns of PLDα1-YFP in Arabidopsis Plants

In order to characterize the roles of PLDα1 in plant development, we performed *in vivo* cell- and tissue-specific expression analysis of the PLDα1-YFP driven by native *PLDα1* promoter in two stably transformed *pldα1* mutants of *A. thaliana*. Thus, both *pldα-1-1* and *pldα-1-2* mutants were stably transformed with *proPLDα1::PLDα1:YFP* construct using the floral dip method (Clough and Bent, 1998). Comparison of *proPLDα1::PLDα1:YFP* expression patterns in different aerial organs and tissues of *pldα1-1* and *pldα1-2* mutants stably expressing PLDα1-YFP is presented in **Figure S1**. To prove the expression of PLDα1-YFP fusion protein in experimental plants (*pldα1-1* and *pldα1-2* mutant plants stably transformed with *proPLDα1::PLDα1:YFP* construct), we performed SDS-PAGE with immunoblot analysis using anti-phospholipase D alpha 1/2 and anti-GFP antibodies. This analysis confirmed the presence of PLDα1-YFP fusion protein with the expected molecular mass of 118 kDa, using both anti-PLDα1 and anti-GFP antibodies (**Figures 1A,B**). In Col-0, which was used as a control, anti-PLDα1 antibody showed a protein band with a molecular mass of 91.8 kDa corresponding to PLDα1. We also confirmed the absence of PLDα1 protein in both *pldα1-1* and *pldα1-2* mutant plants. In addition, Col-0, *pldα1-1*, and *pldα1-2* mutant plants were used as negative controls for the use of the anti-GFP antibody and we did not observe any band in these lines (**Figure 1B**).

Functional Complementation of *pldα1-1* and *pldα1-2* Mutants With PLDα1-YFP Expression Driven Under Its Own Promoter

Cellular levels of abscisic acid (ABA) increase in responses to drought and salt stresses, which promotes stomatal closure in order to prevent water loss. Although PLDα1 is the most predominant PLD in plants, *pldα1* knockout mutants do not exhibit significant phenotypical changes (Fan et al., 1997; Zhang et al., 2012). Nevertheless, PLDα1 controls proper water balance in plants responding to ABA by stomatal closure and this response is impaired in the *pldα1* knockout mutants (Jiang et al., 2014; Pleskot et al., 2014; Zhang et al., 2017a). To verify that *pldα1-1* and *pldα1-2* mutants were complemented with *proPLDα1::PLDα1:YFP* construct and show wild type-like behavior, we examined stomatal closure ability of these revertants by measuring stomatal aperture in cotyledons of 7 days old plants after treatment with 10 μM ABA. We have observed significantly increased stomatal closure after ABA treatment of wild type plants in comparison to *pldα1-1* and *pldα1-2* mutants, which were ABA-insensitive and showed no change in stomatal apertures (**Figure 2**). These results were consistent with published data (Zhang et al., 2004; Jiang et al., 2014). Importantly, *pldα1-1* and *pldα1-2* mutant plants genetically complemented with *proPLDα1::PLDα1:YFP* construct reacted

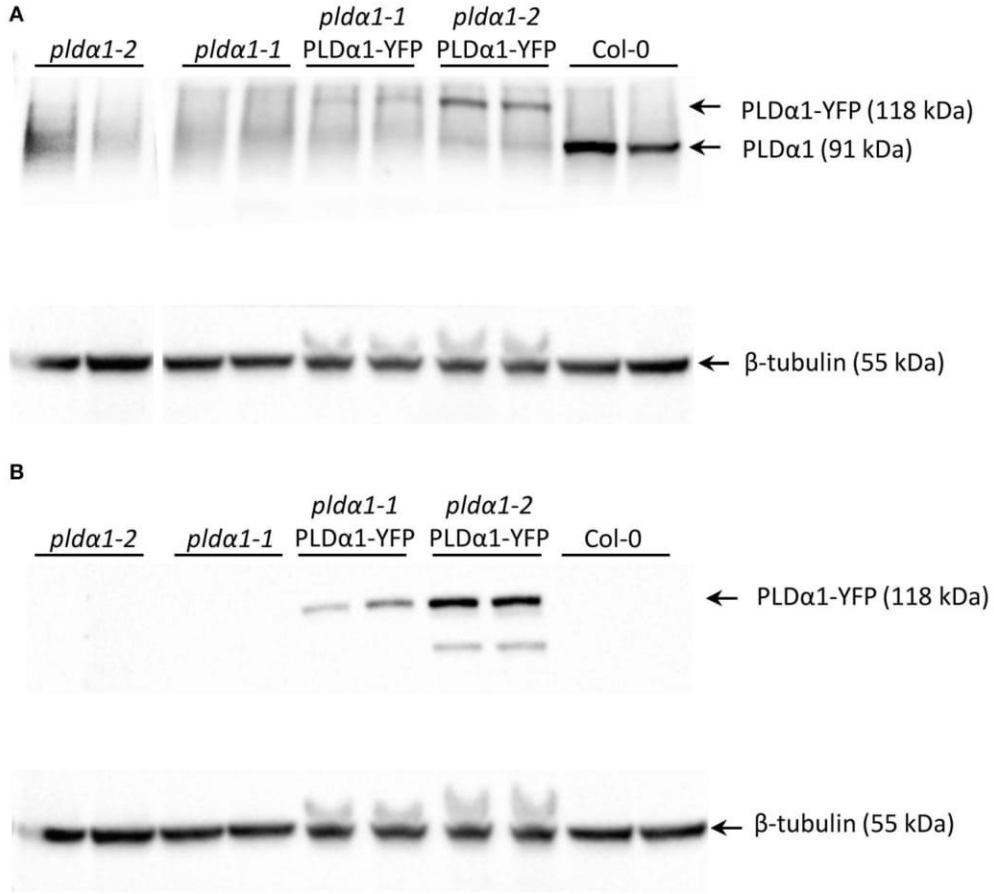

FIGURE 1 | Detection of PLDα1 in roots of *pldα1* mutants and in rescued *pldα1* mutants stably transformed with *proPLDα1::PLDα1:YFP* construct. **(A)** Immunoblots of *pldα1* mutants and rescued *pldα1* mutants probed with anti-PLDα1/2 antibody. **(B)** Immunoblots of *pldα1* mutants and rescued *pldα1* mutants probed with anti GFP antibody. PVDF membranes (BioRad) were probed with anti-beta tubulin as a loading control.

to ABA treatment by substantial decrease of stomatal aperture, similarly to the wild type plants (**Figure 2**). These results confirmed the phenotypical complementation of *pldα1-1* and *pldα1-2* mutants with *proPLDα1::PLDα1:YFP* construct which can be considered as a functional one for further expression and localization studies.

Developmental Expression Pattern and Localization of PLDα1-YFP in Arabidopsis Plants

Observation of developmental expression pattern and localization of PLDα1-YFP fusion protein has been done in *pldα1-1* mutant stably expressing a *proPLDα1::PLDα1:YFP* construct at cell-, tissue- and organ-specific levels using light-sheet fluorescence microscopy (LSFM). Subcellular localization was performed using confocal and spinning disk microscopy. Developmental LSFM has been performed with 2- to 3-days old seedlings that were growing inside of the microscope imaging chamber in time periods ranging from 5 to 20 h. During these imaging periods, roots of experimental plants exhibited continuous growth at constant root growth rates. LSFM offered the possibility not only to localize PLDα1-YFP at the cellular level in root surface tissues (**Figure 3A**), but it also allowed deep root imaging and tissue-specific visualization and localization of PLDα1-YFP in internal root tissues (**Figure 3B**, **Figures S2**, **S3**).

Imaging of tissue-specific expression of PLDα1-YFP in roots using LSFM revealed developmental regulation of PLDα1-YFP amount in the root apex. The expression levels of PLDα1-YFP in the root meristematic zone including rhizodermis, cortex, and procambium were relatively low (**Figure 3B**). On the other hand, particularly strong expression levels were revealed in the apical and lateral root cap cells (**Figure 3C**). Remarkably strong expression was observed in central columella cells and particularly in cells of the third columella layer (**Figures 3B,C**). Semi quantitative evaluation of the PLDα1-YFP amount in different cell layers of root apex (**Figure 3D**) revealed a steep gradient between third and fourth outermost layers of the central root cap (**Figures 3D–F**; profiles 1–2). There was a relatively low amount of PLDα1-YFP in the primary meristems at the position of the stem cell niche in comparison to the lateral root cap cells (**Figures 3D–F**; profile 3). Proximally to the region of initial cells

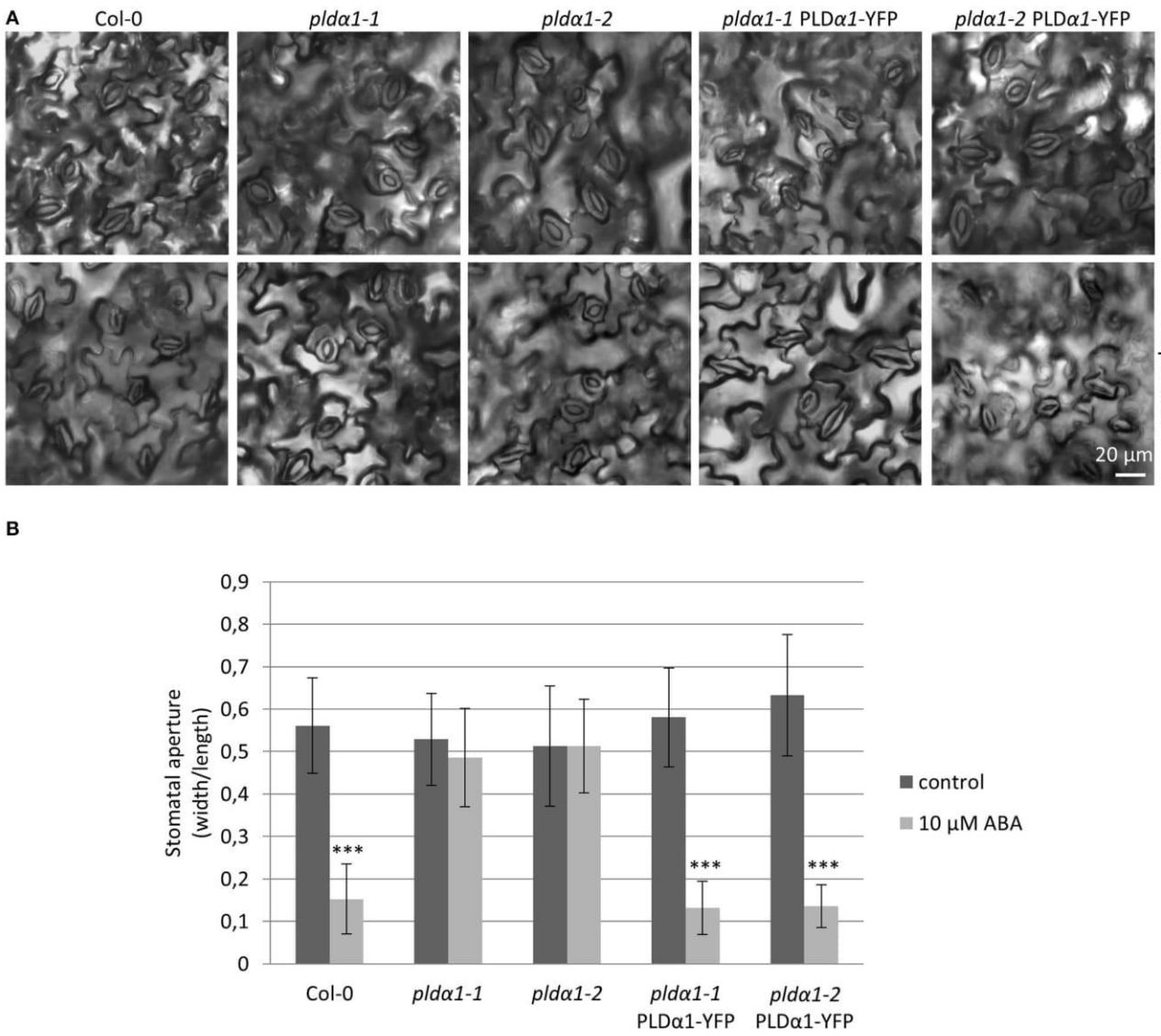

FIGURE 2 | ABA-induced stomatal closure in *pldα1* mutants and rescued plants. **(A)** Cotyledon epidermis of 7 days old Col-0, *pldα1-1*, *pldα1-2*, *pldα1-1* PLDα1-YFP, and *pldα1-2* PLDα1-YFP plants showing opening of stomata in control condition and after 2 h treatment with 10 μM ABA. **(B)** Aperture of cotyledon stomata guard cells of Col-0, *pldα1-1*, *pldα1-2*, *pldα1-1* PLDα1-YFP, and *pldα1-2* PLDα1-YFP (measured as a ratio of aperture width and length, which is reduced upon its closure) in control condition and after 2 h treatment with 10 μM ABA. Bar charts represent the mean ± SD for $n = 40$. Three asterisks indicate statistically significant differences (two-tailed paired *t*-test, $P < 0.001$) in stomatal closure.

there was a clear gradient in the PLDα1-YFP amount within the radial organization of the root meristem with the highest level in the lateral root cap cells, much lower level in the rhizodermis, cortex and endodermis, and the lowest level in central cylinder tissues (**Figures 3D–F**; profile 4). Different expression levels among lateral root cap cells, dermal tissues (rhizodermis, cortex, and endodermis) and central cylinder tissues were clearly visible in the central part of the root meristematic zone (**Figures 3D–F**; profile 5).

In comparison to the relatively low expression level of the PLDα1-YFP in the root meristem, a dramatic enhancement was detected in the root transition zone, particularly in the rhizodermis (**Figure 4A**). Rhizodermal cells showed much stronger expression levels in the trichoblast cell files compared to the atrichoblast ones (**Figures 4B–E**). The relatively strong expression of PLDα1-YFP in trichoblast cells of the transition root zone revealed one additional aspect of particular interest. It was the strongly polarized localization of PLDα1-YFP at the cell corner of the trichoblasts facing the cleft contact with two underlying cortical cells (**Figures 4A,C**). Thereon, the strong expression levels of PLDα1-YFP in trichoblast cell files was also maintained later in the development of root hairs during bulge formation (**Figure 4B**) and in tip-growing root hairs (**Figures 4F–H**). Time-course semi quantitative evaluation

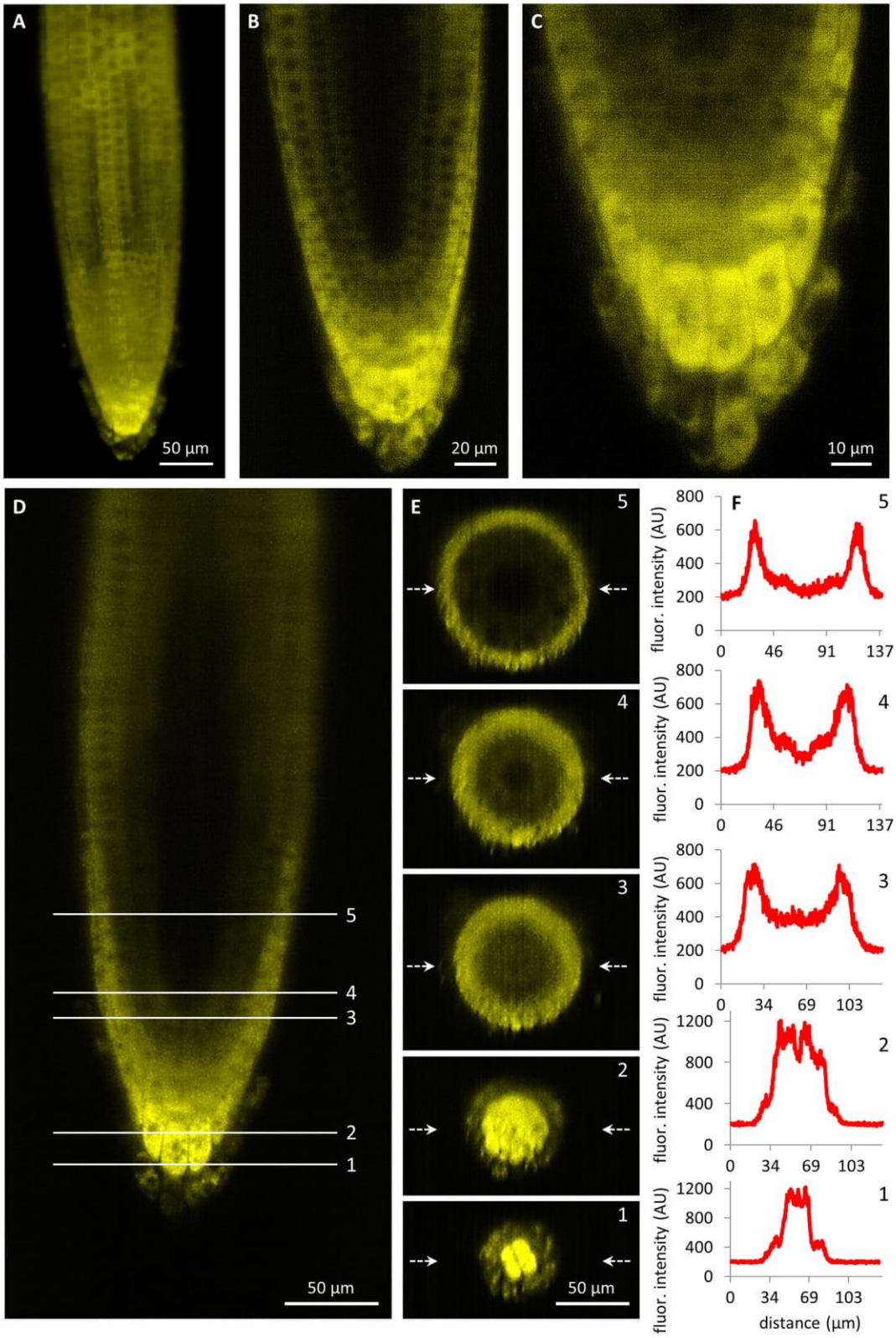

FIGURE 3 | Light-sheet fluorescence microscopy localization of PLDα1-YFP driven by *PLDα1* own promoter in *Arabidopsis thaliana* roots. **(A)** Overview of PLDα1-YFP localization in different tissues of the root tip constructed from maximum intensity projection of 330 optical sections (with thickness of 0.5 µm each).

(Continued)

FIGURE 3 | The amount of PLDα1-YFP fluctuated in root rhizodermal cells while the highest localization was visible in the root cap cells. **(B)** Median optical section of the root tip revealed differential distribution of PLDα1-YFP with the strongest expression in the root cap and lateral root cap cells and with much lower production of PLDα1-YFP in rhizodermal, cortical and endodermal cell layers and with very low production in procambial cells. **(C)** Detail of the root cap showing the strongest expression level of PLDα1-YFP in central columella cells and particularly in cells of the third root cap layer. **(D–F)** Qualitative and semi-quantitative evaluation of the relative PLDα1-YFP distribution in longitudinal and radial zonation of the root tip. Five profiles at different positions of the root tip **(D)** were visualized into orthogonal projections of radial root sections **(E)** and profiles in the median positions of the radial root sections (indicated by arrows) were quantitatively displayed **(F)**. Images were taken from *pldα1-1* mutant plants stably expressing PLDα1-YFP.

of PLDα1-YFP distribution clearly revealed its accumulation in growing tips of root hairs (**Figures 4G,H**). The PLDα1-YFP expression pattern in growing roots thus reflected the tissue-specific and developmentally-regulated transition from low PLDα1-YFP protein levels in actively dividing cells of the root apical meristem to much enhanced protein accumulation in the root transition zone harboring post-mitotic cells preparing for cell elongation (**Figures 3D–F**). Cell differentiation in root tissues led to localized accumulation of PLDα1-YFP, particularly in the developing rhizodermis, where PLDα1-YFP accumulated preferentially in trichoblasts (**Figures 4B–E**), especially during the process of root hair formation (**Figures 4F–H**). In all root tissues expressing moderate levels of PLDα1-YFP (root cap cells, root transition zone, trichoblast cell files and tip growing root hairs) we observed cytoplasmic localization of the fusion protein.

To better identify cell margins and cell types, roots were counterstained with propidium iodide (PI). Although seedling treatment with PI might affect rates of root growth and elongation, expression patterns of PLDα1-YFP in diverse root tissues and cell types were the same as described above (**Figures S2–S5**).

Expression pattern and localization of PLDα1-YFP in different cell types of aerial parts of 6 days old seedlings were documented with confocal and spinning disk microscopy. Relatively high expression level of PLDα1-YFP was observed in hypocotyl epidermal cells (**Figure 5A**), in pavement cells and stomata guard cells of cotyledons (**Figure 5B**), in leaf epidermis and stomata guard cells of leaves (**Figures 5C,D**). Consistently with strong expression level of PLDα1-YFP in rhizodermis and in developing root hairs we observed also strong expression of PLDα1-YFP in leaf trichomes (**Figure 5E**). In more detail, high amounts of PLDα1-YFP were found at tips of trichome branches (**Figure 5E**). A high level of PLDα1-YFP was observed also in epidermal cells of leaf petioles (**Figure 5F**).

In cells of all examined aerial tissues, PLDα1-YFP was localized in the cytosol and predominantly at the cell cortex in the vicinity of the plasma membrane. Additionally, PLDα1-YFP was localized in cytoplasmic strands of interphase cells (**Figure 5F**). Immunofluorescence localization of PLDα1 protein in root meristematic cells of wild type Col-0 plants using anti-PLDα1/2 antibody confirmed its homogeneous localization in the cytosol (**Figure S6**).

Accumulation of PLDα1-YFP in growing root hairs (**Figures 4F–H**) suggested its role in actively growing cell domains. To test this possible scenario in leaf trichomes, we identified individual stages of trichome development in the first true leaf and we performed semiquantitative evaluation of PLDα1-YFP distribution along single profiles in individual trichome branches. To quantify PLDα1-YFP developmental redistribution during trichome formation, we measured profiles of PLDα1-YFP fluorescence in young trichome primordia without branches (**Figure 6A**), in each individual branch of growing trichomes during later developmental stages (**Figures 6B–D**) up to final stage of fully developed three-branched trichomes (**Figure 6E**). Profiling of fluorescence intensity along individual trichome branches clearly revealed higher accumulation of PLDα1-YFP at the tip of actually growing branch during trichome development (**Figure 6F**).

Association of PLDα1-YFP With Microtubules

In order to investigate the localization of PLDα1-YFP fusion protein in respect to cortical and mitotic microtubules we crossed *plda-1-2* mutant plants stably expressing *proPLDα1::PLDα1:YFP* construct with Col-0 plants stably expressing p*UBQ1::mRFP:TUB6* construct (red fluorescent protein marker fused to Arabidopsis alfa-tubulin 6 isoform, Ambrose et al., 2011). Labeling of the plasma membrane in cells of such crossed line was performed with FM4-64. The co-localization experiments were done in non-dividing leaf petiole epidermal cells using confocal laser scanning microscopy (**Figure 7**). 3-D rendering and orthogonal projections showed very close association of cortical microtubules with the plasma membrane and predominant localization of PLDα1-YFP in the cortical cytoplasm (**Figure 7A**). Merge image of all three markers (**Figure 7A**) and semi-quantitative measurement of fluorescence intensities along transversal profile in the cell cortex (**Figure 7B**) revealed only poor co-localization, but rather association of PLDα1-YFP with cortical microtubules. This was evident also from spatial separation of individual optical sections from 3-D scans of the cell cortex starting from the cell surface. By taking individual optical sections of 420 nm thickness (**Figure 7C**), we observed uppermost signal of the FM4-64 related to the plasma membrane first, followed by mRFP signal corresponding to cortical microtubules located beneath the plasma membrane, and only then first appearance of the YFP signal related to the PLDα1. In merge image, the plasma membrane signal was enriched in second and third optical section (0.000 to −0.853 μm from the cell surface), network of cortical microtubules was present in third to fifth optical section (−0.853 to −1.705 μm from the cell surface), while PLDα1-YFP signal was enriched only in fourth to sixth optical section (−1.279 to −2.131 μm from the cell surface). Association and partial colocalization of PLDα1-YFP with cortical microtubules (detected as yellow spots in merge images) is visible only on the cytoplasmic face (**Figure 7C**, optical section −1.279), but not on

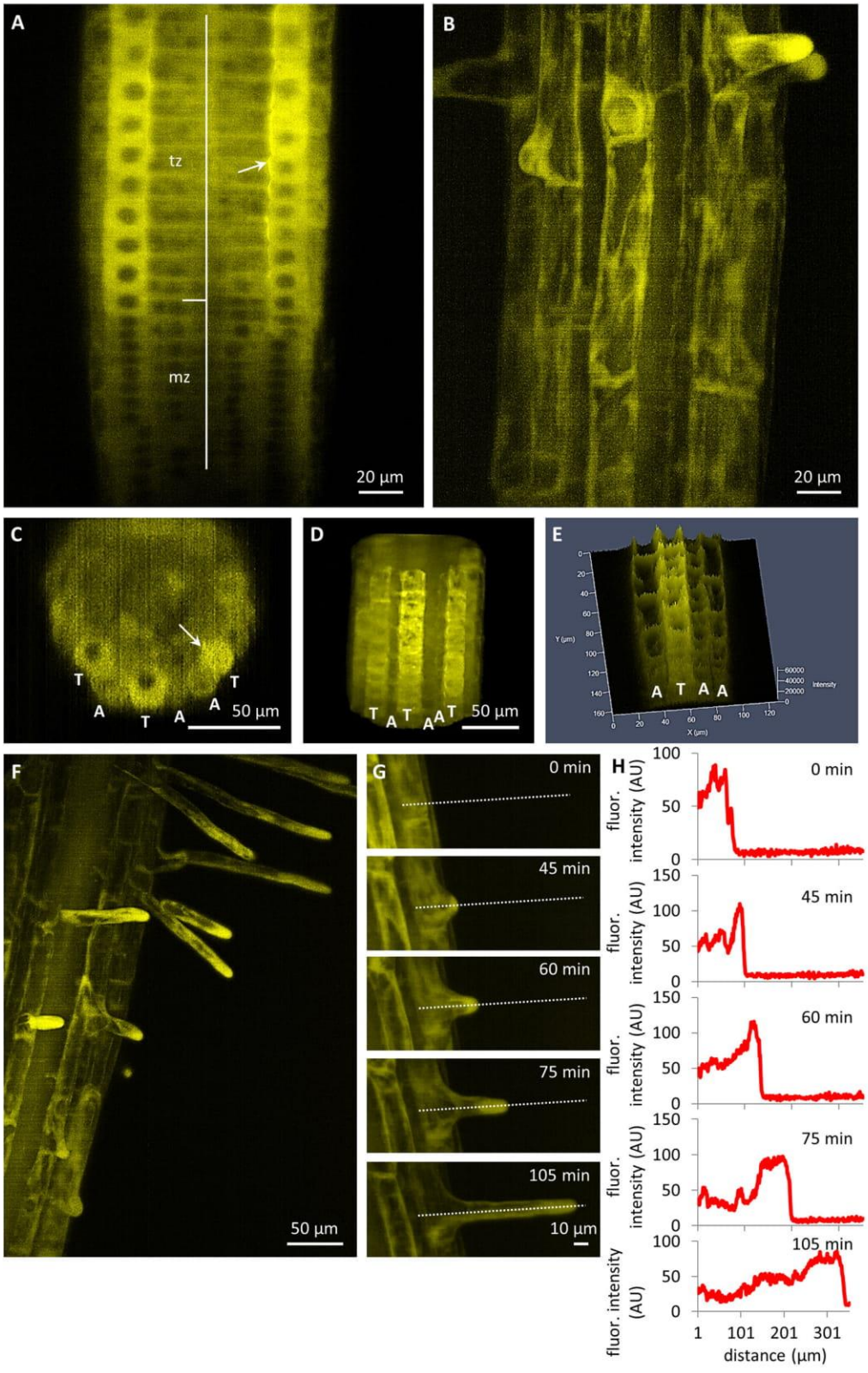

FIGURE 4 | Tissue- and cell-specific localization of PLDα1-YFP driven by its own native promoter in the root of *Arabidopsis thaliana* by light-sheet fluorescence microscopy. **(A)** Distribution of PLDα1-YFP in meristematic zone (mz) with relatively low expression and in transition zone (tz) with enhanced expression.

(Continued)

FIGURE 4 | (B) Differentiation zone of the root with stronger expression level of PLDα1-YFP in trichoblasts and bulges of emerging root hairs and lover expression level in atrichoblast cell files. **(C–E)** Orthogonal projection **(C)**, 3D-rendering **(D)** and intensity-based 3D visualization **(E)** of root differentiation zone showing higher expression level of PLDα1-YFP in rhizodermal trichoblast cell files (labeled as T) and lover expression level in atrichoblast cell files (labeled as A). Arrows in **(A,C)** point local accumulation of PLDα1-YFP at the cell corner of the trichoblasts in the contact with two underlying cortical cells. **(F)** Enhanced localization of PLDα1-YFP in trichoblast cells at the stage of root hair formation and apparent accumulation of PLDα1-YFP in growing root hairs. **(G)** Time-course recording of accumulation and relocation of PLDα1-YFP during the root hair outgrowth in trichoblast root cell. Time frames of individual developmental stages are indicated in min. Dotted lines along the median longitudinal axis of the root hair indicate the position of fluorescence intensity profile measurement. **(H)** Fluorescence intensity profiles of PLDα1-YFP distribution corresponding to particular developmental stages of the root hair formation from the trichoblast root cell in **(G)**. Images were taken from *pldα1-1* mutant plants stably expressing PLDα1-YFP using light-sheet microscopy.

the membrane face (**Figure 7C**, optical section −0.853) of the cortical microtubule network. Sandwich-like arrangement of the plasma membrane, cortical microtubule network, and PLDα1-YFP was evident also from orthogonal view of the examined cell cortex area (**Figure 7D**), proven also by semiquantitative fluorescence profile intensity measurement (**Figure 7E**). These experiments revealed predominantly cytoplasmic localization of PLDα1-YFP.

Colocalization of PLDα1-YFP With Microtubules in Dividing Cells

Colocalization of PLDα1-YFP with mitotic microtubule arrays was observed in dividing epidermal cells of leaf petioles using spinning disk microscopy (**Figures 8A–E**). Association of PLDα1-YFP with the pre-prophase band of microtubules (PPB) was evident in the pre-prophase and prophase stage (**Figure 8A**), with mitotic spindle during metaphase to anaphase (**Figures 8B–D**) and with progressing phragmoplast during cytokinesis (**Figure 8E**). In the pre-prophase and prophase stage PLDα1-YFP accumulated in the cell cortex in a ring-like structure that was broader as PPB. This indicates that PLDα1-YFP, in addition to its colocalization with microtubules inside the PPB, also surrounded PPB in the cortical cytoplasm (**Figures 8A**, **9A**). Additionally, PLDα1-YFP was enriched also in cytoplasmic disk radiating from the nuclear surface to the cell cortex at the PPB plane (**Figure 9A**, **Video S1**). Later on, PLDα1-YFP was strongly accumulated in microtubule arrays of the mitotic spindle which was surrounded by cytoplasmic layer enriched with PLDα1-YFP (**Figures 8B,C**). Association of PLDα1-YFP with microtubules was documented by missing signal in the mitotic spindle occupied by chromosomes during metaphase and anaphase (**Figures 8B–D**). Starting with the segregation of sister chromatids and their pulling to the opposite spindle poles, PLDα1-YFP accumulated also in the central zone of the anaphase spindle (**Figures 8C,D**). Appearance of the early phragmoplast was connected with accumulation of PLDα1-YFP (**Figure 8D**). However, PLDα1-YFP was absent in the late phragmoplast mid-zone during cell plate formation in cytokinesis (**Figure 8E**). In addition, PLDα1-YFP was accumulated also in surrounding cytoplasm (phragmosome) enclosing cytokinetic apparatus in the center of partially vacuolated cells (**Figures 8E**, **9B**, **Video S2**). As the late phragmoplast reached the cell periphery, PLDα1-YFP was associated with emerging cell plate in the central zone of the ring phragmoplast (**Figure 9B**, **Video S2**). Visual comparison of PLDα1-YFP protein level in cortical cytoplasm between dividing cells and neighboring non-dividing cells (**Figures 8A,E**) clearly indicated intracellular relocation and accumulation of PLDα1-YFP within and around mitotic microtubule arrays. It indicates potential cell cycle-dependent cooperation of PLDα1-YFP with microtubules in proliferating cells.

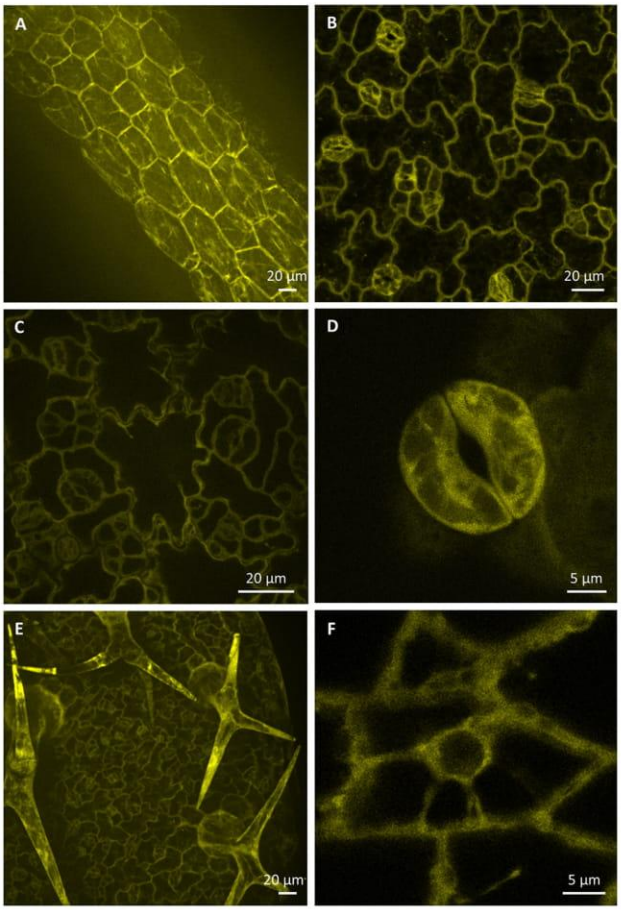

FIGURE 5 | Localization of PLDα1-YFP driven by *PLDα1* own promoter in different aerial organs and tissues of *Arabidopsis thaliana* seedlings. Images were taken from different cell types of aerial tissues of living *pldα1-2* mutants stably expressing PLDα1-YFP driven by its own promoter using confocal and spinning disk microscopy. Localization of PLDα1-YFP in hypocotyl epidermal cells **(A)**, cotyledon epidermal cells and stomata **(B)**, leaf epidermal pavement cells and stomata guard cells **(C)**, leaf stoma guard cells **(D)**, leaf epidermal cells and trichomes **(E)**, and petiole epidermal cell **(F)**. Spinning disk microscopy **(A,C,D)**, confocal microscopy **(B,E,F)**.

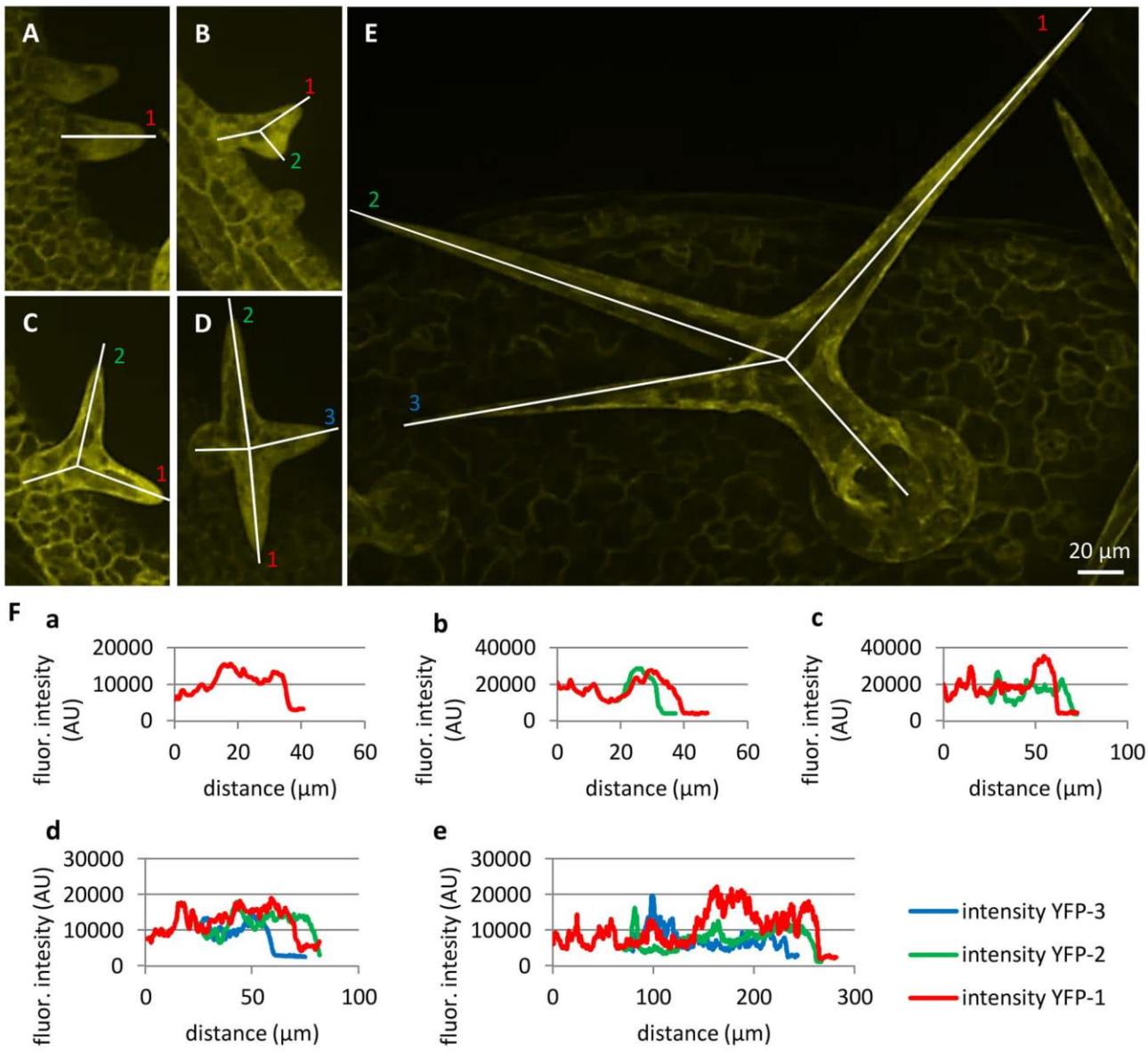

FIGURE 6 | Localization and accumulation of PLDα1-YFP in developing leaf trichomes in *pldα1-2* mutant plants stably expressing PLDα1-YFP driven by *PLDα1* own promoter. Images of maximum intensity projection were reconstructed from individual optical sections taken at the same live cell imaging condition from first **(B,D,E)** and second **(A,C)** true leaves of *pldα1-2* mutants stably expressing PLDα1-YFP. Developing trichomes are displayed from early developing stages with no branches **(A)**, with progressing two branches **(B, C)**, growing three branches **(D)** to maturating three branches **(E)**. **(F)** Profiles of fluorescence intensity of YFP distribution in individual trichome branches indicated by lines in **(A–E)**.

Association of PLDα1-YFP with mitotic microtubule arrays was confirmed using immunofluorescence colocalization of PLDα1-YFP and microtubules in root meristem cells of complemented *pldα1-1* mutant seedlings expressing *proPLDα1::PLDα1:YFP* construct. In non-dividing interphase or pre-mitotic cells PLDα1-YFP protein was localized in the cytoplasm, showing rather homogeneous distribution (**Figure 10A**). However, accumulation as well as partial association of PLDα1-YFP signal with microtubules of PPB, spindle and both early and late phragmoplast was observed in mitotic root cells (**Figure 10A**). Detailed analysis of PLDα1-YFP distribution during cytokinesis revealed its specific association with progressing phragmoplast. 3-D reconstruction, orthogonal projection and rotation of disk phragmoplast with initiated depolymerisation of microtubules in the central part showed predominant association of PLDα1-YFP with leading (outer) edge of the phragmoplast as well as with the trailing (inner) edge, which was created in the central part of the phragmoplast (**Figure 10B**, **Video S3**). Accumulation of PLDα1-YFP at the trailing edge of the late ring phragmoplast was more evident

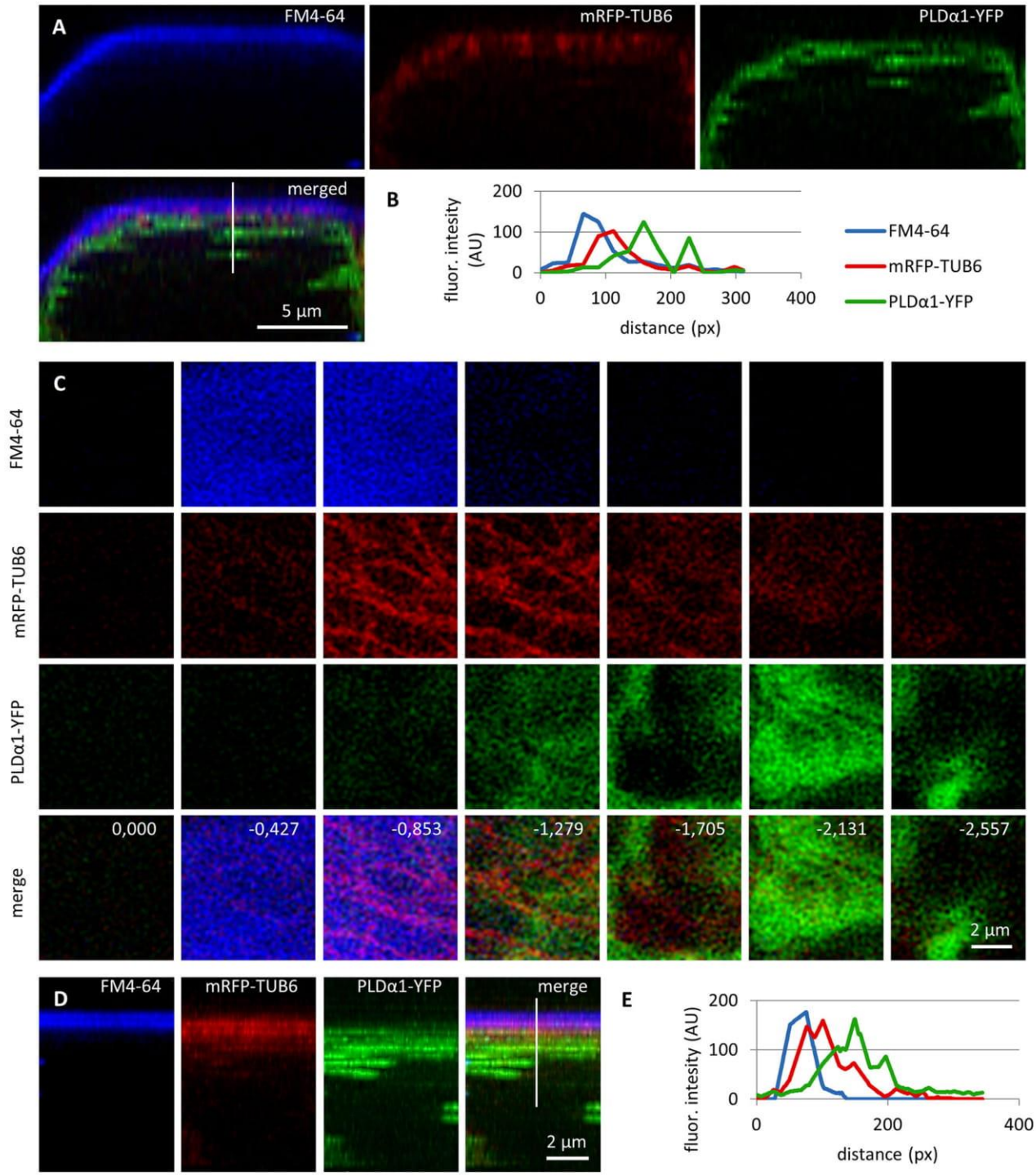

FIGURE 7 | Subcellular localization of PLDα1-YFP and cortical microtubules in respect to the plasma membrane in leaf petiole epidermal cells of the *pldα1-2* mutant plants stably expressing PLDα1-YFP driven by *PLDα1* own promoter. Living interphase petiole cells with the expression of PLDα1-YFP (in green) and mRFP-TUB6 (in red) were counterstained with FM4-64 for delineation of the plasma membrane (in blue). **(A)** Orthogonal view of the 3D-reconstructed petiole cell from the z-stack imaging showing localization of plasma membrane, cortical microtubules and PLDα1. Line in merged image indicates position of measured profile. **(B)** Profile intensity of fluorescence distribution of the plasma membrane (blue), cortical microtubules (red) and PLDα1 (green) based on the distance from the cell surface. **(C)** Frontal view reconstructed from the individual z-stacks starting from the cell surface of the petiole cell to the cortical cytoplasm in steps indicating thickness of individual optical sections in µm. Individual channels are shown separately for the plasma membrane (labeled in blue), cortical microtubules (labeled in red) and PLDα1 (labeled in green), while the merge image shows the overlay of all three channels with the depth annotation. **(D)** Maximum intensity projection of the same image as in C from the side view (orthogonal projection) with the line indicating position of measured profile. **(E)** Profile intensity of fluorescence distribution of the plasma membrane (blue), cortical microtubules (red) and PLDα1 (green) from **(D)** based on the distance from the cell surface. Analysis made in confocal microscope.

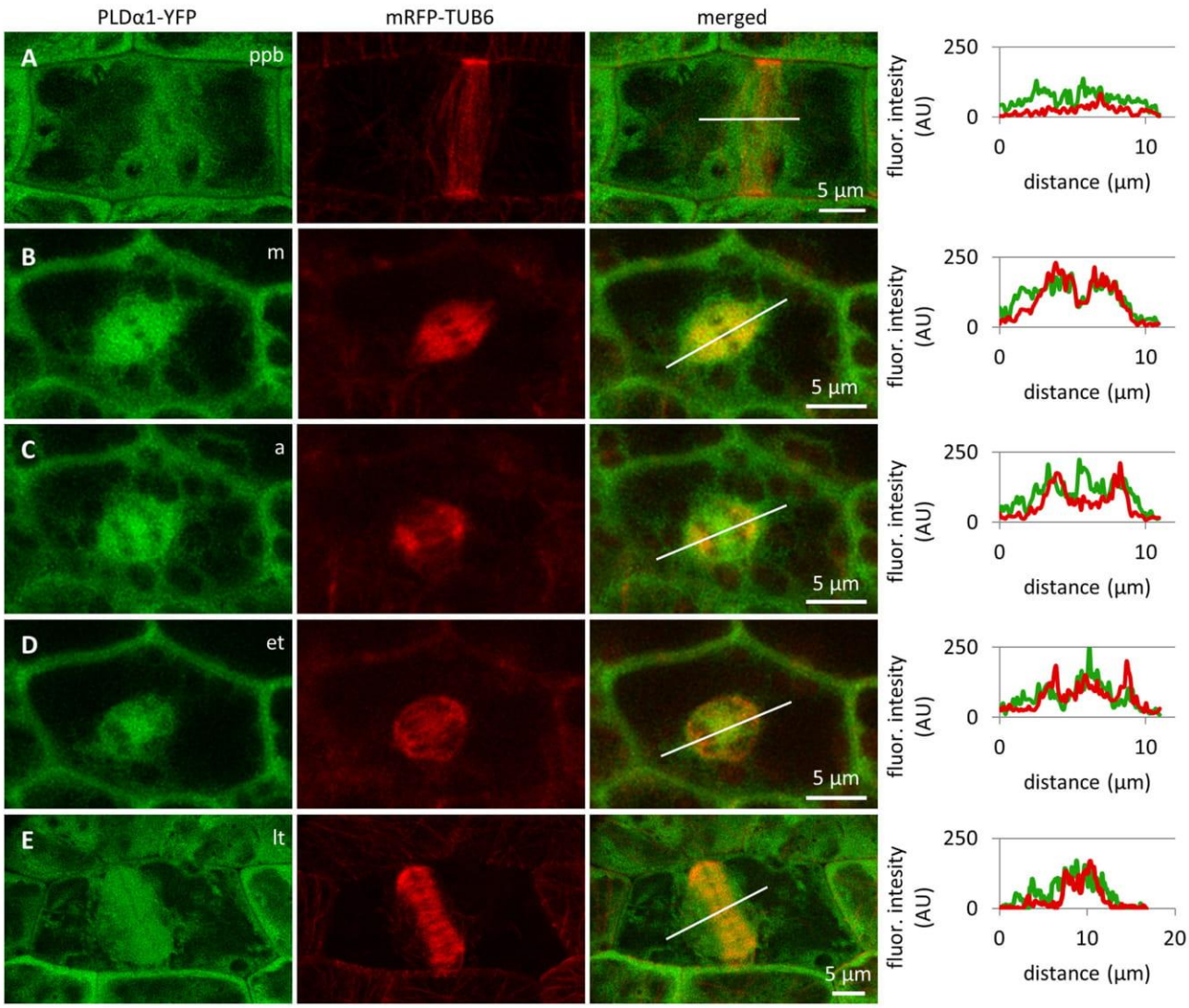

FIGURE 8 | Subcellular localization of PLDα1-YFP during cell division. Live cell imaging of PLDα1-YFP (green) and mRFP-TUB6 (red) in dividing leaf petiole epidermal cell of the *pldα1-2* mutant plants stably expressing PLDα1-YFP driven by *PLDα1* own promoter. PLDα1-YFP was enriched at the location of preprophase band of microtubules (PPB) **(A)**, while it strongly associated with the mitotic spindle **(B–D)**, early **(D),** and late **(E)** phragmoplast. Profiles of fluorescent intensity of YFP and mRFP distribution measured at individual cell division stages are indicated by lines **(A–E)**. ppb, preprophase band of microtubules; m, metaphase; a, anaphase; et, early telophase; lt, late telophase.

at later stages of the phragmoplast expansion (**Figure 10C**, **Video S3**). During phragmoplast enlargement to the cell edges and consolidation of newly formed daughter nuclei, PLDα1-YFP appeared to be more accumulated in the developing cell plate (**Figure 10D**). These results are consistent with PLDα1-YFP accumulation within and around mitotic microtubule arrays during cell division observed by live cell imaging (**Figure 8**).

Next, we employed immunofluorescence localization of tubulin in dividing and non-dividing interphase cells of primary roots of *pldα1-1* mutant to characterize possible involvement of PLDα1 on general microtubule organization (**Figure S7**). However, no obvious differences in the microtubule organization were observed during mitosis, cytokinesis or in non-dividing interphase cells of *pldα1-1* mutant in comparison to wild type Col-0 plants (**Figure S7**).

Association of PLDα1-YFP With Microtubules and CCVs and CCPs

In order to address the functional relationship between mitotic microtubules and PLDα1 in vesicular trafficking, we performed immunofluorescence localization of PLDα1-YFP with microtubules and CCVs and CCPs in dividing and non-dividing rhizodermal cells of complemented *pldα1-1* mutant seedlings expressing *proPLDα1::PLDα1:YFP* construct (**Figure S8**). In cytokinetic cells, PLDα1-YFP was associated with microtubules of the ring phragmoplast, while signal was less abundant in the

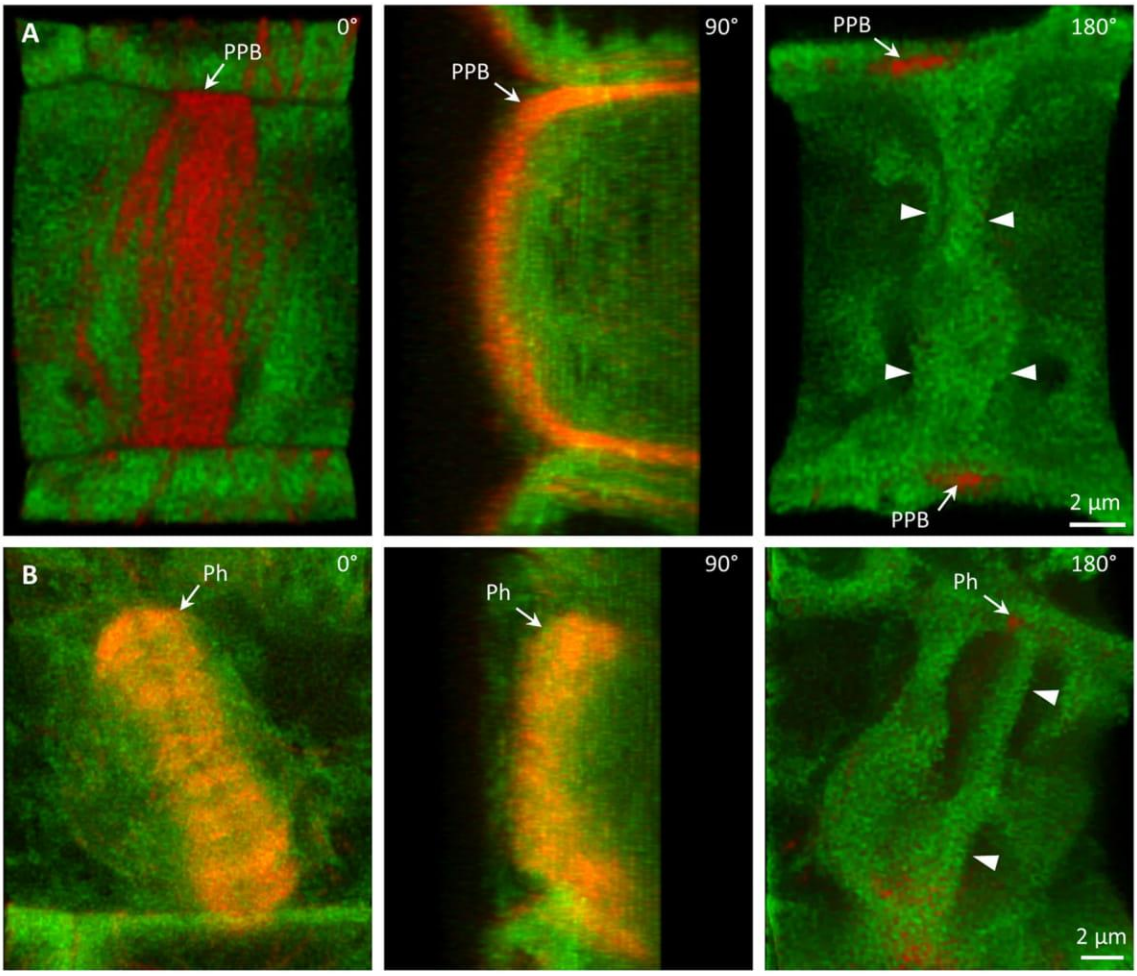

FIGURE 9 | Association of PLDα1-YFP with microtubules during cell division. Live cell imaging of dividing leaf epidermal petiole cells of complemented *pldα1-2 mutant* seedlings expressing PLDα1-YFP and mRFP-TUB6. **(A)** Rotation of 3-D reconstructed pre-prophase cell with established PPB (arrows) showing localization of PLDα1-YFP in cytoplasmic disk between cell nucleus and cortical PPB zone (arrowheads). Individual positions of rotating orthogonal projection correspond to **Video S1**. **(B)** Rotation of 3-D reconstructed cytokinetic cell with ring phragmoplast (Ph, arrows) showing localization of PLDα1-YFP among phragmoplast microtubules, in cytoplasm around the phragmoplast and in emerging cell plate in the central zone of the ring phragmoplast (arrowheads). Individual positions of rotating orthogonal projection correspond to **Video S2**.

phragmoplast central part. The distribution of clathrin signal in this zone was complementary to PLDα1-YFP distribution, with increased abundance in the central part and decreased abundance at the zone of phragmoplast microtubules (**Figure S8A**). Thus, the highest overlap of the clathrin and the PLDα1-YFP signal was observed at the trailing (inner) edge of the enlarging phragmoplast (**Figure S8A**).

In non-dividing rhizodermal cells cortical microtubules were bedecked with PLDα1-YFP closely associated or partially colocalizing with CCVs. PLDα1-YFP was localized in spot-like structures decorating surface of microtubules in close association or partial colocalization with CCVs (**Figure S8B**). For more detailed subcellular study of PLDα1 and microtubules involvement in vesicular trafficking we used super-resolved structural illumination microscopy (SIM). This analysis revealed association and partial colocalization of PLDα1-YFP with CCVs and CCPs in the close vicinity of cortical microtubules, in some cases creating spots and ring-like structures on their surface (**Figure 11A**). Association of PLDα1-YFP with CCVs and CCPs in the cytoplasm between cortical microtubules was observed in clathrin-rich clusters that were in close contact with cortical microtubules (**Figure 11B**). Quantitative analysis of the above colocalization studies of clathrin and microtubules following either SIM or CLSM documentation, showed positive colocalization in Col-0 rhizodermal cells (Pearson's coefficient $R = 0{,}62$) and no colocalization in *pldα1* mutant (Pearson's coefficient $R = 0$). In conclusion, these data document a complex pattern of PLDα1 subcellular localization and its functional relationship to microtubule arrays in both non-dividing and dividing cells of Arabidopsis plants. Combination of different advanced microscopy methods provided data supporting a possible mechanism of interactions between clathrin-dependent endocytosis and cortical (as well as mitotic) microtubules, through the stabilization function of the PLDα1.

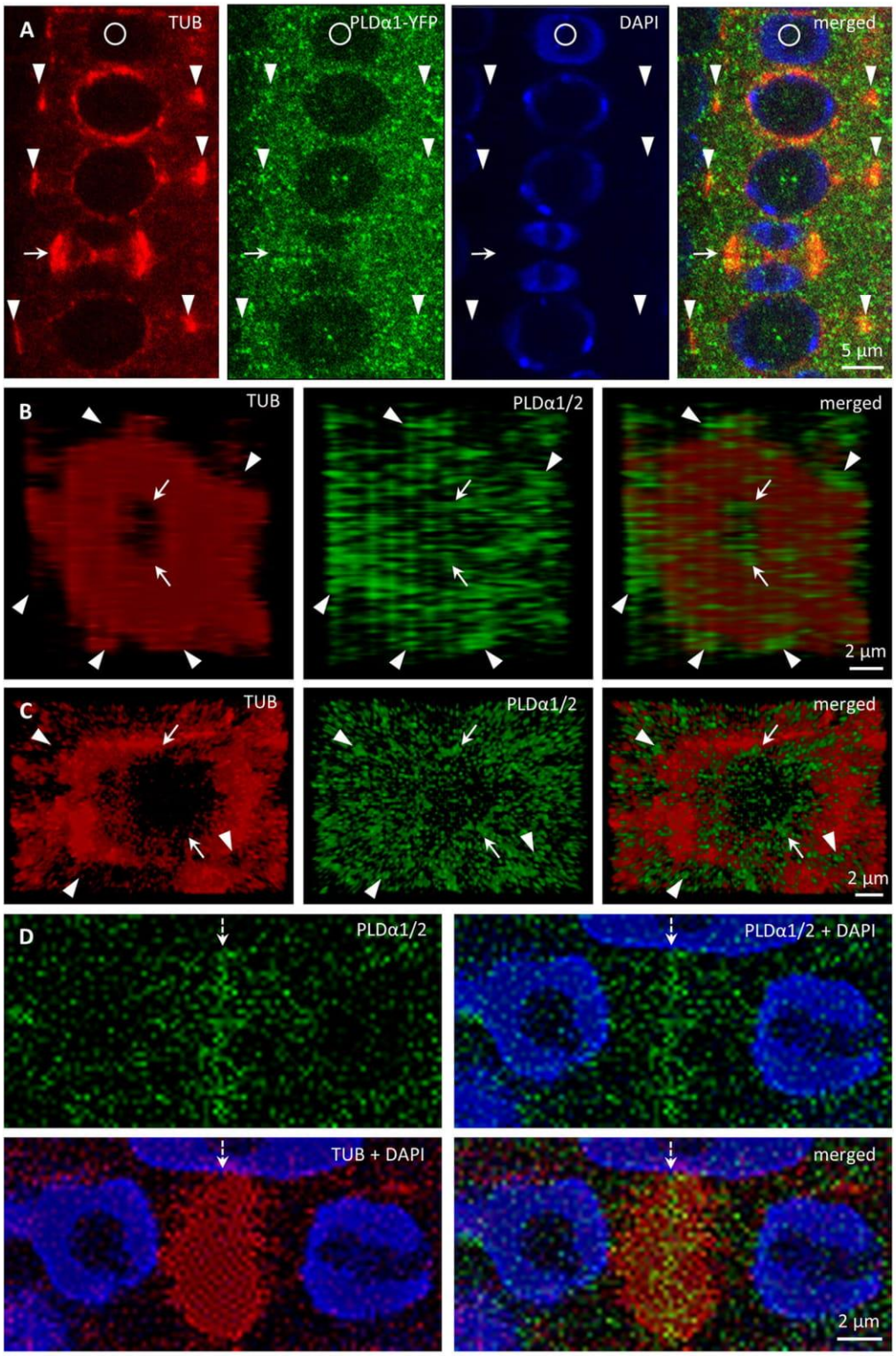

FIGURE 10 | Immunofluorescence colocalization of microtubules and PLDα1–YFP during cell division in Arabidopsis root meristem cells of complemented *pldα1-1* mutant seedlings expressing PLDα1-YFP. **(A)** Colocalization of PLDα1-YFP with microtubules of PPB (arrowheads) and late phragmoplast (arrow). Note that circle indicates non-dividing cell. **(B)** Orthogonal projection of disk phragmoplast stage with the distribution of PLDα1-YFP at the leading (outer) edge (arrowheads) as well as at the trailing (inner) edge in the central part (arrows) of the phragmoplast. Still image of the orthogonal projection corresponds to **Video S3**. **(C)** Orthogonal projection of more advanced ring phragmoplast showing association of PLDα1-YFP with the leading edge (arrowheads) and the trailing edge (arrows) of the phragmoplast. Still image of the orthogonal projection corresponds to **Video S4**. **(D)** Accumulation of PLDα1-YFP in central part of the phragmoplast (arrow) at later stages of cytokinesis.

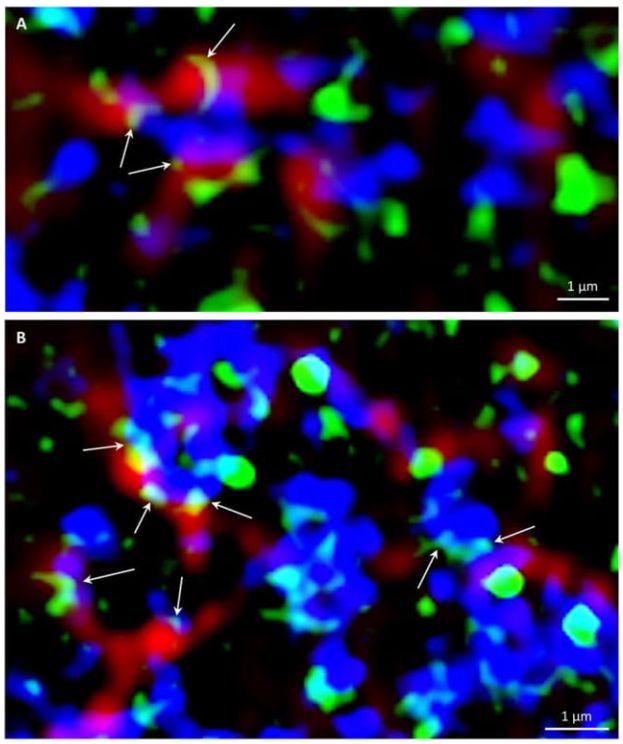

FIGURE 11 | Super-resolved SIM immunofluorescence colocalization of cortical microtubules (red), PLDα1–YFP (green) and clathrin (blue) in Arabidopsis root cells of complemented *pldα1-1* mutant expressing PLDα1–YFP. Arrows indicate spot-like and ring-like structures of PLDα1–YFP in close contact with cortical microtubules and individual CCVs and CCPs **(A)**, or CCVs and CCPs arranged in clusters **(B)**.

Finally, we wanted to test whether stress factors such as high salinity can induce subcellular relocation of PLDα1-YFP in Arabidopsis cells. Indeed, PLDα1-YFP was relocated and accumulated in curved surface areas of plasmolysed protoplasts of hypocotyl cells treated with 500 mM NaCl (**Figure 12**). These data suggest a possible protective role of PLDα1 in these curved areas of retracting protoplasts detached from the cell wall during plasmolysis.

DISCUSSION

The most prominent phospholipid-hydrolyzing enzymes in plants are members of phospholipase D (PLD) family. *A. thaliana* PLDα1 and its product phosphatidic acid (PA) are closely associated with a wide range of cellular and physiological functions, such as regulation of stomatal closure and opening, cytoskeletal reorganization and stress signaling (Qin et al., 1997; Zhang et al., 2004; Bargmann and Munnik, 2006; Pleskot et al., 2013; Hong et al., 2016). Here we employed advanced microscopic methods to reveal precise developmental expression pattern and subcellular localization of PLDα1 in two rescued *pldα1* mutant lines.

ABA is an important hormone that regulates the adaptation of plants to various abiotic stresses (Danquah et al., 2014). It was shown by previous studies that *pldα1* mutant plants did not exhibit significant differences in morphological and developmental characteristics as compared to wild type plants (Fan et al., 1997; Zhang et al., 2012). However, PLDα1 controls proper water balance in plant responding to ABA hormone by stomatal closure which was impaired in *pldα1* knockout mutants (Zhang et al., 2004; Guo et al., 2012; Jiang et al., 2014). Here we transformed *pldα1-1* and *pldα1-2* mutant plants with *proPLDα::PLDα1-YFP* construct and we observed stomatal closure after ABA treatment similar to the wild type, suggesting functional complementation of both mutants by this construct.

Developmental Expression Pattern and Localization of PLDα1-YFP

A previous study assessing organ distribution of PLDα1 protein in Arabidopsis plants by immunoblotting analysis showed higher amounts of this protein in stems, flowers, roots, siliques, and old leaves. Moreover, the highest activity of PLDα1 was found in soluble fractions isolated from roots, flowers, and siliques (Fan et al., 1999). This study, however, lacked cellular resolution within these organs. In contrast, advanced microscopy imaging used in our experiments revealed high expression levels of PLDα1-YFP in the apical and lateral root cap cells. These findings were in agreement with absolute expression levels of PLDα1 transcript from Genevestigator transcriptomic data (Brady et al., 2007). High expression levels of PLDα1-YFP were found also in trichoblast cell files and in developing roots hairs suggesting its role during root hair development. These results are consistent with work of Potocký et al. (2014) reporting PA localization in the plasma membrane of tip-growing pollen tubes. In the aerial part of the plant we observed high PLDα1-YFP protein signal in pavement and stomata guard cells, which is again in accordance to Genevestigator transcriptomic data (Yang et al., 2008). On the other hand, and contrary to Genevestigator transcriptomic data (Marks et al., 2009), we observed high expression levels of PLDα1-YFP in developing trichomes. These results support the role of PLDα1 protein in cell developmental processes and polar cell growth.

Cytoplasmic Localization of PLDα1-YFP

The subcellular distribution of PLDα1 based on immunoblotting analyses of fractionated extracts of Arabidopsis leaves revealed the highest content at the plasma membrane, CCVs, intracellular membranes and mitochondria while only a small amount of protein was detected in nuclei (Fan et al., 1999).

Previously, it was reported that activation of PLD leads to rearrangement of cortical microtubules in suspension BY-2 cells (Dhonukshe et al., 2003). Later it was shown that PLDδ is the cortical microtubule-binding protein (Andreeva et al., 2009; Ho et al., 2009). Moreover, a current study revealed colocalization of the PLDδ with cortical microtubules near to the plasma membrane in the hypocotyl cells of Arabidopsis (Zhang et al., 2017b). Microtubule dynamics controls important processes such as mitosis, cytokinesis, cell elongation, and signal transduction (Wymer and Lloyd, 1996; Hashimoto and Kato, 2006; Jiang et al., 2014). Under normal conditions, knockout mutant *pldα1* showed

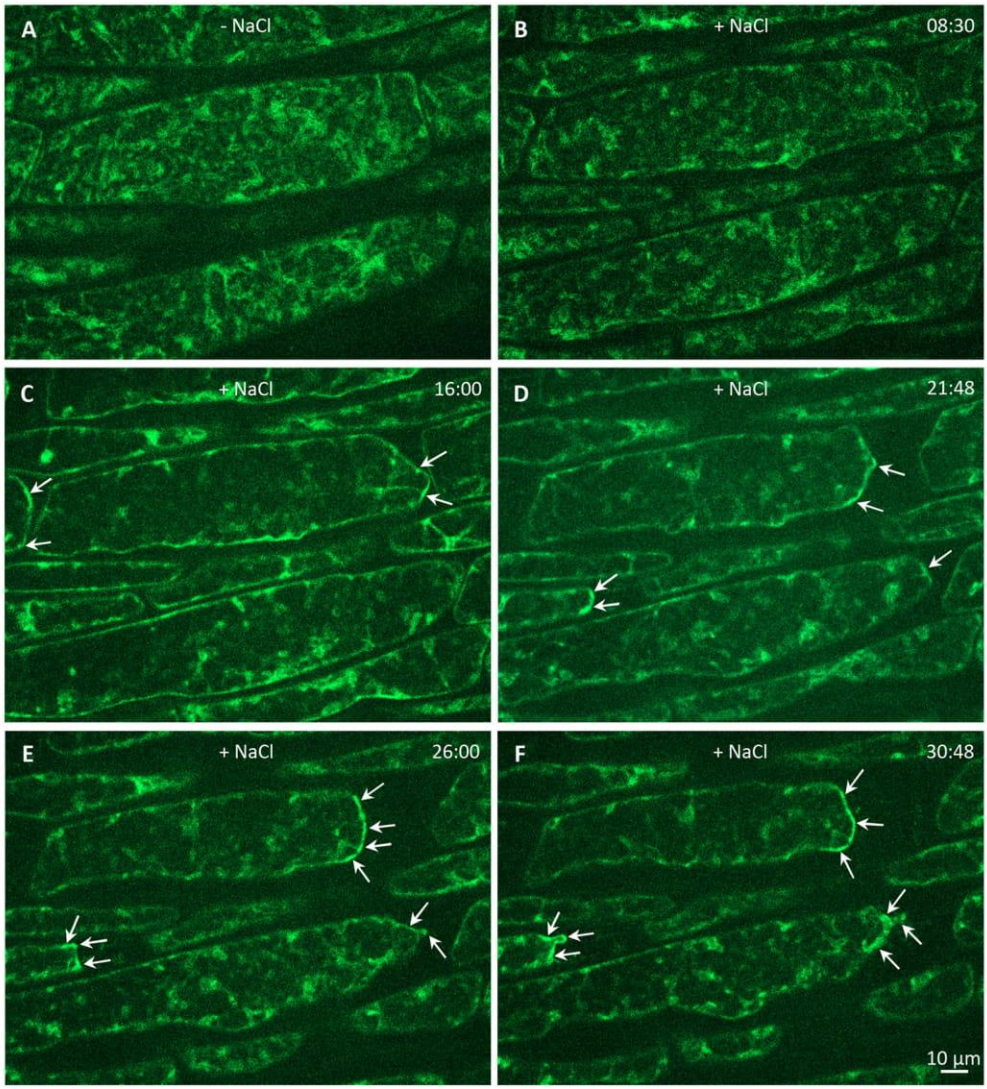

FIGURE 12 | Effect of salt stress on relocalization of PLDα1-YFP (shown in artificial green color) driven by its native promoter in hypocotyl epidermal cells of complemented *pldα1-2* mutant. **(A)** Time-lapse imaging of PLDα1-YFP in hypocotyl epidermal cells under control conditions without salt and **(B–F)** during plasmolysis induced by 500 mM NaCl. The dynamic relocation and accumulation of PLDα1-YFP in plasmolyzed surface areas of detaching protoplasts is depicted by arrows. Time is indicated in min:sec.

no changes in microtubule organization and density as compared to wild type plants (Zhang et al., 2012). However, PLDα1 knockout in Arabidopsis leads to more severe disruption of cortical microtubules by inhibitors (Zhang et al., 2017a) or under salt stress conditions (Zhang et al., 2012). Furthermore, under the salt stress conditions PLDα1 is activated and produce PA which directs AtMAP65-1 to the plasma membrane, leading to microtubule stabilization and enhanced cell protection (Zhang et al., 2012; Pleskot et al., 2014).

PLDα1 is localized in both soluble and membrane fractions. It can translocate from cytosolic to membrane fractions and perform hydrolysis of membrane lipids under stress conditions (Wang et al., 2000; Hong et al., 2016). In our study we observed mainly cytoplasmic localization of PLDα1-YFP, sometimes in the vicinity of cortical microtubules, in non-dividing cells. By contrast, the localization of PLDδ which interacts with cortical microtubules was primarily restricted to the plasma membrane (Zhang et al., 2017b). With the entering of the cell to the mitosis PLDα1-YFP was enriched at mitotic microtubule arrays, namely PPB, microtubules of mitotic spindle in prophase, metaphase and anaphase, as well as to microtubules of the phragmoplast during cytokinesis. Although, colocalization between PLDα1 protein and microtubules was not previously observed in non-dividing protoplasts (Zhang et al., 2012), we detected accumulation of PLDα1-YFP at microtubule arrays during mitotic progression. These results were further confirmed using immunofluorescence colocalization of PLDα1-YFP and microtubules. PLDα1-YFP protein was slightly accumulated and partially colocalized with

microtubules of preprophase band, spindle, and both early and late phragmoplast.

Multiple PLDs have been implicated to have redundant roles in ABA signaling and hyperosmotic stress. However, their mechanisms of action might be different. Single knockouts of either *PLDα1* or *PLDδ* cause the inhibition of ABA-induced stomatal closure while stomata of double mutant are almost completely insensitive to ABA (Zhang et al., 2004; Guo et al., 2012; Uraji et al., 2012; Hong et al., 2016). Moreover, PLDα1, through PA as an intermediate, promotes H_2O_2 production, whereas PLDδ mediates the response to H_2O_2 in the ABA signaling pathway. In this scenario PLDα1 can indirectly regulate PLDδ activity through ROS production (Guo et al., 2012; Hong et al., 2016). GhPLDα1 and H_2O_2 in the upland cotton (*Gossypium hirsutum*) are important components during the onset of the secondary cell wall thickening suggesting a putative role of PLDα1 in the vesicle trafficking (Tang and Liu, 2017). Furthermore, PLDα1 produced PA directs AtMAP65-1 to the plasma membrane and enhances its microtubule stabilizing activity, thus microtubules are stabilized and cell survival is enhanced under salt stress conditions (Zhang et al., 2012; Pleskot et al., 2014). Based on these findings, the question is posed whether PLDα1 can regulate mitotic progress alone or through PA, e.g., through the interaction with e.g., MAP65 proteins and/or PLDδ protein. More experiments should be performed to clarify the molecular mechanism by which PLDα1 affects mitotic microtubule arrays.

In mammals, PLD–PA signaling complexes regulate protein–membrane and membrane–cytoskeleton interactions, as well as vesicle budding and trafficking including exocytosis and endocytosis (McMahon and Gallop, 2005; Donaldson, 2009). Vesicle coating proteins, ARFs, Rho GTPases and soluble N-ethylmaleimide-sensitive factor attachment receptor (SNARE) proteins can interact with PLD and/or PA during vesicle formation at donor membranes, transport, docking, and fusion of vesicles with the target membranes (Chernomordik and Kozlov, 2003; Donaldson, 2009). In plants, there is some evidence that ARFs, Rho GTPases, SNARE proteins and PLDs are involved in vesicle targeting to the cell division plane, vesicle fusion, and cell plate biogenesis, although the exact roles of particular signaling proteins remains elusive (Zárský et al., 2009; El Kasmi et al., 2013; Smertenko et al., 2017).

Spo14 is phospholipase D of *Saccharomyces cerevisiae*, which specifically hydrolyzes phosphatidylcholine to generate choline and PA. Spo14p is localized to the cytoplasm of vegetative cells, however, it relocates to the spindle pole bodies and prospore membrane during sporulation (Rudge et al., 1998; Liu et al., 2007). PA produced by Spo14p is required to localize t-SNARE protein Spo20p to the prospore membrane (Nakanishi et al., 2006; Liu et al., 2007). As mentioned above, PLDα1 was enriched in the CCVs predicting its role in vesicular trafficking (Fan et al., 1999). Furthermore, AP180 (N-terminal homology domain clathrin-assembly) proteins and clathrins were identified as PA binding proteins in a previous proteomic study (McLoughlin et al., 2013). Similarly, epsin-like clathrin adaptor 1 binds PA under the negative membrane curvature stress in Arabidopsis (Putta et al., 2016). Furthermore, PLDα1 coimmunoprecipitates with Arabidopsis AP-2 complex and clathrin (Yamaoka et al., 2013), indicating that PLDα1 contributes to clathrin-mediated endocytosis. These data indicate that proteins involved in the clathrin-dependent endocytosis are potential targets of PLDα1-generated PA. Here we provide evidence for close associations of PLDα1-YFP with cortical and mitotic microtubules during cell division. It has been shown previously that the PPB region at the cell cortex possess a large number of CCPs and CCVs. Expected role of clathrin-mediated endocytosis in the PPB area is related to the regulated modification of the cell cortex by controlled removal of particular membrane proteins by endocytosis, being part of the cell division plane memory establishment (Karahara et al., 2009). Centrifugal expansion of the phragmoplast during cytokinesis is driven by microtubule polymerization with substantial microtubule stabilization by bundling at the leading edge of the phragmoplast (Murata et al., 2013). Phragmoplast microtubules are responsible for delivery of vesicles creating cell plate in the mid-zone region. Cell plate formation, however, is also based on removal of excess membrane and cell wall material. Endocytosis and membrane recycling thus play an indispensable role during cell plate expansion (van Oostende-Triplet et al., 2017). Endocytosis was implicated in the spatial restriction of syntaxin protein KNOLLE to the cell plate (Boutté et al., 2010) and in the removal of the cellulose synthase enzymes from the central part and their recycling to the peripheral growth zone of the cell plate (Miart et al., 2014). Consistently with these observations electron tomography analysis revealed a high density of CCPs and CCVs during the transformation of the tubulo-vesicular network to a planar fenestrated sheet during cell plate formation (Seguí-Simarro et al., 2004). CCPs and CCVs were mostly localized at the trailing (inner) edge of the enlarging phragmoplast. Internalization and recycling of material from the central part and its delivery to the leading edges of maturing cell plate were thus definitely connected to clathrin-dependent endocytosis (Boutté et al., 2010; Ito et al., 2012; Teh et al., 2013; Miart et al., 2014). Based on these findings and on our results we suggest that PLDα1 and its product PA might participate in the complex signaling network involved in the vesicle trafficking and membrane assembly during plant cytokinesis. Although the precise mechanism by which PLDα1 or PA are involved in these processes is unknown, our results indicate that PLDα1 localized on microtubule surface can potentially functions as molecular glue for CCPs and CCVs associated with microtubules. This is further corroborated by the observation that microtubule-colocalized clathrin structures are quantitatively absent in the *pldα1* mutant.

In animal literature it is suggested that PLD and PA participate in vesicle formation at various cellular membranes. One possible mechanism is that physiochemical properties of PLD and PA as well as their protein-protein and lipid-protein interactions (e.g., with dynamin, COPI, kinesin, ARF, small GTPases, phosphatases, kinases, and phosphoinositols) might regulate such vesicle formation (Manifava et al., 2001; Roth, 2008; Brito de Souza et al., 2014). More physiological and functional studies will be needed to prove this concept experimentally. But complex pattern of PLDα1 developmental expression, subcellular localization, and

its close association with cortical and mitotic microtubules in Arabidopsis documented here by advanced microscopy methods substantially contribute to this scenario and will promote further research in this topic.

AUTHOR CONTRIBUTIONS

DN, PV, MO, OŠ, and JC: Conducted experiments; DN, MO, and OŠ: made image post acquisition analyses; GK: Helped with quantitative evaluations and data interpretation; PV, DN, MO, OŠ, and JŠ: Wrote the manuscript with input from all co-authors; JŠ: Proposed experiments and supervised this study, participated on data interpretation and finalized manuscript.

FUNDING

This work was supported by the Czech Science Foundation GACR, grant Nr. 16-22044S.

ACKNOWLEDGMENTS

We thank professor Geoffrey O. Wasteneys for Arabidopsis seeds carrying *pUBQ1:mRFP::TUB6* construct.

SUPPLEMENTARY MATERIAL

The Supplementary Material for this article can be found online at: https://www.frontiersin.org/articles/10.3389/fpls.2018.00371/full#supplementary-material

Figure S1 | Comparison of PLDα1-YFP localization in different aerial organs and tissues of *pldα1-1* **(A–E)** and *pldα1-2* **(F–J)** mutants stably expressing PLDα1-YFP driven by its own promoter: epidermis of first true leaf **(A,F)**, epidermal cells of hypocotyl **(B,G)**, epidermal cells of cotyledon petiole **(C,H)**, epidermal cells of cotyledon **(D,I)** and entire 5 days-old seedling **(E,J)**.

Figure S2 | PLDα1-YFP localization in different tissues of the root tip of rescued *pldα1-1* mutant stably transformed with *proPLDα1::PLDα1:YFP* construct by light-sheet fluorescence microscopy. **(A)** Localization of PLDα1-YFP in cells of the root tip counterstained by propidium iodide and merged image. Profiles at different positions of the root tip are visualized in orthogonal projections of radial root sections in **(B)**.

Figure S3 | PLDα1-YFP localization in different tissues of the root tip of rescued *pldα1-2* mutant stably transformed with *proPLDα1::PLDα1:YFP* construct by light-sheet fluorescence microscopy. **(A)** Localization of PLDα1-YFP in cells of the root tip counterstained by propidium iodide and merged image. Profiles at different positions of the root tip are visualized in orthogonal projections of radial root sections in **(B)**.

Figure S4 | PLDα1-YFP localization in trichoblast (labeled as T) and atrichoblast (labeled as A) rhizodermis cell files of the root tip of rescued *pldα1-1* mutant stably transformed with *proPLDα1::PLDα1:YFP* construct by light-sheet fluorescence microscopy. Localization of PLDα1-YFP, propidium iodide and merged image of the root transition zone in longitudinal **(A)** and transversal **(B)** root projections.

Figure S5 | PLDα1-YFP localization in trichoblast (labeled as T) and atrichoblast (labeled as A) rhizodermis cell files of the root tip of rescued *pldα1-2* mutant stably transformed with *proPLDα1::PLDα1:YFP* construct by light-sheet fluorescence microscopy. Localization of PLDα1-YFP, propidium iodide and merged image of the root transition zone in longitudinal **(A)** and transversal **(B)** root projections.

Figure S6 | Immunofluorescence localization of PLDα1 protein in Arabidopsis root meristem cells of wild type Col-0 seedlings showing homogeneous distribution of PLDα1 in the cytoplasm.

Figure S7 | Organization of microtubule arrays in dividing cells of root meristem in *pldα1-1* mutant in comparison to wild type Col-0. Arrowheads indicate PPBs, red arrows mitotic spindles and white arrows phragmoplasts. Immunofluorescence localization of microtubules with confocal microscopy, nuclei are counterstained with DAPI.

Figure S8 | Immunofluorescence colocalization of microtubules with PLDα1–YFP and clathrin in Arabidopsis root cells of complemented *pldα1-1* mutant expressing PLDα1–YFP. **(A)** Colocalization of microtubules (green), PLDα1–YFP (red), and clathrin (blue) in late phragmoplast of root meristematic cell during the cytokinesis. **(B)** Colocalization of cortical microtubules (green), PLDα1–YFP (blue) and clathrin (red) in interphase root cell. Boxed areas in **(B)** are magnified in **(C)**. Arrows indicate colocalization of PLDα1–YFP with clathrin in association with cortical microtubules.

Video S1 | 3-D rendering of leaf epidermal petiole cell at the pre-prophase stage of cell division with established PPB and localization of PLDα1-YFP.

Video S2 | 3-D rendering of leaf epidermal petiole cell at the cytokinesis with ring phragmoplast and localization of PLDα1-YFP.

Video S3 | 3-D rendering of early disk phragmoplast in root meristematic cell at the cytokinesis with localization of PLDα1-YFP.

Video S4 | 3-D rendering of late ring phragmoplast in root meristematic cell at the cytokinesis with localization of PLDα1-YFP.

REFERENCES

Ambrose, C., Allard, J. F., Cytrynbaum, E. N., and Wasteneys, G. O. (2011). A CLASP-modulated cell edge barrier mechanism drives cell-wide cortical microtubule organization in Arabidopsis. *Nat. Commun.* 16, 430. doi: 10.1038/ncomms1444

Andreeva, Z., Ho, A. Y. Y., Barthet, M. M., Potocký, M., Bezvoda, R., Žárský, V., et al. (2009). Phospholipase D family interactions with the cytoskeleton: isoform δ promotes plasma membrane anchoring of cortical microtubules. *Funct. Plant Biol.* 36, 600–612. doi: 10.1071/FP09024

Bargmann, B. O., and Munnik, T. (2006). The role of phospholipase D in plant stress responses. *Curr. Opin. Plant Biol.* 9, 515–522. doi: 10.1016/j.pbi.2006.07.011

Bargmann, B. O., Laxalt, A. M., ter Riet, B., van Schooten, B., Merquiol, E., Testerink, C., et al. (2009). Multiple PLDs required for high salinity and water deficit tolerance in plants. *Plant Cell Physiol.* 50, 78–89. doi: 10.1093/pcp/pcn173

Boutté, Y., Frescatada-Rosa, M., Men, S., Chow, C. M., Ebine, K., Gustavsson, A., et al. (2010). Endocytosis restricts Arabidopsis KNOLLE syntaxin to the cell division plane during late cytokinesis. *EMBO J.* 29, 546–558. doi: 10.1038/emboj.2009.363

Brady, S. M., Orlando, D. A., Lee, J. Y., Wang, J. Y., Koch, J., Dinneny, J. R., et al. (2007). A high-resolution root spatiotemporal map reveals dominant expression patterns. *Science* 318, 801–806. doi: 10.1126/science.1146265

Brito de Souza, L., Pinto da Silva, L. L., Jamur, M. C., and Oliver, C. (2014). Phospholipase D is involved in the formation of Golgi associated clathrin coated vesicles in human parotid duct cells. *PLoS ONE* 9:91868. doi: 10.1371/journal.pone.0091868

Chernomordik, L. V., and Kozlov, M. M. (2003). Protein-lipid interplay in fusion and fission of biological membranes. *Annu. Rev. Biochem.* 72, 175–207. doi: 10.1146/annurev.biochem.72.121801.161504

Choudhury, S. R., and Pandey, S. (2016). The role of PLDα1 in providing specificity to signal-response coupling by heterotrimeric G-protein components in Arabidopsis. *Plant J.* 86, 50–61. doi: 10.1111/tpj.13151

Choudhury, S. R., and Pandey, S. (2017). Phosphatidic acid binding inhibits RGS1 activity to affect specific signaling pathways in Arabidopsis. *Plant J.* 90, 466–477. doi: 10.1111/tpj.13503

Clough, S. J., and Bent, A. F. (1998). Floral dip: a simplified method for Agrobacterium-mediated transformation of *Arabidopsis thaliana*. *Plant J.* 16, 735–743. doi: 10.1046/j.1365-313x.1998.00343.x

Danquah, A., de Zelicourt, A., Colcombet, J., and Hirt, H. (2014). The role of ABA and MAPK signaling pathways in plant abiotic stress responses. *Biotechnol. Adv.* 32, 40–52. doi: 10.1016/j.biotechadv.2013.09.006

Davis, A. M., Hall, A., Millar, A. J., Darrah, C., and Davis, S. J. (2009). Protocol: streamlined sub-protocols for floral-dip transformation and selection of transformants in *Arabidopsis thaliana*. *Plant Methods* 5:3. doi: 10.1186/1746-4811-5-3

Dhonukshe, P., Laxalt, A. M., Goedhart, J., Gadella, T. W., and Munnik, T. (2003). Phospholipase d activation correlates with microtubule reorganization in living plant cells. *Plant Cell* 15, 2666–2679. doi: 10.1105/tpc.014977

Donaldson, J. G. (2009). Phospholipase D in endocytosis and endosomal recycling pathways. *Biochim. Biophys. Acta* 1791, 845–849. doi: 10.1016/j.bbalip.2009.05.011

El Kasmi, F., Krause, C., Hiller, U., Stierhof, Y. D., Mayer, U., Conner, L., et al. (2013). SNARE complexes of different composition jointly mediate membrane fusion in Arabidopsis cytokinesis. *Mol. Biol. Cell* 24, 1593–1601. doi: 10.1091/mbc.E13-02-0074

Fan, L., Zheng, S., and Wang, X. (1997). Antisense suppression of phospholipase D α retards abscisic acid- and ethylene-promoted senescence of postharvest Arabidopsis leaves. *Plant Cell* 9, 2183–2196. doi: 10.1105/tpc.9.12.2183

Fan, L., Zheng, S., Cui, D., and Wang, X. (1999). Subcellular distribution and tissue expression of phospholipase Dα, Dβ, and Dγ in Arabidopsis. *Plant Phys.* 119, 1371–1378. doi: 10.1104/pp.119.4.1371

Gardiner, J. C., Harper, J. D., Weerakoon, N. D., Collings, D. A., Ritchie, S., Gilroy, S., et al. (2001). A 90-kD phospholipase D from tobacco binds to microtubules and the plasma membrane. *Plant Cell* 13, 2143–2158. doi: 10.1105/tpc.13.9.2143

Guo, L., Mishra, G., Markham, J. E., Li, M., Tawfall, A., Welti, R., et al. (2012). Connections between sphingosine kinase and phospholipase D in the abscisic acid signaling pathway in Arabidopsis. *J. Biol. Chem.* 287, 8286–8296. doi: 10.1074/jbc.M111.274274

Hashimoto, T., and Kato, T. (2006). Cortical control of plant microtubules. *Curr. Opin. Plant. Biol.* 9, 5–11. doi: 10.1016/j.pbi.2005.11.005

Ho, A. Y. Y., Day, D. A., Brown, M. H., and Marc, J. (2009). Arabidopsis phospholipase Dδ as an initiator of cytoskeleton-mediated signalling to fundamental cellular processes. *Funct. Plant Biol.* 36, 190–198. doi: 10.1071/FP08222

Hong, Y., Zhao, J., Guo, L., Kim, S. C., Deng, X., Wang, G., et al. (2016). Plant phospholipases D and C and their diverse functions in stress responses. *Prog. Lipid Res.* 62, 55–74. doi: 10.1016/j.plipres.2016.01.002

Ito, E., Fujimoto, M., Ebine, K., Uemura, T., Ueda, T., and Nakano, A. (2012). Dynamic behavior of clathrin in *Arabidopsis thaliana* unveiled by live imaging. *Plant J.* 69, 204–216. doi: 10.1111/j.1365-313X.2011.04782.x

Jiang, Y., Wu, K., Lin, F., Qu, Y., Liu, X., and Zhang, Q. (2014). Phosphatidic acid integrates calcium signaling and microtubule dynamics into regulating ABA-induced stomatal closure in Arabidopsis. *Planta* 239, 565–575. doi: 10.1007/s00425-013-1999-5

Karahara, I., Suda, J., Tahara, H., Yokota, E., Shimmen, T., Misaki, K., et al. (2009). The preprophase band is a localized center of clathrin-mediated endocytosis in late prophase cells of the onion cotyledon epidermis. *Plant J.* 57, 819–831. doi: 10.1111/j.1365-313X.2008.03725.x

Komis, G., Mistrik, M., Šamajová, O., and Ovečka, M., Bartek, J., and Šamaj, J. (2015). Superresolution live imaging of plant cells using structured illumination microscopy. *Nat. Protoc.* 10, 1248–1263. doi: 10.1038/nprot.2015.083

Liu, S., Wilson, K. A., Rice-Stitt, T., Neiman, A. M., and McNew, J. A. (2007). *In vitro* fusion catalyzed by the sporulation-specific t-SNARE light-chain Spo20p is stimulated by phosphatidic acid. *Traffic* 8, 1630–1643. doi: 10.1111/j.1600-0854.2007.00628.x

Manifava, M., Thuring, J. W., Lim, Z. Y., Packman, L., Holmes, A. B., and Ktistakis, N. T. (2001). Differential binding of traffic-related proteins to phosphatidic acid- or phosphatidylinositol (4,5)- bisphosphate-coupled affinity reagents. *J. Biol. Chem.* 276, 8987–8994. doi: 10.1074/jbc.M010308200

Marks, M. D., Wenger, J. P., Gilding, E., Jilk, R., and Dixon, R. A. (2009). Transcriptome analysis of Arabidopsis wild-type and gl3-sst sim trichomes identifies four additional genes required for trichome development. *Mol. Plant* 2, 803–822. doi: 10.1093/mp/ssp037

McLoughlin, F., Arisz, S. A., Dekker, H. L., Kramer, G., de Koster, C. G., Haring, M. A., et al. (2013). Identification of novel candidate phosphatidic acid-binding proteins involved in the salt-stress response of *Arabidopsis thaliana* roots. *Biochem. J.* 450, 573–581. doi: 10.1042/BJ20121639

McMahon, H. T., and Gallop, J. L. (2005). Membrane curvature and mechanisms of dynamic cell membrane remodelling. *Nature* 438, 590–596. doi: 10.1038/nature04396

Miart, F., Desprez, T., Biot, E., Morin, H., Belcram, K., Höfte, H., et al. (2014). Spatio-temporal analysis of cellulose synthesis during cell plate formation in Arabidopsis. *Plant J.* 77, 71–84. doi: 10.1111/tpj.12362

Munnik, T., and Musgrave, A. (2001). Phospholipid signaling in plants: holding on to Phospholipase D. *Sci. STKE.* 2001:42. doi: 10.1126/stke.2001.111.pe42

Murashige, T., and Skoog, F. (1962). A revised medium for rapid growth and bioassays with tobacco tissue cultures. *Physiol. Plant.* 15, 473–497. doi: 10.1111/j.1399-3054.1962.tb08052.x

Murata, T., Sano, T., Sasabe, M., Nonaka, S., Higashiyama, T., Hasezawa, S., et al. (2013). Mechanism of microtubule array expansion in the cytokinetic phragmoplast. *Nat. Commun.* 4, 1967. doi: 10.1038/ncomms2967

Nakanishi, H., Morishita, M., Schwartz, C. L., Coluccio, A., Engebrecht, J., and Neiman, A. M. (2006). Phospholipase D and the SNARE Sso1p are necessary for vesicle fusion during sporulation in yeast. *J. Cell. Sci.* 119, 1406–1415. doi: 10.1242/jcs.02841

Ovečka, M., Vaškebová, L., Komis, G., Luptovčiak, I., Smertenko, A., and Šamaj, J. (2015). Preparation of plants for developmental and cellular imaging by light-sheet microscopy. *Nat. Protoc.* 10, 1234–1247. doi: 10.1038/nprot.2015.081

Pleskot, R., Li, J., Žárský, V., Potocký, M., and Staiger, C. J. (2013). Regulation of cytoskeletal dynamics by phospholipase D and phosphatidic acid. *Trends Plant Sci.* 18, 496–504. doi: 10.1016/j.tplants.2013.04.005

Pleskot, R., Pejchar, P., Staiger, C. J., and Potocký, M. (2014). When fat is not bad: the regulation of actin dynamics by phospholipid signaling molecules. *Front. Plant Sci.* 5:5. doi: 10.3389/fpls.2014.00005

Potocký, M., Pleskot, R., Pejchar, P., Vitale, N., Kost, B., and Žárský, V. (2014). Live-cell imaging of phosphatidic acid dynamics in pollen tubes visualized by Spo20p-derived biosensor. *New Phytol.* 203, 483–494. doi: 10.1111/nph.12814

Putta, P., Rankenberg, J., Korver, R. A., van Wijk, R., Munnik, T., Testerink, C., et al. (2016). Phosphatidic acid binding proteins display differential binding as a function of membrane curvature stress and chemical properties. *Biochim. Biophys. Acta* 1858, 2709–2716. doi: 10.1016/j.bbamem.2016.07.014

Qin, C., and Wang, X. (2002). The Arabidopsis phospholipase D family. Characterization of a calcium-independent and phosphatidylcholine-selective PLD zeta 1 with distinct regulatory domains. *Plant Physiol.* 128, 1057–1068. doi: 10.1104/pp.010928

Qin, W., Pappan, K., and Wang, X. (1997). Cloning of PLDgamma and regulation of plant PLDγ, -β and -α by polyphosphoinositides and calcium. *J. Biol. Chem.* 272, 28267–28273. doi: 10.1074/jbc.272.45.28267

Rego, E. H., Shao, L., Macklin, J. J., Winoto, L., Johansson, G. A., Kamps-Hughes, N., et al. (2012). Nonlinear structured-illumination microscopy with a photoswitchable protein reveals cellular structures at 50-nm resolution. *Proc. Natl. Acad. Sci. U.S.A.* 109, 135–143. doi: 10.1073/pnas.1107547108

Roth, M. G. (2008). Molecular mechanisms of PLD function in membrane traffic. *Traffic* 9, 1233–1239. doi: 10.1111/j.1600-0854.2008.00742.x

Rudge, S. A., Morris, A. J., and Engebrecht, J. (1998). Relocalization of phospholipase D activity mediates membrane formation during meiosis. *J. Cell Biol.* 140, 81–90. doi: 10.1083/jcb.140.1.81

Šamajová, O., Komis, G., and Šamaj, J. (2014). Immunofluorescent localization of MAPKs and colocalization with microtubules in Arabidopsis seedling whole-mount probes. *Methods Mol. Biol.* 1171, 107–115. doi: 10.1007/978-1-4939-0922-3_9

Seguí-Simarro, J. M., Austin, J. R., White, E. A., and Staehelin, L. A. (2004). Electron tomographic analysis of somatic cell plate formation in meristematic cells of Arabidopsis preserved by high-pressure freezing. *Plant Cell* 16, 836–856. doi: 10.1105/tpc.017749

Smertenko, A., Assaad, F., Baluška, F., Bezanilla, M., Buschmann, H., Drakakaki, G., et al. (2017). Plant cytokinesis: terminology for structures and processes. *Trends Cell Biol.* 27, 885–894. doi: 10.1016/j.tcb.2017.08.008

Takáč, T., Šamajová, O., Pechan, T., Luptovčiak, I., and Šamaj, J. (2017). Feedback microtubule control and microtubule-actin cross-talk in Arabidopsis revealed by integrative proteomic and cell biology analysis of KATANIN1 mutants. *Mol. Cell. Proteomics* 16, 1591–1609. doi: 10.1074/mcp.M117.068015

Tang, K., and Liu, J. Y. (2017). Molecular characterization of GhPLDα1 and its relationship with secondary cell wall thickening in cotton fibers. *Acta Biochim. Biophys. Sin.* 49, 33–43. doi: 10.1093/abbs/gmw113

Teh, O. K., Shimono, Y., Shirakawa, M., Fukao, Y., Tamura, K., Shimada, T., et al. (2013). The AP-1 μ adaptin is required for KNOLLE localization at the cell plate to mediate cytokinesis in Arabidopsis. *Plant Cell Physiol.* 54, 838–847. doi: 10.1093/pcp/pct048

Uraji, M., Katagiri, T., Okuma, E., Ye, W., Hossain, M. A., Masuda, C., et al. (2012). Cooperative function of PLDδ and PLDα1 in abscisic acid-induced stomatal closure in Arabidopsis. *Plant Physiol.* 159, 450–460. doi: 10.1104/pp.112.195578

van Oostende-Triplet, C., Guillet, D., Triplet, T., Pandzic, E., Wiseman, P. W., and Geitmann, A. (2017). Vesicle dynamics during plant cell cytokinesis reveals distinct developmental phases. *Plant Physiol.* 174, 1544–1558. doi: 10.1104/pp.17.00343

Wang, C., Zien, C. A., Afitlhile, M., Welti, R., Hildebrand, D. F., and Wang, X. (2000). Involvement of phospholipase D in wound-induced accumulation of jasmonic acid in Arabidopsis. *Plant Cell* 12, 2237–2246. doi: 10.1105/tpc.12.11.2237

Wang, G., Ryu, S., and Wang, X. (2012). Plant phospholipases: an overview. *Methods Mol. Biol.* 861, 123–137. doi: 10.1007/978-1-61779-600-5_8

Wang, X. (2005). Regulatory functions of phospholipase D and phosphatidic acid in plant growth, development, and stress responses. *Plant Physiol.* 139, 566–573. doi: 10.1104/pp.105.068809

Wymer, C., and Lloyd, C. (1996). Dynamic microtubules: implications for cell wall patterns. *Trends Plant Sci.* 7, 222–228. doi: 10.1016/S1360-1385(96)86899-0

Yamaoka, S., Shimono, Y., Shirakawa, M., Fukao, Y., Kawase, T., Hatsugai, N., et al. (2013). Identification and dynamics of Arabidopsis adaptor protein-2 complex and its involvement in floral organ development. *Plant Cell* 25, 2958–2969. doi: 10.1105/tpc.113.114082

Yang, Y., Costa, A., Leonhardt, N., Siegel, R. S., and Schroeder, J. I. (2008). Isolation of a strong Arabidopsis guard cell promoter and its potential as a research tool. *Plant Methods* 4:6. doi: 10.1186/1746-4811-4-6

Žárský, V., Cvrčková, F., Potocký, M., and Hála, M. (2009). Exocytosis and cell polarity in plants – exocyst and recycling domains. *New Phytol.* 183, 255–272. doi: 10.1111/j.1469-8137.2009.02880.x

Zhang, Q., Lin, F., Mao, T., Nie, J., Yan, M., Yuan, M., et al. (2012). Phosphatidic acid regulates microtubule organization by interacting with MAP65-1 in response to salt stress in Arabidopsis. *Plant Cell* 24, 4555–4576. doi: 10.1105/tpc.112.104182

Zhang, Q., Qu, Y., Wang, Q., Song, P., Wang, P., Jia, Q., et al. (2017a). Arabidopsis phospholipase Dα 1-derived phosphatidic acid regulates microtubule organization and cell development under microtubule-interacting drugs treatment. *J. Plant Res.* 130, 193–202. doi: 10.1007/s10265-016-0870-8

Zhang, Q., Song, P., Qu, Y., Wang, P., Jia, Q., Guo, L., et al. (2017b). Phospholipase Dδ negatively regulates plant thermotolerance by destabilizing cortical microtubules in Arabidopsis. *Plant Cell Environ.* 40, 2220–2235. doi: 10.1111/pce.13023

Zhang, W., Qin, C., Zhao, J., and Wang, X. (2004). Phospholipase D α1-derived phosphatidic acid interacts with ABI1 phosphatase 2C and regulates abscisic acid signaling. *Proc. Natl. Acad. Sci. U.S.A.* 101, 9508–9513. doi: 10.1073/pnas.0402112101

Conflict of Interest Statement: The authors declare that the research was conducted in the absence of any commercial or financial relationships that could be construed as a potential conflict of interest.

Supplement IV

Supplement videos attached on CD.

Movie S1

Root growth of *Arabidopsis thaliana* seedling, expressing EB1c-GFP, observed by light-sheet microscopy. Root of 2-d old plant was recorded for a time period of 5 h. Movie was produced from time-lapse image acquisition of every 2 min and is presented in the speed of 14 fps.

Video S1

3-D rendering of leaf epidermal petiole cell at the pre-prophase stage of cell division with established PPB and localization of PLDα1-YFP.

Video S2

3-D rendering of leaf epidermal petiole cell at the cytokinesis with ring phragmoplast and localization of PLDα1-YFP.

Video S3

3-D rendering of early disk phragmoplast in root meristematic cell at the cytokinesis with localization of PLDα1-YFP.

Video S4

3-D rendering of late ring phragmoplast in root meristematic cell at the cytokinesis with localization of PLDα1-YFP.

Supplement V

Ph.D. Thesis summary

PALACKÝ UNIVERSITY OLOMOUC

Faculty of Science

Department of Biochemistry

Developmental expression and localization of END-BINDING 1 c and PHOSPHOLIPASE D ALPHA 1 proteins

Ph.D. Thesis summary

P1406 Biochemistry

Mgr. Dominik Novák

Olomouc

2018

This Ph.D. thesis has been completed at the Department of Cell Biology, Centre of the Region Haná for Biotechnological and Agricultural Research, Faculty of Science, Palacký University Olomouc under the supervision of Prof. RNDr. Jozef Šamaj, DrSc.

Ph.D. Candidate: **Mgr. Dominik Novák**
Department of Cell Biology, Centre of the Region Haná
for Biotechnological and Agricultural Research
Faculty of Science, Palacký University Olomouc,
Šlechtitelů 241/27, 783 71, Olomouc, Czech Republic

Supervisor: **Prof. RNDr. Jozef Šamaj, DrSc.**
Department of Cell Biology, Centre of the Region Haná
for Biotechnological and Agricultural Research
Faculty of Science, Palacký University Olomouc,
Šlechtitelů 241/27, 783 71, Olomouc, Czech Republic

Reviewers: **Prof. RNDr. Olga Valentová, CSc.**
Department of Biochemistry and Microbiology, University of
Chemistry and Technology, Technická 3, 166 28,
Praha 6 – Dejvice, Czech Republic

doc. Mgr. Martin Lysák, Ph.D., DSc.
Martin Lysák Research Group,
Mendel Centre for Plant Genomics and Proteomics,
Central European Institute of Technology MU, CEITEC,
Masaryk University, Kamenice 5, 625 00 Brno, Czech Republic

The evaluation of the Ph.D. thesis has been written by the Head of Department of Cell Biology CRH, Faculty of Science, Palacký University Olomouc.
The summary of the Ph.D. thesis has been sent out on …….
The oral defence will take place at the Faculty of Science, Šlechtitelů 27, Olomouc on ……
The Ph.D. thesis is available at the Library of the Biological Centre, Šlechtitelů 27, Olomouc

Prof. RNDr. Ivo Frébort, CSc.PhD.
Chairman of Doctoral Study Board in Biochemistry

Content

Abstract

This Ph.D. thesis is focused mainly on END-BINDING protein 1c (EB1c) and PHOSPHOLIPASE D ALPHA 1 (PLDα1) protein including their developmental expression and localization in *Arabidopsis thaliana* seedlings using advanced microscopy techniques.

Primary root of higher plants is anatomically defined laterally by the existence of cell files in particular tissues and longitudinally by the presence of distinct developmental zones. Plant specific EB1c, one of the three members of EB1 proteins of *Arabidopsis thaliana*, shows prominent nuclear localization in non-dividing cells in the root apex. Using advanced light-sheet fluorescence microscopy (LSFM), we quantified developmentally regulated expression levels of GFP-tagged EB1c protein under the control of native *EB1c* promoter. This was done in relation to the nuclear sizes in diverse root tissues (epidermis, cortex and endodermis) and root developmental zones (meristematic, transition and elongation zone). Our results supported the unique role of the transition root zone in the developmental cell reprogramming during the transition of cells from cell proliferation to cell differentiation in the developing root apex. Moreover, *DRONPA*-tagged *EB1c* construct under the control of *EB1c* native promoter was cloned, transiently transformed to *Nicotiana benthamiana* leaves and stably transformed to *Arabidopsis thaliana* plants. Photoactivation localization microscopy showed spot-like accumulation of EB1c-DRONPA in the nucleus.

PLDα1 and its product phosphatidic acid play important roles in many cellular and physiological processes. Here we aimed to study developmental expression pattern and subcellular localization of PLDα1 using combination of LSFM, structured illumination microscopy, spinning disk and confocal microscopy. Complemented knock-out *pldα1* mutants with YFP-tagged PLDα1 under control of *PLDα1* native promoter showed higher accumulation of PLDα1-YFP in the root cap and in tips of growing root hairs. In aerial parts PLDα1-YFP was localized in the cytoplasm with enhanced accumulation in the cortical cytoplasmic layer of epidermal non-dividing cells of leaves, petioles and hypocotyls. However, in dividing root and petiole cells PLDα1-YFP was enriched in mitotic spindles and phragmoplasts, as suggested by co-visualization with microtubules. This study revealed developmentally-controlled expression and subcellular localization of PLDα1 in dividing and non-dividing cells.

Aim of work

- Summary of the recent knowledge on cytoskeleton, mitogen activated protein kinases, end-binding 1 focused on EB1c protein, phospholipases focused on PLDα1 and microscopy.
- Developmental localization and quantification of EB1c protein in Arabidopsis root using light-sheet fluorescence microscopy.
- Preparation of *proEB1c::EB1c:DRONPA* and its transient transformation in *Nicotiana benthamiana* leaves and stable transformation in *Arabidopsis thaliana* plants.
- Identification and transformation of *pldα1* mutant with *proPLDα1::PLDα1:YFP* construct.
- Investigation of developmental expression pattern and subcellular localization of PLDα1-YFP in Arabidopsis seedlings.

Introduction

Microtubules

Microtubules (MTs) in plant cells were first investigated by electron microscope (EM) during the 1960s (Ledbetter and Porter, 1963). They form tubular polymers of 13 protofilaments, which are composed from two globular proteins, α- and β-tubulin making heterodimers. Inner diameter of MT cylinder in EM is 14 nm while outer diameter is 25 nm (Tilney et al., 1973). In Arabidopsis, 6 isoforms of α- and 9 isoforms of β-tubulin were discovered. MT structure is polarized and dynamic plus-end of growing or shrinking MT ends with β-tubulin, while minus-end is ending with α-tubulin.

Plant MT system includes cortical MT array (**Fig. 1A**), preprophase band (PPB), mitotic spindle and phragmoplast. Precise coordination of MT reorganization is necessary for proper cell expansion and division. Cortical MTs are close to the cell wall and usually form parallel arrays coordinated with the axis of expansion. In the G2 phase of the cell cycle, MTs create ring around nucleus which is called PPB (**Fig. 1B**). PPB is the determinant of cell division plane orientation. Decomposition of nuclear envelope and PPB coincide with formation of MT-based mitotic spindle. The function of mitotic spindle (**Fig. 1C**) is separation of chromosomes. In plant cells, spindle poles are not tightly focused in centrosomes as in animal cells (Baskin and Cande, 1990). At the anaphase, the phragmoplast is formed. Phragmoplast is bipolar with MT plus ends orientated to the cell midplane (**Fig. 1D**). Phragmoplast is expanding centrifugally from the middle of the dividing cell to the parent cell wall (**Fig. 1E**). After cell division, MTs are abundant at the periphery of nucleus and radiate toward cell wall. This endoplasmic array of MTs array is transient (Hasezawa et al., 2000). After this stage, MTs accumulate at the cell periphery in the close association with plasma membrane (PM) (**Fig. 1F**).

Plant MTs have been successfully visualized using both green fluorescent protein (GFP) GFP-tubulin fusions (Nakamura et al., 2004) and GFP-tagged microtubule-associated proteins (MAPs) such as mammalian MICROTUBULE-ASSOCIATED PROTEIN 4 (MAP4) (Marc et al., 1998) or several isoforms of Arabidopsis microtubule-associated proteins 65 (MAP65) (Van Damme et al., 2004).

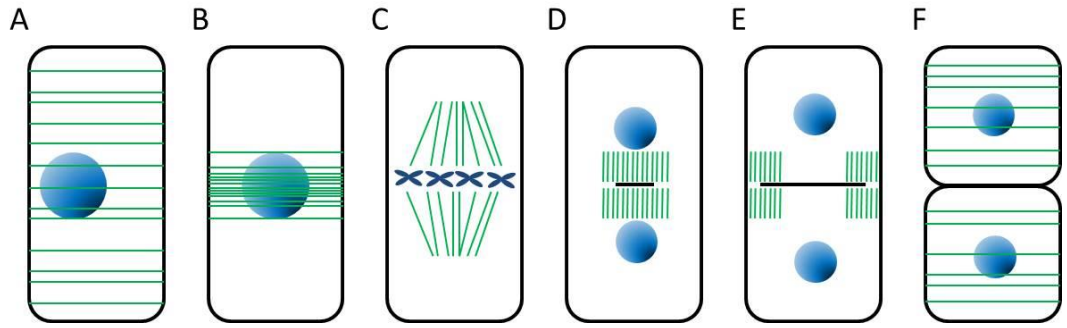

Fig. 1 The schematic illustration of microtubule arrays (green) through plant cell cycle showing position of nuclei and chromosomes (blue). (**A**) Interphase cell with cortical microtubules, (**B**) cell in G2 phase with preprophase band, (**C**) metaphase spindle, (**D**) early phragmoplast, (**E**) late phragmoplast, (**F**) interphase G1 cells. Adapted from Wasteneys, (2002).

Introduction to EB1c

Microtubule plus-end tracking proteins

MT plus-end tracking proteins (+TIPs) are conserved proteins in eukaryotes and regulate MTs plus-end dynamics (Jiang and Akhmanova, 2011). First identified +TIPs were plant proteins from End-Binding 1 (EB1) family (Chan et al., 2003).

EB1

EB1 family of proteins represents a typical example of +TIPs. EB1 proteins regulate spindle MT dynamics (Draviam et al., 2006), serve for recruitment of other +TIPs (Akhmanova and Steinmetz, 2008) and might be targeted to kinetochores (Tirnauer et al., 2002). They are composed of C-terminal EB1 unique homology domain (EBH) responsible for EB1 dimerization and interaction with other proteins. Moreover, C-terminal part contains autoinhibitory domain interacting with amino-terminal (N-terminal) calponin-homology (CH) domain (Hayashi et al., 2005) which is also responsible for the interaction with MTs (Komarova et al., 2009).

Arabidopsis genome encodes three EB1 proteins, namely END-BINDING 1 a (EB1a) (At3g47690), END-BINDING 1 b (EB1b) (At5g62500) and END-BINDING 1 c (EB1c) (At5g67270) (Bisgrove et al., 2008). EB1a and EB1b are typical members of MTs +TIPs. When fused with GFP under the control of native promotor, all EB1 members localize to mitotic spindle and phragmoplast, however, only EB1a and EB1b decorate the plus ends of cortical MTs during the interphase (Chan et al., 2003; Mathur et al., 2003; Komaki et al., 2010). In contrast, EB1c shows nuclear localization during the interphase and seems to have some different functions (Bisgrove et al., 2008; Komaki et al., 2010). EB1a and EB1b share

78% identity at amino acid (AA) level. EB1c shares only 49% homology with EB1a and EB1b (Bisgrove et al., 2008). EB1a and EB1b, but not EB1c, possess acidic AA residues on carboxy-terminal (C-terminal) tail showing autoinhibitory function. EB1a and EB1b can form both homodimers and heterodimers.

EB1c

Plant specific EB1c of *Arabidopsis thaliana* shows prominent nuclear localization in non-dividing interphase and post-cytokinetic cells of root apex (Komaki et al., 2010, Novák et al., 2016). In comparison to EB1a and EB1b, C-terminal part of EB1c contains nuclear localization sequence (NLS) including basic residues and protein becomes actively transported to the nucleus at the end of cytokinesis (Bisgrove et al., 2008). EB1c forms only homodimers. In addition, EB1c contains five Pro directed Ser/Thr motif (SP-motives) at positions 162, 163, 198, 271 and 307 and one docking domain (D-domain) motif KRKLIVNLDV at positions 289-298 which is targeted by protein kinases implicated in the cell cycle including mitogen-activated protein kinases (MAPK) and cyclin-dependent kinase (CDK) (Šamajová et al., 2013). It is known that proteins from animal EB1 family are regulated by phosphorylation (Tamura and Draviam, 2012). Recently, interaction between EB1c and MAPK called MITOGEN-ACTIVATED PROTEIN KINASE 6 (MPK6) was shown in plants (Kohoutová et al., 2015). Knock-out (KO) *eb1c* (mutant of END-BINDING 1 c) mutants are hypersensitive to MT disrupting drugs (Bisgrove et al., 2008) and show fragmented phragmoplasts and collapsed spindles more frequently than double *eb1a eb1b* (mutant of END-BINDING 1 a and END-BINDING 1 b) mutants (Komaki et al., 2010). This effect is more pronounced after treatment with oryzalin, a MT depolymerizing drug. Altogether, these data indicate that EB1c plays important role in chromosome segregation in plants.

Introduction to phospholipases

Lipases are serine hydrolases defined as triacylglycerol acyl hydrolases (E.C. 3.1.1.3.) widespread in nature (Casas-Godoy et al., 2012). Lipases catalyze hydrolysis of the ester bond of mono-, di- and tri-glycerides into glycerol and fatty acid.

Phospholipases

Phospholipids are major components of all biological membranes in all living organisms. Phospholipases (PLs) can cleave various bonds in phospholipids, and they are widespread in nature. PLs are divided to four major classes: A (subdivided in A1 and A2), B, C and D.

These classes are distinguished by the type of catalytic reaction. The phospholipases A (PLA1 and PLA2) produce free fatty acid and 1-acyl lysophospholipid or 2-acyl lysophospolipid, respectively. Phospholipase B (PLB) cleaves fatty acid linked to the lysophospholipid (it is also named lysophospholipase). Phospholipase C (PLC) cleaves glycerophosphate bond like phosphodiesterase while phospholipase D (PLD) cleaves phosphodieteric bond (phosphorus-oxygen) after the phosphate. PLs A1, A2, C and D have been partially characterized in plants (Wang, 2001). They play important roles in cellular regulations, lipid degradation and membrane lipid remodeling (Wang, 2004). These cellular regulations include signalling, responses to drought (Sang et al., 2001), salt (Hong et al., 2008) and other abiotic and biotic stresses, vesicular trafficking, secretion, stomatal opening and closure (Jiang et al., 2014), cytoskeletal remodeling (Zhang et al., 2012) and promoting pollen tube growth. Furthermore, some phospholipases are involved in biosynthesis of storage lipids like triacylglycerol.

PLD

Family of PLD enzymes (E.C. 3.1.4.4.) represents the main group of membrane phospholipid enzymes in plants. PLDs catalyze the hydrolysis of structural glycerophospholipids, e.g. phophatidylcholine (PC), phosphatidylethanolamine (PE) and phosphatidylglycerol (PG) as substrates (Pappan et al., 1998) to produce membrane-derived secondary messenger phosphatidic acid (PA). This process of transphosphatidylation of water producing PA, also produces free soluble head group e.g. choline or ethanolamine, respectively (Munnik and Musgrave, 2001). Genome of the *Arabidopsis thaliana* contains twelve *PLD* genes in comparison to only two genes in animals and one in yeast (Eliáš et al., 2002; Wang et al., 2012). Plant PLDs can be subdivided to six classes: α (α1, α2, α3), β (β1, β2), γ (γ1, γ2, γ3), δ, ε and ζ (ζ1, ζ2) based on their gene architecture, domain structures, sequence similarities, protein sequence homology and biochemical properties (Qin and Wang, 2002).

Reaction catalyzed by PLD

The transphosphatidylation reaction is catalyzed in two steps. In the first step, the head group is removed, and in the second one, covalent phosphatidyl-PLD product is formed between histidine nucleophile residue (in one HKD motif) and phosphorus. Histidine residue from second HKD motif acts as general acid in the cleavage of phosphodiester bond (Stuckey and Dixon, 1999). PLD catalyzes transphosphatidylation reaction in the presence of primary alcohol. This reaction is unique to PLD and can be used for identification of enzyme activity *in vivo*. Phosphatidyl moiety is transferred to a primary alcohol (R-OH), such as 1-buthanol to

produce phosphatidylbuthanol (Heller, 1978; Quarles and Dawson, 1969). Formation of the phosphatidylalcohol can be used like an indicator for PLD activity while alcohol treatments have been used to investigate PLD function. Production of PA is activated in stress responses by both PLDs and PLC while diacylglycerolkinase (DGK) also contributes to PA production (Meijer and Munnik, 2003).

The presence of high concentration of Ca^{2+} (millimolar concentration) and acidic pH are essential for *in vitro* activation of PLDα class but it does not require inclusion of phosphatidylinositolbisphosphate (PIP_2) in the lipid substrate. Ca^{2+} requirement by PHOSPHOLIPASE D ALPHA 1 (PLDα1) is similar to physiological conditions. PHOSPHOLIPASE D BETA (PLDβ) and PHOSPHOLIPASE D GAMMA (PLDγ) classes require PIP_2, neutral pH and micromolar concentration of Ca^{2+} *in vitro*. PHOSPHOLIPASE D DELTA (PLDδ) is PIP_2 independent, active atmicromolar to millimolar concentrations of Ca^{2+} at neutral pH, and it is stimulated by free monounsaturated fatty acid oleate (Qin et al., 2002). PHOSPHOLIPASE D EPSILON (PLDε) is active at similar conditions to PLDα1 and PLDδ, and it requires oleic acid for activity with micromolar concentration of Ca^{2+} (Hong et al., 2009). In contrast, two members of PHOSPHOLIPASE D ZETA (PLDζ) class do not require Ca^{2+} but they require neutral pH and PIP_2 (Qin and Wang, 2002). In plants, PLD activity is also regulated by α-subunits of heterotrimeric G-proteins (Lein and Saalbach, 2001) and by actin cytoskeleton (Kusner et al., 2003). PLDs requirements of PLDs and their distinct biochemical properties are summarized in.

PLD protein domains

Most PLD enzymes in eukaryotes possess at N-terminus calcium-dependent phospholipid-binding domain (C2), whereas mammalian and plant members of PLDζ contain Phox Homology (PX) and Pleckstrin Homology (PH) domains responsible for lipid binding. Characteristic active site at C-terminus consists of two duplicated and conserved HxKxxxxD domains (HKD) essential for lipase activity (Bargmann and Munnik, 2006). Both HKD motifs interact with each other to form the reactive center and they are separated by more than 300 AA in Arabidopsis (Qin and Wang, 2002). Point mutations of conserved histidines to asparagines in the HKD motifs uncovered that these residues are critical for enzyme reactivity (Gottlin et al., 1998). PLDs in Arabidopsis can be subdivided into two groups. Ten PLDs (from subfamilies α, β, γ, δ and ε) contain C2 domain while two (from subfamily ζ) share more homology with mammalian and yeast PLDs and contain PX and PH lipid-binding domains. PX and PH domains mediate binding of PLDs to the membrane where they are

linked to polyphosphoinositide signalling (van Leeuwen et al., 2004). Moreover, C2 PH and PX domains are implicated in protein-protein interactions while C2 domain binds Ca^{2+} and phospholipids. This C2 domain consists of about 130 AA. Studies on mammalian PLDs proved that the PX domain is more critical for PLD activity in comparison to the PH domain. These results were obtained by deletion studies (Sung et al., 1999a; Sung et al., 1999b).

According to their functional domains PLDs can be subdivided into two groups: the Pleckstrin homology and Phox homology domain-containing PLDs (PX/PH-PLDs) and the calcium-dependent phospholipid binding domain-containing PLDs (C2-PLDs) (Hong et al., 2016). Interestingly, PLDβ1 contains actin binding site which is located after second HKD motif (Kusner et al., 2002). PLDα1 protein contains DRY homologue motif (between AA residues 562 and 586) interacting with small G alpha protein and stimulating its GTPase activity (Zhao and Wang, 2004). Finally, PLDδ contains oleate-binding domain which is located after the first HKD motif (Wang and Wang, 2001).

PLD substrates

PLDs with C2 domains mainly utilize these substrates: PC, PE and PG (Qin and Wang, 2002). PLDα1, α3 and ε prefer PC and PE. PLDδ and γ1 prefer PE before PC. PLDα3 and PLDε can hydrolyze phosphatidylserine (PS) with low activity (Hong et al., 2008; Hong et al., 2009). Phosphatidylinositol activity has not been detected in the case of Arabidopsis PLDs tested *in vitro* (Li et al., 2009). PLDs with PX and PH domains mainly utilize PC as substrate (Qin and Wang, 2002).

PLD localization

PLDα1 is the most abundant PLD and its expression and subcellular localization is developmentally controlled (Fan et al., 1999). PLDα1 fluorescently tagged with YELLOW FLUORESCENT PROTEIN (YFP) and expressed under native promoter showed accumulation in the root cap and epidermis with considerably higher expression in thichoblasts before and during root hair formation and growth. PLDα1-YFP accumulated mainly in tips of growing root hairs. In root cap cells and in cells of root transition zone PLDα1-YFP showed cytoplasmic subcellular localization. In aerial parts of plants it was also localized in the cytoplasm showing enhanced accumulation in the cortical cytoplasmic layer of epidermal non-dividing cells of hypocotyls, leaves and leaf petioles (Novák et al., 2018). PLDγ was detected in the PM, intracellular membrane, nuclear and mitochondrial subcellular fractions of Arabidopsis leaves (Fan et al., 1999). PLDζ2 is localized to the tonoplast

(Yamaryo et al., 2008) while PLDα3, PLDδ and PLDε are associated with the PM (Hong et al., 2009; Hong et al., 2008).

PLDα

PHOSPHOLIPASE D ALPHA 2 (PLDα2) is much more similar to PLDα1 than PHOSPHOLIPASE D ALPHA 3 (PLDα3) in terms of sequence and expression pattern while expression level of PLDα1 is much higher than PLDα3. PLDα3 enhances root growth under hyperosmotic stress and plays a positive role during salt and drought stress (Hong et al., 2008). KO mutant of PHOSPHOLIPASE D ALPHA 3 (*pldα3*) plants are more sensitive to hyperosmotic stress caused by salinity in comparison to *PLDα1* overexpressing (OE) plants. Under water deficiency and salt stress *pldα3* mutants show reduced root growth. Moreover, these mutants exhibit delayed flowering. Opposite situation is in OE *PLDα3* plants showing early flowering enabling to complete life cycle earlier (Hong et al., 2008).

PLDα1

Arabidopsis PLDα1 protein (AT3G15730) contain C2 lipid binding domain on N-terminus (position 1-110 in AA sequence) and two HKD domains responsible for lipase activity (position 327-366 and 656-683 in AA sequence). According to PhosPhAt 4.0 database (Durek et al., 2010) SP-motif at position 481 can serve as potential MAPK phosphorylation site. PLDα1 is active in the presence of 20-100 mM Ca^{2+}, by adding detergents it can be lowered to 5mM Ca^{2+}. N-acylethanolamines (NAEs) are endogenous inhibitors of PLDα1 (Motes et al., 2005). These NAEs can by potentially produced by PLDγ and PLDβ (Austin-Brown and Chapman, 2002).

In response to plant wounding, e.g. after herbivore attack, PLDα1 is activated in cells and its product PA plays very important role (Wang, 2000). KO *pldα1* mutant exhibits reduced production of PA while PA production is completely eliminated in double *pldα1/δ* mutant. Surprisingly, JA biosynthesis was not affected in this double *pldα1/δ* mutant (Bargmann et al., 2009a). Abundance of PLDα1 was decreased after wortmannin treatment in Arabidopsis roots (Takáč et al., 2012). Wortmannin inhibits phosphatidyl inositol kinases and causes clustering and fusion of multivesicular bodies and trans-Golgi network which results in the inhibition of vacuolar trafficking.

PA, as product of PLD, regulates MICROTUBULE ASSOCIATED PROTEIN 65-1 (MAP65-1) in response to the salt stress (Zhang et al., 2012). MAP65-1 protein forms 25 nm cross-bridges between MTs during their bundling (Smertenko et al., 2004). This protein binds

to PA localized at the plasma membrane, and enhances MTs polymerization and bundling. Under normal conditions, wild type and *pldα1* showed no obvious differences in MT organization and density. Salt stress affects association of MTs and MAP65-1 leading to MTs disorganization in the *pldα1* mutant. This process can be alleviated by adding PA (16:0-18:2). Treatment with 1-butanol (0.4%) or co-treatment with 1-butanol (0.1%) and NaCl led to MTs depolymerization in wild type and *pldα1* mutant. This process can be also alleviated by adding PA. By contrast, 2-butanol, which is not PLDα1 substrate, has no effect on MTs (Zhang et al., 2012). MAP65-1 binds to PA with fatty acid chains 16:0-18:1; 16:0-18:2; 18:0-18:1 and 18:0-18:2. Thus, PA produced by PLDα1 binds to MAP65-1 which leads to MTs polymerization and stabilization and increase salt tolerance, but PLDα1 itself does not bind to MTs or MAP65-1 (Zhang et al., 2012). Mutation of the PA-binding domain of MAP65-1 resulted in destabilization of cortical MTs and enhanced cell death under salt stress (Zhang et al., 2012). Moreover, overexpression of MAP65-1 improves NaCl tolerance of Arabidopsis cells, which is more obvious in the wild type than in the *pldα1* mutant. On the other hand, double *pldα1 x map65-1* mutant (double knock-out mutant of PHOSPHOLIPASE D ALPHA 1 and MICROTUBULE ASSOCIATED PROTEIN 65-1) showed greater sensitivity to NaCl in comparison to single mutants (Zhang et al., 2012).

During NaCl exposure, Na^+ ions enter root, which leads to signalling response. MAPK called MITOGEN-ACTIVATED PROTEIN KINASE 6 (MPK6) has been identified as target of PA in response to salinity while *pldα1* mutant showed lower level of MPK6 activity. PA binds and stimulates MPK6 which inhibits MAP65-1 activity through phosphorylation (Yu et al., 2010). MAP65-1 inhibition results in less prominent MT bundling, (Smertenko et al., 2006; Beck et al., 2010) which might cause MT disorganization after stress exposure. On the other hand, PA also binds to MAP65-1 and increases MT polymerization activity (Zhang et al., 2012). In Arabidopsis, MAP65-1 contains two microtubule binding domains (MTB), MTB1 and MTB2 (Smertenko et al., 2008). MTB2 harbors the phosphorylation sites (from 495 to 587 residues) which controls MAP65-1 activity (Smertenko et al., 2006; Smertenko et al., 2008). The PA binding domains in MAP65-1 (from 1 to 150 and from 340 to 494 residues) are different from microtubule binding domains (Zhang et al., 2012), which suggest that MAP65-1 regulations by MAPKs and PA are different.

Developmental Nuclear Localization and Quantification of GFP-Tagged EB1c in *Arabidopsis* Root Using Light-Sheet Microscopy

Material and Methods

Protein extraction, SDS-PAGE and immunoblotting

12 d old Arabidopsis plants expressing EB1c-GFP were analysed on fluorescent stereomicroscope Leica MZ FLIII (Leica Microsystems, Germany) for EB1c-GFP signal. Protein extraction was carried out from roots of plants expressing EB1c-GFP and from wild type *Arabidopsis thaliana* (L.) Heynh. (ecotype Columbia). Roots were harvested, weighted, flesh frozen and immediately ground in the liquid nitrogen. Powder was extracted in extraction buffer (1:1, w/v) (50 mM Na-HEPES pH 7.5, 150 mM NaCl, 1 mM $MgCl_2.6H_2O$, 1 mM EGTA, 1 mM DTT, 1 mM NaF) supplemented with protease inhibitors Complete (Roche, Germany) and phosphatase inhibitors PhosStop (Roche, Germany). Crude extract was centrifuged 10 min, 8000 *g* at 4°C. Resulting supernatant was used for sodium dodecyl sulphate-polyacrylamide gel electrophoresis (SDS-PAGE) and subsequent western blot analysis. 15 μg of total protein was loaded on 8% SDS-PAGE gels followed by immunoblotting with polyvinylidene difluoride (PVDF) membrane and Western blotted with antibody against GFP (anti GFP rabbit ABCAM AB290) in dilution of 1:2000. Secondary antibody (goat anti-rabbit, Santa Cruz Biotechnology) was used in dilution of 1:5000. After incubation in enhanced chemiluminescence (ECL) reagents (according to manufacturer instructions), immunoreactive bands were documented using the BioRad ChemiDoc™ MP System.

Plant material and sample preparation for light-sheet imaging

Seeds of *Arabidopsis thaliana* (L.) Heynh. (ecotype Columbia) transgenic line expressing *pEB1::cEB1c:GFP* were surface sterilized, plated onto solidified ½ Murashige & Skoog (MS) medium and kept in 4°C for 4 days. After this period seeds were transferred to round 90 × 25 mm Petri dishes filled with 80 ml of ½ MS medium solidified with 0.6% w/v Phytagel (Sigma-Aldrich, USA), and placed into small depressions facilitating gravitropic root growth inside solidified culture medium. Plates were cultivated in culture chamber horizontally for 2 d at 22°C, 50% humidity, 16/8-h light/dark cycle. After germination of seedlings when they were 1 d old, they were enclosed by fluorinated ethylene propylene (FEP) tube with an inner diameter of 1.1 mm and wall thickness of 0.2 mm (Wolf-Technik, Germany). FEP tubes were carefully inserted into culture medium to enclose individual seedling inside (Ovečka et al.,

2015). After 24 h seedlings in FEP tubes were removed from the plate, transferred to the microscope and prepared for imaging. All experiments and measurements were done on 2 d old seedlings.

Light-sheet microscopy

Developmental live cell imaging was done with the Lightsheet Z.1 fluorescence microscope (Carl Zeiss, Germany), equipped with W Plan-Apochromat 20×/1.0 NA water immersion detection objective (Carl Zeiss, Germany) and LSFM 10x/0.2 NA illumination objective (Carl Zeiss, Germany). Seedlings were imaged using dual-side illumination by a light-sheet modulated into a pivot scan mode, with excitation laser line 488 nm and with emission filter BP505-545. Image acquisition was done every two minutes in Z-stack mode for a time period of 2-5 h. Scaling of images in x, y and z dimensions was 0.228 x 0.228 x 0.477 µm. To prevent the movement of the growing root apex out of the field of view, images were acquired in two subsequent views coordinated to each other in y coordinate. Images were recorded with the PCO.Edge sCMOS camera (PCO AG, Germany) with the exposure time 25 ms.

From images of the whole root acquired using Zen 2014 software (Carl Zeiss, Germany) subsets of data were created, with defined x-, y- and z- dimensions comprising whole volume of several nuclei from one particular cell file. Several subsets were created in order to segment nuclei of all cells of particular cell file in ordered positions from the stem cells surrounding quiescence center of the root up to visible cell differentiation at the end of elongation zone. All subsets were transformed to 2D images using Maximum intensity projection function of the Zen 2014 software. In all images uniform correction of brightness and contrast was done before they were exported for image analysis. All quantitative data were produced with publicly available software CellProfiler 2.1.1 (http://www.cellprofiler.org, Carpenter at al., 2006, Lamprecht et al., 2007). Nuclear area from 2D images that represent surface projection of the nuclear volume (referred herein as nuclear surface area) was measured as the actual number of pixels in the manually defined region multiplied by the pixel area. Mean intensity values were calculated as the average pixel intensity in the defined region, integrated intensity values were calculated as the total pixel intensity in the defined region. Values were subsequently normalized to a 0-1 range using the following formula: $x_N=(x_i-x_{min})/x_{max}-x_{min}$ (where x_N= normalized intensity, x_i=absolute intensity, x_{min}= minimum absolute intensity and x_{max}= maximum absolute intensity). Thus, all biological variables within measured root tips were brought into the comparable proportions and plant – to – plant differences in the expression of EB1c-GFP were compensated. Data

from 4 individual cell files were collected and evaluated separately for epidermis, cortex and endodermis from two independent experiments (two independent roots). Final statistical data evaluation and plot production was done with Microsoft Excel software.

Results

Root growth and development require passage of root cells through successive developmental zones. Large extend of this process from spatial and temporal point of view requires special microscopic applications for effective live cell imaging. Developmental light-sheet microscopy overcomes these limitations and allows real-time or time-lapse imaging of whole developing seedlings (Ovečka et al., 2015). We performed live cell imaging with seedlings growing over a period between 2-5 h inside the light-sheet microscope. EB1c-GFP was localized in nuclei of all non-dividing root cells within the root apex, with particularly strong expression level in cells of the root meristematic zone (**Fig. 2B**). General overview of EB1c-GFP expressing roots revealed zonation of the root apex into different cell developmental zones, namely into meristematic, transition, elongation and differentiation zones (**Fig. 2B**). Seedlings were prepared and cultivated in cylinders of Phytagel-solidified culture medium. During imaging over a range of several hours, seedlings exhibited undisturbed continuous root growth inside of the microscope (**Fig. 2C**). Average root growth rate of 2 d old seedlings expressing EB1c-GFP in the light-sheet microscope was 1.686 (± 0.721) $\mu m.min^{-1}$ (±SD, n=6).

Light-sheet microscopy, in addition to time-lapse imaging of the entire root development, allowed localization of EB1c-GFP at the cellular and subcellular levels. At the level of cellular resolution, this method was suitable for visualization not only surface cells and tissues of the root, like lateral root cap cells and epidermis, but further allowed visualization of individual cells from inner tissues of the Arabidopsis root including the cortex, the endodermis and the central cylinder. In all imaged tissues, light-sheet microscopy revealed clearly nuclear localization of EB1c-GFP in root cells (**Fig. 2D**). Subcellular resolution of the light-sheet microscopy was documented during mitotic cell division of root cells in the meristematic zone, where EB1c-GFP relocated from G2 stage nuclei to mitotic spindles and cytokinetic phragmoplasts during the respective cell division stages and finally was redistributed back to reconstituted G1 stage nuclei after completing cell division (**Fig. 2E**).

Values of nuclear surface area and EB1c-GFP mean signal intensity for quantitative evaluation were plotted against cell position counted from the stem cells surrounding

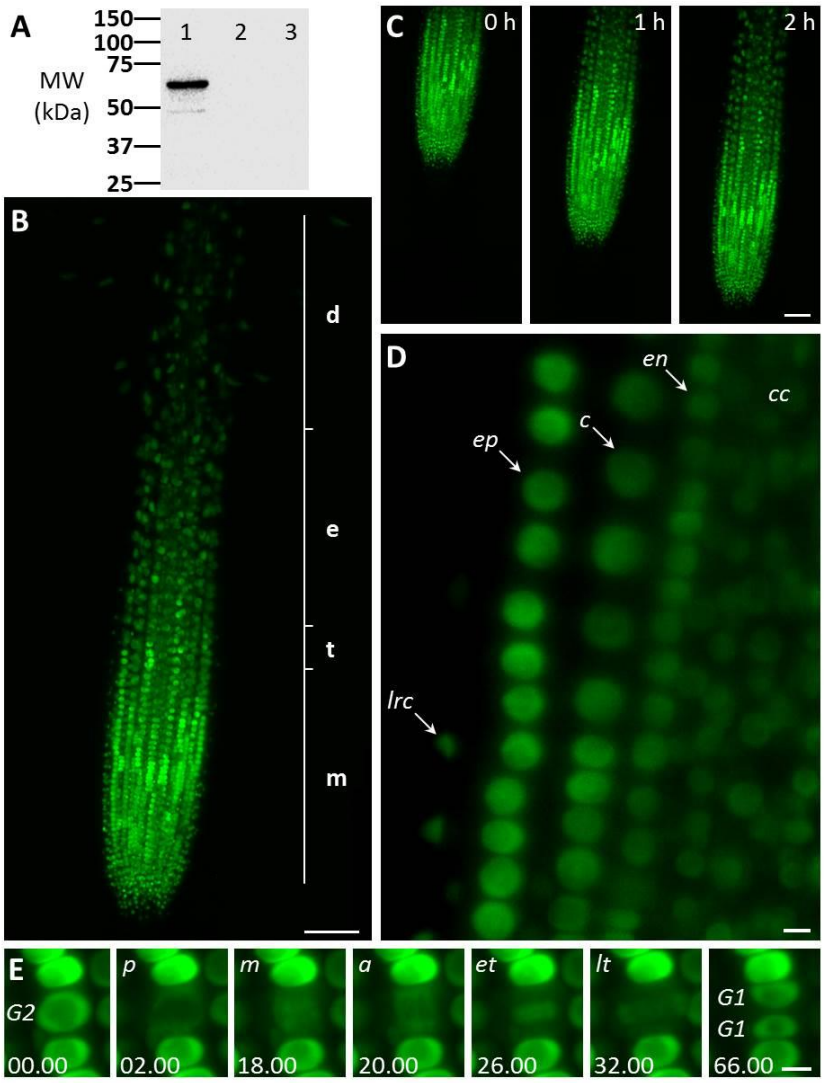

Fig. 2 Characterization of transgenic *Arabidopsis thaliana* plants expressing EB1c-GFP driven by EB1c own promoter and localization of EB1c-GFP. (**A**) SDS-PAGE followed by western blot analysis using anti-GFP antibody from protein extract of *A. thaliana* T2 plants expressing EB1c-GFP (lane 1), protein extract from untransformed Col plants (lane 2) and protein extract from Arabidopsis plants expressing EB1c-GFP immunoblotted only with secondary antibody (lane 3). MW – Molecular weight. (**B**) General overview of the root tip of 2 d old *A. thaliana* seedling expressing EB1c-GFP. Average root zonation into individual cell developmental zones consisting meristematic zone (m), transition zone (t), elongation zone (e) and differentiation zone (d) is depicted. EB1c-GFP was localized in nuclei of root cells, with particularly strong expression level in cells of the root meristematic zone. (**C**) Live cell imaging of seedling growing inside of the light-sheet microscope over the period of 2 h. (**D**) Localization of EB1c-GFP by light-sheet microscopy in cells of individual root tissue layers, in epidermis (ep), cortex (c), endodermis (en), central cylinder (cc) and lateral root cap cells (lrc). In all imaged tissues, light-sheet microscopy revealed clearly nuclear localization of EB1c-GFP in root cells. (**E**) Localization of EB1c-GFP by light-sheet microscopy during mitotic cell division of root cells in the meristematic zone. EB1c-GFP relocated from G2 stage nuclei to spindle in prophase (p), metaphase (m) and anaphase (a), to phragmoplast at early and late telophase (et, lt), and redistributed back to reconstructed G1 stage nuclei after cell division. Time progression of the cell division is indicated in min. Pictures (B-E) were performed in collaboration with Dr. Miroslav Ovečka. Scale bar = 50 µm in (B, C) and 5 µm in (D, E).

quiescence center. Both parameters were measured and evaluated separately for the epidermis, the cortex and the endodermis. We found that in all tissues, as cells proceeded from proliferation to the differentiation, the nuclear surface area increased while fluorescence intensity of EB1c-GFP signal decreased. This trend was apparent from quantification of individual cell files of the epidermis (**Fig. 3A**), the cortex (**Fig. 3B**) and the endodermis (**Fig. 3C**). The meristematic zone, actively dividing cells contained the smallest nuclei exhibiting the highest EB1c-GFP content. In the transition zone, the mean nuclear fluorescence intensity of EB1c-GFP was steeply decreased. This decline in EB1c-GFP fluorescence intensity continued in the elongation zone while the nuclear area progressively increased (**Fig. 3**). Cross-correlation of nuclear EB1c-GFP mean signal intensity of some individual nuclei with their size and shape at certain position within the cell file revealed negative correlation between nuclear size and mean EB1c-GFP signal intensity in the meristematic zone (numbered insets in **Fig. 3A-C**). This negative correlation trend was stabilized in the transition zone and the elongation zone of all measured cell files in all evaluated tissue layers (**Fig. 3**) as evidenced by the continuous decrease in EB1c-GFP fluorescence intensity with the progressive increase in nuclear size.

Further, we quantified collectively measured data from several individual cell files of two independent roots. Data were evaluated separately for epidermis, cortex and endodermis. Quantitative evaluation of nuclear surface area values revealed rather stable distribution of this parameter in the meristematic zone of the epidermis. It increased slightly only in meristematic cells at gradually increasing distances from the stem cell region, surpassing slightly even the average reference value for the size of G2 nuclei (**Fig. 4A**). Further recognizable increase in the nucleus size took place within the transition zone, and dramatic increase in the elongation zone of epidermis (**Fig. 4A**). Mean fluorescence intensity of EB1c-GFP in interphase nuclei of epidermis fluctuated considerably; however, it was high in the meristematic cells. In nuclei of cells entering the transition zone mean fluorescence intensity of EB1c-GFP dropped considerably and in nuclei of elongating cells this drop in mean fluorescence intensity was dramatic, reflecting the inversely proportional increase in the nucleus size (**Fig. 4A**).

A similar tendency of stable nuclear size in the meristematic zone, a gradual increase in the transition zone and a considerable increase in the elongation zone was recorded also in cell files of the cortex layer (**Fig. 4B**). Nuclear size in the meristematic zone did not exceed the

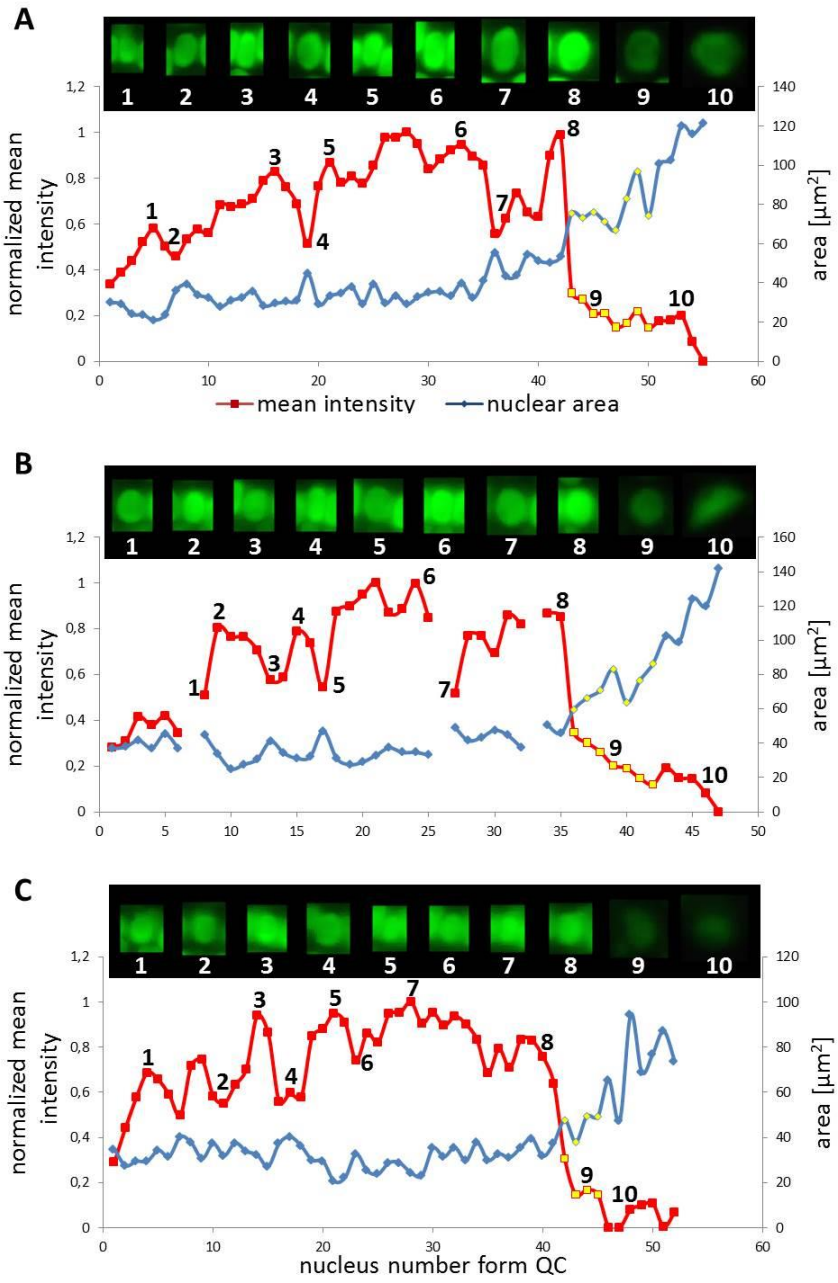

Fig. 3 Nuclear surface area and nuclear EB1c-GFP mean signal intensity distribution in root developmental zones of the root apex in individual cell files. Relationship between nuclear area (blue line) and nuclear EB1c-GFP mean signal intensity (red line) in respect to cell position counted from the stem cells surrounding quiescent center in individual cell file of epidermis (**A**), cortex (**B**) and endodermis (**C**). Values for nuclei in the transition zone are highlighted by yellow points, which allow distinguishing also meristematic zone (appearing before the transition zone) and elongation zone (appearing after the transition zone). Inset images over the lines show individual nuclei of cells at the actual position, documenting changes in nuclear shape, size and mean EB1c-GFP fluorescence intensity. Major vertical axis (on the left) represents the values for the normalized mean intensity and minor vertical axis (on the right) represents values for area measurements. Horizontal axis represents the actual cell position counted from the stem cells surrounding quiescent center (QC). Data are shown for one representative cell file from each tissue layer. Interruptions of the curve in the cortex (**B**) are caused by presence of dividing cells within the file. Graphs were prepared in collaboration with Dr. Miroslav Ovečka and Dr. Anna Kuchařová.

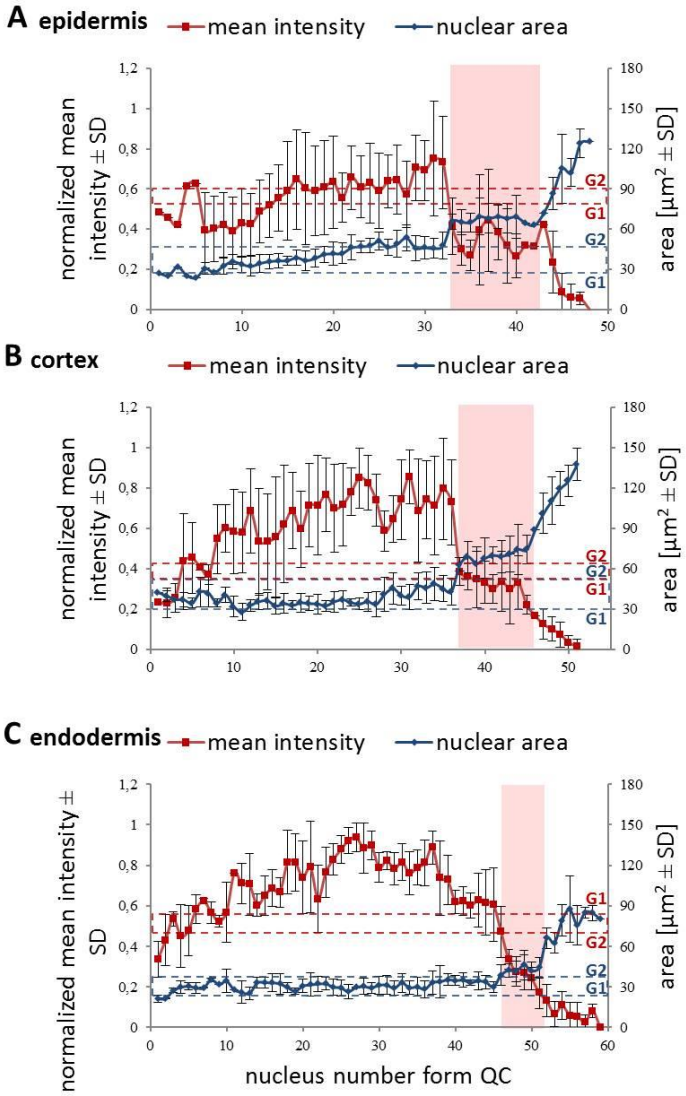

Fig. 4 Nuclear surface area and nuclear EB1c-GFP mean signal intensity in cells of different tissues along diverse developmental root zones. Average values of nuclear surface area (blue line) and EB1c-GFP mean signal intensity (red line) plotted against cell position counted from the stem cells surrounding quiescence center (QC). Data from 4 individual cell files were collected and evaluated separately for epidermis (**A**), cortex (**B**), and endodermis (**C**) from two independent roots. The transition zone is highlighted in pink colour. Dashed red lines for average mean intensity and dashed blue lines for average nuclear area of G1 and G2 nuclei are indicated as reference values. Major vertical axis (on the left) represents the values for the normalized mean intensity and minor vertical axis (on the right) represents values for area measurements. Horizontal axis represents the actual cell position counted from the stem cells surrounding quiescence center (QC). Because number of cells in cell files is not the same, data from individual cell files in average graphs were aligned according to their meristem-to-transition zone borders. Graphs were created by Dr. Miroslav Ovečka and Dr. Anna Kuchařová.

reference value for the size of G2 nuclei (**Fig. 4B**). Mean fluorescence intensity of EB1c-GFP in interphase nuclei of cortex cells was highest in the meristematic zone. However, it

decreased dramatically in the transition zone, keeping further decreasing in the elongation zone as well (**Fig. 4B**).

Size of nuclei of endodermal cells in the meristematic zone was constant, not exceeding the reference value of size measured for G2 nuclei, showing increase only after passage of meristematic cells into the transition zone. Size distribution of nuclei in the transition zone and the elongation zone of endodermis was wider as in cortex and epidermis, but the general tendency of gradual nuclear size increase from meristem through transition zone to elongation zone was maintained also in endodermis (**Fig. 4C**).

Discussion

Nuclear localization of EB1c

EB1c localization and function was previously documented in dividing cells of *Arabidopsis thaliana* (Dixit et al., 2006; Bisgrove et al., 2008; Komaki et al., 2010; Ho et al., 2011). In all the above studies, EB1c was studied in the context of cell division and studies were focused on the localization of EB1c at the microtubule plus ends with special emphasis on phragmoplast.

However, the evident interphase nuclear localization and function of EB1c was not systematically addressed in these former studies. For this reason we surveyed the nuclear occurrence of EB1c not only in the interphase cells of the meristematic zone, but also in post-mitotic non-dividing cells of the root transition and elongation zones. Measuring nuclear parameters revealed clear distinction among root developmental zones and correlated them with specific patterns of EB1c accumulation in the nuclei of different tissues and in both meristematic and post-meristematic root zones. Thus, EB1c-GFP can be considered a reliable physiological nuclear marker for root developmental studies including post-meristematic cells. With the help of previously published data about longitudinal root zonation (Dello Ioio et al., 2007; Baluska and Mancuso, 2013; Panteris et al., 2013), we identified particular zones in Arabidopsis plants expressing EB1c-GFP. As expected, EB1c-GFP signal was present in all nuclei across the studied root zones and tissues. We thus employed correlative quantitative studies monitoring developmental fluctuations in EB1c-GFP expression levels with the trend of nuclear size increase which is observed in the shoot-ward root growth gradient. Inversely to the nuclear area increase, expression of EB1c-GFP showed root-ward trend within all tissues along the longitudinal root axis with the highest intensity peak in the meristematic zone. The highest expression level and the lowest correlation between EB1c-GFP mean intensity and

nuclear surface area in the meristematic zone are in accordance to previously published data about the role of EB1c in the cell division progression. *eb1c* mutants showed defects in spindle pole alignment, chromosomal segregation and phragmoplast orientation, however, the organization of the preprophase band was not impaired (Komaki et al., 2010). Nevertheless, EB1c might have a dual function in meristematic cells, depending on its subcellular localization (one on microtubule plus ends during mitosis and another one in nuclei during interphase).

More importantly we demonstrate for the first time, an evident persistent localization of EB1c in the nuclei of post-meristematic, non-dividing root cells residing within the transition and the elongation zones. As such this is the first study using quantitative advanced light-sheet microscopy to follow nuclear changes in correlation to the nuclear accumulation of a native cytoskeletal protein (EB1c was expressed under its native promoter) during development of the primary root. In the transition zone, where division is ceased while differentiation and endoreduplication goes on, it seems to be a turning point for the expression of EB1c protein. From this point more than genetically regulated, expression of EB1c seems to be mechanistically related to increase in cell nucleus size which is carried out by endoreduplication. What exactly happens at the transition point and how switch from mitotic division to endoreduplication occurs is not well documented (del Pozo et al., 2006; Ishida et al., 2009; Ishida et al., 2010; Adachi et al., 2011; Heyman et al., 2011; Doskočilová et al., 2013). Our analyses highlight the nuclear localization of EB1c, opening in this way the hitherto unexplored field with several possible questions. One matter that needs to be resolved concerns whether nuclear recruitment of EB1c has a functional sense as well as the nature of its putative nuclear functional role(s). It is also opening the question on the mechanism of EB1c nuclear transport and export as it was not deciphered before.

Gene Expression Pattern and Protein Localization of Arabidopsis Phospholipase D Alpha 1 Revealed by Advanced Light-Sheet and Super-Resolution Microscopy

Material and Methods

Preparation of complemented PLDα1-YFP

To generate the complementation transgenic lines, the coding sequence of wild type *PLDα1*(AT3G15730) under the control the native *PLDα1* promoter (1,944 bp upstream of the initiation codon ATG of *PLDα1*) was introduced into pGreen0229-YFP-Tnos vector using *Bam*HI-*Kpn*I restriction digest to generate *proPLDα1::PLDα1:YFP* construct. The constructs were confirmed by sequencing and transformed by floral dipping (Clough and Bent, 1998; Davis et al., 2009) to Arabidopsis wild type Col-0 as well as to *pldα1-1*(SALK_067533) and *pldα1-2* (SALK_053785) mutants using *Agrobacterium tumefaciens* strain GV 3101. In T1 generation we have selected 3 independent transgenic lines with the same fluorescent properties. One line was chosen and T2 or T3 progeny of BASTA-resistant transformants, carrying a single homozygous insertion, were used for experiments.

Preparation of transgenic line carrying PLDα1-YFP and mRFP-TUB6

Arabidopsis *pldα1-2* stably expressing *proPLDα1::PLDα1:YFP* in T2 generation were crossed with Col-0 plants stably expressing *pUBQ1:mRFP::TUB6* kindly provided by Geoffrey O. Wasteneys (Ambrose et al., 2011). F1 generation plants with PLDα1-YFP and mRFP-TUB6 (mRFP = red fluorescent protein, TUB6 = β-TUBULIN 6) expression were selected based on fluorescence signal in the epifluorescence microscope (Axio Imager.M2, Carl Zeiss, Germany).

Whole mount immunofluorescence labelling

Immunolocalization of microtubules, PLDα1, PLDα1-YFP and clathrin in root wholemounts was done as described previously (Šamajová et al., 2014). Samples were immunolabeled with rat anti-α-tubulin (clone YOL1/34; ABD Serotec), rabbit anti-phospholipase D alpha 1/2 (Agrisera, Sweden), mouse monoclonal anti-clathrin LC (Sigma-Aldrich) or mouse anti-GFP (Abcam) primary antibodies diluted 1:300, 1:300, 1:300 and 1:100, respectively in 3% (w/v) BSA in PBS at 4 °C overnight. In the case of double or triple co-immunolocalization a sequential immunolabeling was performed. Secondary antibodies included Alexa-Fluor 488 goat anti-rat, Alexa-Fluor 488 goat anti-mouse or Alexa-Fluor 546 goat anti-rat IgGs were

diluted 1:500 in PBS containing 3% (w/v) BSA for 3 h (1.5 h at 37 °C and 1.5 h at room temperature). Where necessary, nuclei were counterstained with 4′,6-diamidino-2-phenylindole (DAPI). Microscopic analysis of immunolabeled samples was performed with a Zeiss 710 CLSM platform (Carl Zeiss, Germany), using excitation lines at 405, 488 and 561 nm from argon, HeNe, diode and diode pumped solid-state lasers.

Light-Sheet Fluorescence Microscopy

Developmental live cell imaging of 2-3 days old Arabidopsis plants with PLDα1-YFP expression was done with the light-sheet Z.1 fluorescence microscope (Carl Zeiss, Germany) equipped with W Plan-Apochromat 20x/1.0 NA objective (Carl Zeiss, Germany) and two LSFM 10x/0.2 NA illumination objectives (Carl Zeiss, Germany). Seedlings were prepared in FEP tubes with an inner diameter of 2.8 mm and wall thickness of 0.2 mm (Wolf-Technik, Germany) according to the "open system" protocol for long-term live-cell imaging of *Arabidopsis thaliana* seedlings described by Ovečka et al. (2015). Root was growing in the block of the culture medium inside of the FEP tube and upper green part of the seedling developed in an open space of the FEP tube with the access to air. Sample holder with the sample was placed into observation chamber of the light-sheet microscope tempered to 22°C using Peltier heating/cooling system. Before insertion of the sample to the microscope plants were ejected slightly out of the FEP tube allowing imaging of the root in the block of solidified culture medium, but without the FEP tube. Before the imaging, liquid medium filling the observation chamber was filter-sterilized using a sterile syringe filter. Roots were imaged using dual-side light-sheet illumination with excitation laser line 514 nm, beam splitter LP 580 and with emission filter BP525-565. Images were recorded with the PCO.Edge sCMOS camera (PCO AG, Germany) with the exposure time 30 ms and the imaging frequency of every 5 min in z-stack mode for 5-20 hours. Scaling of recorded images in x, y and z dimensions was 0.228 x 0.228 x 0.499 µm.

Spinning disk and Confocal laser scanning microscopy

Hypocotyls, leaves with pavement cells, stomata and trichomes of 5-8 days after germination Arabidopsis plants with PLDα1-YFP expression were documented with spinning disk microscope (Cell Observer SD, Carl Zeiss, Germany) equipped with Plan-Apochromat 20x/0.8 (Carl Zeiss, Germany) and Plan-Apochromat 63x/1.40 Oil (Carl Zeiss, Germany) objectives. Cells were imaged with excitation laser 514 nm and with emission filter BP535/30 for YFP. Cotyledons, petioles and guard cells were documented with confocal laser scanning microscope LSM 710 (Carl Zeiss, Germany) equipped with Plan-Apochromat 20x/0.8 (Carl

Zeiss, Germany) and alpha Plan-Apochromat 63x/1.46 Oil (Carl Zeiss, Germany) objectives. Plants of 6 days after germination were stained with 4 μM FM4-64 (styryl dye for plasma membrane visualisation, Invitrogen, USA) diluted in half-strength liquid MS medium for 90 min before imaging. Samples were imaged with excitation lasers 514 nm for YFP and 561 nm for mRFP and FM4-64, beam splitters MBS 458/514 for YFP, MBS 458/561 for mRFP and MBS 488/561 for FM4-64. Emission filters used were 519 – 550 nm for YFP, 590 – 610 nm for mRFP and 651 – 759 nm for FM4-64.

Structured Illumination Microscopy

The same immunolabeled wholemount samples examined with confocal laser scanning microscopy (CLSM) were also analyzed via a Zeiss SIM platform coupled with a PCO.Edge 5.5 sCMOS camera (Elyra PS.1, Carl Zeiss, Germany). Fluorophores were excited with the 405, 488, 561 and 647 nm laser lines. For acquisition with a 63x/1.40 oil immersion objective, the grating pattern was set to 5 rotations with 5 standard phase shifts per angular position. In case of z-stacks, Nyquist sampling was selected to be the smallest one (corresponding to DAPI channel with 91 nm section thickness), leading to oversampling of the rest of the channels. Image reconstruction was done according to previously published procedure (Komis et al., 2015).

Results

Expression patterns of PLDα1-YFP in Arabidopsis plants

In order to characterize roles of PLDα1 in the plant development, we performed *in vivo* cell- and tissue-specific expression analysis of the PLDα1-YFP driven by native *PLDα1* promoter in two stably transformed *pldα1* mutants of *Arabidopsis thaliana*. Thus, both *pldα1-1* and *pldα1-2* mutants were stably transformed with *proPLDα1::PLDα1:YFP* construct using the floral dip method (Clough and Bent, 1998). Comparison of *proPLDα1::PLDα1:YFP* expression patterns in different aerial organs and tissues of *pldα1-1* and *pldα1-2* mutants stably expressing PLDα1-YFP is presented in.

Developmental expression pattern and localization of PLDα1-YFP in Arabidopsis plants

Observation of developmental expression pattern and localization of PLDα1-YFP fusion protein has been done in *pldα1-1* mutant stably expressing a *proPLDα1::PLDα1:YFP* construct at cell-, tissue- and organ-specific levels using light-sheet fluorescence microscopy. Subcellular localization was performed using confocal and spinning disk microscopy. Developmental light-sheet fluorescence microscopy (LSFM) has been performed with 2- to 3-

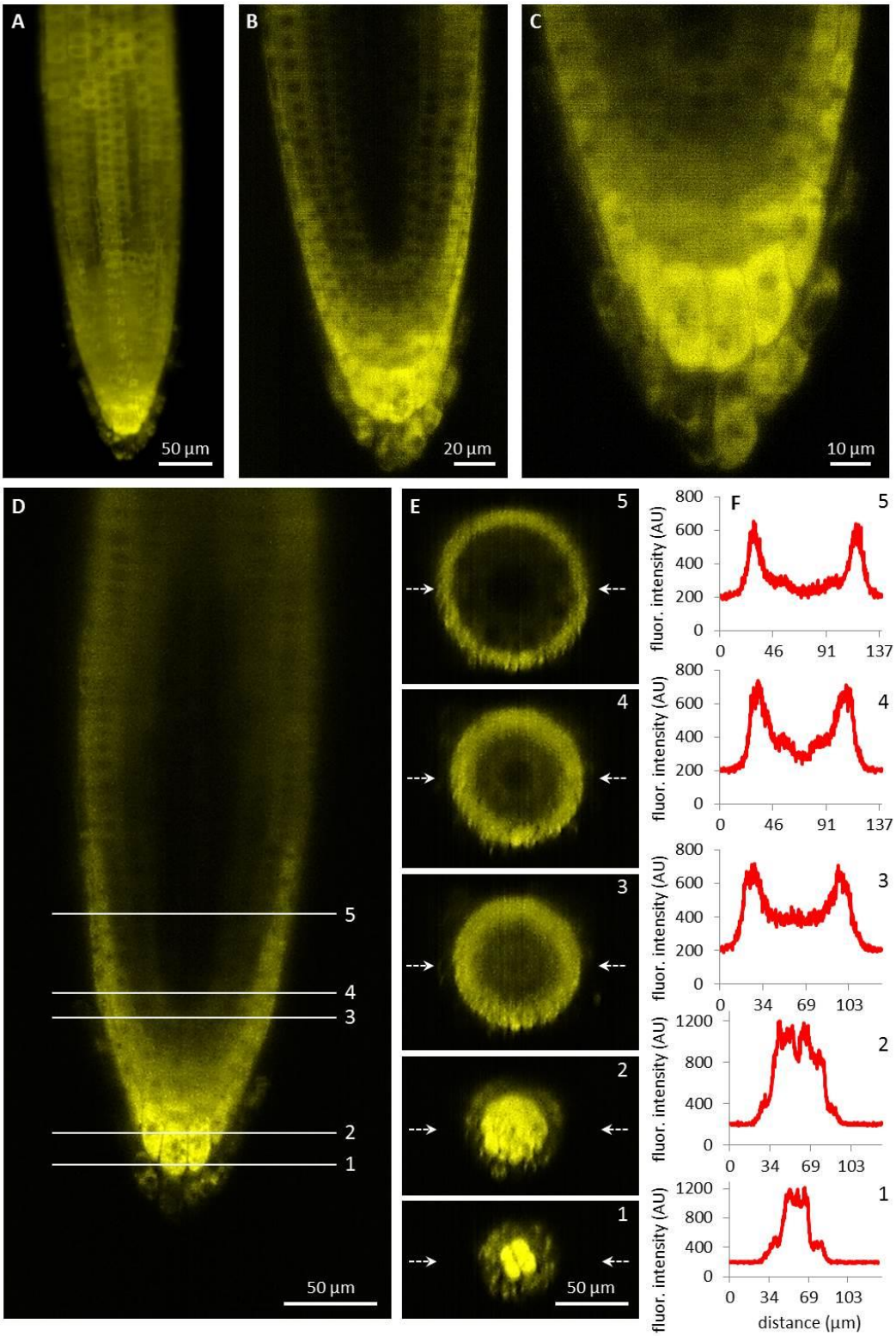

Fig. 5 Light-sheet fluorescence microscopy localization of PLDα1-YFP driven by *PLDα1* own promoter in *Arabidopsis thaliana* roots. (**A**) Overview of PLDα1-YFP localization in different tissues of the root tip constructed from maximum intensity projection of 330 optical sections (with thickness of 0.5 µm each). Amount of PLDα1-YFP fluctuated in root rhizodermal cells while the highest localization was visible in the root cap cells. (**B**) Median optical section of the root tip revealed differential distribution of PLDα1-YFP with the strongest expression in the root cap and lateral root cap cells and with much lower production of PLDα1-YFP in rhizodermal, cortical and endodermal cell

layers and with very low production in procambial cells. (**C**) Detail of the root cap showing the strongest expression level of PLDα1-YFP in central columella cells and particularly in cells of the third root cap layer. (**D-F**) Qualitative and semi-quantitative evaluation of the relative PLDα1-YFP distribution in longitudinal and radial zonation of the root tip. Five profiles at different positions of the root tip (**D**) were visualized into orthogonal projections of radial root sections (**E**) and profiles in the median positions of the radial root sections (indicated by arrows) were quantitatively displayed (**F**). Images were taken from *pldα1-1* and *pldα1-2* mutant plants stably expressing PLDα1-YFP. LSFM images were performed by Dr. Miroslav Ovečka.

days old seedlings that were growing inside of the microscope imaging chamber in time periods ranging from 5 to 20 h. During these imaging periods, roots of experimental plants exhibited continuous growth at constant root growth rates. LSFM offered the possibility not only to localize PLDα1-YFP at the cellular level in root surface tissues (**Fig. 5A**), but it also allowed deep root imaging and tissue-specific visualization and localization of PLDα1-YFP in internal root tissues (**Fig. 5B**).

Imaging of tissue-specific expression of PLDα1-YFP in roots using LSFM revealed developmental regulation of PLDα1-YFP amount in the root apex. The expression levels of PLDα1-YFP in the root meristematic zone including rhizodermis, cortex and procambium were relatively low (**Fig. 5B**). On the other hand, particularly strong expression levels were revealed in the apical and lateral root cap cells (**Fig. 5C**). Remarkably strong expression was observed in central columella cells and particularly in cells of the third columella layer (**Fig. 5B-C**). Semi quantitative evaluation of the PLDα1-YFP amount in different cell layers of root apex (**Fig. 5D**) revealed a steep gradient between third and fourth outermost layers of the central root cap (**Fig. 5D-F**; profiles 1-2). There was a relatively low amount of PLDα1-YFP in the primary meristems at the position of the stem cell niche in comparison to the lateral root cap cells (**Fig. 5D-F**; profile 3). Proximally to the region of initial cells there was a clear gradient in the PLDα1-YFP amount within the radial organization of the root meristem with the highest level in the lateral root cap cells, much lower level in the rhizodermis, cortex and endodermis, and the lowest level in central cylinder tissues (**Fig. 5D-F**; profile 4). Different expression levels among lateral root cap cells, dermal tissues (rhizodermis, cortex and endodermis) and central cylinder tissues were clearly visible in the central part of the root meristematic zone (**Fig. 5D-F**; profile 5).

In comparison to the relatively low expression level of the PLDα1-YFP in the root meristem, a dramatic enhancement was detected in the root transition zone, particularly in the rhizodermis (**Fig. 6A**). Rhizodermal cells showed much stronger expression levels in the trichoblast cell files compared to the atrichoblast ones (**Fig. 6B-E**). Relatively strong

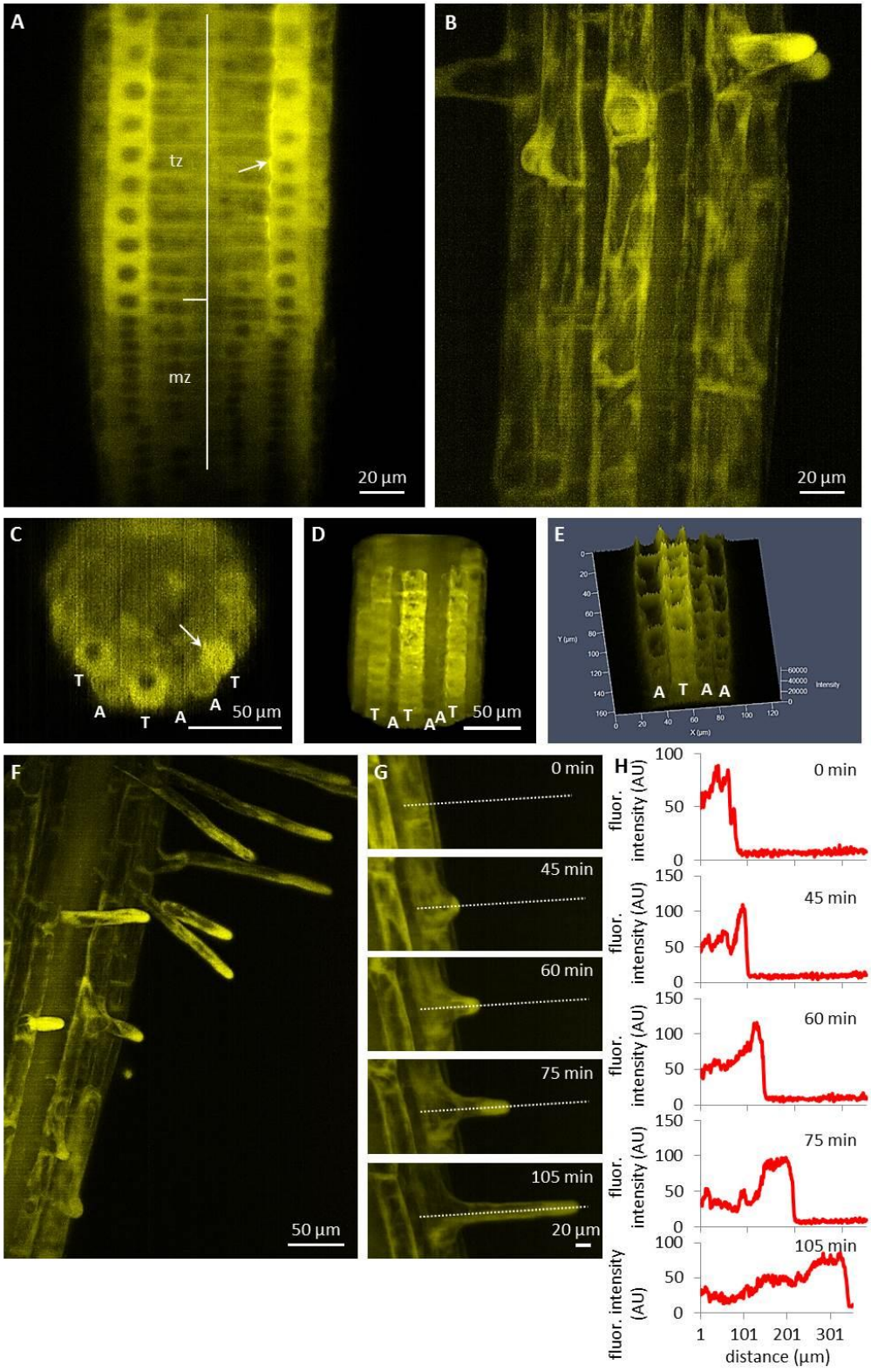

Fig. 6 Tissue- and cell-specific localization of PLDα1-YFP driven by its own native promoter in the root of *Arabidopsis thaliana* by light-sheet fluorescence microscopy. (**A**) Distribution of PLDα1-YFP in meristematic zone (mz) with relatively low expression and in transition zone (tz) with enhanced expression. (**B**) Differentiation zone of the root with stronger expression level of PLDα1-YFP in trichoblasts and bulges of emerging root hairs and lover expression level in atrichoblast cell files. (**C-E**) Orthogonal projection (**C**), 3D-rendering (**D**) and intensity-based 3D visualization (**E**) of root

differentiation zone showing higher expression level of PLDα1-YFP in rhizodermal trichoblast cell files (labelled as T) and lover expression level in atrichoblast cell files (labelled as A). Arrows in A and C point local accumulation of PLDα1-YFP at the cell corner of the trichoblasts in the contact with two underlying cortical cells. (**F**) Enhanced localization of PLDα1-YFP in trichoblast cells at the stage of root hair formation and apparent accumulation of PLDα1-YFP in growing root hairs. (**G**) Time-course recording of accumulation and relocation of PLDα1-YFP during the root hair outgrowth in trichoblast root cell. Time frames of individual developmental stages are indicated in min. Dotted lines along the median longitudinal axis of the root hair indicate the position of fluorescence intensity profile measurement. (**H**) Fluorescence intensity profiles of PLDα1-YFP distribution corresponding to particular developmental stages of the root hair formation from the trichoblast root cell in (**G**). Images were taken from *pldα1-1* and *pldα1-2* mutant plants stably expressing PLDα1-YFP using light-sheet microscopy. LSFM images were performed by Dr. Miroslav Ovečka.

expression of PLDα1-YFP in trichoblast cells of the transition root zone revealed one additional aspect of particular interest. It was the strongly polarized localization of PLDα1-YFP at the cell corner of the trichoblasts facing the cleft contact with two underlying cortical cells (**Fig. 6A, C**). Thereon, the strong expression level of PLDα1-YFP in trichoblast cell files was also maintained later in the development of root hairs during bulge formation (**Fig. 6B**) and in tip-growing root hairs (**Fig. 6F-H**). Time-course semi quantitative evaluation of

PLDα1-YFP distribution clearly revealed its accumulation in growing tips of root hairs (**Fig. 6G, H**). The PLDα1-YFP expression pattern in growing roots thus reflected the tissue-specific and developmentally-regulated transition from low PLDα1-YFP protein levels in actively dividing cells of the root apical meristem to much enhanced protein accumulation in the root transition zone harbouring post-mitotic cells preparing for cell elongation (**Fig. 5D-F**). Cell differentiation in root tissues led to localized accumulation of PLDα1-YFP, particularly in the developing rhizodermis, where PLDα1-YFP accumulated preferentially in trichoblasts (**Fig. 6B-E**), especially during the process of root hair formation (**Fig. 6F-H**). In all root tissues expressing moderate levels of PLDα1-YFP (root cap cells, root transition zone, trichoblast cell files and tip growing root hairs) we observed cytoplasmic localization of the fusion protein.

Expression pattern and localization of PLDα1-YFP in different cell types of aerial parts of 6 days old seedlings were documented with confocal and spinning disk microscopy. Relatively high expression level of PLDα1-YFP was observed in hypocotyl epidermal cells (**Fig. 7A**), in pavement cells and stomata guard cells of cotyledons (**Fig. 7B**), in leaf epidermis and stomata guard cells of leaves (**Fig. 7D**). Consistently with strong expression level of PLDα1-YFP in root rhizodermis and in developing root hairs we observed also strong expression of PLDα1-YFP in leaf trichomes (**Fig. 7E**). In more detail, high amounts of PLDα1-YFP were found at

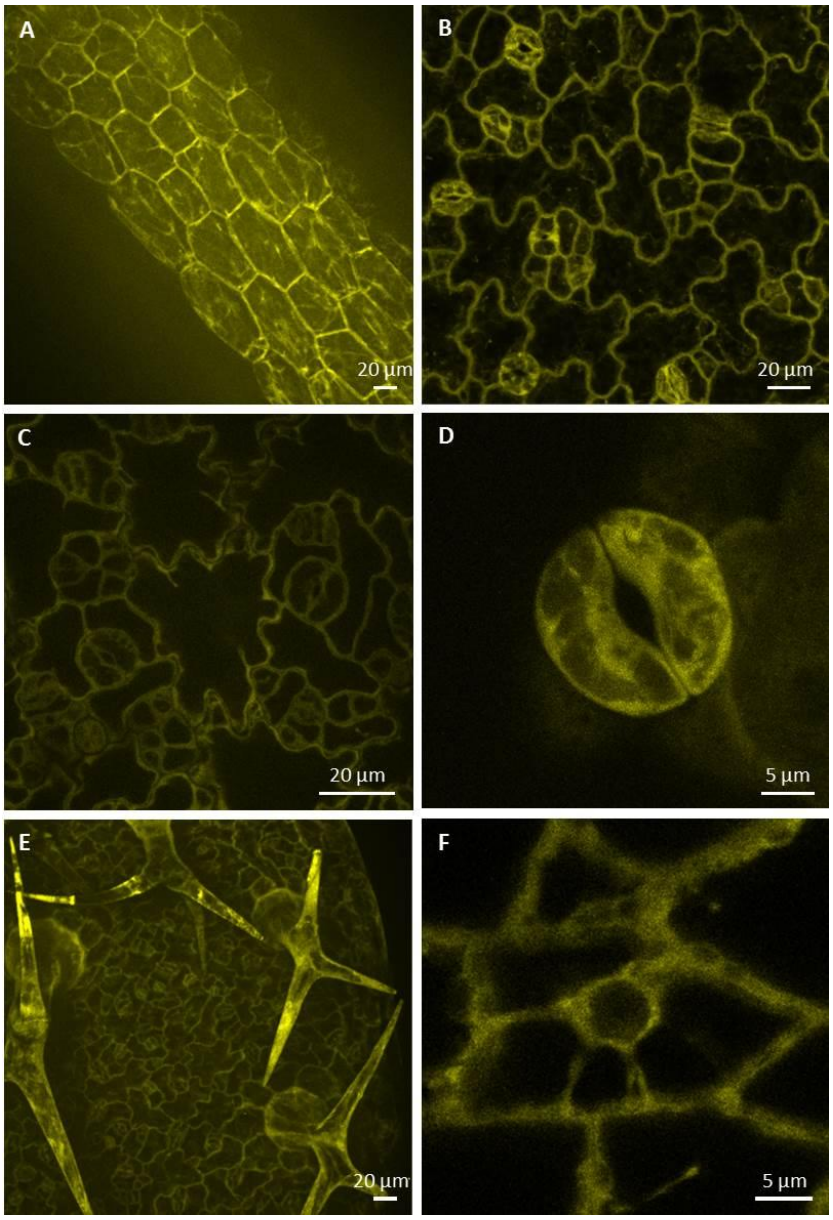

Fig. 7 Localization of PLDα1-YFP driven by *PLDα1* own promoter in different aerial organs and tissues of *Arabidopsis thaliana* seedlings. Images were taken from different cell types of aerial tissues of living *pldα1-2* mutants stably expressing PLDα1-YFP driven by its own promoter using confocal and spinning disk microscopy. Localization of PLDα1-YFP in hypocotyl epidermal cells (**A**), cotyledon epidermal cells and stomata (**B**), leaf epidermal pavement cells and stomata guard cells (**C**), leaf stoma guard cells (**D**), leaf epidermal cells and trichomes (**E**), and petiole epidermal cell (**F**). Spinning disk microscopy (**A, C, D**), confocal microscopy (**B, E, F**).

tips of trichome branches (**Fig. 7E**). A high level of PLDα1-YFP was observed also in epidermal cells of leaf petioles (**Fig. 7F**).

Accumulation of PLDα1-YFP in growing root hairs (**Fig. 6F-H**) suggested its role in actively growing cell domains. To test this possible scenario in leaf trichomes, we identified individual stages of trichome development in the first true leaf and we performed semiquantitative

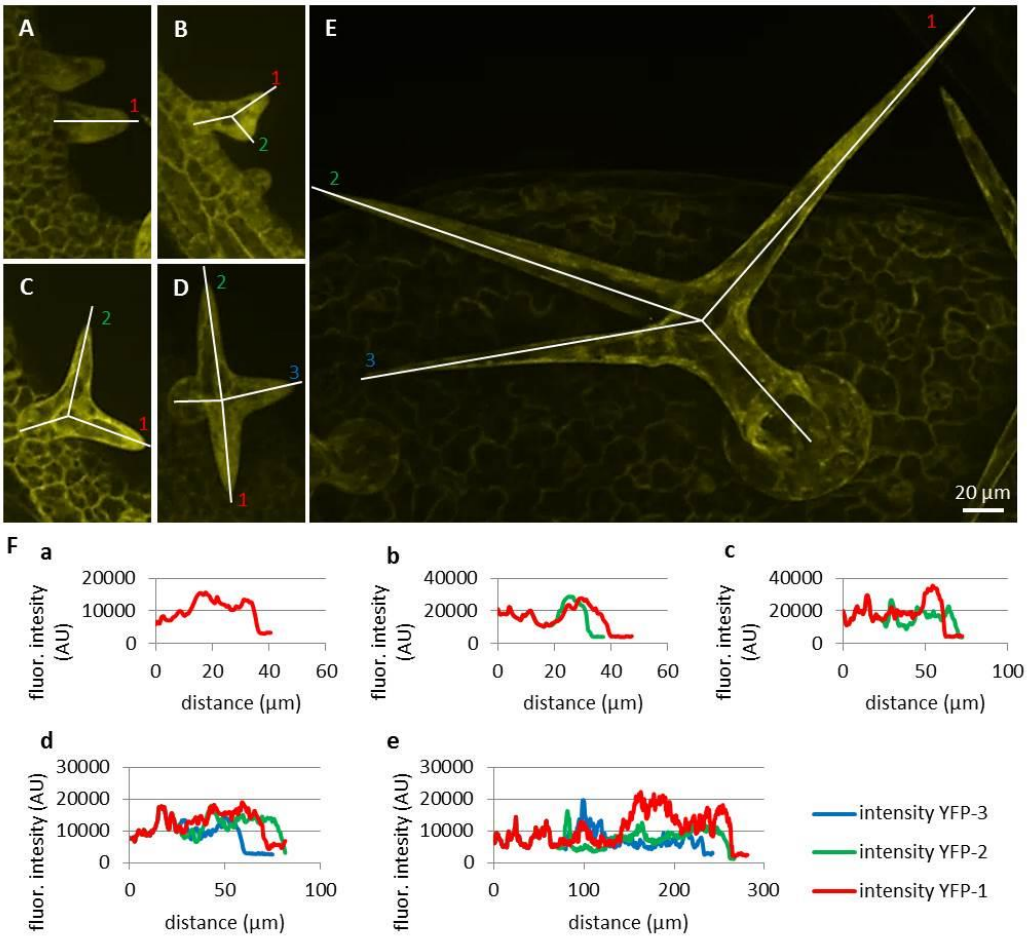

Fig. 8 Localization and accumulation of PLDα1-YFP in developing leaf trichomes in *pldα1-2* mutant plants stably expressing PLDα1-YFP driven by *PLDα1* own promoter. Images of maximum intensity projection were reconstructed from individual optical sections taken at the same live cell imaging condition from first (**B, D, E**) and second (**A, C**) true leaves of *pldα1-2* mutants stably expressing PLDα1-YFP. Developing trichomes are displayed from early developing stages with no branches (**A**), with progressing two branches (**B, C**), growing three branches (**D**) to maturating three branches (**E**). (**F**) Profiles of fluorescence intensity of YFP distribution in individual trichome branches indicated by lines in (**A-E**).

evaluation of PLDα1-YFP distribution along single profiles in individual trichome branches. To quantify PLDα1-YFP developmental redistribution during trichome formation, we

measured profiles of PLDα1-YFP fluorescence in young trichome primordia without branches (**Fig. 8A**), in each individual branch of growing trichomes during later developmental stages (**Fig. 8B-D**) up to final stage of fully developed three-branched trichomes (**Fig. 8E**). Profiling of fluorescence intensity along individual trichome branches clearly revealed higher accumulation of PLDα1-YFP at the tip of actually growing branch during trichome development (**Fig. 8F**).

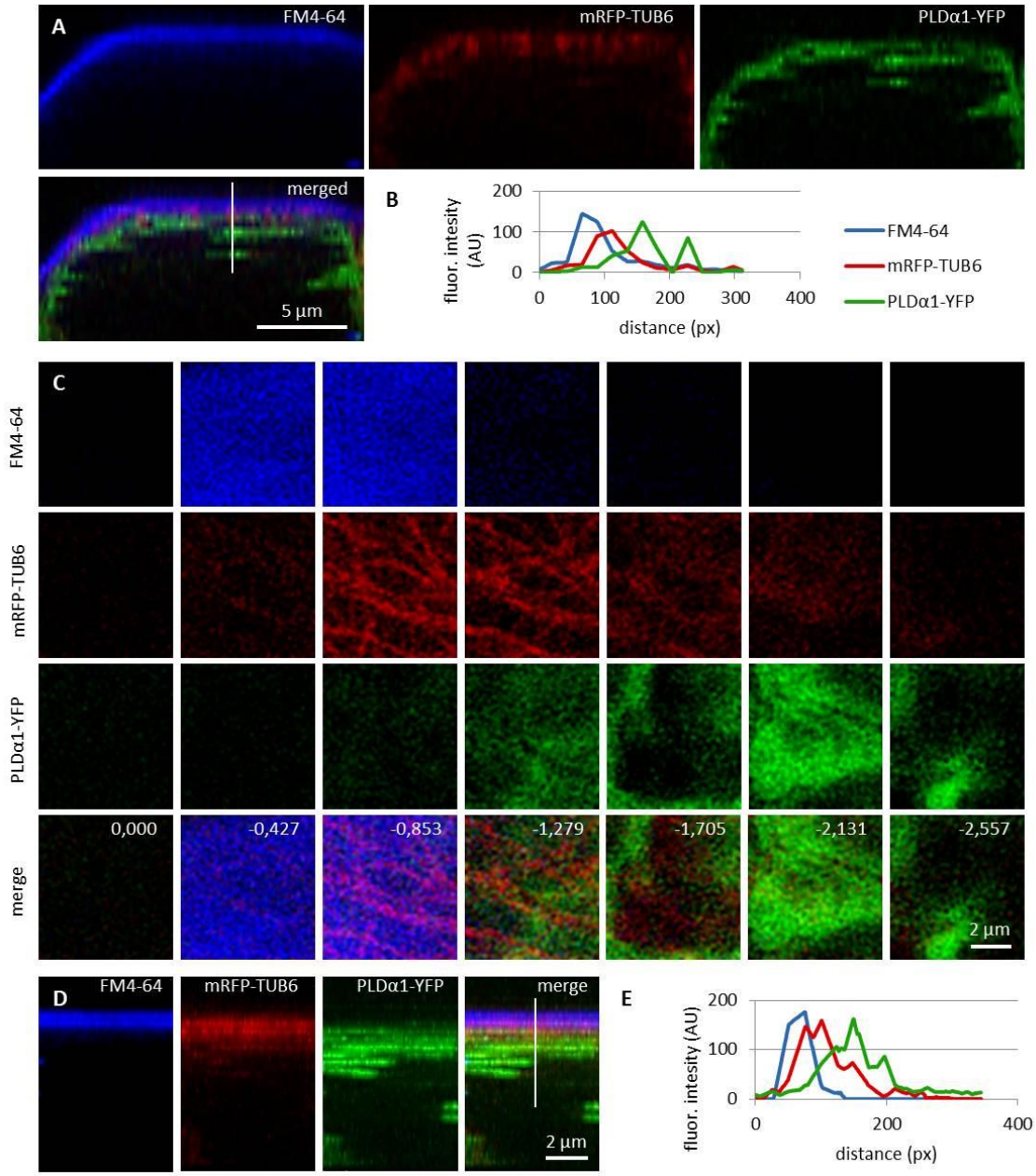

Fig. 9 Subcellular localization of PLDα1-YFP and cortical microtubules in respect to the plasma membrane in leaf petiole epidermal cells. Living interphase petiole cells with the expression of PLDα1-YFP (in green) and mRFP-TUB6 (in red) were counterstained with FM4-64 for delineation of the plasma membrane (in blue). (**A**) Orthogonal view of the 3D-reconstructed petiole cell from the z-stack imaging showing localization of plasma membrane, cortical microtubules and PLDα1. Line in merged image indicates position of measured profile. (**B**) Profile intensity of fluorescence distribution of the plasma membrane (blue), cortical microtubules (red) and PLDα1 (green) based on the distance from the cell surface. (**C**) Frontal view reconstructed from the individual z-stacks starting from the cell surface of the petiole cell to the cortical cytoplasm in steps indicating thickness of individual optical sections in µm. Individual channels are shown separately for the plasma membrane (labelled in blue), cortical microtubules (labelled in red) and PLDα1 (labelled in green), while the merge image shows the overlay of all three channels with the depth annotation. (**D**) Maximum intensity projection of the same image as in C from the side view (orthogonal projection) with the line indicating position of measured profile. (**E**) Profile intensity of fluorescence distribution of the plasma membrane (blue), cortical microtubules (red) and PLDα1 (green) from D based on the distance from the cell surface. Analysis made in confocal microscope.

Association of PLDα1-YFP with microtubules

In order to investigate the localization pattern of PLDα1-YFP in respect to cortical and mitotic microtubules we crossed *plda-1-2* mutant plants stably expressing *proPLDα1::PLDα1:YFP* construct with Col-0 plants stably expressing p*UBQ1::mRFP:TUB6* construct (red fluorescent protein fused to Arabidopsis alfa-tubulin 6 isoform, Ambrose et al., 2011). Labelling of the plasma membrane in cells of such crossed line was performed with FM4-64. The co-localization experiments were done in non-dividing leaf petiole epidermal cells using confocal laser scanning microscopy (**Fig. 9**). 3-D rendering and orthogonal projections showed very close association of cortical microtubules with the plasma membrane and predominant localization of PLDα1-YFP in the cortical cytoplasm (**Fig. 9A**). Merge image of all three markers (**Fig. 9A**) and semi-quantitative measurement of fluorescence intensities along transversal profile in the cell cortex (**Fig. 9B**) revealed only poor co-localization, but rather association of PLDα1-YFP with cortical microtubules. This was evident also from spatial separation of individual optical sections from 3-D scans of the cell cortex starting from the cell surface. By taking individual optical sections of 420 nm thickness (**Fig. 9C**), we observed uppermost signal of the FM4-64 related to the plasma membrane first, followed by mRFP signal corresponding to cortical microtubules located beneath the plasma membrane, and only then first appearance of the YFP signal related to the PLDα1. In merge image, the plasma membrane signal was enriched in second and third optical section (0.000 to -0.853 μm from the cell surface), network of cortical microtubules was present in third to fifth optical section (-0.853 to -1.705 μm from the cell surface), while PLDα1-YFP signal was enriched only in fourth to sixth optical section (-1.279 to -2.131 μm from the cell surface). Association and partial colocalization of PLDα1-YFP with cortical microtubules (detected as yellow spots in merge images) is visible only on the cytoplasmic face (**Fig. 9C**, optical section -1.279), but not on the membrane face (**Fig. 9C**, optical section -0.853) of the cortical microtubule network. Sandwich-like arrangement of the plasma membrane, cortical microtubule network and PLDα1-YFP was evident also from orthogonal view of the examined cell cortex area (**Fig. 9D**), proven also by semiquantitative fluorescence profile intensity measurement (**Fig. 9E**). These experiments revealed predominantly cytoplasmic localization of PLDα1-YFP.

Colocalization of PLDα1-YFP with microtubules in dividing cells

Colocalization of PLDα1-YFP with mitotic microtubule arrays was observed in dividing epidermal cells of leaf petioles using spinning disk microscopy (**Fig. 10A-E**). Association of PLDα1-YFP with PPB was evident in the pre-prophase and prophase stage (**Fig. 10A**), with

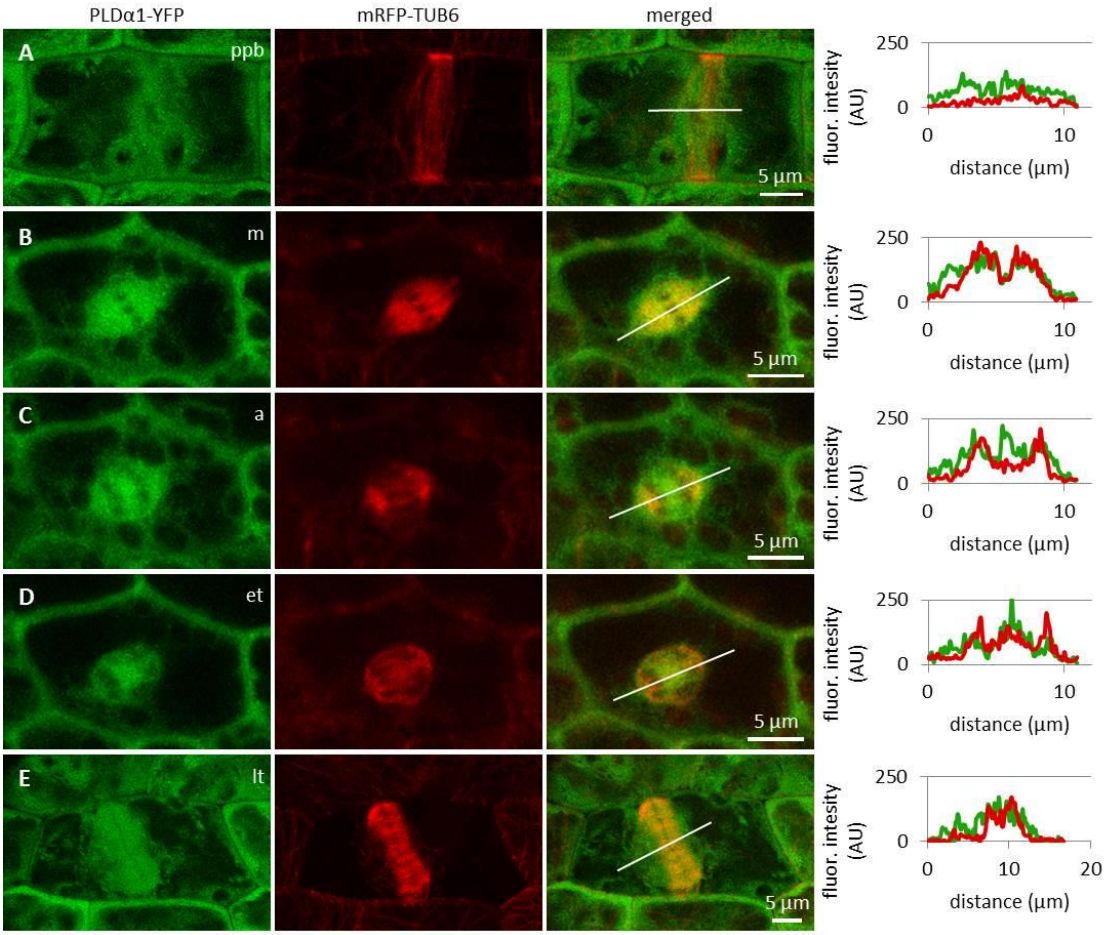

Fig. 10 Subcellular localization of PLDα1-YFP during cell division. Live cell imaging of PLDα1-YFP (green) and mRFP-TUB6 (red) in dividing leaf petiole epidermal cell. PLDα1-YFP was enriched at the location of preprophase band of microtubules (PPB) (**A**), while it strongly associated with the mitotic spindle (**B, C, D**), early (**D**) and late (**E**) phragmoplast. Profiles of fluorescent intensity of YFP and mRFP distribution measured at individual cell division stages are indicated by lines (**A-E**). ppb – preprophase band of microtubules, m – metaphase, a – anaphase, et – early telophase, lt – late telophase.

mitotic spindle during metaphase to anaphase (**Fig. 10B-D**) and with progressing phragmoplast during cytokinesis (**Fig. 10E**). In the pre-prophase and prophase stage PLDα1-YFP accumulated in the cell cortex in a ring-like structure that was broader as PPB.

This indicates that PLDα1-YFP, in addition of colocalization with microtubules inside PPB, also surrounded PPB in the cortical cytoplasm (**Fig. 10A**). Additionally, PLDα1-YFP was enriched also in cytoplasmic disk radiating from the nuclear surface to the cell cortex at the PPB plane (**Fig. 10A**). Later on, PLDα1-YFP was strongly accumulated in microtubule arrays of the mitotic spindle which was surrounded by cytoplasmic layer enriched with PLDα1-YFP (**Fig. 10B-C**). Association of PLDα1-YFP with microtubules was documented by missing signal in the mitotic spindle occupied by chromosomes during metaphase and anaphase (**Fig.**

10B-D). Starting with the segregation of sister chromatids and their pulling to the opposite spindle poles, PLDα1-YFP accumulated also in the central zone of the anaphase spindle (**Fig. 10C-D**). Appearance of the early phragmoplast was connected with accumulation of PLDα1-YFP (**Fig. 10D**). However, PLDα1-YFP was absent in the late phragmoplast mid-zone during cell plate formation in cytokinesis (**Fig. 10E**). In addition, PLDα1-YFP was accumulated also in surrounding cytoplasm (phragmosome) enclosing cytokinetic apparatus in the centre of partially vacuolated cells (**Fig. 10E, 10B**). As the late phragmoplast reached the cell periphery, PLDα1-YFP was associated with emerging cell plate in the central zone of the ring phragmoplast. Visual comparison of PLDα1-YFP protein level in cortical cytoplasm between dividing cells and neighbouring non-dividing cells (**Fig. 10A, E**) clearly indicated intracellular relocation and accumulation of PLDα1-YFP within and around mitotic microtubule arrays. It indicates potential cell cycle-dependent cooperation of PLDα1-YFP with microtubules in proliferating cells.

Association of PLDα1-YFP with microtubules and CCVs and CCPs

In order to address the functional relationship between mitotic microtubules and PLDα1 in vesicular trafficking, we performed immunofluorescence localization of PLDα1-YFP with microtubules and clathrin-coated vesicles (CCVs) and clathrin-coated pits (CCPs) in dividing and non-dividing root rhizodermal cells of complemented *pldα1-1* mutant seedlings expressing *proPLDα1::PLDα1:YFP* construct. In cytokinetic cells, PLDα1-YFP was associated with microtubules of the ring phragmoplast, while signal was less abundant in the phragmoplast central part. The distribution of clathrin signal in this zone was complementary to PLDα1-YFP distribution, with increased abundance in the central part and decreased abundance at the zone of phragmoplast microtubules. Thus, the highest overlap of the clathrin and the PLDα1-YFP signal was observed at the trailing (inner) edge of the enlarging phragmoplast.

In non-dividing root rhizodermal cells cortical microtubules were bedecked with PLDα1-YFP closely associated or partially colocalized with CCVs. PLDα1-YFP was localized in spot-like structures decorating surface of microtubules in close association or partial colocalization with CCVs. For more detailed subcellular study of PLDα1 and microtubules involvement in vesicular trafficking we used super-resolved structured illumination microscopy (SIM). This analysis revealed association and partial colocalization of PLDα1-YFP with CCVs and CCPs in the close vicinity of cortical microtubules, in some cases creating spots and ring-like structures on their surface.

Association of PLDα1-YFP with CCVs and CCPs in the cytoplasm between cortical microtubules was observed in clathrin-rich clusters that were in close contact with cortical microtubules. Quantitative analysis of the above colocalization studies of clathrin and microtubules following either SIM or CLSM documentation, showed positive colocalization in Col-0 root rhizodermal cells (Pearson's coefficient R=0,62) and no colocalization in *pldα1* mutant (Pearson's coefficient R=0). In conclusion, these data document a complex pattern of PLDα1 subcellular localization and its functional relationship to microtubule arrays in both non-dividing and dividing cells of Arabidopsis plants. Combination of different advanced microscopy methods provided data supporting a possible mechanism of interactions between clathrin-dependent endocytosis and cortical (as well as mitotic) microtubules, through the stabilization function of the PLDα1.

Discussion

PLD is a major family of membrane phospholipid-hydrolyzing enzymes in plants. *A. thaliana* PLDα1 and its product PA are involved in a variety of cellular and physiological processes, such as regulation of stomatal closure and opening, biotic and abiotic stress signalling, and regulation of cytoskeletal organization (Qin et al., 1997; Zhang et al., 2004; Bargmann and Munnik, 2006; Pleskot et al., 2013; Hong et al., 2016). Here we employed advanced microscopic methods to reveal precise developmental expression pattern and subcellular localization of PLDα1 in two rescued *pldα1* mutant lines.

Developmental expression pattern and localization of PLDα1-YFP

A previous study assessing organ distribution of PLDα1 protein in Arabidopsis plants by immunoblotting analysis showed higher amounts of this protein in flowers, stems, roots and siliques rather than in other organs. Moreover, the highest activity of PLDα1 was found in soluble fractions isolated from roots, flowers and siliques (Fan et al., 1999). This study, however, lacked cellular resolution within these organs. In contrast, advanced microscopy imaging used in our experiments revealed high expression levels of PLDα1-YFP in the apical and lateral root cap cells. These findings were in agreement with absolute expression levels of PLDα1 transcript from Genevestigator transcriptomic data (Brady et al., 2007). High expression levels of PLDα1-YFP were found also in trichoblast cell files and in developing roots hairs suggesting its role during root hair development. These results are supported by work of Potocký et al. (2014) reporting PA localization in the plasma membrane of tip-growing pollen tubes. In the aerial part of the plant we observed high PLDα1-YFP protein signal in pavement and stomata guard cells, which is again in accordance to Genevestigator

transcriptomic data (Yang et al., 2008). On the other hand, and in contrary to Genevestigator transcriptomic data, we observed high expression levels of PLDα1-YFP in developing trichomes (Marks et al., 2009). These results support the role of PLDα1 protein in cell developmental processes and polar cell growth.

Cytoplasmic localization of PLDα1-YFP

Previously, PLD was implicated to link cortical microtubules to the plasma membrane (Dhonukshe et al., 2003). Later it was shown that PLDδ is the cortical microtubule-binding protein (Ho et al., 2009; Andreeva et al., 2009). Moreover, a current study showed colocalization of the PLDδ with cortical microtubules near to the plasma membrane in Arabidopsis hypocotyl cells (Zhang et al., 2017b). Many microtubule-dependent processes, e.g. mitosis, cytokinesis, cell elongation and signal transduction are controlled by microtubule dynamics (Wymer and Lloyd, 1996; Hashimoto and Kato, 2006; Jiang et al., 2014). Under normal conditions, *pldα1* plants showed no changes in microtubule organization and density as compared to wild type plants (Zhang et al., 2012). However, PLDα1 KO in Arabidopsis leads to more severe disruption of cortical microtubules by inhibitors (Zhang et al., 2017a) or under salt stress conditions (Zhang et al., 2012). Furthermore, PA produced by activated PLDα1 directs AtMAP65-1 to the plasma membrane and enhances its microtubule stabilizing activity, thus microtubules are stabilized and cell survival is enhanced under the salt stress conditions (Zhang et al., 2012; Pleskot et al., 2014).

PLDα1 is the most abundant PLD present in both soluble and membrane fractions. It translocates from cytosolic to membrane fractions to hydrolyze membrane lipids under stress conditions (Wang et al., 2000; Hong et al., 2016). In our study we observed mainly cytoplasmic localization of PLDα1-YFP, sometimes in the vicinity of cortical microtubules, in non-dividing cells. By contrast, the localization of PLDδ which interacts with cortical microtubules was primarily restricted to the plasma membrane (Zhang et al., 2017b). With the entering of the cell to the mitosis PLDα1-YFP was enriched at mitotic microtubule arrays, namely PPB, microtubules of mitotic spindle in prophase, metaphase and anaphase, as well as to microtubules of the phragmoplast during cytokinesis. Although, colocalization between PLDα1 protein and microtubules was not previously observed in non-dividing protoplasts (Zhang et al., 2012), we detected accumulation of PLDα1-YFP at microtubule arrays during mitotic progression. These results were further confirmed using immunofluorescence colocalization of PLDα1-YFP and microtubules. PLDα1-YFP protein was slightly

accumulated and partially colocalized with microtubules of preprophase band, spindle and both early and late phragmoplast.

SPO14 is phospholipase D in *Saccharomyces cerevisiae*, which specifically hydrolyzes phosphatidylcholine to generate choline and PA. In vegetative cells, SPO14p localizes to the cytoplasm and is not required for normal growth. However, during sporulation, SPO14p localizes to the spindle pole bodies and prospore membrane where it is required for sporulation (Rudge et al., 1998; Liu et al., 2007). One function of SPO14p generated PA is to localize t-SNARE protein Spo20p to the prospore membrane (Nakanishi et al., 2006; Liu et al., 2007). As mentioned above, PLDα1 was enriched in the CCVs which predicts its role in vesicular trafficking (Fan et al., 1999). Furthermore, clathrin heavy chain isoforms and AP180 N-terminal homology domain clathrin-assembly proteins were identified as a PA binding proteins in a previous proteomic study (McLoughlin et al., 2013). Similarly, epsin-like clathrin adaptor 1 binds PA under the negative membrane curvature stress in Arabidopsis (Putta et al., 2016). Furthermore, PLDα1 coimmunoprecipitates with Arabidopsis AP-2 complex and clathrin (Yamaoka et al., 2013), indicating that PLDα1 contributes to clathrin-mediated endocytosis. These data indicate that proteins involved in the clathrin-dependent endocytosis are potential targets of PLDα1-generated PA. Here we provide evidence for close associations of PLDα1-YFP with cortical and mitotic microtubules during cell division. It has been shown previously that the PPB region at the cell cortex possess a large number of CCPs and CCVs. Expected role of clathrin-mediated endocytosis in the PPB region is related to the regulated modification of the cell cortex by controlled removal of particular membrane proteins by endocytosis, being part of the cell division plane memory establishment (Karahara et al., 2009). Centrifugal expansion of the phragmoplast during cytokinesis is driven by microtubule polymerization with substantial microtubule stabilization by bundling at the leading edge of the phragmoplast (Murata et al., 2013). Phragmoplast microtubules are responsible for delivery of vesicles creating cell plate in the mid-zone region. Cell plate formation, however, is also based on removal of excess membrane and cell wall material. Endocytosis and membrane recycling thus play an indispensable role during cell plate expansion (van Oostende-Triplet et al., 2017). Endocytosis was implicated in the spatial restriction of syntaxin protein KNOLLE to the cell plate (Boutté et al., 2010) and in the removal of the cellulose synthase enzymes from the central part and their recycling to the peripheral growth zone of the cell plate (Miart et al., 2014). Consistently with these observations electron tomography analysis revealed a high density of CCPs and CCVs during

the transformation of the tubulo-vesicular network to a planar fenestrated sheet during cell plate formation (Seguí-Simarro et al., 2004). CCPs and CCVs were mostly localized at the trailing (inner) edge of the enlarging phragmoplast. Internalization and recycling of material from the central part and its delivery to the leading edges of maturing cell plate were thus definitely connected to clathrin-dependent endocytosis (Boutté et al., 2010; Ito et al., 2012; Teh et al., 2013; Miart et al., 2014). Based on these findings and on our results we suggest that PLDα1 and its product PA might participate in the complex signalling network involved in the vesicle trafficking and membrane assembly during plant cytokinesis. Although the precise mechanism by which PLDα1 or PA are involved in these processes is unknown. Our results indicate that PLDα1 localized on microtubule surface can potentially functions as molecular glue for CCPs and CCVs associated with microtubules. This is further corroborated by the observation that microtubule-colocalized clathrin structures are quantitatively absent in the *pldα1* mutant.

Conclusions

First part of this thesis briefly summarizes current knowledge on plant microtubules and microtubule end-binding protein family, focused on EB1c protein. Further it introduces phospholipases, especially PLDα1 protein and potential connection of EB1c and PLDα1 to mitogen activated protein kinases. Likewise, conventional and advanced microscopy techniques are briefly explained.

Experimental part of this work describes developmental localization of microtubule EB1c protein in Arabidopsis root using advanced LSFM. Construct *proEB1c::EB1c:GFP* was stably transformed to *Arabidopsis thaliana*. Presence of chimeric EB1c-GFP protein was confirmed in T2 generation by protein extraction followed by SDS-PAGE and immunoblot using anti-GFP antibody. Arabidopsis seedlings showing EB1c-GFP expression were observed using minimally invasive and phototoxic LSFM. We were able to address and quantify nuclear localization of EB1c in meristematic, transition and elongation root zones in three important root tissues such as epidermis, cortex and endodermis. Moreover, we correlated nuclear sizes with EB1c expression levels. Results demonstrate high potential of LSFM for 4-D live fluorescent imaging of plant samples such as growing roots. One indisputable advantage of LSFM is capacity to visualize proteins in deeper cell layers (e.g. endodermis) with minimal optical aberrations. Our results supported the unique role of the transition root zone in the cell reprogramming during their developmental transition from proliferation to differentiation in the developing root apex. We also cloned *EB1c* gene under control of native *EB1c* promotor and fused with *DRONPA*. Expression of chimeric EB1c-DRONPA protein was checked using transient transformation of *Nicotiana benthamina* before stable transformation of *A.thaliana*. This chimeric protein was localized to nuclear subdomains using super-resolution PALM microscopy.

In this study, we utilized advanced microscopy, namely LSFM, for developmental imaging of PLDα1 under natural conditions to explore cell-type specific expression patterns of this protein. KO *pldα1* mutants were complemented with *PLDα1* under control of native *PLDα1* promotor and fused with *YFP*. Stomatal guard cells of cotyledons from wild type plants and plants complemented with PLDα1-YFP closed in response to ABA, in contrast to *pldα1* mutants insensitive to ABA in this respect. Microscopic observations revealed high accumulation of PLDα1-YFP in the root cap, trichoblasts and tips of root hairs. A relatively high expression of PLDα1-YFP was observed in hypocotyl epidermal cells, pavement and stomatal guard cells of cotyledons, and in leaf epidermis, stomata guard cells, trichomes and

petioles. PLDα1-YFP was colocalized with microtubules visualized by *pUBQ1:mRFP::TUB6* construct in both dividing and non-dividing cells. This experiment showed accumulation of PLDα1-YFP on mitotic spindles and phragmoplasts. Thus, we provided a high-resolution subcellular localization of PLDα1 in both dividing and non-dividing Arabidopsis cells in the root meristem and leaf petioles.

References

Adachi S, Minamisawa K, Okushima Y, Inagaki S, Yoshiyama K, Kondou Y, Kaminuma E, Kawashima M, Toyoda T, Matsui M, Kurihara D, Matsunaga S, Umeda M. (2011) Programmed induction of endoreduplication by DNA double-strand breaks in Arabidopsis. *Proc Natl Acad Sci U S A*. 108: 10004–10009. doi: 10.1073/pnas.1103584108

Akhmanova A, Steinmetz MO. (2008) Tracking the ends: a dynamic protein network controls the fate of microtubule tips. *Nat Rev Mol Cell Biol*. 9: 309–322. doi: 10.1038/nrm2369

Ambrose C, Allard JF, Cytrynbaum EN, Wasteneys GO. (2011) A CLASP-modulated cell edge barrier mechanism drives cell-wide cortical microtubule organization in Arabidopsis. *Nat Commun*. 2: 430. doi: 10.1038/ncomms1444

Andreeva Z, Ho AYY, Barthet MM, Potocký M, Bezvoda R, Žárský V, Marc J. (2009) Phospholipase D family interactions with the cytoskeleton: isoform δ promotes plasma membrane anchoring of cortical microtubules. *Funct Plant Biol.* 36: 600–612. doi: 10.1071/FP09024

Austin-Brown SL, Chapman KD. (2002) Inhibition of phospholipase D alpha by N-acylethanolamines. *Plant Physiol*. 129: 1892–1898. doi: 10.1104/pp.001974

Baluška F, Mancuso S. (2013) Root apex transition zone as oscillatory zone. *Front Plant Sci*. 4: 354. doi: 10.3389/fpls.2013.00354

Bargmann BO, Laxalt AM, ter Riet B, Testerink C, Merquiol E, Mosblech A, Leon-Reyes A, Pieterse CM, Haring MA, Heilmann I, Bartels D, Munnik T. (2009a) Reassessing the role of phospholipase D in the Arabidopsis wounding response. *Plant Cell Environ*. 32: 837–50. doi: 10.1111/j.1365-3040.2009.01962.x

Bargmann BO, Munnik T. (2006) The role of phospholipase D in plant stress responses. *Curr Opin Plant Biol*. 9: 515–522. doi: 10.1016/j.pbi.2006.07.011

Baskin TI, Cande WZ. (1990) The Structure and Function of the Mitotic Spindle in Flowering Plants. *Annu Rev Plant Physiol Plant Mol Biol* 41: 277–315. doi: https://doi.org/10.1146/annurev.pp.41.060190.001425

Beck M, Komis G, Müller J, Menzel D, Samaj J. (2010) Arabidopsis homologs of nucleus- and phragmoplast-localized kinase 2 and 3 and mitogen-activated protein kinase 4 are essential for microtubule organization. *Plant Cell*. 22: 755–771. doi: 10.1105/tpc.109.071746

Bisgrove SR, Lee YR, Liu B, Peters NT, Kropf DL. (2008) The microtubule plus-end binding protein EB1 functions in root responses to touch and gravity signals in Arabidopsis. *Plant Cell*. 20: 396–410. doi: 10.1105/tpc.107.056846

Boutté Y, Frescatada-Rosa M, Men S, Chow CM, Ebine K, Gustavsson A, Johansson L, Ueda T, Moore I, Jürgens G, Grebe M. (2010) Endocytosis restricts Arabidopsis KNOLLE syntaxin to the cell division plane during late cytokinesis. *EMBO J*. 29: 546–558. doi: 10.1038/emboj.2009.363

Brady SM, Orlando DA, Lee JY, Wang JY, Koch J, Dinneny JR, Mace D, Ohler U, Benfey PN. (2007) A high-resolution root spatiotemporal map reveals dominant expression patterns. *Science*. 318: 801–806. doi: 10.1126/science.1146265

Carpenter AE, Jones TR, Lamprecht MR, Clarke C, Kang IH, Friman O, Guertin DA, Chang JH, Lindquist RA, Moffat J, Golland P, Sabatini DM. (2006) CellProfiler: image analysis software for identifying and quantifying cell phenotypes. *Genome Biol*. 7: R100. doi: 10.1186/gb-2006-7-10-r100

Casas-Godoy L, Duquesne S, Bordes F, Sandoval G, Marty A. (2012) Lipases: an overview. *Methods Mol Biol*. 861: 3–30. doi: 10.1007/978-1-61779-600-5_1

Chan J, Calder GM, Doonan JH, Lloyd CW. (2003) EB1 reveals mobile microtubule nucleation sites in Arabidopsis. *Nat Cell Biol*. 5: 967–971. doi: 10.1038/ncb1057

Clough SJ, Bent AF. (1998) Floral dip: a simplified method for Agrobacterium-mediated transformation of Arabidopsis thaliana. *Plant J*. 16: 735–743. doi: 10.1046/j.1365-313x.1998.00343.x

Davis AM, Hall A, Millar AJ, Darrah C, Davis SJ. (2009) Protocol: Streamlined sub-protocols for floral-dip transformation and selection of transformants in Arabidopsis thaliana. *Plant Methods*. 5: 3. doi: 10.1186/1746-4811-5-3

del Pozo JC, Diaz-Trivino S, Cisneros N, Gutierrez C. (2006) The balance between cell division and endoreplication depends on E2FC-DPB, transcription factors regulated by the ubiquitin-SCFSKP2A pathway in Arabidopsis. *Plant Cell*. 18: 2224–2235. doi: 10.1105/tpc.105.039651

Dello Ioio R, Linhares FS, Scacchi E, Casamitjana-Martinez E, Heidstra R, Costantino P, Sabatini S. (2007) Cytokinins determine Arabidopsis root-meristem size by controlling cell differentiation. *Curr Biol*. 17: 678–682. doi: 10.1016/j.cub.2007.02.047

Dhonukshe P, Laxalt AM, Goedhart J, Gadella TW, Munnik T. (2003) Phospholipase d activation correlates with microtubule reorganization in living plant cells. *Plant Cell*. 15: 2666–2679. doi: 10.1105/tpc.014977

Dixit R, Chang E, Cyr R. (2006) Establishment of polarity during organization of the acentrosomal plant cortical microtubule array. *Mol Biol Cell*. 17: 1298–1305. doi: 10.1091/mbc.E05-09-0864

Doskočilová A, Kohoutová L, Volc J, Kourová H, Benada O, Chumová J, Plíhal O, Petrovská B, Halada P, Bögre L, Binarová P. (2013) NITRILASE1 regulates the exit from proliferation, genome stability and plant development. *New Phytol*. 198: 685–698. doi: 10.1111/nph.12185

Draviam VM, Shapiro I, Aldridge B, Sorger PK. (2006) Misorientation and reduced stretching of aligned sister kinetochores promote chromosome missegregation in EB1- or APC-depleted cells. *EMBO J*. 25: 2814–2827. doi: 10.1038/sj.emboj.7601168

Durek P, Schmidt R, Heazlewood JL, Jones A, MacLean D, Nagel A, Kersten B, Schulze WX. (2010) PhosPhAt: the Arabidopsis thaliana phosphorylation site database. An update. *Nucleic Acids Res*. 38: 828–834. doi: 10.1093/nar/gkp810

Eliáš M, Potocký M, Cvrčková F, Žárský V. (2002) Molecular diversity of phospholipase D in angiosperms. *BMC Genomics*. 3: 2. doi: 10.1186/1471-2164-3-2

Fan L, Zheng S, Cui D, Wang X. (1999) Subcellular distribution and tissue expression of phospholipase Dalpha, Dbeta, and Dgamma in Arabidopsis. *Plant Physiol*. 119: 1371–1378. doi: https://doi.org/10.1104/pp.119.4.1371

Gottlin EB, Rudolph AE, Zhao Y, Matthews HR, Dixon JE. (1998) Catalytic mechanism of the phospholipase D superfamily proceeds via a covalent phosphohistidine intermediate. *Proc Natl Acad Sci U S A*. 95: 9202–9207. doi: https://doi.org/10.1073/pnas.95.16.9202

Hasezawa S, Ueda K, Kumagai F. (2000) Time-sequence observations of microtubule dynamics throughout mitosis in living cell suspensions of stable transgenic Arabidopsis--direct evidence for the origin of cortical microtubules at M/G1 interface. *Plant Cell Physiol*. 4: 244–250. doi: https://doi.org/10.1093/pcp/41.2.244

Hashimoto T, Kato T. (2006) Cortical control of plant microtubules. *Curr Opin Plant Biol*. 9: 5–11. doi: 10.1016/j.pbi.2005.11.005

Hayashi I, Wilde A, Mal TK, Ikura M. (2005) Structural basis for the activation of microtubule assembly by the EB1 and p150Glued complex. *Mol Cell*. 19: 449–460. doi: 10.1016/j.molcel.2005.06.034

Heller M (1978) Phospholipase D. *Adv Lipid Res* 16: 267–326. doi: https://doi.org/10.1016/B978-0-12-024916-9.50011-1

Heyman J, Van den Daele H, De Wit K, Boudolf V, Berckmans B, Verkest A, Alvim Kamei CL, De Jaeger G, Koncz C, De Veylder L. (2011) Arabidopsis ULTRAVIOLET-B-INSENSITIVE4 maintains cell division activity by temporal inhibition of the anaphase-promoting complex/cyclosome. *Plant Cell*. 23: 4394–4410. doi: 10.1105/tpc.111.091793

Ho AYY, Day DA, Brown MH, Marc J. (2009) Arabidopsis phospholipase Dd as an initiator of cytoskeleton-mediated signalling to fundamental cellular processes. *Functional Plant Biology*. 36: 190–198. doi: https://doi.org/10.1071/FP08222

Ho CM, Hotta T, Guo F, Roberson RW, Lee YR, Liu B. (2011) Interaction of antiparallel microtubules in the phragmoplast is mediated by the microtubule-associated protein MAP65-3 in Arabidopsis. *Plant Cell*. 23: 2909–2923. doi: 10.1105/tpc.110.078204

Hong Y, Devaiah SP, Bahn SC, Thamasandra BN, Li M, Welti R, Wang X. (2009) Phospholipase D epsilon and phosphatidic acid enhance Arabidopsis nitrogen signaling and growth. *Plant J*. 58: 376–87. doi: 10.1111/j.1365-313X.2009.03788.x

Hong Y, Pan X, Welti R, Wang X. (2008) The effect of phospholipase Dalpha3 on Arabidopsis response to hyperosmotic stress and glucose. *Plant Signal Behav*. 3: 1099–1100. doi: 10.1105/tpc.107.056390

Hong Y, Zhao J, Guo L, Kim SC, Deng X, Wang G, Zhang G, Li M, Wang X. (2016) Plant phospholipases D and C and their diverse functions in stress responses. *Prog Lipid Res*. 62: 55–74. doi: 10.1016/j.plipres.2016.01.002

Ishida T, Adachi S, Yoshimura M, Shimizu K, Umeda M, Sugimoto K. (2010) Auxin modulates the transition from the mitotic cycle to the endocycle in Arabidopsis. *Development*. 137: 63–71. doi: 10.1242/dev.035840

Ishida T, Fujiwara S, Miura K, Stacey N, Yoshimura M, Schneider K, Adachi S, Minamisawa K, Umeda M, Sugimoto K. (2009) SUMO E3 ligase HIGH PLOIDY2 regulates endocycle onset and meristem maintenance in Arabidopsis. *Plant Cell*. 21: 2284–2297. doi: 10.1105/tpc.109.068072

Ito E, Fujimoto M, Ebine K, Uemura T, Ueda T, Nakano A. (2012) Dynamic behavior of clathrin in Arabidopsis thaliana unveiled by live imaging. *Plant J*. 69: 204–216. doi: 10.1111/j.1365-313X.2011.04782.x

Jiang K, Akhmanova A. (2011) Microtubule tip-interacting proteins: a view from both ends. *Curr Opin Cell Biol*. 23: 94–101. doi: 10.1016/j.ceb.2010.08.008

Jiang Y, Wu K, Lin F, Qu Y, Liu X, Zhang Q. (2014) Phosphatidic acid integrates calcium signaling and microtubule dynamics into regulating ABA-induced stomatal closure in Arabidopsis. *Planta*. 239: 565–575. doi: 10.1007/s00425-013-1999-5

Karahara I, Suda J, Tahara H, Yokota E, Shimmen T, Misaki K, Yonemura S, Staehelin LA, Mineyuki Y. (2009) The preprophase band is a localized center of clathrin-mediated endocytosis in late prophase cells of the onion cotyledon epidermis. *Plant J*. 57: 819–831. doi: 10.1111/j.1365-313X.2008.03725.x

Kohoutová L, Kourová H, Nagy SK, Volc J, Halada P, Mészáros T, Meskiene I, Bögre L, Binarová P. (2015) The Arabidopsis mitogen-activated protein kinase 6 is associated with γ-tubulin on microtubules, phosphorylates EB1c and maintains spindle orientation under nitrosative stress. *New Phytol*. 207: 1061–1074. doi: 10.1111/nph.13501

Komaki S, Abe T, Coutuer S, Inzé D, Russinova E, Hashimoto T. (2010) Nuclear-localized subtype of end-binding 1 protein regulates spindle organization in Arabidopsis. *J Cell Sci*. 123: 451–459. doi: 10.1242/jcs.062703

Komarova Y, De Groot CO, Grigoriev I, Gouveia SM, Munteanu EL, Schober JM, Honnappa S, Buey RM, Hoogenraad CC, Dogterom M, Borisy GG, Steinmetz MO, Akhmanova A. (2009) Mammalian end binding proteins control persistent microtubule growth. *J Cell Biol*. 184: 691–706. doi: 10.1083/jcb.200807179

Komis G, Mistrik M, Šamajová O, Ovečka M, Bartek J, Šamaj J. (2015) Superresolution live imaging of plant cells using structured illumination microscopy. *Nat Protoc*. 10: 1248–63. doi: 10.1038/nprot.2015.083

Kusner DJ, Barton JA, Qin C, Wang X, Iyer SS. (2003) Evolutionary conservation of physical and functional interactions between phospholipase D and actin. *Arch Biochem Biophys*. 412: 231–241. doi: https://doi.org/10.1016/S0003-9861(03)00052-3

Kusner DJ, Barton JA, Wen KK, Wang X, Rubenstein PA, Iyer SS. (2002) Regulation of phospholipase D activity by actin. Actin exerts bidirectional modulation of Mammalian phospholipase D activity in a polymerization-dependent, isoform-specific manner. *J Biol Chem*. 277: 50683–50692. doi: 10.1074/jbc.M209221200

Lamprecht MR, Sabatini DM, Carpenter AE. (2007) CellProfiler: free, versatile software for automated biological image analysis. *Biotechniques*. 42: 71–75. doi: 10.2144/000112257

Ledbetter MC, Porter KR. (1963) A "MICROTUBULE" IN PLANT CELL FINE STRUCTURE. *J Cell Biol*. 19: 239–250. doi: 10.1083/jcb.19.1.239

Lein W, Saalbach G. (2001) Cloning and direct G-protein regulation of phospholipase D from tobacco. *Biochim Biophys Acta*. 1530: 172–183. doi: https://doi.org/10.1016/S1388-1981(00)00182-7

Li M, Hong Y, Wang X. (2009) Phospholipase D- and phosphatidic acid-mediated signaling in plants. *Biochim Biophys Acta*. 1791: 927–935. doi: 10.1016/j.bbalip.2009.02.017

Liu S, Wilson KA, Rice-Stitt T, Neiman AM, McNew JA. (2007) In vitro fusion catalyzed by the sporulation-specific t-SNARE light-chain Spo20p is stimulated by phosphatidic acid. *Traffic*. 8: 1630–1643. doi: 10.1111/j.1600-0854.2007.00628.x

Marc J, Granger CL, Brincat J, Fisher DD, Kao Th, McCubbin AG, Cyr RJ. (1998) A GFP-MAP4 reporter gene for visualizing cortical microtubule rearrangements in living epidermal cells. *Plant Cell*. 10: 1927–1940. doi: https://doi.org/10.1105/tpc.10.11.1927

Marks MD, Wenger JP, Gilding E, Jilk R, Dixon RA. (2009) Transcriptome analysis of Arabidopsis wild-type and gl3-sst sim trichomes identifies four additional genes required for trichome development. *Mol Plant*. 2: 803–822. doi: 10.1093/mp/ssp037

Mathur J, Mathur N, Kernebeck B, Srinivas BP, Hülskamp M. (2003) A novel localization pattern for an EB1-like protein links microtubule dynamics to endomembrane organization. *Curr Biol*. 13: 1991–1997. doi: https://doi.org/10.1016/j.cub.2003.10.033

McLoughlin F, Arisz SA, Dekker HL, Kramer G, de Koster CG, Haring MA, Munnik T, Testerink C. (2013) Identification of novel candidate phosphatidic acid-binding proteins involved in the salt-stress response of Arabidopsis thaliana roots. *Biochem J*. 450: 573–581. doi: 10.1042/BJ20121639

Meijer HJ, Munnik T. (2003) Phospholipid-based signaling in plants. *Annu Rev Plant Biol*. 54: 265–306. doi: 10.1146/annurev.arplant.54.031902.134748

Miart F, Desprez T, Biot E, Morin H, Belcram K, Höfte H, Gonneau M, Vernhettes S. (2014) Spatio-temporal analysis of cellulose synthesis during cell plate formation in Arabidopsis. *Plant J*. 77: 71–84. doi: 10.1111/tpj.12362

Motes CM, Pechter P, Yoo CM, Wang YS, Chapman KD, Blancaflor EB. (2005) Differential effects of two phospholipase D inhibitors, 1-butanol and N-acylethanolamine, on in

vivo cytoskeletal organization and Arabidopsis seedling growth. *Protoplasma*. 226: 109–123. doi: 10.1007/s00709-005-0124-4

Munnik T, Musgrave A. (2001) Phospholipid Signaling in Plants: Holding On to Phospholipase D. *Sci STKE.* 2001: 42. doi: 10.1126/stke.2001.111.pe42

Murashige T, Skoog F. (1962) A revised medium for rapid growth and bioassays with tobacco tissue cultures. *Physiol. Plant*. 15: 473–497. doi: 10.1111/j.1399-3054.1962.tb08052.x

Murata T, Sano T, Sasabe M, Nonaka S, Higashiyama T, Hasezawa S, Machida Y, Hasebe M. (2013) Mechanism of microtubule array expansion in the cytokinetic phragmoplast. *Nat Commun*. 4: 1967. doi: 10.1038/ncomms2967

Nakamura M, Naoi K, Shoji T, Hashimoto T. (2004) Low concentrations of propyzamide and oryzalin alter microtubule dynamics in Arabidopsis epidermal cells. *Plant Cell Physiol*. 45: 1330–1334. doi: 10.1093/pcp/pch300

Nakanishi H, Morishita M, Schwartz CL, Coluccio A, Engebrecht J, Neiman AM. (2006) Phospholipase D and the SNARE Sso1p are necessary for vesicle fusion during sporulation in yeast. *J Cell Sci*. 119: 1406–1415. doi: 10.1242/jcs.02841

Novák D, Kuchařová A, Ovečka M, Komis G, Šamaj J. (2016) Developmental Nuclear Localization and Quantification of GFP-Tagged EB1c in Arabidopsis Root Using Light-Sheet Microscopy. *Front Plant Sci*. 6: 1187. doi: 10.3389/fpls.2015.01187

Novák D, Vadovič P, Ovečka M, Šamajová O, Komis G, Colcombet J, Šamaj J. (2018) Gene Expression Pattern and Protein Localization of Arabidopsis Phospholipase D Alpha 1 Revealed by Advanced Light-Sheet and Super-Resolution Microscopy. *Front Plant Sci*. 9: 371. doi: 10.3389/fpls.2018.00371

Ovečka M, Vaškebová L, Komis G, Luptovčiak I, Smertenko A, Šamaj J. (2015) Preparation of plants for developmental and cellular imaging by light-sheet microscopy. *Nat Protoc*. 10: 1234–1247. doi: 10.1038/nprot.2015.081

Panteris E, Adamakis ID, Daras G, Hatzopoulos P, Rigas S. (2013) Differential responsiveness of cortical microtubule orientation to suppression of cell expansion among the developmental zones of Arabidopsis thaliana root apex. *PLoS One*. 8: e82442. doi: 10.1371/journal.pone.0082442

Pappan K, Austin-Brown S, Chapman KD, Wang X. (1998) Substrate selectivities and lipid modulation of plant phospholipase D alpha, -beta, and -gamma. *Arch Biochem Biophys*. 353: 131–140. doi: 10.1006/abbi.1998.0640

Pleskot R, Li J, Zárský V, Potocký M, Staiger CJ. (2013) Regulation of cytoskeletal dynamics by phospholipase D and phosphatidic acid. *Trends Plant Sci*. 18: 496–504. doi: 10.1016/j.tplants.2013.04.005

Pleskot R, Pejchar P, Staiger CJ, Potocký M. (2014) When fat is not bad: the regulation of actin dynamics by phospholipid signaling molecules. *Front Plant Sci*. 5: 5. doi: 10.3389/fpls.2014.00005

Potocký M, Pleskot R, Pejchar P, Vitale N, Kost B, Zárský V. (2014) Live-cell imaging of phosphatidic acid dynamics in pollen tubes visualized by Spo20p-derived biosensor. *New Phytol*. 203: 483–494. doi: 10.1111/nph.12814

Putta P, Rankenberg J, Korver RA, van Wijk R, Munnik T, Testerink C, Kooijman EE. (2016) Phosphatidic acid binding proteins display differential binding as a function of membrane curvature stress and chemical properties. *Biochim Biophys Acta*. 1858: 2709–2716. doi: 10.1016/j.bbamem.2016.07.014

Qin C, Wang C, Wang X (2002) Kinetic analysis of Arabidopsis phospholipase D delta. Substrate preference and mechanism of activation by Ca2+ and phosphatidylinositol 4,5-biphosphate. *J Biol Chem*. 277: 49685–49690. doi: 10.1074/jbc.M209598200

Qin C, Wang X. (2002) The Arabidopsis phospholipase D family. Characterization of a calcium-independent and phosphatidylcholine-selective PLD zeta 1 with distinct regulatory domains. *Plant Physiol*. 128: 1057–1068. doi: 10.1104/pp.010928

Qin W1, Pappan K, Wang X. (1997) Molecular heterogeneity of phospholipase D (PLD). Cloning of PLDgamma and regulation of plant PLDgamma, -beta, and -alpha by polyphosphoinositides and calcium. *J Biol Chem*. 272: 28267–28273. doi: 10.1016/j.tplants.2013.04.005

Quarles RH, Dawson RM. (1969) The distribution of phospholipase D in developing and mature plants. *Biochem J*. 112: 787–794. doi: 10.1042/bj1120787

Rudge SA, Morris AJ, Engebrecht J. (1998) Relocalization of phospholipase D activity mediates membrane formation during meiosis. *J Cell Biol*. 140: 81–90. doi: 10.1083/jcb.140.1.81

Šamajová O, Komis G, Šamaj J. (2013) Emerging topics in the cell biology of mitogen-activated protein kinases. *Trends Plant Sci*. 18: 140–148. doi: 10.1016/j.tplants.2012.11.004

Šamajová O, Komis G, Šamaj J. (2014) Immunofluorescent localization of MAPKs and colocalization with microtubules in Arabidopsis seedling whole-mount probes. *Methods Mol Biol*. 1171: 107–115. doi: 10.1007/978-1-4939-0922-3_9

Sang Y, Zheng S, Li W, Huang B, Wang X. (2001) Regulation of plant water loss by manipulating the expression of phospholipase D alpha. *Plant J*. 28:135–44. doi: https://doi.org/10.1046/j.1365-313X.2001.01138.x

Seguí-Simarro JM, Austin JR 2nd, White EA, Staehelin LA. (2004) Electron tomographic analysis of somatic cell plate formation in meristematic cells of Arabidopsis preserved by high-pressure freezing. *Plant Cell*. 16: 836–856. doi: 10.1105/tpc.017749

Smertenko AP, Chang HY, Sonobe S, Fenyk SI, Weingartner M, Bögre L, Hussey PJ. (2006) Control of the AtMAP65-1 interaction with microtubules through the cell cycle. *J Cell Sci*. 119: 3227–3237. doi: 10.1242/jcs.03051

Smertenko AP, Chang HY, Wagner V, Kaloriti D, Fenyk S, Sonobe S, Lloyd C, Hauser MT, Hussey PJ. (2004) The Arabidopsis microtubule-associated protein AtMAP65-1: molecular analysis of its microtubule bundling activity. *Plant Cell*. 16: 2035–2047. doi: 10.1105/tpc.104.023937

Smertenko AP, Kaloriti D, Chang HY, Fiserova J, Opatrny Z, Hussey PJ. (2008) The C-terminal variable region specifies the dynamic properties of Arabidopsis microtubule-associated protein MAP65 isotypes. *Plant Cell*. 20: 3346–3358. doi: 10.1105/tpc.108.063362

Stuckey JA, Dixon JE. (1999) Crystal structure of a phospholipase D family member. *Nat Struct Biol*. 6: 278–284. doi: 10.1038/6716

Sung TC, Altshuller YM, Morris AJ, Frohman MA. (1999a) Molecular analysis of mammalian phospholipase D2. *J Biol Chem*. 274: 494–502. doi: 10.1074/jbc.274.1.494

Sung TC, Zhang Y, Morris AJ, Frohman MA. (1999b) Structural analysis of human phospholipase D1. *J Biol Chem*. 274: 3659–3666. doi: 10.1074/jbc.274.6.3659

Takáč T, Pechan T, Samajová O, Ovečka M, Richter H, Eck C, Niehaus K, Samaj J. (2012) Wortmannin treatment induces changes in Arabidopsis root proteome and post-Golgi compartments. *J Proteome Res*. 11: 3127–3142. doi: 10.1021/pr201111n

Tamura N, Draviam VM. (2012) Microtubule plus-ends within a mitotic cell are 'moving platforms' with anchoring, signalling and force-coupling roles. *Open Biol*. 2: 120132. doi: 10.1098/rsob.120132

Teh OK, Shimono Y, Shirakawa M, Fukao Y, Tamura K, Shimada T, Hara-Nishimura I. (2013) The AP-1 μ adaptin is required for KNOLLE localization at the cell plate to

mediate cytokinesis in Arabidopsis. *Plant Cell Physiol*. 54: 838–847. doi: 10.1093/pcp/pct048

Tilney LG, Bryan J, Bush DJ, Fujiwara K, Mooseker MS, Murphy DB, Snyder DH. (1973) Microtubules: evidence for 13 protofilaments. *J Cell Biol*. 59: 267–275. doi: 10.1083/jcb.59.2.267

Tirnauer JS, Canman JC, Salmon ED, Mitchison TJ. (2002) EB1 targets to kinetochores with attached, polymerizing microtubules. *Mol Biol Cell*. 13: 4308–4316. doi: 10.1091/mbc.E02-04-0236

Van Damme D, Van Poucke K, Boutant E, Ritzenthaler C, Inzé D, Geelen D. (2004) In vivo dynamics and differential microtubule-binding activities of MAP65 proteins. *Plant Physiol*. 136: 3956–3967. doi: 10.1104/pp.104.051623

van Leeuwen W, Okrész L, Bögre L, Munnik T. (2004) Learning the lipid language of plant signalling. *Trends Plant Sci*. 9: 378–384. doi: 10.1016/j.tplants.2004.06.008

van Oostende-Triplet C, Guillet D, Triplet T, Pandzic E, Wiseman PW, Geitmann A. (2017) Vesicle Dynamics during Plant Cell Cytokinesis Reveals Distinct Developmental Phases. *Plant Physiol*. 174: 1544–1558. doi: 10.1104/pp.17.00343

Wang C, Wang X. (2001) A novel phospholipase D of Arabidopsis that is activated by oleic acid and associated with the plasma membrane. *Plant Physiol*. 127: 1102–1112. doi: https://doi.org/10.1104/pp.010444

Wang C, Zien CA, Afitlhile M, Welti R, Hildebrand DF, Wang X. (2000) Involvement of phospholipase D in wound-induced accumulation of jasmonic acid in arabidopsis. *Plant Cell*. 12: 2237–2246. doi: https://doi.org/10.1105/tpc.12.11.2237

Wang G, Ryu S, Wang X. (2012) Plant phospholipases: an overview. *Methods Mol Biol*. 861: 123–137. doi: 10.1007/978-1-61779-600-5_8

Wang X. (2000) Multiple forms of phospholipase D in plants: the gene family, catalytic and regulatory properties, and cellular functions. *Prog Lipid Res*. 39: 109–149. doi: https://doi.org/10.1016/S0163-7827(00)00002-3

Wang X. (2001) PLANT PHOSPHOLIPASES. *Annu Rev Plant Physiol Plant Mol Biol*. 52: 211–231. doi: 10.1146/annurev.arplant.52.1.211

Wang X. (2004) Lipid signaling. *Curr Opin Plant Biol*. 7: 329–36, doi: 10.1016/j.pbi.2004.03.012

Wasteneys GO. (2002) Microtubule organization in the green kingdom: chaos or self-order? *J Cell Sci*. 115: 1345–1354. doi: http://jcs.biologists.org/content/115/7/1345.long

Wymer C, Lloyd C. (1996) Dynamic microtubules: implications for cell wall patterns. *Trends Plant Sci*. 7: 222–228. doi: 10.1016/1360-1385(96)86899-3

Yamaoka S, Shimono Y, Shirakawa M, Fukao Y, Kawase T, Hatsugai N, Tamura K, Shimada T, Hara-Nishimura I. (2013) Identification and dynamics of Arabidopsis adaptor protein-2 complex and its involvement in floral organ development. *Plant Cell*. 25: 2958–2969. doi: 10.1105/tpc.113.114082

Yamaryo Y, Dubots E, Albrieux C, Baldan B, Block MA. (2008) Phosphate availability affects the tonoplast localization of PLDzeta2, an Arabidopsis thaliana phospholipase D. *FEBS Lett*. 582: 685–690. doi: 10.1016/j.febslet.2008.01.039

Yang Y, Costa A, Leonhardt N, Siegel RS, Schroeder JI. (2008) Isolation of a strong Arabidopsis guard cell promoter and its potential as a research tool. *Plant Methods*. 4: 6. doi: 10.1186/1746-4811-4-6

Yu L, Nie J, Cao C, Jin Y, Yan M, Wang F, Liu J, Xiao Y, Liang Y, Zhang W. (2010) Phosphatidic acid mediates salt stress response by regulation of MPK6 in Arabidopsis thaliana. *New Phytol*. 188: 762–773. doi: 10.1111/j.1469-8137.2010.03422.x

Zhang Q, Lin F, Mao T, Nie J, Yan M, Yuan M, Zhang W. (2012) Phosphatidic acid regulates microtubule organization by interacting with MAP65-1 in response to salt stress in Arabidopsis. *Plant Cell*. 24: 4555–4576. doi: 10.1105/tpc.112.104182

Zhang Q, Qu Y, Wang Q, Song P, Wang P, Jia Q, Guo J. (2017a) Arabidopsis phospholipase D alpha 1-derived phosphatidic acid regulates microtubule organization and cell development under microtubule-interacting drugs treatment. *J Plant Res*. 130: 193–202. doi: 10.1007/s10265-016-0870-8

Zhang Q, Song P, Qu Y, Wang P, Jia Q, Guo L, Zhang C, Mao T, Yuan M, Wang X, Zhang W. (2017b) Phospholipase Dδ negatively regulates plant thermotolerance by destabilizing cortical microtubules in Arabidopsis. *Plant Cell Environ*. 40: 2220–2235. doi: 10.1111/pce.13023

Zhang W, Qin C, Zhao J, Wang X. (2004) Phospholipase D alpha 1-derived phosphatidic acid interacts with ABI1 phosphatase 2C and regulates abscisic acid signaling. *Proc Natl Acad Sci U S A*. 101: 9508–9513. doi: 10.1073/pnas.0402112101

Zhao J, Wang X. (2004) Arabidopsis phospholipase Dalpha1 interacts with the heterotrimeric G-protein alpha-subunit through a motif analogous to the DRY motif in G-protein-coupled receptors. *J Biol Chem*. 279: 1794–1800. doi: 10.1074/jbc.M309529200

List of publications

Novák D, Kuchařová A, Ovečka M, KomisG, Šamaj J. (2016) Developmental Nuclear Localization and Quantification of GFP-Tagged EB1c in *Arabidopsis* Root Using Light-Sheet Microscopy. *Front. Plant Sci*. 6: 1187. doi: 10.3389/fpls.2015.01187

Komis G, Novák D, Ovečka M, Šamajová O, Šamaj J. (2018) Advances in Imaging Plant Cell Dynamics. *Plant Physiol*. 176: 80–93. doi: 10.1104/pp.17.00962

Novák D, Vadovič P, Ovečka M, Šamajová O, Komis G, Colcombet J, Šamaj J. (2018) Gene Expression Pattern and Protein Localization of Arabidopsis Phospholipase D Alpha 1 Revealed by Advanced Light-Sheet and Super-Resolution Microscopy. *Front. Plant Sci*. 9: 371. doi: 10.3389/fpls.2018.00371

Supplements

Abstrakt v českém jazyce

Tato disertační práce je zaměřena na END BINDING protein 1c (EB1c) a protein FOSFOLIPASA D ALFA 1 (PLDα1) a zahrnuje jejich vývojovou expresi a lokalizaci v semenáčcích *Arabidopsis thaliana* za použití pokročilých mikroskopických technik.

Hlavní kořen vyšších rostlin je anatomicky definován v bočním směru existencí zástupů buněk v konkrétních pletivech, podélně pak přítomností odlišných vývojových zón. Pro rostliny specifický EB1c, který je u *Arabidopsis thaliana* jedním ze tří členů EB1 proteinové rodiny, vykazuje v nedělících se buňkách kořenové špičky výraznou jadernou lokalizaci. Za použití moderního „light-sheet" fluorescenčního mikroskopu (LSFM) jsme kvantifikovali vývojově regulovanou expresi GFP-značeného proteinu EB1c, který byl pod kontrolou nativního *EB1c* promotoru. Kvantifikace byla provedena ve vztahu k velikosti buněčných jader v různých kořenových pletivech (epidermis, primární kůra, endodermis) a v jednotlivých kořenových vývojových zónách (meristém, přechodná a prodlužovací zóna). Naše výsledky podpořily teorii, že v kořenové špičce hraje přechodná zóna jedinečnou úlohu v programování buněk během vývoje při přechodu buněk z rychlého dělení k jejich diferenciaci. Kromě toho byl klonován fúzní *DRONPA* a *EB1c* konstrukt pod kontrolou vlastního *EB1c* promotoru, který byl přechodně transformován do listů *Nicotiana benthamiana* a stabilně do rostlin *Arabidopsis thaliana*. Fotoaktivační lokalizační mikroskopie (PALM) ukázala bodovou akumulaci EB1c-DRONPA proteinu v buněčných jádrech.

PLDα1 protein a jeho produkt fosfatidová kyselina, hrají důležitou roli v mnoha fyziologických a buněčných procesech. Zaměřili jsme se na studium vývojového expresního vzoru a subcelulární lokalizaci tohoto proteinu za použití kombinace LSFM, strukturované osvětlovací mikroskopie (SIM), mikroskopie s rotujícím diskem a konfokální mikroskopie. Knock-out *pldα1* mutanti, komplementovaní fúzním proteinem PLDα1-YFP pod kontrolou vlastního *PLDα1* promotoru, vykazovali vyšší akumulaci PLDα1-YFP v kořenové čepičce a ve špičkách rostoucích kořenových vlásků. V epidermálních buňkách listů, řapíků a hypokotylů byl PLDα1-YFP lokalizován v cytoplazmě, a vykazoval zvýšenou akumulaci v oblasti kortikální cytoplazmatické vrstvy. Nicméně v dělících se kořenových a řapíkových buňkách byl PLDα1-YFP obohacený v dělícím vřeténku a fragmoplastu, což naznačila jeho kolokalizace s mikrotubuly. Tato studie ukázala vývojově kontrolovanou expresi a subcelulární lokalizaci PLDα1 proteinu jak v dělících se, tak nedělících se buňkách.